Università
degli Studi di
Messina

Department of Mathematical and Computer Sciences,
Physical Sciences and Earth Sciences
Department of Biomedical, Dental and Morphological and Functional Imaging

PhD in Bioengineering Applied to Medical Sciences [ING-IND/31]

THESIS FOR THE DEGREE OF PHILOSOPHIAE DOCTOR

Design and simulations of spintronic devices for conventional applications and unconventional computing

PhD program coordinator
Ch.mo Prof. Michele GAETA

Candidate
Eleonora RAIMONDO
Mat. 521044

Thesis supervisor
Ch.mo Prof. Ing. Giovanni FINOCCHIO

Academic Year 2022-2023 (XXXVI cycle)

Abstract

Spintronic technologies have emerged as promising candidates for ultralow power and CMOS-compatible technology. In addition, spintronics can have a role in facing the von Neumann architecture bottlenecks.
The main potential applications of spintronics are microwave detection/generation, biomedicine, energy harvesting, memories – with solutions where the information can be stored in topological magnetic textures (i.e. skyrmions) –, neuromorphic computing, and unconventional computing applications such as probabilistic computing.

This thesis deals with two main topics:

1) the design and modeling of magnetic tunnel junctions (MTJs), one of the key spintronic devices, which are characterized by compact size, high-speed operation (up to tens of GHz), and versatility;

2) the exploration of the static and dynamic properties of topological textures (i.e. magnetic skyrmions) for their potential use in many applications and for the development of skyrmionics as a promising technology for hybrid skyrmionics-CMOS technology.

Chapter 1 introduces the micromagnetic formalism, fundamental for the understanding of the magnetization behavior in ferromagnetic materials at the nanoscale. This chapter describes a micromagnetic solver developed in C/C++ language able to efficiently perform data-driven tests of MTJ designs. In addition, a user-friendly interface has been developed and benchmarked. The main outcomes of this chapter include solutions for the development of MTJ-based electromagnetic energy harvesting, verified with experimental activities implemented in the laboratory of Prof. Yang at National University of Singapore, and spintronic accelerometers.

Chapter 2 presents static and dynamic properties of magnetic skyrmions stabilized in different magnetic materials and heterostructures. In particular, we identified a protocol for the characterization of the type of skyrmion, pure Neel vs Hybrid skyrmion. This activity has been implemented in collaboration with Prof. Wanjung Jiang's group at Tsinghua University of China. The last part of the chapter deals with skyrmion manipulation driven by temperature gradients.

Chapter 3 introduces the main concepts of neuromorphic computing and deep learning, with a particular focus on how spintronics can be used to develop the field of neuromorphic spintronics. In particular, we show how to use intrinsic nonlinearity of time nonlocality to implement different types of neurons and operations, including the extraction of dark knowledge.

Chapter 4 provides a brief introduction on the idea behind the Ising model and its use in facing combinatorial optimization problems. The primary focus is the implementation of probabilistic Ising machines based on the idea of probabilistic computing with p-bits (PC). We present a PC solver developed in C/C++ with CUDA^{TM} acceleration that incorporates several energy minimization algorithms, such as standard annealing and parallel tempering. Many potential solutions of probabilistic bits with MTJs are also explored and an experimental implementation of PC achieved in collaboration with Prof. Pedram Khalili Amiri at Northwestern University (USA) is presented.

Acknowledgements

Sono tante le persone che hanno reso questi anni di dottorato ricchi di diverse emozioni e le parole per ringraziarle sono sicuro riduttive. Senza dubbio, il primo e profondo ringraziamento va al mio supervisore, il Prof. Giovanni Finocchio, senza il quale tutto questo non sarebbe stato possibile. Il Prof. Finocchio non solo mi ha costantemente motivato, ma mi ha anche offerto l'opportunità di vivere tantissime esperienze e incontrare persone che hanno arricchito la mia vita culturalmente e personalmente. Trovo difficile esprimere quanto gli sia grata per tutto ciò.

Ricordo il primo viaggio, in Spagna, per collaborare con la Prof.ssa Oksana Chubykalo-Fesenko. Mi terrorizzava l'idea di presentare i risultati ad una persona così preparata e al di fuori del nostro gruppo ma, grazie al sostegno del Prof. Finocchio e del Prof. Riccardo Tomasello, tutto andò per il meglio. Quel viaggio è stato solo l'inizio di molte esperienze. Parlando di Riccardo, tutto il mio sapere sugli skyrmioni è dovuto a lui, ma ringraziarlo solo per questo sarebbe troppo poco. Lo ringrazio per avermi ascoltato e consigliato ma soprattutto per i momenti divertenti che abbiamo condiviso, come il mese a Chicago insieme ad Emily Darwin, le canzoncine durante la preparazione dei pasti, il viaggio a Toronto e la visita alle Cascate del Niagara.

Il periodo di studio alla Northwestern University è stata una delle più grandi esperienze vissute in questi anni, sei mesi lontana da casa e fuori dalla mia confort zone, un'opportunità che mi ha portato ad una crescita personale e scientifica che mai avrei potuto immaginare. Lì ho conosciuto il Prof. Pedram Khalili Amiri, una delle persone più gentili e accoglienti che io potessi avere la fortuna di incontrare, oltre che dall'indubbia preparazione scientifica. Ho conosciuto Víctor López-Domínguez, Yixin Shao, Banibrato Sinha e Sevdenur Arpaci che ringrazio per avermi fatto comprendere un po' di più quello che è il mondo sperimentale. Questa esperienza è stata resa ancora più speciale con l'arrivo del Prof. Finocchio e la Prof.ssa Francesca Garescì, che hanno portato vitalità non solo in ufficio ma in tutto il piano, con loro la pausa caffè era diventata una regola. Li ringrazio per avermi trattato come una di famiglia, per i pranzi insieme e le uscite anche durante il fine settimana.

Un ringraziamento speciale va ad Andrea Grimaldi, con cui ho condiviso così tante esperienze in questi tre anni che ho come l'impressione di conoscerlo da sempre. Questi anni di dottorato avrebbero perso gran parte del loro valore senza di lui: le continue risate, le lezioni di meme (anche se con scarso successo), la pazienza nel sopportare i miei momenti negativi. Lo ringrazio per essere sempre presente.

Ringrazio la Prof.ssa Anna Giordano per avermi dato in ogni occasione la carica morale (e del PC), e per essere stata presente nei momenti difficili, come i primi mesi di dottorato, e belli, come la conferenza a Dallas. Ringrazio il Prof. Azzerboni, per avermi trasmesso l'importanza dell'insegnamento e del senso di appartenenza ad un gruppo.

Un grazie va anche alla parte del gruppo Petaspin che si trova a Bari, il Prof. Mario Carpentieri, il Prof. Vito Puliafito e il Prof. Davi Rodrigues, ed ai ragazzi Andrea Meo, Michalis Lianeris, Luciano Mazza e Pietro Tullo, con cui è sempre un piacere condividere momenti anche al di fuori della ricerca.

Ringrazio l'INGV e, in particolare, il Dr. Stefano Chiappini per la disponibilità per le simulazioni.

Ringrazio i miei amici per i momenti spensierati.

Infine, non posso che ringraziare la mia meravigliosa famiglia per aver trovato sempre la parole giuste a darmi supporto e incoraggiamento, e per aver dimostrato grande comprensione. In particolare, ringrazio mia sorella Clarissa per aver ascoltato tutti i miei racconti, per avermi aiutato e consigliato, gioendo insieme a me per ogni piccola vittoria.

Contents

List of Figures

List of Tables

List of Algorithms

List of Abbreviations

AF	Activation function
ANN	Artificial neural network
CCW	Counter-clockwise
CMOS	Complementary metal-oxide semiconductor
CNN	Convolutional neural network
COP	Combinatorial optimization problem
CW	Clockwise
DMI	Dzyaloshinskii-Moriya interaction
*b*DMI	Bulk Dzyaloshinskii-Moriya interaction
*i*DMI	Interfacial Dzyaloshinskii-Moriya interaction
DOM	Degree of match
DOR	Degree of rectification
DW	Domain wall
EHM	Energy harvesting module
FC	Fully connected
FL	Free layer
FM	Ferromagnetic
FPGA	Field-programmable gate array
FWHM	Full width at half maximum (linewidth)
GPU	Graphics processing unit
GUI	Graphical user interface
IM	Ising machine
LFSR	Linear-feedback shift register
LLG	Landau-Lifshitz-Gilbert
LLGS	Landau-Lifshitz-Gilbert-Slonczewski
MAC	Multiply-accumulate
Max-Cut	Maximum cut problem
Max-SAT	Maximum satisfiability problem
MEMS	Microelectromechanical system

MNIST	Mixed national institute of standards and technology database
MTJ	Magnetic tunnel junction
NP	Nondeterministic polynomial time
P	Polynomial time
p-bit	Probabilistic bit
PC	Probabilistic computing with p-bits
PC-CUDA	Probabilistic computing with p-bits solver in CUDA
PL	Pinned layer
PRNG	Pseudorandom number generator
PT	Parallel tempering
ReLU	Rectified linear unit
RF	Radiofrequency
RKKY	Ruderman-Kittel-Kasuya-Yosida interaction
RNG	Random number generator
RNG	Random number generator
SA	Simulated annealing
SAF	Synthetic antiferromagnetic
SOC	Spin-orbit coupling
SOT	Spin-orbit torque
SQA	Simulated quantum annealing
STD	Spin-torque diode
STNO	Spin-transfer nano-oscillator or spin-torque nano-oscillator
STT	Spin-transfer torque
TRNG	True random number generator
VCMA	Voltage-controlled magnetic anisotropy
wMax-SAT	Weighted maximum satisfiability problem

List of Symbols

Symbols regarding the micromagnetism

A_{ex}	Exchange interaction constant
A^{ex}	Antiferromagnetic interlayer exchange coupling constant
dt	Simulation step
dV	Volume of magnetic material or infinitesimal volume
D	Dzyaloshinskii-Moriya parameter
e	Electron's charge
f	Frequency
g	Landé factor
$g_T\left(\boldsymbol{m}, \boldsymbol{m}_p\right)$	Polarization function
$\boldsymbol{H}_{ani}$	Anisotropy field
$\boldsymbol{H}_{dmg}$	Demagnetizing field (or magnetostatic field or stray field or dipolar field)
$\boldsymbol{H}_{eff}$	Effective field
$\boldsymbol{H}_{ext}$	External field
$\boldsymbol{H}_{th}$	Thermal field
$\boldsymbol{h}_{FLT_{SOT}}$	Field-like torque SOT field
$\boldsymbol{h}_{FLT_{STT}}$	Field-like torque STT field
$\boldsymbol{h}_{SOT}$	Normalized SOT field
$\boldsymbol{h}_{STT}$	Normalized STT field
$\boldsymbol{h}_{ani}$	Normalized anisotropy field
$\boldsymbol{h}_{dmg}$	Normalized demagnetizing field
$\boldsymbol{h}_{eff}$	Normalized effective field
$\boldsymbol{h}_{ext}$	Normalized external field
$\boldsymbol{h}_{th}$	Normalized thermal field
h_{VCMA}	Normalized VCMA field
J_{AC}	Alternating current density

J_{DC}	Direct current density
J_{SOT}	Current density inducing SOT
J_{STT}	Current density inducing STT
J_{th}	Threshold current
k_B	Boltzmann constant
K_u	Uniaxial anisotropy constant
$\boldsymbol{m}$	Normalized magnetization vector (of the FL)
m_x, m_y, m_z	x-, y- and z- component of the normalized magnetization
$\boldsymbol{m}_p$	Normalized magnetization of the PL
$\boldsymbol{M}$	Magnetization vector
M_S	Saturation magnetization
N	Demagnetizing tensor
N_{sk}	Skyrmion winding number
p	power
P	Spin polarization factor
P_{RF}	Radiofrequency power
q_{SOT}	Coefficient of the $\tau_{FLT_{SOT}}$
q_{STT}	Coefficient of the $\tau_{FLT_{STT}}$
Q	Quality factor
Q_h	Helicity number
Q_v	Vorticity number
$\boldsymbol{r}_{ij}$	Positional vector
R_{AP}	Antiparallel electrical resistance
R_P	Parallel electrical resistance
$\boldsymbol{S}$	Spin
t_z	Thickness of the free layer
T	Temperature
u_{DMI}	DMI energy density
u_{ani}	Anisotropy energy density
u_{dmg}	Demagnetizing energy density
u_{exch}	Exchange energy density
u_{ext}	Zeeman (or external field) energy density
$\boldsymbol{u}_k$	Unit vector along the anisotropy axis
V_{DC}	Rectified voltage
α_G	Gilber damping
γ	Gyromagnetic ratio

$\Delta m_x, \Delta m_y, \Delta m_z$	x-, y- and z- component of the magnetization amplitude
$\Delta x, \Delta y, \Delta z$	x-, y- and z- dimension of the cell
ε	Sensitivity
ξ	Supercriticality parameter
θ_{SHE}	Spin-Hall angle
$\boldsymbol{\mu}$	Spin angular momentum (or magnetic moment)
μ_0	Vacuum permeability
μ_B	Bohr's magneton
σ	STT coefficient
$\boldsymbol{\sigma}_{SHE}$	Electron spin polarization
$\boldsymbol{\tau}$	Torque
$\tau_{FLT_{SOT}}$	Field-like torque due to SOT
$\tau_{FLT_{STT}}$	Field-like torque due to STT
τ_{PT}	Precessional (or non-adiabatic) damping torque
τ_{SL}	Slonczewski torque
ϕ_{SkH}	Skyrmion Hall angle

Symbols regarding the artificial intelligence

L	Loss function
w	Weights
y	Output of the neuron
z	Output of the neuron before the AF
η	Learning rate

Symbols regarding the Ising model

σ_i	Ising spin
$\boldsymbol{\sigma}$	Spin configuration
I	Input signal
$\boldsymbol{J}, J_{ij}$	Coupling matrix
$\boldsymbol{h}, h_i$	External bias field
N	Number of iterations
β	Inverse pseudo-temperature
J_T	Transverse field

Chapter 1

Spintronic devices: fundamental and applications

There are different ideas on how to use spintronic technology in biomedical applications. The most challenging is the use of magnetoresistive sensors based on magnetic tunnel junctions (MTJs) to measure the magnetic activity of the brain. This can be achieved with several device solutions. Here we have explored the basic properties of MTJs working as spintronic diodes. We have developed a general purpose numerical code able to perform a fast search in the enormous phase space of the parameters that are necessary for the design of MTJs. Another category of sensors which are very useful in biomedical applications are the accelerometers. For example, accelerometers can be used for physical activity monitoring, Parkinson disease monitoring, and vibration analysis for bone health. Here we have designed a spintronic accelerometer that can potentially have a smaller size (sub-micrometer) and a simpler reading scheme than current state-of-the art solutions. The last study of this chapter is linked to the development of applications of MTJs that can be useful for size reduction of implantable devices. In particular, we have explored the potential use of spintronic technology for the development of electromagnetic energy harvesting, which can be used for the design of battery-less implantable devices.

1.1 Introduction to micromagnetic modeling

The spontaneous magnetization observed in ferromagnetic materials is a quantum phenomenon that emerges at the atomic level [1]. However, employing a quantum model becomes computationally intractable when dealing with real systems. To address this bottleneck, various mesoscopic models have been proposed to approximate the behavior of ferromagnetic materials above the nanometric scale. Depending on the assumptions introduced by a given model, it can accurately describe the system only within a certain length scale. At the mesoscopic level, micromagnetic models are still required while at larger scale, systems can be approximated with macromagnetic models, as illustrated in Figure 1.1.

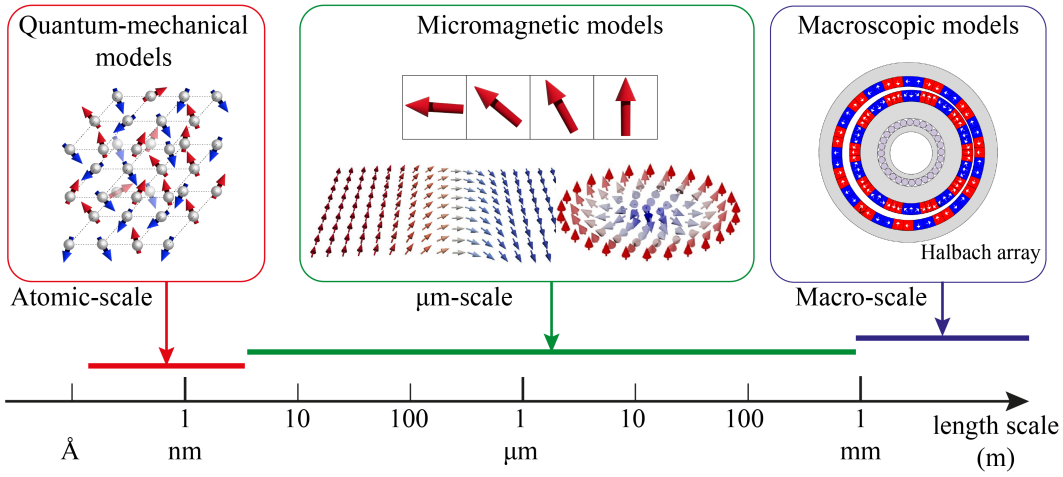

FIGURE 1.1: Overview of established models for describing ferromagnets at different length scales.

The studies developed within this thesis are based on the micromagnetic theory. Originating in 1935 with Landau and Lifshitz's calculations of domain walls [2], micromagnetism garnered substantial attention from researchers, such as W. Brown, in 1960. Micromagnetism analyzes materials on a scale large enough to define a continuous magnetization vector rather than individual spins but is still sufficiently small to describe the transition between different domains [3]. This allows the study of spin textures such as DWs and skyrmions.

In the late 1950s, Brown was the first to propose solving micromagnetic models through numerical integration methods rather than analytically [4]. However, in

the mid-1980s this approach experienced a significant improvement thanks to the availability of larger computational power. This progress enabled the implementation of powerful micromagnetic tools such as GPU-based solvers [5], facilitating the investigation of realistic systems, making calculations more easily comparable with experimental data, and creating tools for data-driven design of technologies based on micromagnetic systems, such as spintronics and magnonics.

This section introduces the micromagnetic formalism with the derivation of the dynamical equation that characterizes the ferromagnetic behavior – the Landau-Lifshitz-Gilbert equation. The latter part focuses on introducing and modeling the state-of-the-art of spintronic devices based on MTJs. The developed C/CUDA solver for MTJ design is described in detail. The chapter concludes by presenting two main results achieved during this PhD program.

1.2 Assumptions of the micromagnetic theory

Ferromagnetic materials exhibit spontaneous magnetization in absence of an external magnetic field. The individual magnetic moments μ_i are strongly coupled through the exchange interactions, promoting the alignment of neighboring moments along the same direction. This alignment results in a local magnetization that can be expressed as a continuous vector field, function of the space and time, $M(r,t)$, with constant magnitude, called saturation magnetization M_S. As a result, the ferromagnetic material can be idealized as a set of infinitesimal volumes dV, each containing a number of spins N that is large enough to guarantee a constant magnetization M_S, and has to be small enough to guarantee the continuous nature of the magnetization. The size of this volume is strongly linked with the exchange interactions. In other words, the magnetization represents the density of magnetic moments $\boldsymbol{\mu}_i$ in a ferromagnetic volume dV:

$$\boldsymbol{M}(r,t) = \frac{1}{dV}\sum_{i=1}^{N}\boldsymbol{\mu}_i \tag{1.1}$$

The direction of the magnetization is determined by the unit vector $\boldsymbol{m}(r,t) = \boldsymbol{M}(r,t)/M_S$, which smoothly varies between each element of volumes. Figure 1.2 illustrates the main assumptions of the micromagnetic theory.

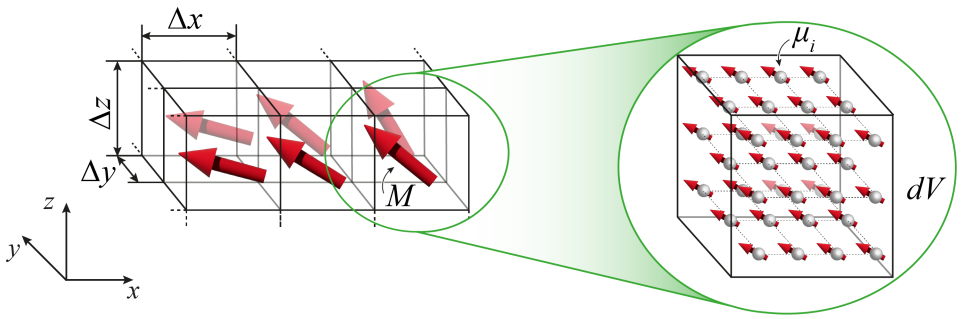

FIGURE 1.2: Illustration of the main assumptions of the micromagnetic theory. Magnetization vector $\boldsymbol{M}$ is the sum of all magnetic moments $\boldsymbol{\mu}_i$ inside the volume dV. The magnetization smoothly varies between each element of volumes, in accordance with the continuous nature of the magnetization.

From a computational point of view, the continuous problem is spatially discretized for numerical solutions by using, for example, finite differences or finite elements approaches. Variables in the discretized system represent the magnetization values at each cell of the computational mesh in 3D space (x, y, z). Finite elements use a non-uniform mesh, while finite differences use a uniform regular mesh. Here, we focus on the finite differences.

From a modeling point of view, the size of the volumes dV is the size of the computational cells in which the magnetic material sample is spatially discretized. The micromagnetic theory deals with parameters defining the characteristic lengths, representing the scale at which magnetization varies substantially. Therefore, numerically, the smallest size of the computational cells $(\Delta x,\ \Delta y,\ \Delta z)$ must be smaller than these characteristic lengths. Two characteristic lengths resulting from the competition between different energy terms are derived in paragraph 1.3.1 and 1.3.3.

Although the exchange interaction is one of the main contributions in ferromagnetic materials, other physical mechanisms are essential to fully describe their energy.

1.3 Energy contributions

Micromagnetic theory takes into account energy contributions of both quantum nature and classical nature. Quantum contributions include interactions like exchange and anisotropy, while classical ones involve magnetostatic and Zeeman

energies. In the following sections, we will describe free and thermal energy contributions.

1.3.1 Exchange energy

As discussed previously, the exchange energy is a short-range interaction responsible for the type of alignment between neighboring spins. It arises from the Pauli exclusion principle and the electrostatic Coulomb interaction. The Heisenberg Hamiltonian that describes the exchange interaction between two neighboring spins $\boldsymbol{S}_i$ and $\boldsymbol{S}_j$ is given by:

$$\mathcal{H}_{exch} = -2 \sum_{\langle i,j \rangle} J_{ij} \boldsymbol{S}_i \cdot \boldsymbol{S}_j \tag{1.2}$$

The sum is over all pairs of first-neighboring spins, where J_{ij} is the exchange integral between the i^{th} and the j^{th} spins. The value of J_{ij} decreases rapidly with the distance between spins, and it is positive for ferromagnetic materials (favoring parallel alignment) and negative for antiferromagnetic materials (favoring antiparallel alignment). At micromagnetic scale, it is a good assumption to consider that the exchange integral is the same for every pair of neighboring spins $J_{ij} = J$, and the spin operators are replaced by vectors with constant spin modulus $|\boldsymbol{S}_i| = |\boldsymbol{S}_j| = S$, $\boldsymbol{S}_{i,j} = S\boldsymbol{s}_{i,j}$. The equivalent continuum expression of the Heisenberg Hamiltonian is:

$$\mathcal{U}_{exch} = -2JS^2 \sum_{\langle i,j \rangle} \cos\theta_{ij} \tag{1.3}$$

where θ_{ij} is the angle between i^{th} and j^{th} spin. For the assumptions of continuity of the model, this angle is very small, allowing the approximation $\cos\theta_{ij} = 1 - \left(\theta_{ij}^2/2\right)$:

$$\mathcal{U}_{exch} \approx JS^2 \sum_i \sum_j \theta_{ij}^2 \tag{1.4}$$

In micromagnetic theory, the unit spin vector $\boldsymbol{s}_i$ of each magnetic moment $\boldsymbol{\mu}_i$ is replaced by the unit vector of the magnetization $\boldsymbol{m}_i = \boldsymbol{M}_i / M_S$, as illustrated in Figure 1.3. The small angle can be expressed as the difference between two neighboring magnetization vectors: $\theta_{ij} \approx |\boldsymbol{m}_i - \boldsymbol{m}_j| \approx |(\boldsymbol{r}_{ij} \cdot \nabla)\, \boldsymbol{m}|$ where $\boldsymbol{r}_{ij}$ is

the position vector between the i^{th} and j^{th} magnetizations.

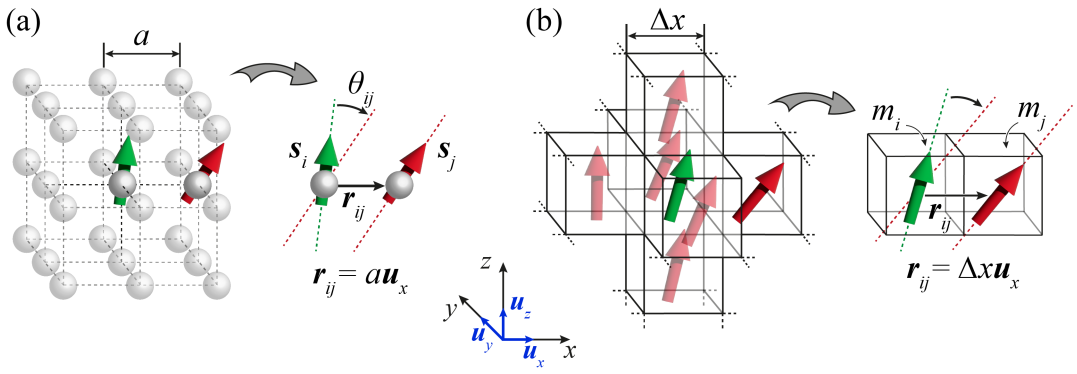

FIGURE 1.3: A schematic representation of the exchange interaction between first neighbors in $\boldsymbol{u}_x$ direction in (a) the atomic Heisenberg model using a simple cubic crystal and (b) the micromagnetic model, where the spins are replaced by the magnetization vectors, and the lattice parameter a is replaced by the size of the computational cell Δx (Δy, Δz).

In the continuous representation, the summation is replaced by an integral over the volume of the ferromagnetic material. The exchange energy is:

$$\mathcal{U}_{exch} = \int_V u_{exch}\, dV = \int_V \left(A_{ex} \left(\nabla \boldsymbol{m} \right)^2 \right)\, dV \tag{1.5}$$

We use u to denote the energy density. $(\nabla \boldsymbol{m})^2 \equiv (\nabla m_x)^2 + \left(\nabla m_y\right)^2 + (\nabla m_z)^2$ and A_{ex} is the exchange constant in J/m, a material-dependent parameter. For a cubic crystal, $A_{ex} = JS^2 c/a$, where a is the lattice parameter, i.e. the distance between first neighbors, and $c = 1, 2$, and 4 for simple, body-centered, and face-centered cubic lattices, respectively.

A characteristic length resulting from the competition between the exchange interaction and the magnetostatic field is known as exchange length l_{ex}:

$$l_{ex} = \sqrt{\frac{2A_{ex}}{\mu_o M_s^2}} \tag{1.6}$$

where μ_0 is the magnetic permeability of vacuum and M_S is the saturation magnetization. The length l_{ex} is relevant when the magneto-static dipolar interactions are dominant over the anisotropy, like in soft magnetic materials.

1.3.2 Dzyaloshinskii-Moriya interaction

The DMI is a chiral energetic term, introducing an antisymmetric exchange contribution, resulting from the spin-orbit coupling (SOC) [6, 7]. In contrast to the exchange interaction, which favors parallel alignment of neighboring spins, the DMI promotes orthogonal alignment, facilitating the formation of rotational magnetization textures such as skyrmions. There are two types of DMI: bulk DMI (*b*DMI) originating from a break of the crystal inversion symmetry and the presence of high SOC atoms in a ferromagnetic alloy (for instance B20 materials), and the interfacial DMI (*i*DMI) occurring at the interface of non-equivalent layers, typically an ultrathin ferromagnetic layer and an heavy metal with strong SOC, like Pt [8]. At the atomic scale, the energy of the antisymmetric counterpart of the exchange interaction is given by:

$$\mathcal{U}_{\mathrm{DMI}} = \sum_{\langle i,j \rangle} \boldsymbol{d}_{ij} \cdot (\boldsymbol{S}_i \times \boldsymbol{S}_j) \tag{1.7}$$

The sum is over all pairs of first-neighboring spins, where $\boldsymbol{d}_{ij}$ is the DMI vector coupling the i^{th} and j^{th} spin, $\boldsymbol{S}_i$ and $\boldsymbol{S}_j$, respectively, and depends on the system under study. For ultrathin isotropic ferromagnetic layers, $\boldsymbol{d}_{ij} = d\, \boldsymbol{u}_{ij} \times \boldsymbol{u}_n$ where $\boldsymbol{u}_{ij}$ is the unit vector between $\boldsymbol{S}_i$ and $\boldsymbol{S}_j$, and $\boldsymbol{u}_n$ is the unit vector normal to the interface. Figure 1.4 illustrates an example of spin orientation for (a) *b*DMI and (b) *i*DMI. In the assumption of an ultrathin layer, a constant DMI parameter d can be considered.

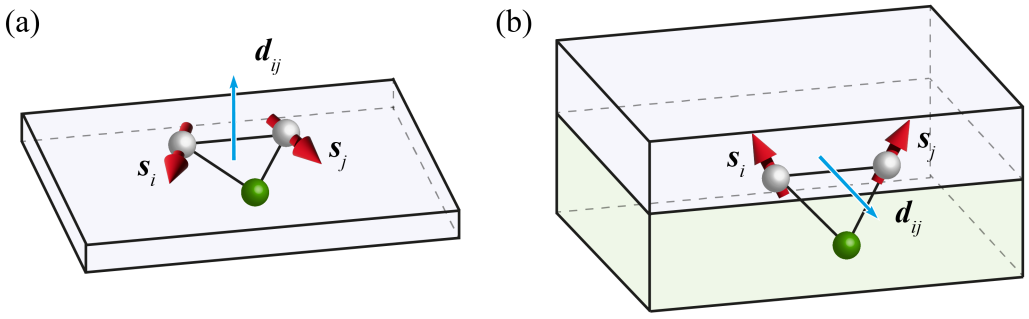

FIGURE 1.4: A sketch of (a) *b*DMI generated in a ferromagnetic layer between two atomic spins $\boldsymbol{S}_i$ and $\boldsymbol{S}_j$ and an atom with a strong spin-orbit coupling (green sphere). (b) *i*DMI at the interface between a ferromagnetic layer (gray) and a heavy metal with strong spin-orbit coupling (green).

In presence of a perpendicular magnetic anisotropy along the z-axis, the micromagnetic iDMI energy is given by:

$$\begin{aligned}\mathcal{U}_{i\text{DMI}} &= \int_V u_{i\text{DMI}}\, dV \\ &= \int_V \left(D\ \left(\boldsymbol{m}\cdot\nabla m_z - m_z\cdot\nabla\boldsymbol{m}\right)\right)\ dV \\ &= \int_V \left(D\ \left(m_x\frac{\partial m_z}{\partial x} - m_z\frac{\partial m_x}{\partial x} + m_y\frac{\partial m_z}{\partial y} - m_z\frac{\partial m_y}{\partial y}\right)\right)\ dV\end{aligned} \tag{1.8}$$

Where D is a material-dependent parameter expressed in $\mathrm{J/m^2}$.

The bDMI energy is given by:

$$\mathcal{U}_{b\text{DMI}} = \int_V u_{b\text{DMI}} dV = \int_V \left(D\ \left(\boldsymbol{m}\cdot\nabla\times\boldsymbol{m}\right)\right)\ dV \tag{1.9}$$

The DMI affects the boundary condition (BC) of the ferromagnet as following [9, 10]:

$$\begin{aligned}b\text{DMI BC: } &\frac{d\boldsymbol{m}}{dn} = \frac{D}{2A_{ex}}\left(\boldsymbol{m}\times\boldsymbol{n}\right) \\ i\text{DMI BC: } &\frac{d\boldsymbol{m}}{dn} = \frac{D}{2A_{ex}}\left(\hat{z}\times\boldsymbol{n}\right)\times\boldsymbol{m}\end{aligned} \tag{1.10}$$

Where $\boldsymbol{n}$ is an arbitrary orientation of the edge normal.

1.3.3 Anisotropy energy

Experiments have demonstrated that magnetic materials are not isotropic and thus exhibit an energetically favored crystallographic direction, referred to as the easy axis, along which they are easier to magnetize. On contrary, the direction that is energetically unfavored is termed hard axis. This anisotropic behavior arises from spin-orbit interactions at the atomic scale. The magnetocrystalline anisotropy energy can be defined as the excess of energy required to magnetize a material in a certain direction different from the easy one. In this thesis, we specifically refer to materials with uniaxial anisotropy which are the most common when dealing with spintronic devices. The expression of the uniaxial magnetocrystalline anisotropy energy, considering the first term of its Taylor expansion, is given by:

$$\mathcal{U}_{ani} = \int_V u_{ani}\, dV = \int_V \left(K_0 - K_1\left(\boldsymbol{m}\cdot\boldsymbol{u}_k\right)^2\right)\ dV \tag{1.11}$$

Where K_0 and K_1 (in J/m^3) are coefficients determined experimentally, with $K_1 \equiv K_u$ indicating the perpendicular anisotropy constant (easy axis along the z-axis). $\boldsymbol{u}_k$ is the unit vector along the anisotropy axis, either an easy or hard axis, depending on the sign of K_u. A positive value of K_u corresponds to an energetically favored axis (as illustrated in Figure 1.5 (a)), aligning the magnetization vector parallel (P) or antiparallel (AP) to the easy axis. On the contrary, a negative value of K_u corresponds to an energetically unfavored axis (as illustrated in Figure 1.5 (b)), promoting the magnetization to lie in the plane perpendicular to $\boldsymbol{u}_k$.

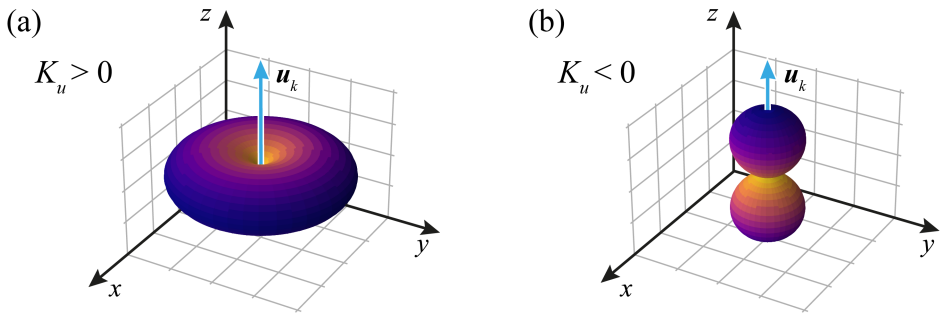

FIGURE 1.5: Energy density of the uniaxial magnetic anisotropy for (a) $K_u > 0$: $\boldsymbol{u}_k$ is the energetically favored axis, the magnetization tends to align parallel to it, and (b) $K_u < 0$: $\boldsymbol{u}_k$ is the energetically unfavored axis, the magnetization tends to lie in the plane perpendicular to it.

A characteristic length resulting from the competition between the exchange interaction and magnetocrystalline anisotropy is known as wall width l_w, and it is computed as follow:

$$l_w = \sqrt{\frac{A_{ex}}{K_u}} \tag{1.12}$$

It is usually relevant in materials with large anisotropy.

1.3.4 Magnetostatic energy

The magnetostatic energy arises from the interactions between the magnetic dipoles within a material. It leads to a magnetic field, opposed to the internal $\boldsymbol{M}$, that tends to demagnetize the sample. From this, it takes the name of demagnetizing field $\boldsymbol{H}_{dmg}$ (also known as magnetostatic field or stray field or

dipolar field). Derived from the solution of the magnetostatic problem based on Maxwell's equations which can be expressed as follows:

$$\begin{aligned} \nabla \cdot \boldsymbol{B}(\boldsymbol{r}) &= 0 \\ \nabla \times \boldsymbol{H}_{dmg}(\boldsymbol{r}) &= 0 \end{aligned} \tag{1.13}$$

Here, $\boldsymbol{B}(\boldsymbol{r})$ is the magnetic induction field, representing the sum of the magnetization $\boldsymbol{M}(\boldsymbol{r})$ (inside the material) and the demagnetizing field $\boldsymbol{H}_{dmg}$ (outside the material), as illustrated in Figure 1.6. This relationship is defined as:

$$\boldsymbol{B}(\boldsymbol{r}) = \mu_0 \left(\boldsymbol{M}(\boldsymbol{r}) + \boldsymbol{H}_{dmg}(\boldsymbol{r}) \right) \tag{1.14}$$

where μ_0 is the vacuum permeability.

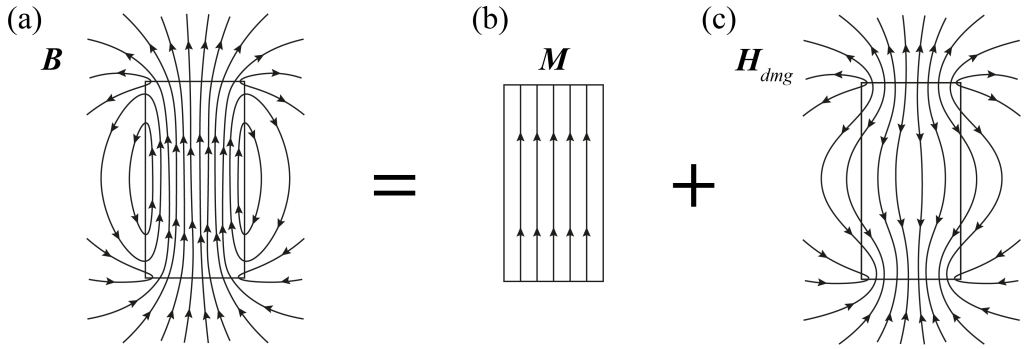

FIGURE 1.6: A schematic representation of (a) the magnetic induction field $\boldsymbol{B}$, sum of (b) internal magnetic field $\boldsymbol{M}$ and (c) the demagnetizing field $\boldsymbol{H}_{dmg}$ generated by $\boldsymbol{M}$.

By incorporating Eq. (1.14) into Eq.(1.13), they can be rewritten as:

$$\begin{aligned} \nabla \cdot \mu_0 \left(\boldsymbol{M}(\boldsymbol{r}) + \boldsymbol{H}_{dmg}(\boldsymbol{r}) \right) &= 0 \\ \nabla \times \boldsymbol{H}_{dmg}(\boldsymbol{r}) &= 0 \end{aligned} \tag{1.15}$$

The general solution of the second equation of Eq.(1.15) is expressed as $\boldsymbol{H}_{dmg}(\boldsymbol{r}) = -\nabla U_{dmg}(\boldsymbol{r})$. By substituting this into the first equation of Eq. (1.15), the potential $U_{dmg}(\boldsymbol{r})$ inside the sample can be derived:

$$\nabla^2 U_{dmg}(\boldsymbol{r}) = -\nabla \boldsymbol{M}(\boldsymbol{r}) \tag{1.16}$$

The calculation of $\boldsymbol{H}_{dmg}(\boldsymbol{r})$ also involves the magnetic charges on the surface. To fulfill the surface boundary condition that $\boldsymbol{H}_{dmg}(\boldsymbol{r})$ must obey, fictitious volume and surface magnetic charge densities, respectively $\rho_m(\boldsymbol{r})$ and $\sigma_m(\boldsymbol{r})$, are defined as:

$$\begin{aligned} \rho_m(\boldsymbol{r}) &= -\nabla \boldsymbol{M}(\boldsymbol{r}) \\ \sigma_m(\boldsymbol{r}) &= \boldsymbol{M}(\boldsymbol{r}) \cdot \boldsymbol{n} \end{aligned} \tag{1.17}$$

Where $\boldsymbol{n}$ is the unit vector perpendicular to the surface S of the magnetic material. Finally, the demagnetizing field at each point $\boldsymbol{r}$ of the sample is given by:

$$\boldsymbol{H}_{dmg}(\boldsymbol{r}) = \frac{1}{4\pi}\left[\int_{V'} \frac{(\boldsymbol{r}-\boldsymbol{r}')\,\rho_m}{|\boldsymbol{r}-\boldsymbol{r}'|^3} dV' + \int_{S'} \frac{(\boldsymbol{r}-\boldsymbol{r}')\,\sigma_m}{|\boldsymbol{r}-\boldsymbol{r}'|^3} dS'\right] \tag{1.18}$$

Where V' and S' are, respectively, the volume and the surface of the sample, and $|\boldsymbol{r}-\boldsymbol{r}'|$ is the distance between the point in which the field is being calculated $\boldsymbol{r}$ and all other field-creating magnetic moments at $\boldsymbol{r}'$. The magnetostatic energy is given by [1]:

$$\mathcal{U}_m = \int_V u_m dV = -\frac{1}{2}\mu_0 \int_V \left(\boldsymbol{H}_{dmg}(\boldsymbol{r}) \cdot \boldsymbol{M}(\boldsymbol{r})\right)\, dV \tag{1.19}$$

The magnetostatic energy minimizes the presence of isolated magnetic charges. This effect can be interpreted as an anisotropy contribution, known as shape anisotropy. In simpler words, it implies that the orientation of magnetization can be influenced by altering the geometry of the magnetic structure rather than modifying the intrinsic material anisotropy. This contribution is energetically unfavored from the exchange point of view. Therefore, the magnetization configuration is a balance between the exchange and the magnetostatic energy. The trade off between these two terms is the main origin of domains in ferromagnets.

In a discrete scenario, the magnetostatic field in each cell can be expressed as [11, 12]:

$$\boldsymbol{H}_{dmg}(\boldsymbol{r}) = -M_S \sum_{\boldsymbol{r}'}^{N_c} N\left(\boldsymbol{r}-\boldsymbol{r}'\right) \cdot \boldsymbol{m}\left(\boldsymbol{r}'\right) \tag{1.20}$$

where the sum is over the total number of cells N_c, and $N(\boldsymbol{r}-\boldsymbol{r}')$ is the demagnetizing tensor, a $3 \times 3 \times N_c$ symmetric tensor that depends on the relative position

between the cells and on the geometry of the sample. Therefore, it can be computed one time for a given geometry, and $\boldsymbol{H}_{dmg}(\boldsymbol{r})$ can be calculated as a discrete 3D convolution of N with $\boldsymbol{m}$. This can be more efficiently computed in the Fourier domain [12].

The computation of this energetic field is the most time and resource consuming among all contributions because, as discussed, it is a non-local term. This means that the field at point $\boldsymbol{r}$ depends on the magnetization of all the other points $\boldsymbol{r}'$ within the volume of the sample, as illustrated in Figure 1.7.

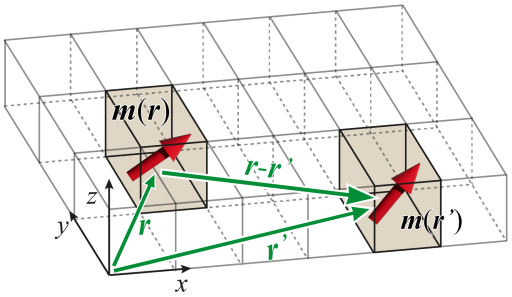

FIGURE 1.7: An illustration highlighting that the magnetostatic field computation at each computational cell takes into account the contribution from all cells of the sample. Depicted are two representative computational cells with magnetization $\boldsymbol{m}(\boldsymbol{r})$ and $\boldsymbol{m}(\boldsymbol{r}')$.

1.3.5 Zeeman energy

The Zeeman field is an external field $\boldsymbol{H}_{ext}$ applied to the sample, enabling the magnetization of the sample in any given direction, as illustrated in Figure 1.8.

It is characterized by a vectorial field with a known module and direction. The Zeeman energy is defined as:

$$\mathcal{U}_{ext} = \int_V u_{ext} dV = -\mu_0 \int_V \left(\boldsymbol{H}_{ext}(\boldsymbol{r}) \cdot \boldsymbol{M}(\boldsymbol{r})\right) \, dV \tag{1.21}$$

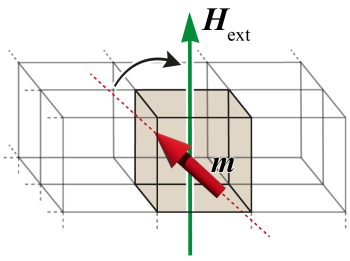

FIGURE 1.8: The magnetization $\boldsymbol{m}$ tends to align with the external applied field $\boldsymbol{H}_{ext}$.

1.3.6 Oersted field

The flow of electrical current within a conductor generates a magnetic field, known as Oersted field $\boldsymbol{H}_{Oe}$, as illustrated in Figure 1.9 (a).

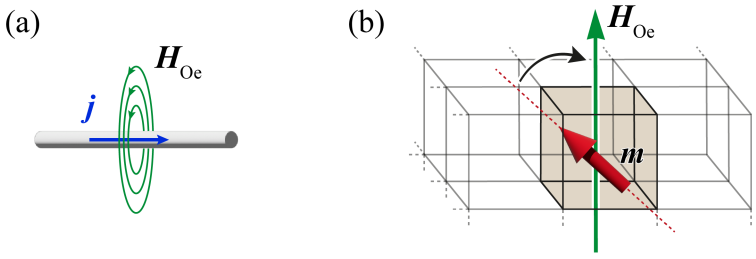

FIGURE 1.9: (a) A current j flowing in a wire generates a magnetic field $\boldsymbol{H}_{Oe}$ and the field lines form concentric circles around the wire. (b) The magnetization $\boldsymbol{m}$ tends to align with the local direction of the Oersted field $\boldsymbol{H}_{Oe}$.

The Biot-Savart law determines the magnetic field $\boldsymbol{H}_{Oe}$ generated by a distributed current of density $\boldsymbol{j}(\boldsymbol{r})$ flowing in a wire:

$$\boldsymbol{H}_{oe}(\boldsymbol{r}) = \frac{1}{4\pi}\int_{V'}\left(\boldsymbol{j}(\boldsymbol{r}) \times \frac{\boldsymbol{r}-\boldsymbol{r}'}{|\boldsymbol{r}-\boldsymbol{r}'|^3}\right) dV' \tag{1.22}$$

where $\boldsymbol{r}-\boldsymbol{r}'$ is the distance between the position r at which the field is evaluated and each position $\boldsymbol{r}'$ within the sample volume V'. The Oersted field acts qualitatively as a non-uniform external field, causing the magnetization to align along its direction, as illustrated in Figure 1.9 (b). Its energy is defined similarly to the

Zeeman energy:

$$\mathcal{U}_{Oe} = \int_V u_{Oe} dV = -\mu_0 \int_V \left(\boldsymbol{H}_{Oe}\left(\boldsymbol{r}\right) \cdot \boldsymbol{M}\left(\boldsymbol{r}\right) \right) \, dV \tag{1.23}$$

1.4 Equilibrium states

Micromagnetic theory predicts the spatial configuration of the magnetization under specific conditions, associating an energy value with each configuration. In accordance with the variational principle, at equilibrium, the magnetization configuration inside a sample $\{\boldsymbol{m}\left(\boldsymbol{r},t\right) | r \in V, \, \boldsymbol{m}\left(\boldsymbol{r},t\right)| = 1\}$ satisfies the conditions (energy minimization):

$$\begin{cases} \delta u_{tot}(\boldsymbol{m}) = 0 \\ \delta^2 u_{tot}(\boldsymbol{m}) > 0 \end{cases} \tag{1.24}$$

where $\delta u_{tot}\left(\boldsymbol{m}\right) = \delta u_{tot}\left(\boldsymbol{m} + \delta \boldsymbol{m}\right) - \delta u_{tot}\left(\boldsymbol{m}\right)$ is the infinitesimal variation of the energy density induced by a small variation of the magnetization $\delta \boldsymbol{m}$. The total energy of the system is the sum of the different energy contributions in each elementary volume ΔV, described in paragraph 1.3. The total energy density of a ferromagnetic sample is given by:

$$u_{tot} = u_{exh} + u_{ani} + u_{ext} + \ldots \tag{1.25}$$

The equilibrium state is determined by the competition among these different energy terms. The energy landscape can have several local minima, satisfying the conditions (1.24), corresponding to metastable states, and these states depend on the initial configuration. Eventually, for $t \to \infty$ the system can reach the ground state, which is the global minimum. An illustrative example of an energy landscape is presented in Figure 1.10.

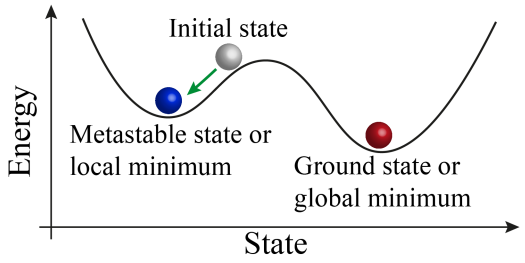

FIGURE 1.10: Sketch of an energy landscape, featuring the initial state (gray sphere), a local minimum (blue sphere), and a global minimum (red sphere).

The system can only feel the magnetic field that results from the energy change, therefore we derive a total effective field, $\boldsymbol{H}_{eff}$, acting on the magnetization as a functional derivative of the energy density of the volume, u_V:

$$\boldsymbol{H}_{eff} = -\frac{1}{\mu_0 M_S}\frac{\delta u_V}{\delta \boldsymbol{m}} \tag{1.26}$$

Usually, we refer to the dimensionless effective field: $\boldsymbol{h}_{eff} = \boldsymbol{H}_{eff}/M_S$.

At the equilibrium, from the Eq. (1.24) the derivative $\delta u_{tot}(\boldsymbol{m}) = 0$, and the Brown's equations must be satisfied:

$$\begin{cases} \boldsymbol{m} \times \boldsymbol{H}_{eff} = 0 \\ \boldsymbol{m} \times \left[-\dfrac{\partial u_s}{\partial \boldsymbol{m}} - \dfrac{\partial u_V}{\partial(\nabla \boldsymbol{m})} \cdot \boldsymbol{n} \right] = 0 \end{cases} \tag{1.27}$$

The first expression, regarding the volume of the sample, states that the static equilibrium is reached when the torque $\boldsymbol{\tau} = \mu_0 \boldsymbol{M} \times \boldsymbol{H}_{eff}$ vanishes at each point of the volume while the second equation sets the boundary conditions at the surface.

The effective field components resulting from the derivative of the energy density (described in paragraph 1.2) include the exchange $\boldsymbol{H}_{exh}$, the iDMI field $\boldsymbol{H}_{i\text{DMI}}$, the anisotropy field $\boldsymbol{H}_{ani}$:

$$
\begin{aligned}
\boldsymbol{H}_{exh} &= \frac{2A_{ex}}{\mu_0 M_S} \nabla \cdot (\nabla \boldsymbol{m}) \\
\boldsymbol{H}_{iDMI} &= \frac{2D}{\mu_0 M_S} \Big[\nabla (\boldsymbol{m} \cdot \boldsymbol{u}_n) - (\nabla \cdot \boldsymbol{m}) \ \boldsymbol{u}_n \Big] \\
\boldsymbol{H}_{bDMI} &= \frac{2D}{\mu_0 M_S} (\nabla \times \boldsymbol{m}) \\
\boldsymbol{H}_{ani} &= \frac{2K_u}{\mu_0 M_S} (\boldsymbol{m} \cdot \boldsymbol{u}_k) \, \boldsymbol{u}_k
\end{aligned}
\tag{1.28}
$$

1.5 Dynamical equations: Landau-Lifshitz-Gilbert equation

To describe the relaxation processes to the equilibrium point, it is necessary to study the dynamical equation of the magnetization.

Let consider, the torque acting on a magnetic moment $\boldsymbol{\mu}$ due to an external magnetic field $\boldsymbol{H}$. It is expressed as:

$$
\boldsymbol{\tau} = \mu_0 \boldsymbol{\mu} \times \boldsymbol{H} \tag{1.29}
$$

This torque is equivalent to a change in the angular momentum $\boldsymbol{J}$:

$$
\frac{d\boldsymbol{J}}{dt} = \boldsymbol{\tau} \tag{1.30}
$$

The total angular momentum $\boldsymbol{J}$ is the sum of the orbital angular momentum L and the electron spin $\boldsymbol{S}$: $\boldsymbol{J} = \boldsymbol{B} + \boldsymbol{S}$. However, in most ferromagnetic materials, the orbital contribution is small, making it reasonable to consider $\boldsymbol{J} \approx \boldsymbol{S}$. The spin $\boldsymbol{S}$ and the magnetic moment $\boldsymbol{\mu}$ are related by the gyromagnetic ratio γ:

$$
\boldsymbol{\mu} = -\frac{|e| \, g}{2m_e} \boldsymbol{S} = -\gamma \boldsymbol{S} \tag{1.31}
$$

where e is the electron change, m_e is its mass, and g is the Landé factor, approximately $g \approx 2$. The dynamic equation for magnetic moment can be expressed as:

$$
\frac{d\boldsymbol{\mu}}{dt} = -\gamma \mu_0 \boldsymbol{\mu} \times \boldsymbol{H} \tag{1.32}
$$

Since the micromagnetic theory considers the magnetization $\boldsymbol{M}$ as the volume density of the uniform magnetic moments and treats the effective field $\boldsymbol{H}_{eff}$ as an external field that accounts all the interactions, the conservative dynamic equation for the magnetization becomes:

$$\frac{d\boldsymbol{M}}{dt} = -\gamma_0 \boldsymbol{M} \times \boldsymbol{H}_{eff} \tag{1.33}$$

Where $\gamma_0 = \gamma\mu_0 = 2.21 \times 10^5$ m/(A s). The Eq. (1.33) implies that, in the presence of a magnetic field $\boldsymbol{H}_{eff}$, the magnetization $\boldsymbol{M}$ rotates indefinitely perpendicularly to both magnetization and the field (precession mode) with angular velocity given by γ_0, as illustrated in Figure 1.11 (a).

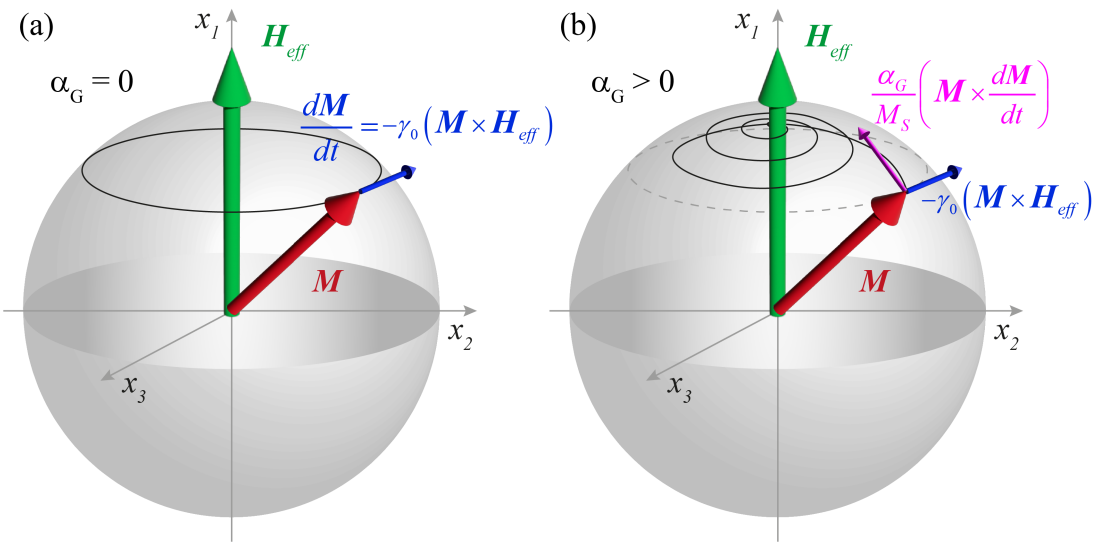

FIGURE 1.11: Dynamic of the magnetization $\boldsymbol{M}$ in the presence of a magnetic field $\boldsymbol{H}_{eff}$. (a) In absence of dissipation ($\alpha_G = 0$), the magnetization $\boldsymbol{M}$ rotates indefinitely around the field $\boldsymbol{H}_{eff}$. (b) Adding damping ($\alpha_G > 0$) results in a damped precession of the magnetization until it aligns itself with the field $\boldsymbol{H}_{eff}$.

However, real systems have dissipative mechanisms such as scattering and lattice interactions, leading the magnetization to relax to an equilibrium state. In the micromagnetic model all the dissipative processes are included phenomenologically by adding a dissipative term, called Gilbert damping parameter α_G, in the

dynamic equation. The resulting Gilbert equation is:

$$\frac{d\boldsymbol{M}}{dt} = -\gamma_0 \boldsymbol{M} \times \boldsymbol{H}_{eff} + \frac{\alpha_G}{M_S}\left(\boldsymbol{M} \times \frac{d\boldsymbol{M}}{dt}\right) \tag{1.34}$$

This equation ensures modulus conservation because the $d\boldsymbol{M}/dt$ is perpendicular to $\boldsymbol{M}$. The second term, perpendicular to the magnetization and its time derivative, enables the final alignment of the magnetization with the field, as shown in Figure 1.11 (b).

For the numerical computation, it is possible to derive an explicit form of the Gilbert equation (Eq. (1.34)). Multiply both sides by $\boldsymbol{M}\times$:

$$\boldsymbol{M} \times \frac{d\boldsymbol{M}}{dt} = -\gamma_0 \boldsymbol{M} \times \left(\boldsymbol{M} \times \boldsymbol{H}_{eff}\right) + \frac{\alpha_G}{M_S}\boldsymbol{M} \times \left(\boldsymbol{M} \times \frac{d\boldsymbol{M}}{dt}\right) \tag{1.35}$$

The cross product in the second term on the right side of the equation can be expressed using the vector triple product identity: $A \times (B \times C) = (A \cdot C)\, B - (A \cdot B)\, C$:

$$\boldsymbol{M} \times \frac{d\boldsymbol{M}}{dt} = -\gamma_0 \boldsymbol{M} \times \left(\boldsymbol{M} \times \boldsymbol{H}_{eff}\right) + \frac{\alpha_G}{M_S}\left(\boldsymbol{M} \cdot \frac{d\boldsymbol{M}}{dt}\right)\boldsymbol{M} - \frac{\alpha_G}{M_S}\left(\boldsymbol{M} \cdot \boldsymbol{M}\right)\frac{d\boldsymbol{M}}{dt} \tag{1.36}$$

Knowing that $\boldsymbol{M} \cdot \boldsymbol{M} = |\boldsymbol{M}|^2 = M_S^2$ and $\boldsymbol{M} \cdot \dfrac{d\boldsymbol{M}}{dt} = 0$ since $d\boldsymbol{M}/dt$ is perpendicular to $\boldsymbol{M}$, the Eq. (1.36) becomes:

$$\boldsymbol{M} \times \frac{d\boldsymbol{M}}{dt} = -\gamma_0 \boldsymbol{M} \times \left(\boldsymbol{M} \times \boldsymbol{H}_{eff}\right) - \alpha_G M_S \frac{d\boldsymbol{M}}{dt} \tag{1.37}$$

Substituting Eq. (1.37) into the Gilbert equation (Eq. (1.34)):

$$\begin{aligned} \frac{d\boldsymbol{M}}{dt} &= -\gamma_0 \boldsymbol{M} \times \boldsymbol{H}_{eff} + \frac{\alpha_G}{M_S}\left(-\gamma_0 \boldsymbol{M} \times \left(\boldsymbol{M} \times \boldsymbol{H}_{eff}\right) - \alpha_G M_S \frac{d\boldsymbol{M}}{dt}\right) \\ \left(1 + \alpha_G^2\right)\frac{d\boldsymbol{M}}{dt} &= -\gamma_0 \boldsymbol{M} \times \boldsymbol{H}_{eff} - \frac{\gamma_0 \alpha_G}{M_S}\boldsymbol{M} \times \left(\boldsymbol{M} \times \boldsymbol{H}_{eff}\right) \end{aligned} \tag{1.38}$$

The resulting expression is known as Landau-Lifshitz-Gilbert (LLG) equation:

$$\frac{d\boldsymbol{M}}{dt} = -\frac{\gamma_0}{1 + \alpha_G^2}\boldsymbol{M} \times \boldsymbol{H}_{eff} - \frac{\gamma_0 \alpha_G}{\left(1 + \alpha_G^2\right) M_S}\boldsymbol{M} \times \left(\boldsymbol{M} \times \boldsymbol{H}_{eff}\right) \tag{1.39}$$

To express the LLG equation in terms of the normalized magnetization m, both sides of the of the equation are divided by M_S:

$$\frac{d\boldsymbol{m}}{dt} = -\frac{\gamma_0}{1+\alpha_G^2}\boldsymbol{m} \times \boldsymbol{H}_{eff} - \frac{\gamma_0\, \alpha_G}{1+\alpha_G^2}\boldsymbol{m} \times \left(\boldsymbol{m} \times \boldsymbol{H}_{eff}\right) \tag{1.40}$$

It is also convenient to write the effective field in dimensionless form $\boldsymbol{h}_{eff} = \boldsymbol{H}_{eff}/M_S$. Thus, the final expression of the LLG equation is:

$$\frac{d\boldsymbol{m}}{dt} = \frac{\gamma_0 M_S}{1+\alpha_G^2}\left(-\boldsymbol{m} \times \boldsymbol{h}_{eff} - \alpha_G \boldsymbol{m} \times \left(\boldsymbol{m} \times \boldsymbol{h}_{eff}\right)\right) \tag{1.41}$$

Each term in the form $\boldsymbol{m} \times \boldsymbol{h}_{eff}$, which induces a precessional mode of the magnetization, is referred to as a non-adiabatic term. On the other hand, the term in the form $\boldsymbol{m} \times \left(\boldsymbol{m} \times \boldsymbol{h}_{eff}\right)$, which induces a relaxation dynamics of the magnetization toward the direction of the effective field, is referred to as an adiabatic term.

1.6 Additional terms in the LLG equation

The LLG equation accounts for different interactions present in the sample through the effective field. However, when an electrical current is applied, additional torques need to be included in the LLG equation to describe phenomena such as STT and SOT, as discussed in the following sections.

Furthermore, while the LLG equation provides the dynamics of the magnetization described at zero temperature, simulating finite temperature effects requires the addition of thermal effects. These effects are added into the effective field as a stochastic field, as described in the paragraph 1.6.4

1.6.1 Spin-transfer torque

An efficient way to control the magnetization of a magnetic material is to leverage the STT effect, which was theoretically predicted independently by Slonczewski [13] and Berger [14] in 1996. The STT effect occurs when a spin-polarized current (or spin current) flows through a magnetic material with a noncollinear magnetization direction. In a simplified description, part of the injected spin electrons

is transmitted and becomes aligned with the magnetization direction of the magnetic material, and part is reflected with the same direction of the transmitted ones but opposite polarity, as illustrated in Figure 1.12. Due to the conservation of the angular momentum, a torque of equal magnitude but opposite sign is exerted on the magnetization of the ferromagnet $\boldsymbol{m}$, causing its rotation. This torque is known as STT [15].

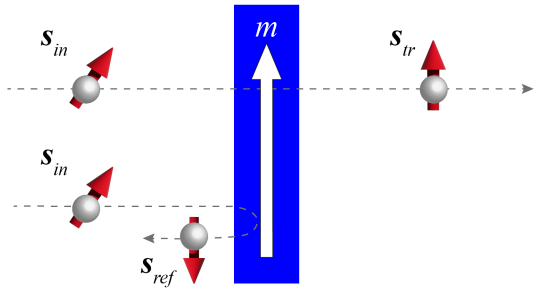

FIGURE 1.12: Representation of two spins S_{in} injected into a magnetic material, subjected to a torque exerted by the magnetization $\boldsymbol{m}$ of the magnetic material. This torque reorients the spins in the direction of $\boldsymbol{m}$. The transmitted spin S_{tr} becomes parallel to $\boldsymbol{m}$, while the reflected spin S_{ref} becomes antiparallel to $\boldsymbol{m}$ (or to S_{tr}).

In this thesis, the focus is specifically on the spin current generated by a charge current flowing perpendicular to the sample plane of a multilayer structure consisting of two ferromagnetic (FM) layers sandwiching a spacer layer. One FM layer is designed to have a fixed or pinned magnetization direction, and it is called pinned layer (PL), while the other FM layer is free to rotate, and it is called free layer (FL). When the spacer is an electrical conductor, the device is named spin valve; when it is an insulator, the device is an MTJ. The latter usually exhibits better properties, as discussed ahead in the text, especially in paragraph 1.7. The STT contribution acting on the magnetization $\boldsymbol{m}$ due a charge current density J_{STT} can be modeled as an additional damping term, known as Slonczewski torque or STT, τ_{SL}, in the Gilbert equation:

$$\begin{aligned}\frac{d\boldsymbol{m}}{dt} = -\gamma_0 M_S \left(\boldsymbol{m} \times \boldsymbol{h}_{eff}\right) + \alpha_G \left(\boldsymbol{m} \times \frac{d\boldsymbol{m}}{dt}\right) \\ + \gamma_0 M_s \sigma J_{STT} g_T \left(\boldsymbol{m}, \boldsymbol{m}_p\right) \left(\boldsymbol{m} \times \left(\boldsymbol{m} \times \boldsymbol{m}_p\right)\right)\end{aligned} \tag{1.42}$$

here the pre-factor σ is equal to $\frac{g\mu_B}{\gamma_0 |e| M_S^2 t_z}$, where g is the Landé factor, μ_B is the Bohr's magneton, and t_z is the thickness of the FL. $\boldsymbol{m}_p = \boldsymbol{M}_p / M_{Sp}$ is the normalized magnetization of the PL, and $g_T(\boldsymbol{m}, \boldsymbol{m}_p)$ is the polarization function, whose expression depends on the relative orientation between the FL and the PL. In particular, for the MTJ:

$$g_T(\boldsymbol{m}, \boldsymbol{m}_p) = \frac{2P}{1 + P^2(\boldsymbol{m} \cdot \boldsymbol{m}_p)} \tag{1.43}$$

where P is the spin polarization, describing the degree to which the charge current is spin-polarized. $P = 1$ means that all the electrons are spin-polarized.

The Slonczewski torque is an adiabatic (relaxational) torque, $\boldsymbol{m} \times (\boldsymbol{m} \times \boldsymbol{m}_p)$, leading the magnetization $\boldsymbol{m}$ to align along the magnetization $\boldsymbol{m}_p$. If $\boldsymbol{m}_p$ is in the same direction of the effective field, depending on the sign of the current, τ_{SL} can be parallel or antiparallel to the damping torque, as illustrated in Figure 1.13 (a) (it, of course, depends on the direction of $\boldsymbol{m}_p$).

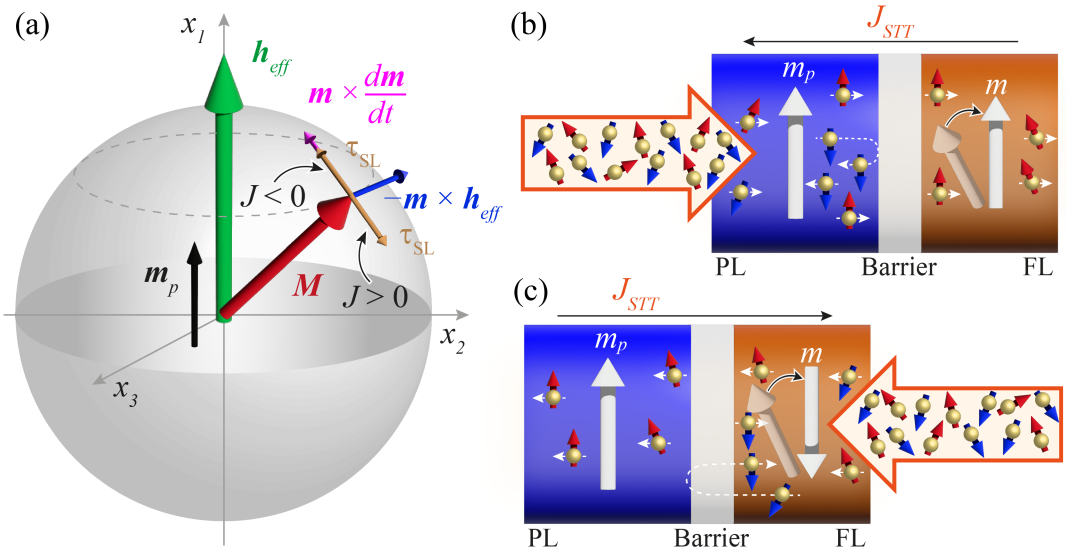

FIGURE 1.13: Sketches of STT affecting the dynamic of the magnetization $\boldsymbol{m}$. (a) Vector diagram representing of all the torques acting on $\boldsymbol{m}$ in the presence of a magnetic field $\boldsymbol{h}_{eff}$ and a spin polarized current J. (b)-(c) STT in a MTJ device: (b) when a charge current flows from the PL to the FL, the FL magnetization $\boldsymbol{m}$ tends to become parallel to the PL magnetization $\boldsymbol{m}_p$ due to the STT torque generated by transmitted spins. (c) When a charge current flows from the FL to the PL, the $\boldsymbol{m}$ tends to become antiparallel to $\boldsymbol{m}_p$ due to the STT torque generated by the reflected spins.

This results in the magnetization of the FL becoming either parallel or antiparallel to the PL. In Figure 1.13 (b)-(c) these mechanisms are shown, where in the first case (b) the STT torque is due to transmitted spins, aligning the FL magnetization with the PL magnetization, whereas in the second case (c) the STT is due to the reflected spins, resulting in an antiparallel configuration of the magnetization.

The obtain the explicit form of the Gilbert equation with the added Slonczewski term, let us multiply both sides of the Eq. (1.42) by $\alpha_G \boldsymbol{m}\times$[16]:

$$\begin{aligned}\alpha_G \boldsymbol{m} \times \frac{d\boldsymbol{m}}{dt} = &- \gamma_0 M_S \alpha_G \boldsymbol{m} \times \left(\boldsymbol{m} \times \boldsymbol{h}_{eff}\right) + \alpha_G^2 \, \boldsymbol{m} \times \left(\boldsymbol{m} \times \frac{d\boldsymbol{m}}{dt}\right) \\ &+ \alpha_G \gamma_0 M_s \sigma J_{STT} g_T \left(\boldsymbol{m}, \boldsymbol{m}_p\right) \, \boldsymbol{m} \times \Big(\boldsymbol{m} \times \left(\boldsymbol{m} \times \boldsymbol{m}_p\right)\Big)\end{aligned} \tag{1.44}$$

The cross product in the second term on the right side of the equation can be expressed using the vector triple product identity: $A \times (B \times C) = (A \cdot C)\, B - (A \cdot B)\, C$, with the same considerations made to obtain the Eq. (1.37):

$$\boldsymbol{m} \times \left(\boldsymbol{m} \times \frac{d\boldsymbol{m}}{dt}\right) = -\frac{d\boldsymbol{m}}{dt} \tag{1.45}$$

The vector triple product identity can also be exploited for the third term on the right side of the equation, maintaining $\boldsymbol{m} \times \boldsymbol{m}_p$ as a vector. Knowing that $\boldsymbol{m} \cdot \boldsymbol{m} = 1$ and $\boldsymbol{m} \cdot (\boldsymbol{m} \times \boldsymbol{m}_p) = 0$:

$$\Big(\boldsymbol{m} \cdot \left(\boldsymbol{m} \times \boldsymbol{m}_p\right)\Big)\boldsymbol{m} - \left(\boldsymbol{m} \cdot \boldsymbol{m}\right)\left(\boldsymbol{m} \times \boldsymbol{m}_p\right) = -\left(\boldsymbol{m} \times \boldsymbol{m}_p\right) \tag{1.46}$$

Substituting Eq. (1.45) and Eq. (1.46) into the Eq. (1.44):

$$\begin{aligned}\alpha_G \boldsymbol{m} \times \frac{d\boldsymbol{m}}{dt} = &- \gamma_0 M_S \alpha_G \boldsymbol{m} \times \left(\boldsymbol{m} \times \boldsymbol{h}_{eff}\right) - \alpha_G^2 \frac{d\boldsymbol{m}}{dt} \\ &- \alpha_G \gamma_0 M_s \sigma J_{STT} g_T \left(\boldsymbol{m}, \boldsymbol{m}_p\right) \left(\boldsymbol{m} \times \boldsymbol{m}_p\right)\end{aligned} \tag{1.47}$$

By setting the Eq. (1.47) into the Eq.(1.42), and reorganizing the terms, the so-called Landau-Lifshitz-Gilbert-Slonczewski (LLGS) equation is obtained:

$$\begin{aligned}\frac{d\boldsymbol{m}}{dt} = \frac{\gamma_0 M_S}{1+\alpha_G^2}\Big(&-\boldsymbol{m}\times\boldsymbol{h}_{eff} - \alpha_G \boldsymbol{m}\times\left(\boldsymbol{m}\times\boldsymbol{h}_{eff}\right) \\ &+ \sigma J_{STT} g_T\left(\boldsymbol{m},\boldsymbol{m}_p\right)\Big(\boldsymbol{m}\times\left(\boldsymbol{m}\times\boldsymbol{m}_p\right) - \alpha_G\left(\boldsymbol{m}\times\boldsymbol{m}_p\right)\Big)\Big)\end{aligned} \tag{1.48}$$

In the explicit form of the LLG equation, a field-like torque term is also present. This is a non-adiabatic or precessional damping torque $-\boldsymbol{m}\times\boldsymbol{m}_p, \tau_{PT}$, which has the same structure of the torque due to the effective field.

Experimentally, another term of the STT should be taken into account in MTJs: the out-of-plane torque or field-like torque τ_{FLTSTT}, which can be very large ($\tau_{FLT_{STT}} \approx 30\%$ of τ_{SL}) [17–21]. The LLGS equation can be then written as:

$$\begin{aligned}\frac{d\boldsymbol{m}}{dt} = \frac{\gamma_0 M_S}{1+\alpha_G^2}\Big(&-\boldsymbol{m}\times\boldsymbol{h}_{eff} - \alpha_G \boldsymbol{m}\times\left(\boldsymbol{m}\times\boldsymbol{h}_{eff}\right) \\ &+ \sigma J_{STT} g_T\left(\boldsymbol{m},\boldsymbol{m}_p\right)\Big(\boldsymbol{m}\times\left(\boldsymbol{m}\times\boldsymbol{m}_p\right) - \alpha_G\left(\boldsymbol{m}\times\boldsymbol{m}_p\right) \\ &+ q_{STT}\left(\boldsymbol{m}\times\boldsymbol{m}_p\right) + q_{STT}\alpha_G\left(\boldsymbol{m}\times\left(\boldsymbol{m}\times\boldsymbol{m}_p\right)\right)\Big)\Big)\end{aligned} \tag{1.49}$$

Where q_{STT} is a phenomenological coefficient, expressed in terms of the amount of field-like torque compared to the damping-like torque. Similarly to the Slonczewski torque, in the explicit form of the LLG equation this torque has two components: $\tau'_{FLTSTT} \propto \left(\boldsymbol{m}\times\boldsymbol{m}_p\right)$, and $\tau''_{FLTSTT} \propto \alpha_G\left(\boldsymbol{m}\times\boldsymbol{m}\times\boldsymbol{m}_p\right)$. It can be added in the effective field of the LLGS equation: $\boldsymbol{h}_{eff} = \boldsymbol{h}_{eff} + q_{STT}\sigma J_{STT} g_T\left(\boldsymbol{m},\, \boldsymbol{m}_p\right)\boldsymbol{m}_p$.

Figure 1.14 shows a comprehensive illustration of all the torques acting on $\boldsymbol{m}$.

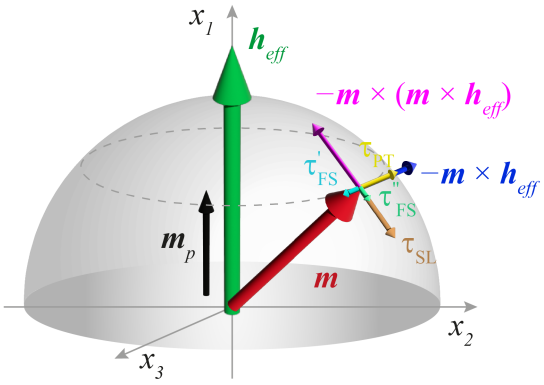

FIGURE 1.14: Representative vector diagram of all the torque acting on the FL magnetization $\boldsymbol{m}$ in the presence of a magnetic field $\boldsymbol{h}_{eff}$ and a spin polarized current J_S, to highlight the adiabatic τ_{SL} and non-adiabatic τ_{PT} and the component of τ_{FLTSTT} (in figure $\tau\prime_{FS}$ and $\tau\prime\prime_{FS}$) contributions of the STT.

Examining the energy landscape of the FL magnetization $\boldsymbol{m}$ in a tri-layer device, the damping-like torque terms of the STT $\left(\boldsymbol{m} \times \left(\boldsymbol{m} \times \boldsymbol{m}_p\right)\right)$ destabilize the FL magnetization, bringing it toward either the P or AP state, while the field-like torque terms modify the energy barrier, as shown in Figure 1.15.

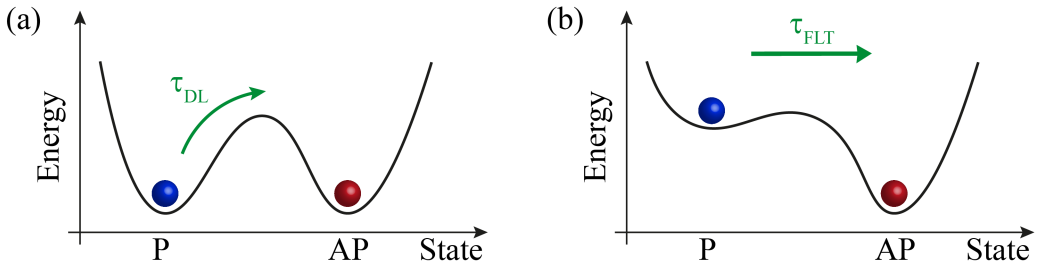

FIGURE 1.15: A schematic representation showing the impact of the STT terms on the energy landscape of the FL magnetization $\boldsymbol{m}$ as a function of different states. (a) The damping like torque terms $\left(\boldsymbol{m} \times \left(\boldsymbol{m} \times \boldsymbol{m}_p\right)\right)$, τ_{DL} destabilizes $\boldsymbol{m}$ (b) the field-like torque τ_{FLT} modifies the energy landscape.

1.6.2 Spin-orbit torque

The presence of an electrical current in systems with large SOC generates an additional torque attributed to two mechanisms: the Rashba effect and the spin Hall effect (SHE). The SOT acts on the magnetization of the FM material deposited on a heavy metal (HM) strip, such as Pt or Co, i.e. an MTJ on top of HM, with its

FL in contact with the HM. When unpolarized electrons (charge current density $\boldsymbol{J}_{SOT}$) flow through the HM material, due to the large SOC, electrons with opposite spins scatter in opposite direction, accumulating on opposite boundaries and creating spin current $\boldsymbol{J}_S$ in the HM, with transverse direction to $\boldsymbol{J}_{SOT}$ and the interface normal. This effect is called SHE [22]. The electron spin polarization σ_{SHE} is transverse to the direction of both $\boldsymbol{J}_{SOT}$ and $\boldsymbol{J}_S$:

$$\boldsymbol{J}_S = \theta_{SHE}(\boldsymbol{\sigma}_{SHE} \times \boldsymbol{J}_{SOT}) \tag{1.50}$$

where θ_{SHE} is the spin Hall angle, which represents the amount $\boldsymbol{J}_{SOT}$ converted into $\boldsymbol{J}_S$. $\boldsymbol{J}_S$ is injected into the FL to exert a torque, known as SOT, on the FL magnetization $\boldsymbol{m}$, as illustrated in Figure 1.16.

The SOT contribution in the LLG equation has an analogous derivation of the STT, where $g_T(\boldsymbol{m}, \boldsymbol{m}_p)$ is replaced by the θ_{SHE} and $\boldsymbol{m}_p$ by $\boldsymbol{\sigma}_{SHE}$:

$$\begin{aligned}\frac{d\boldsymbol{m}}{dt} = \frac{\gamma_0 M_S}{1+\alpha_G^2}\Big(&- \boldsymbol{m} \times \boldsymbol{h}_{eff} - \alpha_G \boldsymbol{m} \times (\boldsymbol{m} \times \boldsymbol{h}_{eff}) \\ &+ \sigma J_{SOT} \theta_{SHE} \Big(\boldsymbol{m} \times (\boldsymbol{m} \times \boldsymbol{\sigma}_{SHE}) - \alpha_G (\boldsymbol{m} \times \boldsymbol{\sigma}_{SHE}) \Big) \Big)\end{aligned} \tag{1.51}$$

Taking into account the field-like torque of the SOT, the LLG equation is given by:

$$\begin{aligned}\frac{d\boldsymbol{m}}{dt} = \frac{\gamma_0 M_S}{1+\alpha_G^2}\Big(&- \boldsymbol{m} \times \boldsymbol{h}_{eff} - \alpha_G \boldsymbol{m} \times (\boldsymbol{m} \times \boldsymbol{h}_{eff}) \\ &+ \sigma J_{SOT} \theta_{SHE} \Big(\boldsymbol{m} \times (\boldsymbol{m} \times \boldsymbol{\sigma}_{SHE}) - \alpha_G (\boldsymbol{m} \times \boldsymbol{\sigma}_{SHE}) \\ &+ q_{SOT} (\boldsymbol{m} \times \boldsymbol{\sigma}_{SHE}) + q_{SOT} \alpha_G \big(\boldsymbol{m} \times (\boldsymbol{m} \times \boldsymbol{\sigma}_{SHE}) \big) \Big) \Big)\end{aligned} \tag{1.52}$$

Where q_{SOT} is a phenomenological coefficient.

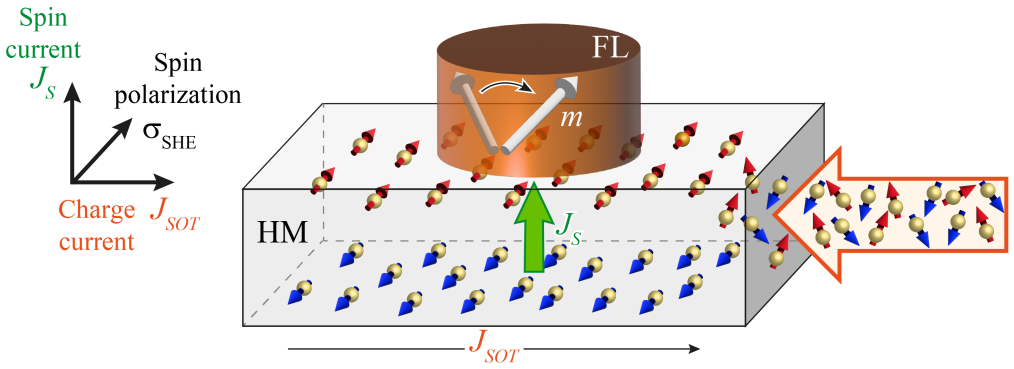

FIGURE 1.16: Sketch of SOT. A charge current $\boldsymbol{J}_{SOT}$ flowing through a HM is converted into a spin current $\boldsymbol{J}_S$ due to the SOC, generating the SHE. The directions of the spin polarization σ_{SHE}, $\boldsymbol{J}_{SOT}$ and $\boldsymbol{J}_S$ are mutually perpendicular. The $\boldsymbol{J}_S$ flowing into the FL exerts a torque (SOT) on the FL magnetization $\boldsymbol{m}$.

1.6.3 Voltage-controlled magnetic anisotropy

The VCMA enables the modulation of the magnetic anisotropy with an electric field (or external voltage) enforcing potential low-power and high-speed switching of the FL magnetization of an MTJ [23–26]. This effect is observed at the interface between an ultrathin FM layer and oxide (Ox) dielectric layer, such as CoFeB | MgO, exhibiting strong interface perpendicular anisotropy. The electric field induces an accumulation of electron charges, leading to a change in the occupation of atomic orbitals at the interface in conjunction with spin-orbit interaction, resulting in a modification of the magnetic anisotropy [27]. However, other possible mechanisms, including oxygen migration [28], and Rashba effect [29–31] are also considered to account for the origins of the VCMA effect. The presence of the VCMA effect models the energy barrier between the two out-of-plane stable states of the FL magnetization in an MTJ as a function of the applied voltage V_b [23, 32]:

$$\Delta\left(V_b\right) = \frac{E_b\left(V_b\right)}{k_B T} = \Delta\left(0\right) - \frac{\xi A V_b}{k_B T t_{ox}} \tag{1.53}$$

Where $\Delta\left(0\right)$ is the thermal stability factor at zero voltage, t_{ox} is the thickness of the oxide layer, A is the sectional area of the MTJ, and ξ is the linear VCMA coefficient (in J/(Vm)) quantifying the change of the interfacial anisotropy energy (J/m^2) per unit electric field (V/m). By setting $\Delta\left(V_b\right) = 0$, it is possible to derive the critical voltage V_c of the VCMA effect ($V_c = \Delta\left(0\right) k_B T t_{ox}/\xi A$), which is

the voltage required to reduce the energy barrier at zero. Figure 1.17 (a) illustrates the different energy profiles. For a voltage pulse of amplitude $V_b \geq V_c$ the magnetic easy-axis is oriented along the in-plane direction, the energy profile is then defined by the shape anisotropy. This results into an unstable state of the FL magnetization, which precessionally oscillates between the P and AP states (precessional switching regime), leading to a nondeterministic switching, as illustrated in Figure 1.17 (b). For $V_b < V_c$ the energy barrier is lowered, and the FL magnetization can either be damped back to the initial state or flipped to the other state, due to thermal activation (thermally-activated switching regime), resulting in deterministic switching. For $V_b < 0$ the energy barrier is enhanced [23, 32].

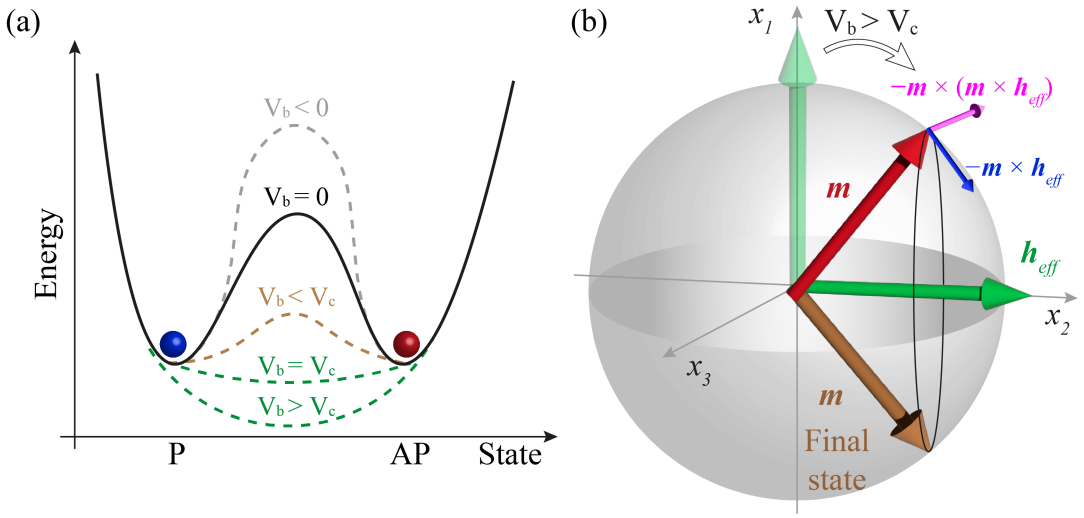

FIGURE 1.17: (a) Illustration of the impact of voltage on the energy barrier of an MTJ with out-of-plane FL magnetization $\boldsymbol{m}$, in presence of the VCMA effect. At equilibrium ($V_b = 0$), the energy barrier separates the two stable states of $\boldsymbol{m}$ (P and AP). A high a voltage ($V_b > V_c$) can eliminate the energy barrier, while a low positive voltage ($0 < V_b < V_c$) reduces the energy barrier. A negative voltage ($V_b < 0$) enhances the energy barrier. (b) Vectorial diagram of the FL magnetization of the MTJ for $V_b > V_c$ resulting in a precessional mode.

The VCMA effect is incorporated into the LLG equation as an additional term in the effective field. Experimental observations often indicate a linear relationship between the voltage-dependent magnetic anisotropy and the applied voltage, in

the working range. In case of uniaxial perpendicular anisotropy, the voltage-dependent anisotropy field can be expressed as [32–35]:

$$h_{VCMA} = -\frac{2\xi V_b}{\mu_0 M_s^2 t_z t_{ox}} \left(\boldsymbol{m} \times \boldsymbol{u}_k\right) u_{kz} \tag{1.54}$$

This field acts on the out-of-plane component of the anisotropy field, defined by the unit vector $\boldsymbol{u}_k$. For convenience, in this thesis, we typically use a single coefficient VCMA, expressed in Tesla, so that: $h_{VCMA} = \dfrac{VCMA}{\mu_0 M_S} \left(\boldsymbol{m} \times \boldsymbol{u}_k\right) u_{kz}$.

1.6.4 Thermal field

At zero temperature, in absence of external excitations, the magnetic configuration remains unchanged indefinitely. However, in real-world scenarios, the temperature effects cannot be neglected. Thermal fluctuations can provide enough energy to the system to overpass the energy barrier and let the magnetization evolves to another minimum. This phenomenon is particularly pronounced in small samples, leading to what is known as superparamagnetic effect [36]. In micromagnetic modeling, the temperature effect is incorporated through a stochastic field $\boldsymbol{H}_{th}$ added to the effective field acting on the magnetization: $\boldsymbol{H}_{eff} \leftarrow \boldsymbol{H}_{eff} + \boldsymbol{H}_{th}$. With this modification the LLG equation takes the name of Langevin equation. The thermal field, at each cell i, is given by:

$$\boldsymbol{H}_{th,i}\left(t\right) = \boldsymbol{\eta}_i\left(t\right) \sqrt{\frac{2\alpha_G k_B T}{\left(1+\alpha_G^2\right)\gamma_0 \mu_0 M_S V dt}} \tag{1.55}$$

where dt is the simulation step, $\boldsymbol{\eta}_i\left(t\right)$ is a Gaussian stochastic process with zero mean and unit standard deviation.

$$\begin{aligned} &\langle H_{th,\alpha,i}(t)\rangle = 0 \\ &\langle H_{th,\alpha,i}(t) H_{th,\alpha,j}(t')\rangle = 2D\delta_{ij}\delta_{\alpha\beta}\delta(t-t') \end{aligned} \tag{1.56}$$

In Eq. (1.56) the angular bracket denoted the time average, i and j are the indices of the cells, $\alpha, \beta = x, y, z$ refer to the Cartesian components of the field. The three components of the thermal field are spatial and time uncorrelated. The constant D representing the strength of $\boldsymbol{H}_{th}$, $D = \alpha_G k_B T / \left(\left(1-\alpha_G^2\right)\gamma_0 \mu_0 M_S V\right)$ where V is the volume of each cell [5]. Figure 1.18 shows a representative magnetization

dynamics with (a) and without (b) the thermal field.

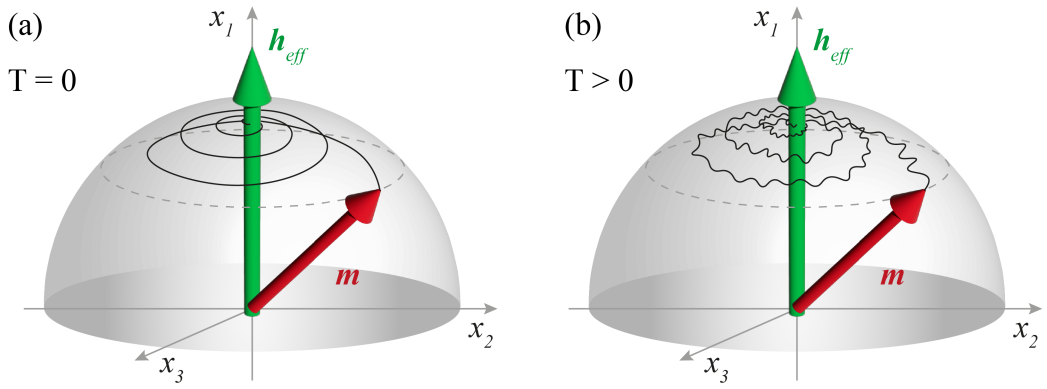

FIGURE 1.18: Effect of temperature on the dynamics of the magnetization $\boldsymbol{m}$. A representative vector diagram of the $\boldsymbol{m}$ dynamics in presence of an effective field $\boldsymbol{H}_{eff}$ at (a) zero temperature and (b) with the influence of a thermal stochastic field.

1.7 Magnetic tunnel junctions

The MTJ is a key and emerging device in spintronic technology, having several important properties such as low power consumption, compact size, high-speed operation, and compatibility with CMOS technology [37]. Such characteristics make it a suitable device for logic and memory applications.

As previously mentioned, the MTJ is a nano-pillar of magnetic multilayers, with an ultra-thin insulator sandwiched between a fixed or pinned layer (PL) with fixed magnetization $\boldsymbol{m}_p$, and a free layer (FL) with magnetization $\boldsymbol{m}$ free to rotate.

Moreover, both the FL and the PL magnetizations can exhibit time-evolution behavior, and in such configuration, two coupled LLG equations (1.41) describe the dynamics of the two coupled magnetizations. Throughout this thesis, unless explicitly stated, the PL magnetization remains fixed.

Based on the easy axis of the magnetizations $\boldsymbol{m}$ and $\boldsymbol{m}_p$, two primary configurations can be identified:

- In-plane MTJ (i-MTJ): both magnetizations lie within the plane of the MTJ (x-y plane).

- Perpendicular MTJ (p-MTJ): the magnetizations are oriented perpendicular to the plane of the MTJ (along z-axis).

The MTJ resistance depends on the relative orientation of the two magnetizations: if $\boldsymbol{m}$ is in the same direction of/parallel to $\boldsymbol{m}_p$ the MTJ offers a low resistance (R_P), if $\boldsymbol{m}$ is antiparallel to $\boldsymbol{m}_p$ the MTJ exhibits a high resistance (R_{AP}). Figure 1.19 (a)-(b) shows these configurations. The two stable states (P and AP) are separated by an energy barrier E_b (see Figure 1.19 (c)) which determines the thermal stability of the MTJ. It is worth noting that hybrid configurations are also possible, where the magnetizations are non collinear. In addition, larger MTJs can have non uniform spin texture such as a vortex [38] or a skyrmion [39, 40] as a ground state.

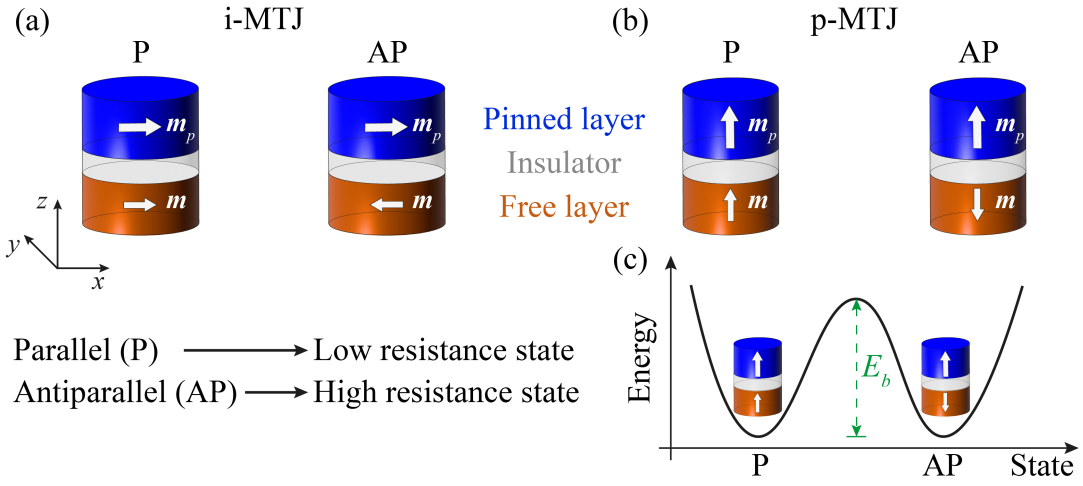

FIGURE 1.19: Different configurations of an MTJ based on the absolute and relative orientation of the FL magnetization $\boldsymbol{m}$ and the PL magnetization $\boldsymbol{m}_p$. (a) In-plane MTJ: $\boldsymbol{m}$ and $\boldsymbol{m}_p$ lie in the plane of the MTJ, (b) perpendicular MTJ: $\boldsymbol{m}$ and $\boldsymbol{m}_p$ are perpendicular to the plane of the MTJ. $\boldsymbol{m}$ in the same direction of $\boldsymbol{m}_p$ (parallel) leads to a low resistance state (left of (a)-(b)), while in the opposite direction (antiparallel) it leads to a high resistance state (right of (a)-(b)) (c) An energy barrier E_b separates the two states of the MTJ (in this example, a p-MTJ).

The tunnel magnetoresistance (TMR) ratio quantifies the resistance variation between these two states of the device:

$$\text{TMR} = \frac{R_{AP} - R_P}{R_P} \tag{1.57}$$

This parameter is crucial for high performance MTJ. TMR has achieved remarkable values, reaching 631% at room temperature with an MgO tunnel barrier [41].

In general, the resistance is a function of the angle θ between the magnetizations of the two ferromagnetic layers [42, 43]:

$$R(\theta) = R_P + \frac{R_{AP} - R_P}{2}\left(1 - \boldsymbol{m} \cdot \boldsymbol{m}_p\right) \tag{1.58}$$

Several factors such as shape, size thickness and materials influence the resistance, and thus the TMR value. In present of interfacial perpendicular anisotropy, it is possible to control the easy axis of the MTJ with the thickness. In particular, there exists a critical thickness of the FL above which the in-plane configuration is favored. In thin films, the in-plane can be controlled also by an elliptical shape, leveraging the shape anisotropy due to the demagnetizing field.

In paragraph 1.6 different methods for manipulating the magnetization have been introduced, each requiring a different structure of the MTJ which can have two terminals or three terminals, as illustrated in Figure 1.20.

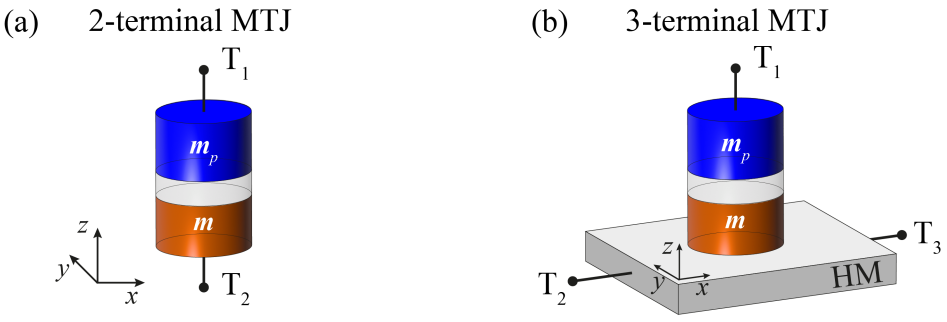

FIGURE 1.20: Sketches of two different structures of MTJ: (a) 2-terminal MTJ (b) 3-terminal MTJ.

The 2-terminal MTJ allows the STT and VCMA mechanisms, while the 3-terminal MTJ can also be controlled with SOT, or with a combination of such effects [44]. The 2-terminal MTJ is more compact and scalable, but there is the risk of erroneously writing into the MTJ when the read current flows through it, because the same path is used for both operations. On the other hand, the 3-terminal MTJ has larger area occupancy, but it offers the advantage to have separate paths for reading and writing.

The different dynamic behavior of the FL magnetization in the MTJ opens the door to a range of applications: for instance, current-induced switching offers

promising applications in magnetic random access memory (STT-MRAM), spintronic oscillators, diodes, etc..

1.8 Spintronic oscillators and diodes

As already discussed, a bias spin-polarized current can exert an STT on the FL magnetization of an MTJ, i.e. an antidamping torque. When this torque is driven by a DC current and it compensates the Gilbert damping, it is possible to excite a persistent oscillation of the magnetization characterized by an oscillatory regime (self-oscillation) of the MTJ resistance. This is the smallest self-oscillator know in nature and has useful properties such as frequency tunability by DC current and field, which make this device effective for a wide range of applications. On the other hand, a dual effect is achieved in STD, where the magnetization is excited by a spin-polarized AC current, generating an oscillating resistance. In this case, the voltage across the MTJ is characterized by a rectified component (i.e. diode effect) [45, 46].

1.8.1 Spin-torque nano-oscillators

As already anticipated, a large enough spin-polarized direct electric current I_{DC}, can cancel out the Gilbert damping losses of the FL, exerting an STT torque to the FL magnetization and driving it into a steady-state precession [13, 14]. This phenomenon is known as auto- or self-oscillation [47]. Due to the magnetoresistance effect, the magnetization oscillation gives rise to a temporal variation of the resistance, $r(t) = R_m + \Delta R \cos(\omega t)/2$, where R_m is the average resistance value (DC resistance), ΔR and ω denoted the amplitude and the angular frequency of the resistance, respectively. This resistance variation results in a microwave (alternating) voltage across the MTJ: $v(t) = J_{DC}\, r(t)$.

The MTJ operating in this mode is called spin-torque nano-oscillator or spin-transfer nano-oscillator (STNO). Figure 1.21 shows a sketch of an *i*-MTJ device working as STNO, accompanied by the experimental time traces of the voltage oscillations observed at room temperature in devices characterized in Ref. [48].

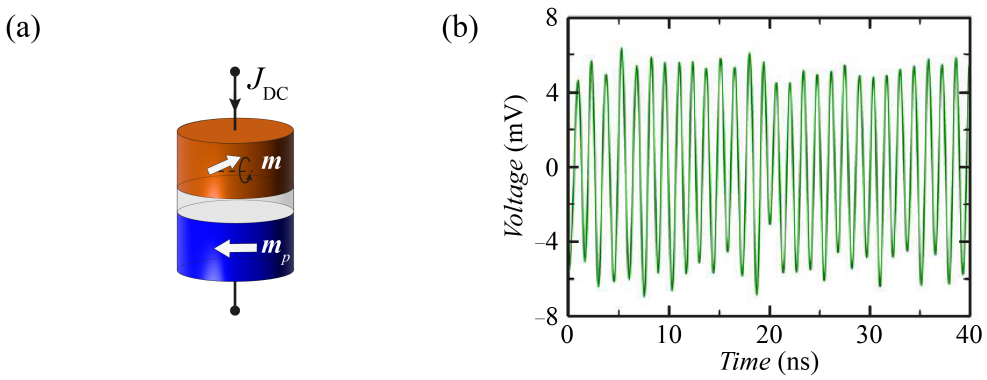

FIGURE 1.21: (a) A sketch of an STNO device with in-plane PL magnetization and tilted FL magnetization. A large enough DC current density J_{DC} can excite the magnetization self-oscillation. (b) An example of experimental time domain voltage produced by the steady-state precession of the FL magnetization for the STNO in (a) [48].

Two of the most important parameters of the STNOs are the output power P_{out} and the linewidth Δf, where the linewidth is defined as the full width at half maximum ($FWHM$) of the power spectra. Achieving devices with both high output power and a narrow linewidth is currently a challenge [48–50]. In Figure 1.22, typical microwave emissions for an STNO device (sketched on the left side) are presented as a function of the applied current I_{DC}, revealing a red-shift of the oscillation frequency. This shift is highlighted in the inset along with the $FHVM$ variation.

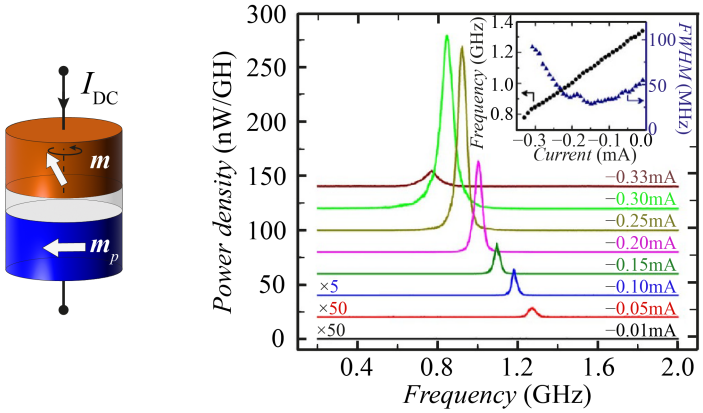

FIGURE 1.22: Experimental microwave emissions as a function of the bias current I_{DC}, for the sketched STNO devices. In inset: peak of the oscillation frequency and $FHWD$ as a function of I_{DC}, highlighting the red-shift phenomenon [51].

Considering an STNO connected through a bias tee to a load R_L, the output voltage can be approximated as $v_{out}(t) \approx \frac{I_{DC}}{2}\frac{\Delta R\, R_L}{R_m + R_L}\cos(\omega t)$. The time-averaged power delivered can be expressed as [48, 49]:

$$P_{out} = \frac{V_{out}^2}{2R_L} = \frac{I_{DC}^2}{8}\frac{\Delta R^2\, R_L}{(R_m + R_L)^2} \tag{1.59}$$

From Eq. (1.59), it is evident that increasing the output power requires enhancing the ratio R_L/R_mas well as the value of ΔR, therefore increasing the current, in agreement with the experimental observation in Figure 1.22.

1.8.1.1 Analytical model of the STNOs

Slavin *et al*. [47, 52, 53] have developed an analytical model based on the universal model of non-linear oscillators with negative damping, that we refer to as Slavin model in the rest of the text, to describe the nonlinear dynamics of the STNOs:

$$\frac{dc}{dt} + i\omega\left(c^2\right)c + \Gamma_+\left(\left|c^2\right|\right)c - \Gamma_-\left(\left|c^2\right|\right)c = f(t) \tag{1.60}$$

where $c(t) = \sqrt{p}e^{i\phi(t)}$ is the complex amplitude of the oscillations, which measures the power $p = \left|c^2\right|$ and the phase $\phi = \arg(c)$ of the oscillations. $\omega(p)$ is the frequency of the excited mode, $\Gamma_+\left(\left|c^2\right|\right)$accounts for the natural positive damping of the system related to the energy dissipation, and $\Gamma_-\left(\left|c^2\right|\right)$ represents the effective negative damping introduced by external or internal energy sources, such as spin-polarized currents. The term $f(t)$ incorporates the influence of external signals, including thermal fluctuations (in autonomous regime of auto-oscillation $f(t) = 0$).

While a detailed explanation of this model is not the primary focus of this thesis, key information relevant to STNO are discussed herein. The computation of $\omega(p)$ and $\Gamma_\pm(p)$ for real geometry is mathematically complicated, and in the most case a weakly-nonlinear ($p \ll 1$) Taylor expansion is considered:

$$\begin{aligned}
&\omega(p) \approx \omega_0 + Np \\
&\Gamma_+(p) \approx \Gamma_G(1 + Qp) \\
&\Gamma_-(p) \approx \sigma J(1 - p)
\end{aligned} \tag{1.61}$$

Where ω_0 is the resonance frequency of the frequency of the self-oscillation at the critical current, N is the nonlinear frequency shift coefficient, Q is the nonlinear damping coefficient, $\Gamma_G = \alpha_G \omega_0$, σ is the STT coefficient and J is the current. The expression for the STNO in auto-oscillation with the approximation (1.61) is:

$$\frac{dc}{dt} = i\left(\omega_0 + Np\right)c + \Gamma_G\left(1 + Qp\right)c - \sigma J\left(1 - p\right)c \tag{1.62}$$

Examining the expression (1.62) a straightforward comparison with the LLGS equation in the form of Eq. (1.42) can be made: the first term is the precessional torque, the second one is the damping-like torque and the third term is the STT.

Knowing that $c\left(t\right) = \sqrt{p}e^{i\phi(t)}$, the Eq. (1.60) can be rewritten as:

$$\frac{e^{i\phi}}{2\sqrt{p}}\frac{dp}{dt} + ie^{i\phi}\sqrt{p}\frac{d\phi}{dt} = -i\omega\left(p\right)\sqrt{p}e^{i\phi} - \left(\Gamma_+\left(p\right) - \Gamma_-\left(p\right)\right)\sqrt{p}e^{i\phi} \tag{1.63}$$

Dividing by $e^{i\phi}\sqrt{p}$, it becomes:

$$\frac{1}{2\sqrt{p}}\frac{dp}{dt} + i\frac{d\phi}{dt} = -i\omega\left(p\right) - \left(\Gamma_+\left(p\right) - \Gamma_-\left(p\right)\right) \tag{1.64}$$

From this expression, the Slavin model can be reformulated as a system of two real equations, one for the power and the other for the phase of the oscillations:

$$\begin{cases} \dfrac{dp}{dt} = -2\left(\Gamma_+\left(p\right) - \Gamma_-\left(p\right)\right)p \\ \dfrac{d\phi}{dt} = -\omega\left(p\right) \end{cases} \tag{1.65}$$

There are two possible stationary $(dp/dt = 0)$ solutions of the first equation. The first is the trivial one for $p = 0$, representing an absence of oscillations. The second is obtained from the equation:

$$-2\left(\Gamma_+\left(0\right) - \Gamma_-\left(0\right)\right)p = 0 \tag{1.66}$$

when $\Gamma_+\left(0\right) > \Gamma_-\left(0\right)$, and $\Gamma_+\left(0\right) = \Gamma_-\left(0\right)$ is the condition to determine the threshold value for the generation of the self-oscillation. In detail, the threshold current J_{th} for the microwave generation in a STNO, is obtained by substituting

the Eq. (1.61):

$$J_{th} = \frac{\Gamma_G}{\sigma} \tag{1.67}$$

The nonzero solution of the stationary power is $p = p_0$, and p_0 can be derive from the condition $\Gamma_+ (p_0) = \Gamma_- (p_0)$:

$$p_0 = \frac{\sigma J - \Gamma_G}{\Gamma_G Q + \sigma J} = \frac{\dfrac{\sigma J}{\Gamma_G} - 1}{Q + \dfrac{\sigma J}{\Gamma_G}} = \frac{\zeta - 1}{\zeta + Q} \tag{1.68}$$

Where ζ is the dimensionless supercriticality parameter:

$$\zeta = \frac{J}{J_{th}} \tag{1.69}$$

The stationary power is zero for $J = J_{th}$ (thus $\zeta = 1$), increasing with current (or ζ), until reaching the limit $p_\infty = 1$ for $\zeta \to \infty$.

However, the maximum injected current is constrained by the MTJ barrier breakdown voltage.

1.8.2 Spin-torque diodes

An alternating current, $i_{\mathrm{AC}}(t) = I_{\mathrm{AC}} \sin(\omega t + \varphi_I)$, injected into an MTJ can exert a torque of the FL magnetization. If the frequency of the input current is close to the precession frequency of the FL magnetization $\boldsymbol{m}$, the resonance phenomenon strongly amplifies the oscillations. Due to the magnetoresistance effect, these oscillations of the $\boldsymbol{m}$ lead to the resistance oscillations with the same frequency of the input current: $r(t) = \Delta R_s \sin(\omega t + \varphi_R)$. This process is explained considering that for half of the period of the alternating current the FL magnetization is tilted toward the PL magnetization, resulting in low resistance; in the next half of the AC current oscillation, $\boldsymbol{m}$ is tilted in the opposite direction, resulting in high resistance. In such a condition, a rectified voltage is generated across the MTJ. This rectification phenomenon is known as spin-diode effect, and the corresponding device as spin-torque diode [45, 54–56]. This process can be easily demonstrated

as follows:

$$v(t) = i_{\mathrm{AC}}(t)\, r(t) = \Delta R_S I_{\mathrm{AC}} \sin(\omega t + \varphi_I) \sin(\omega t + \varphi_R) \tag{1.70}$$

By leveraging the trigonometric identity: $\sin A \sin B = (\cos(A-B) + -\cos(A+B))/2$, the expression can be rewritten as:

$$v(t) = \frac{1}{2}\Delta R_S I_{\mathrm{AC}} \cos(\varphi_I - \varphi_R) - \frac{1}{2}\Delta R_S I_{\mathrm{AC}} \cos(2\omega t + \varphi_I + \varphi_R) \tag{1.71}$$

The DC component of the voltage is $V_{\mathrm{DC}} = \frac{1}{2}\Delta R_S I_{\mathrm{AC}} \cos(\varphi_S)$ where φ_S is the intrinsic phase shift between the AC current and the oscillating resistance. Figure 1.23 provides a visual representation of the output voltage from the Eq. (1.71), highlighting the DC component of the voltage.

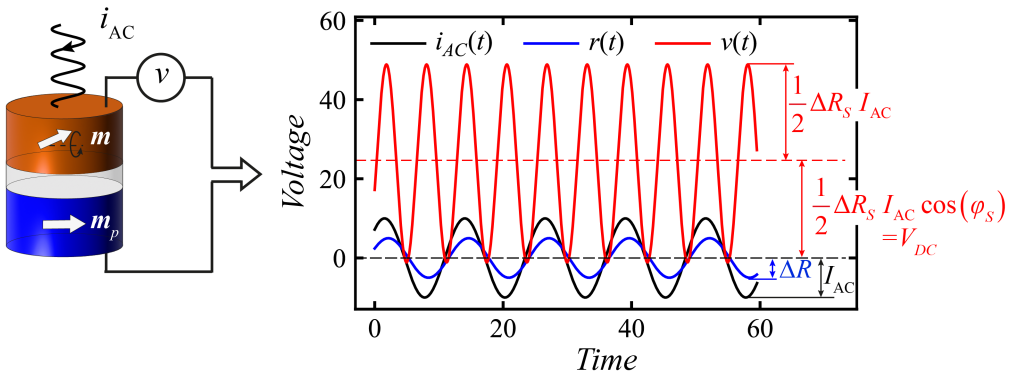

FIGURE 1.23: A schematic explanation of the spin-diode effect. An AC current i_{AC} (black curve), with frequency close to the natural frequency of the oscillator, induces an oscillating resistance (blue curve) with the same frequency of i_{AC}. This resistance partially rectified the input current, giving rise to an output voltage (red curve) characterized by a DC component (dashed red line).

Tulapurkar *et al.* in 2005 [55] provide the first measurement of the spin-diode effect, shown in Figure 1.24. This figure illustrates the DC voltage generated by the STD in response of the frequency of the AC current at a fixed amplitude value, for different values of the field.

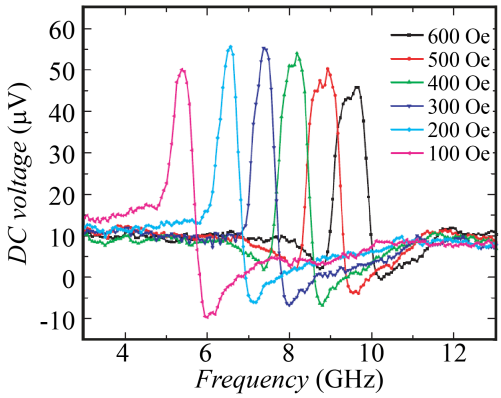

FIGURE 1.24: Rectification response: DC voltage generated by the STD as a function of the frequency of the AC current, for different external field [55].

One of the most important metrics for evaluating the STD performance is the sensitivity, which is the efficiency in converting the AC input power P_{in} into a rectified voltage V_{DC}. It is expressed as:

$$\varepsilon = \frac{V_{\mathrm{DC}}}{P_{in}} \tag{1.72}$$

For instance, the sensitivity of the diode characterized by Tulapurkar STD [55] is $\varepsilon = 1.4$ V/W, which is very low compared to the nowadays devices, which exceed 10^5 V/W [57]. Another parameter is the conversion efficiency, that in a general formulation is defined as:

$$\eta = \frac{P_{out}}{P_{in}} \tag{1.73}$$

where P_{out} is the output power. For the STD, P_{out} is the output DC power which can be delivered to a load.

Based on their working regime, STDs can be classified into two main categories: passive STDs (unbiased) and active STDs (biased) [56].

1.8.2.1 STDs working in passive regime

Passive STDs can exhibit either a resonant or non-resonant response.

The resonance response can be linear or nonlinear. Under low input power P_{in} the resonance response of the STD can be described within a linear theory. An

example of such STD response is found in the work of Tulapurkar [55]. Further improvements have been done in order to improve the sensitivity, including the use of VCMA [58] as well as the control of the interfacial perpendicular anisotropy and the design of hybrid MTJs [46]. If the input AC current is increased over a certain threshold, a transition from linear to nonlinear response occurs, and the rectification voltage as a function of the AC current frequency becomes asymmetric [59].

The nonresonant response of unbiased STDs can have different behaviors: broadband response [60, 61] and low-frequency tail response (where the rectified output increases as the frequency of the AC input decreases) [62, 63]. Induced by a large enough power in MTJs with a specific design, a broadband response characterized by a flat rectified output across a wide range of input frequencies can be observed. Figure 1.25 provides a comparison of the STD response at two different input powers, showing for those MTJs the transition from resonant to broadband response. This broadband response behavior is very useful for the development of electromagnetic energy harvesting applications, a topic that will be further discussed in paragraph 1.10.1.

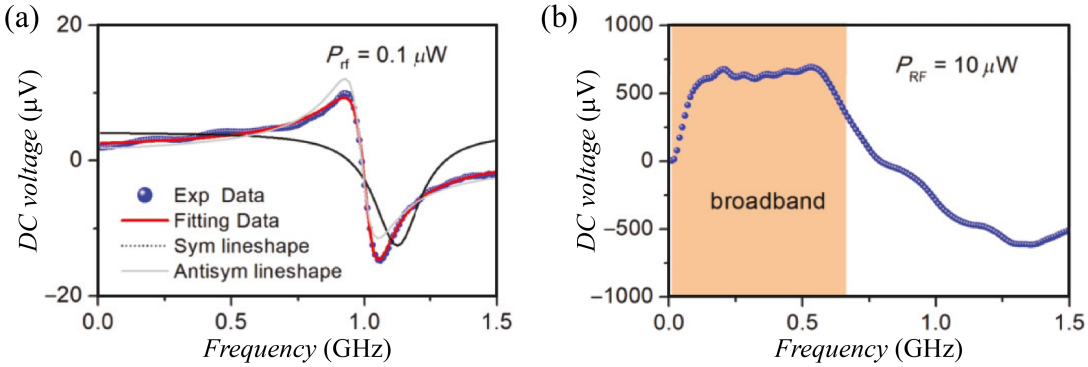

FIGURE 1.25: Rectified voltage as a function of the frequency of the AC current for two distinct input powers P_{RF} applied to the STD. (a) $P_{RF} = 0.1$ μW induced a resonance response. (b) $P_{RF} = 10$ μW induced a broadband response of the STD [60].

1.8.2.2 STDs working in active regime

When a DC bias current able to drive self-oscillations is applied together with the AC current to the STD, it can induce a nonlinear effect which enhances the STD performance, opening the path for effective solutions in several applications such

as compact microwave detection [45, 46, 64, 65]. This is because, in the presence of the DC current, the rectified voltage is enhanced by an additional component proportional to this DC current and to the variation of the DC resistance of the MTJ, known as the nonlinear rectification effect [56, 64, 66]:

$$V_{DC} = \frac{1}{2}\Delta R_S I_{AC} \cos(\varphi_S) + I_{DC}\Delta R_{DC}(I_{AC}) \tag{1.74}$$

Where the $\Delta R_{DC}(I_{AC}) = R_{DC}(I_{AC}) - R_{DC}(0)$ is the difference between the time-averaged MTJ resistance (DC resistance) in the presence and in the absence of I_{AC}. The term $I_{DC}\Delta R_{DC}$ can be generated with different phenomena. For instance, Cheng *et al.* [66] employed both field and current to bias a superparamagnetic MTJ achieving nonadiabatic stochastic resonance. Miwa *et al.* [64] worked at DC currents which do not drive a self-oscillation of the FL magnetization (sub-critical regime). However, in the active regime, the most efficient way to increase the sensitivity of STDs is the injection locking. The DC current excites self-oscillation of the FL magnetization (at $I_{AC} = 0$) and when an AC current at a frequency close to that of the auto-oscillator is injected into the MTJ, the FL magnetization locks to it. Within this locking region, both ac current and ac resistance oscillates at the same frequency ,and the rectification effect can be observed as in passive STDs. Figure 1.26 reported the experimental observation of the injection locking by Fang *et al.* [46].

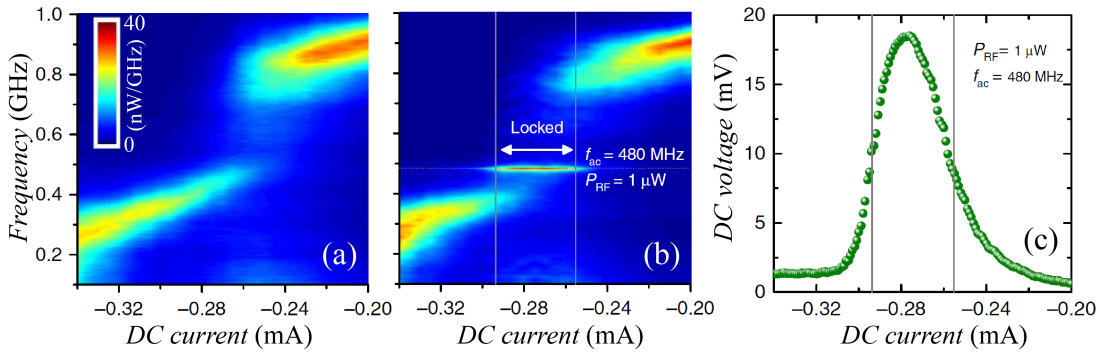

FIGURE 1.26: Injection locking of the STD to an external AC current I_{AC} visualized through microwave emissions as a function of the DC bias current with amplitude encoded in the color. (a) Self-oscillation regime ($I_{AC} = 0$) (b) Injection locking regime ($I_{AC} \neq 0$) (c) Rectified voltage as a function of the DC current, with vertical lines indicating the region of the injection locking [46].

In this thesis we exploit the STDs in injection looking regime for an application in neuromorphic computing [67] (paragraph 3.4.4), and for a spintronic accelerometer [68] (paragraph 1.10.2).

1.9 Micromagnetic solver

The LLG equation (1.41) is a partial differential equation describing the dynamics of the magnetization influenced by an effective field, comprising of long-range (magnetostatic), short-range (exchange) and local (anisotropy, DMI, external field, spin torque) interactions. In this thesis, the full micromagnetic computations are performed with PETASPIN, a well-established micromagnetic GPU-based solver developed by the PetaSpin team (`www.petaspin.com`) [5, 69]. PETASPIN adopts a finite difference approach to discretize the magnetic material into uniform computational cells, and Adams-Bashforth algorithms to numerically integrate the LLGS equation associated with each magnetization within the cells. While this model effectively captures diverse magnetization configurations, including intricate spin textures such as skyrmions or vortex, it comes with a trade-off of high computational costs.

For scenarios with weak anisotropy, where spins are tightly coupled by the exchange interaction, forming a huge macrospin, the so-called macrospin approximation is applied. Therefore, to analyze the dynamics of a uniform magnetization configuration, we have implemented an efficient solver for the micromagnetic model within the macrospin approximation.

The solver has been developed and used for the deliverable 1.1 of the SWAN-on-chip project (`www.swanonchip.eu`) and for the Samothrace project (`www.samothrace.eu`).

The solver integrates the LLG equation (1.41), with additional terms like STT and SOT. Furthermore, it allows the investigation of the coupled dynamics of two magnetic FM layers. Developed in C/C++ programming language, with a version in CUDA^{TM} language for GPU-acceleration, this solver offers the advantage of calculating, in a single simulation, the response of the MTJ under excitations across a user-defined range of frequencies. This approach allows the study of both linear and nonlinear response of the MTJ, such as resonance and broadband response in a single run.

A notable feature of the solver is its design geared toward a straightforward benchmarking, allowing users to set simulation parameters using text files. In particular, the configuration files required to setup the simulations and run the solver are the following (shorthand notation in parenthesis):

- *LayerFree_parameters.txt* (fileLF).
- *LayerPolarizer_parameters.txt* (fileLP).
- *ExternalExcitations_parameters.txt* (fileExtExc).
- *Output_settings.txt* (fileOut).
- *Run_parameters.txt* (fileRun).

Each file name reflects the nature of the parameters it contains.

In the paragraph 1.9.1, a more user-friendly version of the solver is presented through the development of a graphical user interface (GUI).

The pseudocode provided in Algorithm 1.1 outlines the main structure of the code. To simplify the explanation, we will only focus on the scenario in which the PL magnetization is fixed.

All simulation parameters are stored in variables and pointers, organized into several structures (structs), defined at the beginning of the program (DEFINESTRUCTS). To optimize memory usage, performance, and flexibility, we have chosen to employ only 1D pointers. The variables in the structs are populated with configuration parameters loaded from the text files (LOADINPUTS). Subsequent setting of the inputs (SETINPUTS), which involves defining constants (like μ_0, μ_B, k_B), the seed, converting input dimensional parameters into dimensionless ones, and populating the pointers with the user-defined range of frequency. Additionally, time domain excitations are loaded from text files. The definition of the initial conditions of the magnetization is a crucial step in evaluating the dynamics of the magnetization, and these conditions are specified in the configuration files. After normalization, they are set for each frequency under examination (INITSTATE).

Based on the computation platform - CPU or GPU – used to perform the LLG integration, two different functions are called - SOLVERLLG and SOLVERLLG_CUDA, respectively. The results of the calculation at each time step are stored in pointers with a frequency defined by the user. After a

given number of saving operations (*Nsave*), the pointers are printed to text files (WRITEOUTPUTS).

By setting *FLAG_RES* to 1, the amplitude of the magnetization for each Cartesian component and frequency is computed (COMPUTEAMPLITUDE) and saved in text files (WRITERES).

Algorithm 1.1: Main structure of macrospin solver

structs$\leftarrow$ DEFINESTRUCTS()

structs$\leftarrow$ LOADINPUTS(structs)

structs$\leftarrow$ SETINPUTS(structs)

$\boldsymbol{m} \leftarrow$ INITSTATE(structs)

$t \leftarrow 0$

while $t \leq t_{tot}$ **do**

  if $FLAG\_GPU \leftarrow 0$ **then**

    $\boldsymbol{m} \leftarrow$ SOLVERLLG(t, structs) ▷ `CPU computation`

  else

    $\boldsymbol{m} \leftarrow$ SOLVERLLG_CUDA(t, structs) ▷ `GPU computation`

  end

  if $counter \mod Nsave = 0$ **then**

    WRITEOUTPUTS(t, $\boldsymbol{m}$, structs)

  end

  $t \leftarrow t + dt$

end

if $FLAG\_RES \leftarrow 1$ **then**

  for $f \leftarrow 0$ to N_f **do**

    $\boldsymbol{A_m} \leftarrow$ COMPUTEAMPLITUDE(t, $\boldsymbol{m}$, structs)

  end

  WRITERES($\boldsymbol{A_m}$, structs)

end

The LLG equation, with additional terms like STT and SOT, is numerically integrated using the Heun algorithm, in the SOLVERLLG function, as outlined in Algorithm 1.2. A concise explanation of the Heun algorithm is provided below. Given an ordinary differential equation with an initial condition $y(t_0)$:

$$\frac{dy}{dt} = f(t, y), \qquad y(t_0) = y_0 \tag{1.75}$$

The value of the function y at the instant $t + dt$, can be calculated as:

$$y(t + dt) = y(t) + \frac{dt}{2}\left[f(t, y(t)) + f(t + dt,\ \widetilde{y}(t + dt))\right] \tag{1.76}$$

where

$$\widetilde{y}(t + dt) = y(t) + dt\ f(t, y(t)) \tag{1.77}$$

where dt is the time step.

Algorithm 1.2: SOLVERLLG function

for $f \leq N_f$ **do**

- $\boldsymbol{h}_{eff} \leftarrow$ COMPUTEHEFF(t,$\boldsymbol{m}$, structs)
- $\boldsymbol{dm} \leftarrow$ COMPUTEDERIVATIVE(t, $\boldsymbol{m}$, $\boldsymbol{h}_{eff}$, structs) ▷ LLG equation
- $\boldsymbol{m}_{Temp} \leftarrow \boldsymbol{m} + dt\ \boldsymbol{dm}$ ▷ First estimate of Heun's method
- $\boldsymbol{m}_{Temp} \leftarrow \boldsymbol{m}_{Temp} / \text{norm}(\boldsymbol{m})$ ▷ Normalize m
- $t_{Temp} \leftarrow t + dt$
- $\boldsymbol{h}_{eff} \leftarrow$ COMPUTEHEFF(t_{Temp}, $\boldsymbol{m}_{Temp}$, structs) ▷ Update h_{eff}
- $\boldsymbol{dm}_{Temp} \leftarrow$ COMPUTEDERIVATIVE(t_{Temp}, $\boldsymbol{m}_{Temp}$, $\boldsymbol{h}_{eff}$, structs) ▷ Derivative at the first estimate
- $\boldsymbol{m} \leftarrow \boldsymbol{m} + \frac{dt}{2}(\ \boldsymbol{dm} + \boldsymbol{dm}_{Temp}\ )$ ▷ Heun's method update
- $\boldsymbol{m} \leftarrow \boldsymbol{m}\ /\ \text{norm}(\boldsymbol{m})$

end

Each Cartesian magnetization component is stored in a different pointer, containing the magnetization values for each frequency. The Heun algorithm is employed to update the values of the magnetization at each time step for each input frequency.

The COMPUTEHEFF function is responsible for calculating the effective field, and its components are summarized in Algorithm 1.3.

The COMPUTEDERIVATIVE function performs the LLG equation.

Algorithm 1.3: Effective field components (COMPUTEHEFF)

$$\boldsymbol{h}_{dmg} \leftarrow -\boldsymbol{N}\,\boldsymbol{m} \qquad \triangleright \texttt{Demagnetizing field}$$

$$\boldsymbol{h}_{ext} \leftarrow \frac{1}{\mu_0 M_S}\left(\boldsymbol{h}_{ext_{\mathrm{DC}}} + \boldsymbol{h}_{ext\,\mathrm{AC}} \sin\left(2\pi f_h t + \boldsymbol{\varphi}_h\right)\right) \qquad \triangleright \texttt{External field}$$

$$\boldsymbol{h}_{th} \leftarrow \frac{\boldsymbol{\eta}}{M_S}\sqrt{\frac{2\alpha_G k_B T}{\gamma \mu_0 M_S V dt}} \text{ with } \boldsymbol{\eta} \leftarrow \mathcal{N}(0,1) \qquad \triangleright \texttt{Thermal field}$$

$$\boldsymbol{h}_{VCMA} \leftarrow \left(\frac{VCMA_{\mathrm{DC}}}{\mu_0 M_S} + \frac{VCMA_{\mathrm{AC}}}{\mu_0 M_S}\sin\left(2\pi f_V t + \varphi_V\right)\right)(\boldsymbol{m}\cdot\boldsymbol{u}_k)\,\boldsymbol{u}_k \qquad \triangleright \texttt{VCMA field}$$

$$\boldsymbol{h}_{ani} \leftarrow \frac{2K_u}{\mu_0 M_S^2}(\boldsymbol{m}\cdot\boldsymbol{u}_k)\,\boldsymbol{u}_k \qquad \triangleright \texttt{Anisotropy field}$$

$$\boldsymbol{h}_{STT} \leftarrow \sigma J_{STT} g_T\left(\boldsymbol{m},\,\boldsymbol{m}_p\right)\left(\boldsymbol{m}\times\boldsymbol{m}_p\right) \qquad \triangleright \texttt{STT field}$$

$$\boldsymbol{h}_{FLT_{STT}} \leftarrow q_{STT}\sigma J_{STT} g_T\left(\boldsymbol{m},\boldsymbol{m}_p\right)\boldsymbol{m}_p \qquad \triangleright \texttt{Field-like torque STT field}$$

$$\boldsymbol{h}_{SOT} \leftarrow \sigma J_{SOT}\theta_{SHE}\left(\boldsymbol{m}\times\boldsymbol{\sigma}_{SHE}\right) \qquad \triangleright \texttt{SOT field}$$

$$\boldsymbol{h}_{FLT_{SOT}} \leftarrow q_{SOT}\sigma J_{SOT}\theta_{SHE}\boldsymbol{\sigma}_{SHE} \qquad \triangleright \texttt{Field-like torque SOT field}$$

$$\boldsymbol{h}_{eff} \leftarrow \boldsymbol{h}_{demag} + \boldsymbol{h}_{ext} + \boldsymbol{h}_{th} + \boldsymbol{h}_{ani} + \boldsymbol{h}_{VCMA} + \boldsymbol{h}_{STT} + \boldsymbol{h}_{FLTSTT} + \boldsymbol{h}_{SOT} + \boldsymbol{h}_{FLTSOT}$$

In the CUDA version of the solver, individual kernels are dedicated to calculating each field and for the computation of the LLG equation.

We want to point out that the structure of the code is highly scalable, paving the way for the integration of future features and improvements.

1.9.1 Graphical user interface of the macrospin solver

In order to create a user-friendly macrospin solver, a GUI has been developed using the tkinter package in Python. This interface provides a clear visualization of all the simulation parameters extracted from the text configuration files, and it has received very positive feedback from members involved in the SWAN-on-chip projects for which the macrospin solver was delivered.

Upon launching the interface, a preliminary GUI appears, providing options to create a new project or open a previous one, as illustrated in Figure 1.27.

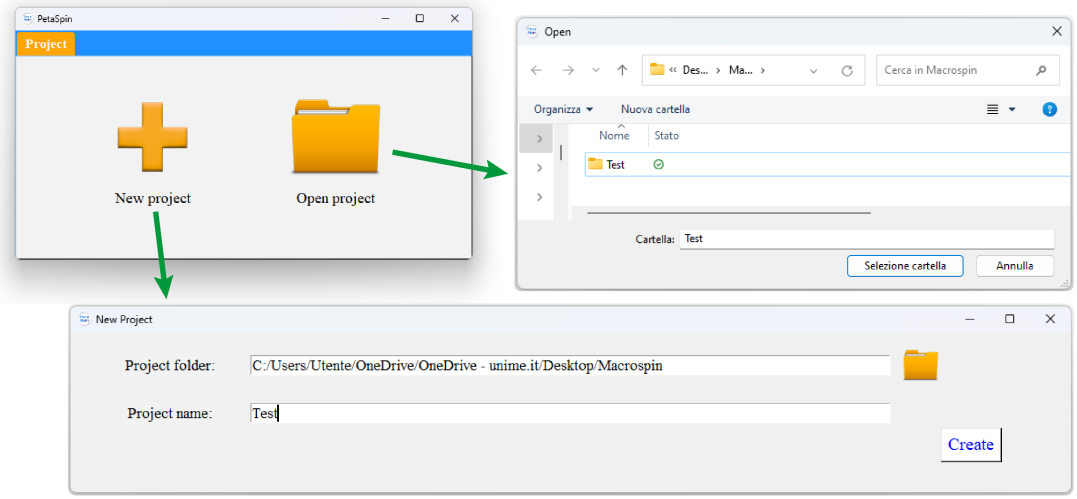

FIGURE 1.27: Welcome screen of the GUI, provides options to either create a new project or open an existing one.

Figure 1.28 shows the main panel, featuring two tabs – one for the configuration of all the simulation parameters and the other for the post-processing of results. Four buttons on the top right side enable users to create a new project, open an existing project, save and run the project, respectively. At the bottom of the GUI, the current project folder is visible along with zoom in and zoom out buttons on the right side. A sketch of the MTJ in the two main configurations – fixed or dynamic PL magnetization – is presented, highlighting the coordinate system and the external excitations. Each vertical configuration tab on the left side of the GUI corresponds to a configuration text file, simplifying the parameter comparison between text files and GUI settings.

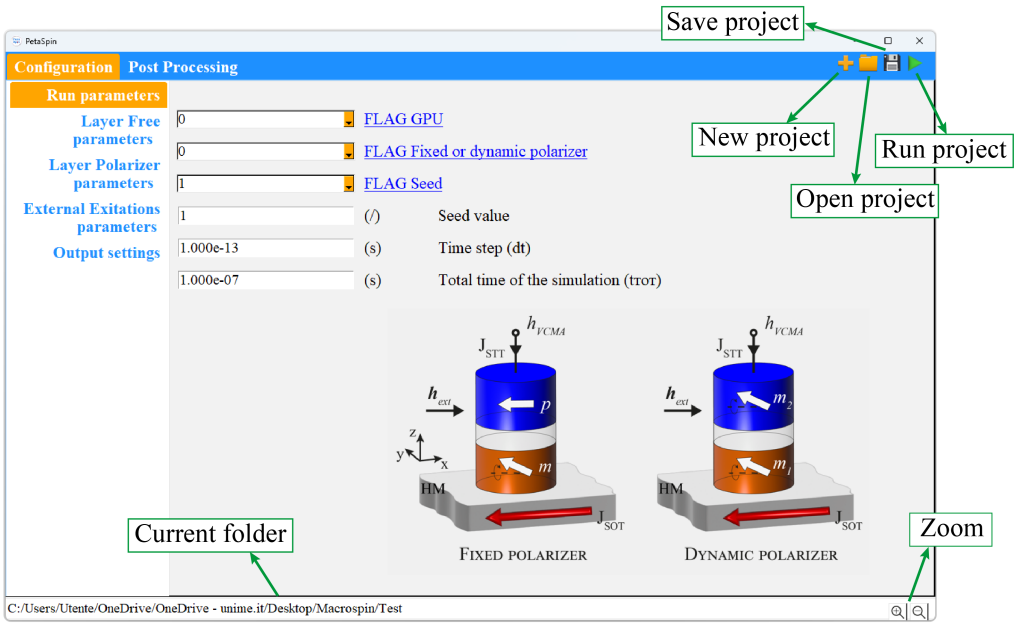

FIGURE 1.28: Main panel of the GUI, featuring several highlighted commands.

Specific conditions of the simulations are configured through a drop-down menu, indicated by the underline blue word "FLAG" label followed by the corresponding condition. A tooltip provides additional information when the cursor hovers over the condition. In Figure 1.29, the configuration for the STT field is shown as an example. The first FLAG activates the computation of the STT field and also determines the nature of the current – DC, AC, DC+AC or user-defined through a text file. To enhance visibility, active parameters are displayed in black font, while inactive ones, not computed by the solver, are in gray font.

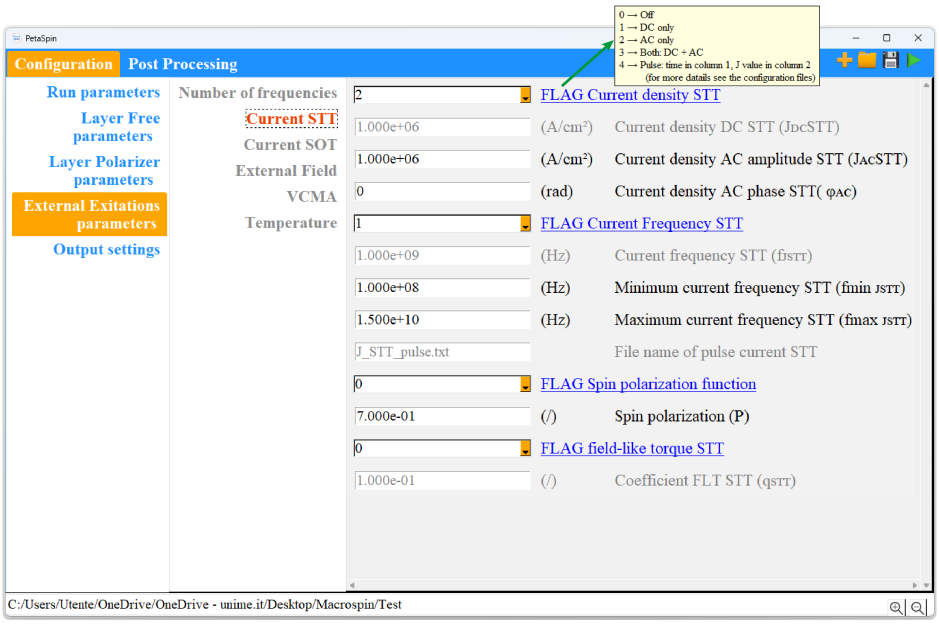

FIGURE 1.29: Example of configuration setting of the STT field in the GUI.

One project can be set up at a time, however the solver, launched using a separate thread, allows the opening of different projects and running multiple instances of micromagnetic simulations simultaneously. In the current version, the post-processing includes two options. The first one involves the plotting of the magnetization amplitude as a function of the frequency for the three Cartesian components. The frequency range can vary for different excitations (but it is the same in number), and a preliminary GUI allows the selection of the frequency range to be considered in the plot, as illustrated in Figure 1.30. Additionally, a tooltip displaying the coordinates of the data appears when the cursor hovers over the data points. The resulting plot is automatically saved as a PNG image in the output folder.

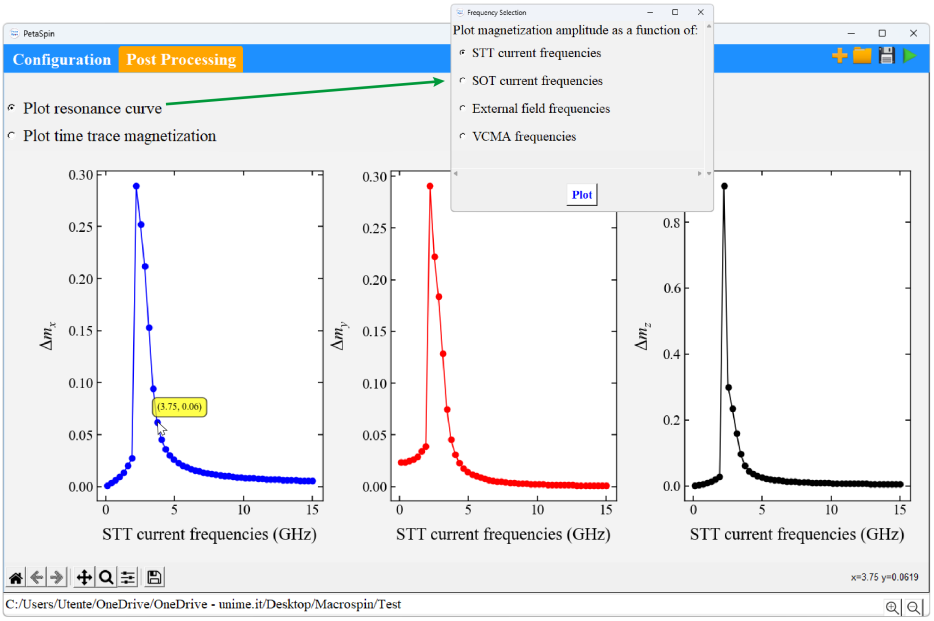

FIGURE 1.30: Post-processing tab in the GUI: plotting the three Cartesian components of the oscillating magnetization amplitude as a function of the input frequency of a selected excitation.

The second option involves the plotting of the time trace of each Cartesian component of the magnetization, as shown in Figure 1.31. A separate GUI enables the selection of one or more frequencies to plot.

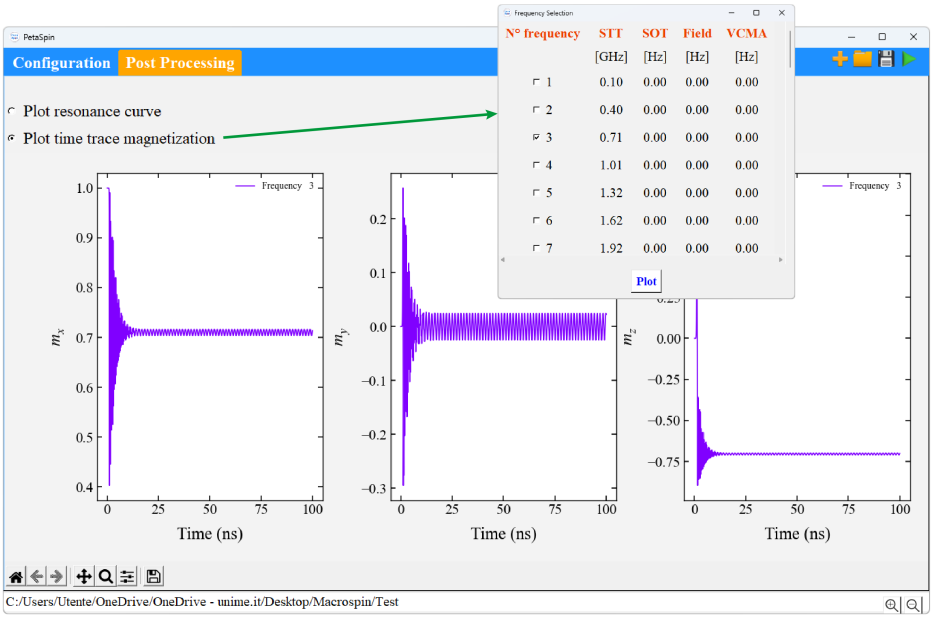

FIGURE 1.31: Post-processing tab in the GUI: plotting the time trace of the three Cartesian components of the magnetization.

1.10 Applications of MTJs

As previously mentioned, MTJs can find applications in various domains. We leveraged MTJs in neuromorphic computing [67, 70] (Chapter 3), probabilistic computing [71, 72] (Chapters 4) and oscillator-based Ising machine [71]. This section presents our results in utilizing MTJs for electromagnetic RF energy harvesting (paragraph 1.10.1) and accelerometers (paragraph 1.10.2) [68]. In these applications, the devices are modeled using our micromagnetic solver within the macrospin approximation.

1.10.1 Nanoscale STDs for harvesting ambient radiofrequency energy

The extensive network of sensors and IoT devices worldwide demands a massive number of radiofrequency (RF) source for data exchange. Unfortunately, a considerable amount of the ambient RF energy from these source remains unutilized. Properly harvesting this energy could provide an abundant source of energy useful to supply electronic devices and sensors [60, 73–75]. The energy harvesting

module (EHM) developed in collaboration with the group of Prof. Yang at the National University of Singapore is composed of a receiver, an STD as rectifier, a power management module and a load that utilizes the harvested power, as illustrated in Figure 1.32. The main element of the EHM is the rectifier. Up to now, the challenge is to develop a device that can effectively capture the ambient RF power P_{RF}, which is typically less than -20 dBm, in range $-82 < P_{RF} < -20$ dBm (6.3 pW $< P_{RF} < 10$ μW).

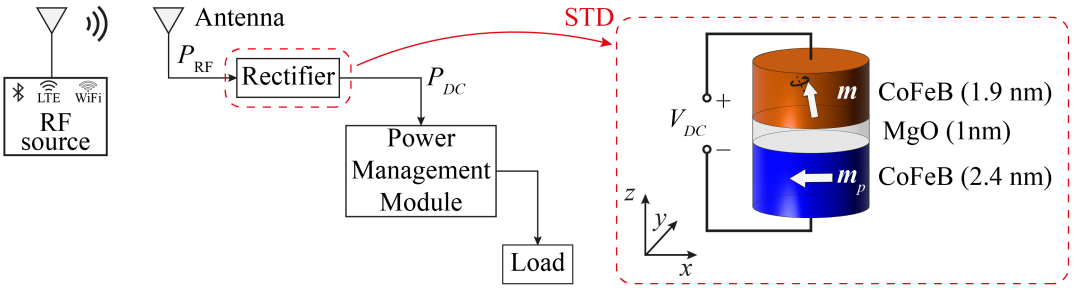

FIGURE 1.32: An illustrative example of the RF energy harvesting from environment sources using STD, with in-plane polarizer and tilted out-of-plane FL magnetization.

We explore the potential application of the STD as a rectifier (or spin-rectifier, SRs) element of the EHM, coupled with a properly designed matched antenna, referred to as STD-rectenna. In particular, we demonstrated the technical feasibility of STDs by designing two prototypes: (i) a single STD-rectenna for ambient energy harvesting (ii) a STD-array for broadband rectification, achieving a record zero-bias sensitivity (≈ 34.5 V/mW), high efficiency (7.81%) and STD-based EHM operational at $P_{RF} < -20$ dBm.

The employed MTJs are composed of CoFeB for both the FL and PL, separated by an MgO spacer layer. Through extensive experimental measurements, the best rectification results have been consistently observed in devices with 40×100 nm^2 and 80×200 nm^2 (the first dimension corresponds to the hard axis (y-axis), while the second corresponds to the easy axis (x-axis)), with 1.9 nm and 1 nm, thickness of the FL and spacer layer, respectively, as illustrate in Figure 1.32.

The response of the devices under zero-bias and zero magnetic field condition have been studied. In Figure 1.33 (a) the rectification response of the two devices at $P_{RF} = -30$ dBm is presented, showing a resonant behavior. These devices

are specifically chosen to operate at frequencies close to WiFi (2.4 GHz), 4G (2.3-2.6 GHz) and 5G (3.5 GHz). At $P_{RF} = -55$ and -40 dBm, the 80×200 nm^2 and 40×100 nm^2 respectively achieved a maximum sensitivity ≈ 2.4 and ≈ 1.0 V/mW, surpassing the reported zero-bias sensitivity [46, 64, 75] and the state-of-the-art zero-bias Schottky diode (which is state-of-the-art RF rectifier). As the P_{RF} is reduced to -20 dBm, the two STDs exhibits different responses, as shown in Figure 1.33 (b) and (c) for 40×100 nm^2 and 80×200 nm^2 STDs, respectively. While the 80×200 nm^2 STD shows a resonant behavior similar to the one observed at $P_{RF} = -30$ dBm, the 40×100 nm^2 STD shows a broadband response (from 0.1 to 3.5 GHz).

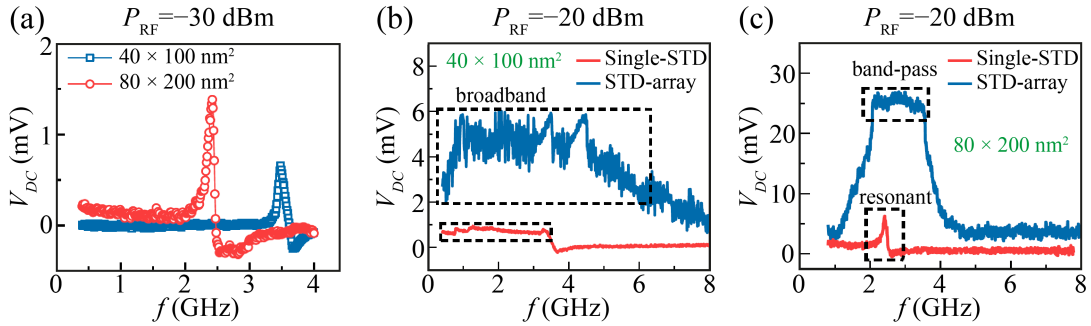

FIGURE 1.33: Experimental rectification curves for 40×100 nm^2 and 80×200 nm^2 STDs at different input powers. (a) Resonant response for both STDs (blue line 40×100 nm^2 and red line 80×200 nm^2) at $P_{RF} = -30$ dBm. (b) Broadband rectification from 40×100 nm^2 single STD (red line) and 10 STDs connected in series (blue line), at $P_{RF} = -20$ dBm. (c) Resonant and band-pass response from the 80×200 nm^2 single STD (red line) and a 10 STDs connected in series (blue line).

However, the output rectified voltage is not enough for the EHM. To address this, we propose to use an array of STDs connected in series. Figure 1.33 (b) and (c) show the results for two arrays of 10 STDs, the first made of 40×100 nm^2 STDs, the second of 80×200 nm^2 STDs. The 10 STDs are connected in series without any external antenna. The excitation is provided directly by wireless RF energy, which is the key challenge to face for the development of ultra-compact EHMS. The 40×100 nm^2 STD-array shows a broadband frequency response compatible with the single STD response, while the 80×200 nm^2 one exhibits a transition from resonant to broadband. The latter shows a narrow detection band compared to the 40×100 nm^2 STD-array (suitable for a band-pass filter rectifier) but with

high output voltage, indicating high sensitivity. To further understand the experimentally observed transition from resonant to broadband in 40×100 nm^2 single STDs, we performed micromagnetic simulations within the macrospin approximation.

We simulated an elliptical device with FL dimensions of 40×100 nm^2 and thickness 1 nm, featuring an in-plane polarizer and tilted out-of-plane FL magnetization. The main micromagnetic parameters used to solve the LLGS equation are: $M_S = 800$ kA/m, $K_u = 0.39$ MJ/m^3, $\alpha_G = 0.02$, and STT parameters $g = 2$, $P = 0.7$. The demagnetizing field originated by the polarizer is added as a constant external field $H_{\mathrm{DC}} = -5$ mT. The rectification curves are computed for AC current density raging from $J_{\mathrm{AC}} = 0.1$ to 10 MA/cm^2 and frequencies scanned from $f = 0.1$ to 15 GHz. Figure 1.34 presents the results: (a) the phase diagram of the rectification curves as a function of the amplitude of the AC current density, where the color identifies the amplitude of the x-component of the FL magnetization Δm_x. For clarity, the maximum value of Δm_x as a function of the AC current in shown in (b), and four examples of rectification curves are displayed in (c), highlighting the transition from resonant to broadband response. Furthermore, we observed that a small variation of the anisotropy coefficient has a big impact on the resonance frequency value. Keeping the AC current constant at a value for which the STD is resonant, $J_{\mathrm{AC}} = 0.1$ MA/cm^2, Figure 1.34 (c) shows a linear behavior of the resonance frequency as a function of the anisotropy parameter K_u. For $K_u = 0.419$ MJ/m^3 the frequency value is close to the 5G frequency ($\approx$ 3.5 GHz), matching experimental measurement for similar devices.

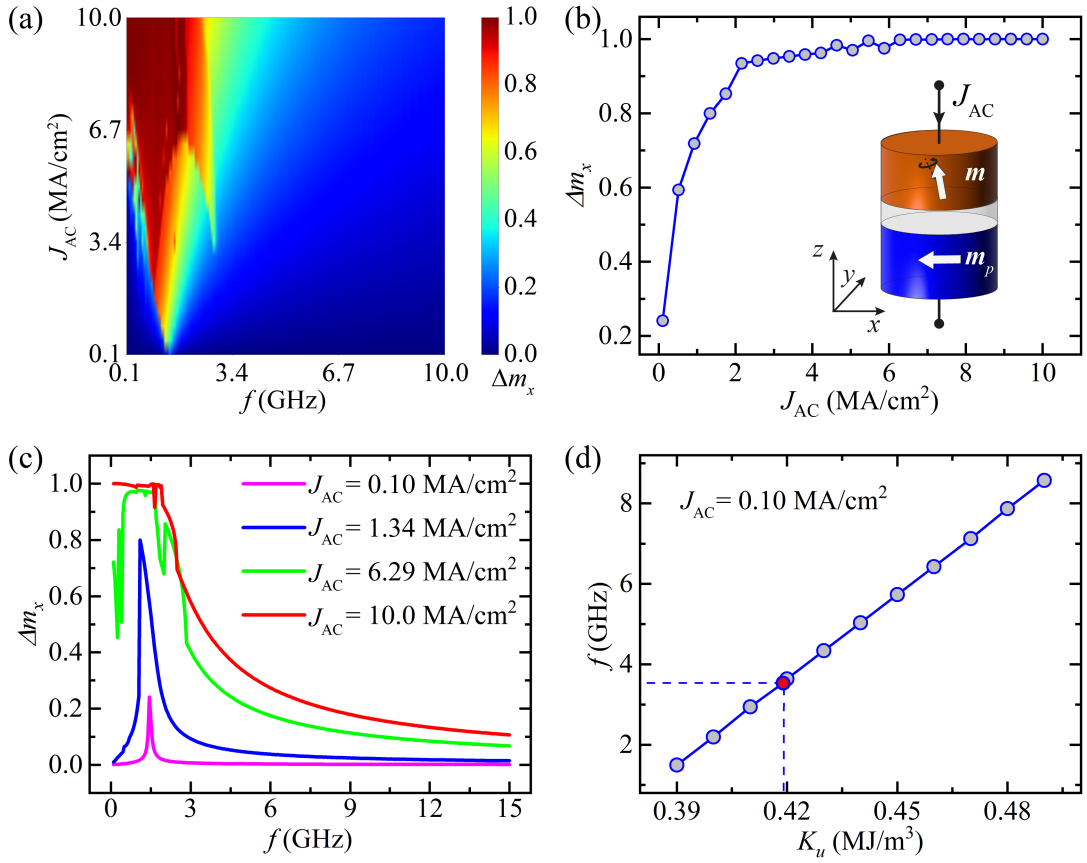

FIGURE 1.34: Simulated results for a 40×100 nm^2 illustrate the transition from resonant to broadband response. (a) STD phase diagram of the precession amplitude of the x-component of the FL magnetization (Δm_x) as a function of the microwave frequency f and AC current density amplitude (J_{AC}). (b) Maximum Δm_x as a function of J_{AC}. (c) Four examples of rectification curves at different J_{AC} to highlight the transition from resonant to broadband response. (d) Linear behavior of microwave frequency as a function of the anisotropy coefficient K_u. Red dot: the 5G frequency, matching the experimental measurement for a similar device.

In order to understand the origin of the transition from resonant to broadband response, additional experiments have been performed, involving a single and two serially-connected 40×100 nm^2 STDs, driven by an AC current at angular frequency ω (and $I_{DC} = 0$ mA). Figure 1.35 (a) and (b) show the respective recorded microwave emissions. The single STD exhibits a weak second harmonic (2ω component) at 6 GHz, while in the two STDs connected in series the second harmonic is enhanced by one order of magnitude.

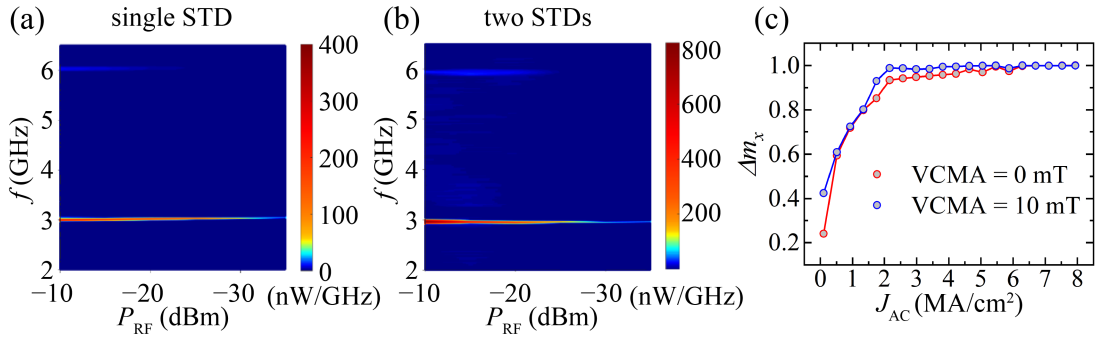

FIGURE 1.35: Experimental spectrum emitted from 40×100 nm^2 (a) single STD (b) two serially-connected STDs, excited by a RF signal ($I_{DC} = 0$ mA). The presence of a second harmonics at 6 GHz is evident and enhanced in (b). (c) Amplitude of the x-component FL magnetization as a function of the AC input current for VCMA of 0 and 10 mT. The VCMA-driven enhancement of the magnetization precession can be observed.

The presence of the second harmonics can be understood from the rectification voltage formulation in Eq. (1.71). Its enhancement is due to the large VCMA of the device. When connected in series, the voltage at 2ω in one STD drives a parametric excitation in the other STD, enhancing the magnetization precession angle. To support this claim, we also perform a micromagnetic simulation with AC current at ω and VCMA applied at 2ω, with a VCMA amplitude of 10 mT, and compare the response with zero VCMA, as shown in Figure 1.35 (c). The micromagnetic parameters are the same as those used for results in Figure 1.34. The simulation results confirm that the amplitude of the magnetization precession increases with VCMA, indicating a potential enhancement of the sensitivity.

Finally, the feasibility of the EHM module is demonstrated by integrating the 80×200 nm^2 STD-array (10 STDs in series) in an EHM in an ambient environment without an extra antenna. The EHM is used to power a temperature sensor, as illustrated in Figure 1.36 (a). In Figure 1.36 (b), the rectification response of the STD-array using the 2.45, 3.5 and $2.5 + 3.5$ GHz RF sources, is presented. The voltage threshold of the boost is 20 mV, which the STD-array achieves at 22 dBm at 2.45 GHz. The boost converter steps up the STD-array voltage from 20 – 50 mV to 1.6 – 4 V. The temperature sensor turns on at $V_{step} \approx 1.2$ V, achieved at –27 dBm and –22 dBm using the dual sources (2.45 and 3.5 GHz) and a single 2.45 source, respectively. To mitigate the fast charging-discharging effect of STDs due to the low capacitance, an external capacitor of 0.01 F (capacity 3.3 V) is used to maintain a stable rectified voltage.

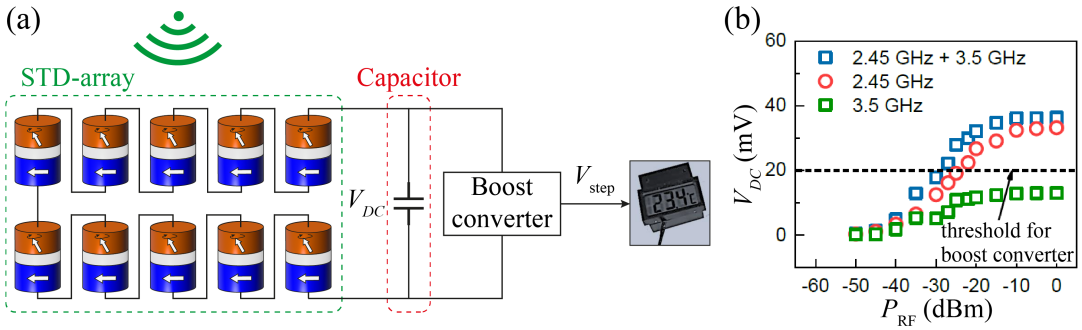

FIGURE 1.36: (a) A schematic representation of the energy harvesting module based on STDs. The harvested voltage (V_{DC}) from the STD-array is stored in the capacitor, and a boost converter steps it up to a high-voltage ($V_{step} \approx 1.6 - 4$ V) to power a temperature sensor. (b) Experimental results of rectified voltage from STD-array using 2.45 and 3.5 GHz antenna. The dashed line represents the threshold voltage for the boost converter ($V_{DC} \approx$ 20 mV).

In comparison with the state-of-the-art RF rectifiers, STDs are ultra-compact, less prone to the parasitic effect, easy to integrate, scalable and more efficient in the ambient condition. Combining these features of STDs, a new benchmark is demonstrated for rectifier applications in the low-power regime and compact technology.

1.10.2 Spintronic accelerometer based on MTJs

Accelerometers are an essential component in many applications, including automotive ones [76], seismic monitoring [77] and human-computer interaction [78]. Conventional accelerometers often rely on micro electro-mechanical systems (MEMSs). The most predominant type is the capacitive MEMS-based accelerometer, illustrated in Figure 1.37 (a). These devices operate by detecting changes in capacitance, resulting from external accelerations, between a fixed electrode and a movable one attached to a proof mass coupled by a spring [77, 79]. However, these systems have drawbacks such as difficulties in down-scaling, lack of electromagnetic radiation hardness and high-power consumption, due to the need to charge capacitive plates [77].

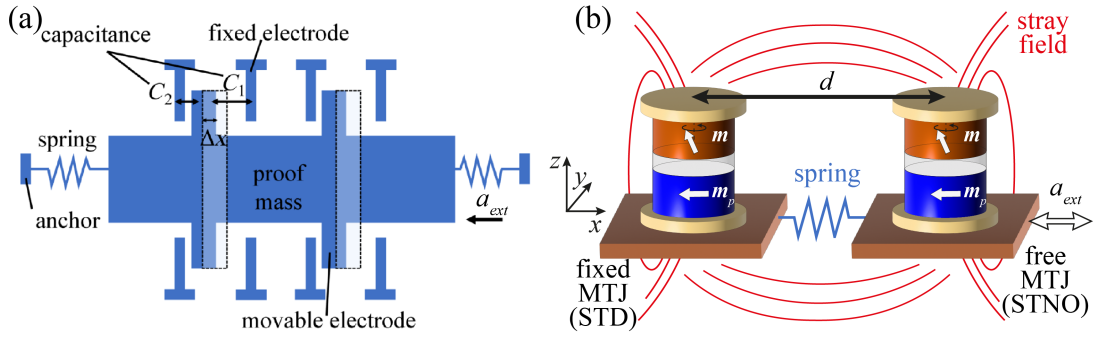

FIGURE 1.37: (a) Schematic description of a capacitive MEMS-based accelerometer, consisting of a fixed electrode and a movable one. Change in the relative position lead to variations in capacitance. (b) MTJ-based accelerometer configuration, with a fixed MTJ, operating as an STD, and a free MTJ, acting as a STNO, coupled magnetically (via the stray field) and elastically (through the spring).

Spintronic-based accelerometers have been proposed [80–82], however these rely on the mechanical stresses acting on the MTJ, which can potentially lead to rapid degradation. Moreover, these solutions often required intricate fabrication processes for the MTJ, making them expensive and complex products.

Inspired by the concept of capacitive MEMS-based accelerometers, we propose an innovative design for MTJ-based accelerometers. Our approach involves magnetically (via dipolar interactions) and elastically (through the substrate) coupling the two MTJs working as STNOs. Figure 1.37 (b) shows the device concept: one MTJ is attached on top of a stationary substrate (fixed MTJ), while the other MTJ is placed on a substrate that is free to move (free MTJ) but elastically connected to the fixed MTJ. The fixed MTJ operates as an STD in injection-locking regime, and the free MTJ is designed in such a way that the rectified voltage in the fixed MTJ changes linearly with the distance between the two devices. This changes in rectified voltage is directly linked to the external acceleration acting on the free MTJ, as the magnetization dynamics is faster than the elastic ones.

The detailed results of this work can be found in Ref.[68], and a patent is pending.

1.10.2.1 Model

To demonstrate the feasibility of the proposed MTJ-based MEMS accelerometer, we performed simulations that account for both magnetic and elastic coupling. The magnetic behavior of the spintronics MEMS accelerometer is simulated by numerically integrating two coupled LLGS equations (Eq. (1.48))

for the free and fixed MTJs. The effective field includes the anisotropy field, the demagnetizing field and the dipolar field acting on MTJ i due to MTJ j: $h_{dip,\,j\to i} = (\mu_0/4\pi r_{ij}^3)\ \left(3\,\boldsymbol{u}_{r_{ij}}\left(m_j\cdot\boldsymbol{u}_{r_{ij}}\right)-\boldsymbol{m}_j\right) = \bar{\bar{D}}\cdot\boldsymbol{m}_j$ where $\boldsymbol{u}_{r_{ij}}$ is the unit vector of magnitude r_{ij} representing the distance between MTJ i and MTJ j, and $\bar{\bar{D}}$ is the position-dependent dipole matrix. The MTJs employed have an in-plane PL and out-of-plane FL magnetization, patterned into pillars with elliptical cross-section dimensions of 150×70 nm^2 (in x and y direction, respectively) and 1.6 nm-thick FL of CoFeB. The micromagnetic parameters are: $M_S = 0.95$ MJ/(Tm^3), $K_u = 0.545$ MJ/m^3, $A_{ex} = 20$ pJ/m, $\alpha_G = 0.02$, and the STT parameters are $g = 2$, $P = 0.77$, and $q_{STT} = 0.1$. The nominal electrical resistances are $R_P = 640\ \Omega$ and $R_{AP} = 1200\ \Omega$.

The elastic dynamics of the free MTJ can be described as a one-dimensional damped spin-mass harmonic oscillator, expressed as:

$$m_{tot}\frac{d^2u_{MTJ}}{dt^2} = -b\frac{du_{MTJ}}{dt} - k_{el}u_{MTJ} - F_{mag} + F_{ext} \tag{1.78}$$

Where u_{MTJ} is the displacement of the free-MTJ along the direction connecting the two devices; m_{tot} is the total mass of the accelerometer; b is the viscous damping coefficient; k_{el} is the elastic constant, with resonance frequency $\omega_0^2 = k_{el}/m_{tot}$; $F_{mag} = \nabla\left(\boldsymbol{m}_i M_s V_{FL}\cdot\boldsymbol{h}_{dip,i\to j}\right)$ is the magnetic interaction between the MTJs, and $F_{ext} = m_{tot}a_{ext}(t)$ is the driven external force acting on the devices due to the external acceleration $a_{ext}(t)$. These forces are applied to the center of mass of the free MTJ.

1.10.2.2 Results

A preliminary study involves the characterization of the fixed MTJ in order to identify the value of DC current ($I_{\mathrm{DC},1}$), inducing the self-oscillation, and the AC current ($I_{\mathrm{AC},1}$ and $f_{\mathrm{AC},1}$) controlling the oscillation frequency through the injection-locking phenomenon (described in paragraph 1.8.2.2). We found $I_{\mathrm{DC},1} = -0.09$ mA, $I_{\mathrm{AC},1} = 50\ \mu$A, and $f_{\mathrm{AC},1} = 0.5$ GHz.

After the characterization of the STD, mutual synchronization of the free and fixed MTJs is studied at varying distance d. The fixed MTJ is set in the injection locking regime and the free MTJ is biased with a second DC current ($I_{\mathrm{DC},2}$) driving the self-oscillations. The rectification voltage of the isolated fixed MTJ

($V^0_{DC,1}$) serves as a reference for calibration, with the rectification voltage given by $\Delta V_{DC} = V_{DC,1} - V^0_{DC,1}$, where $V_{DC,1}$ is the rectification voltage measured across the fixed MTJ when the two MTJs are coupled. Figure 1.38 (a) shows ΔV_{DC} as a function of the distance (ranging from 350 to 650 nm) for various $I_{DC,2}$. The intrinsic phase shift φ_{DC} between the AC current and the oscillating magnetization depends on the distance between the MTJs, as shown in Figure 1.38 (b) for $I_{AC,2} = -0.10035$ mA. The phase shift can be easily measured, thus the latter results offer a good advantage.

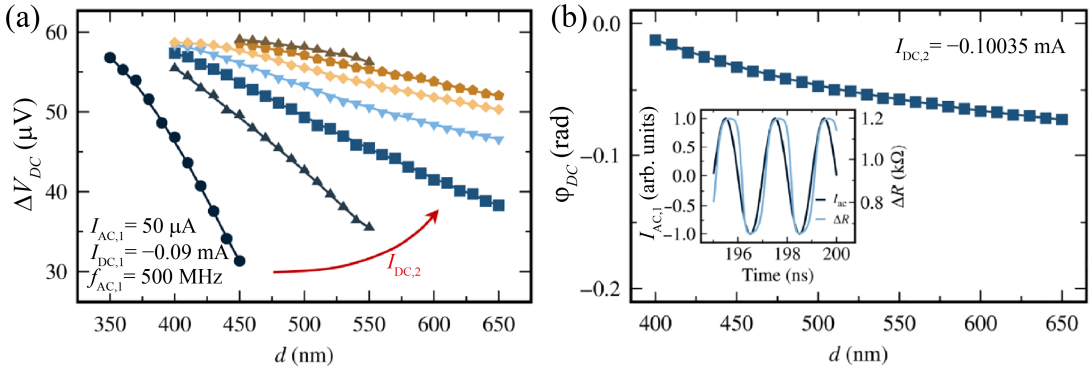

FIGURE 1.38: (a) Rectification voltage ΔV_{DC} as a function of the distance d between the fixed MTJ and the free MTJ, for different DC current injected into the free MTJ $I_{DC,2}$: -0.099 mA (black dots), -0.1 mA (dark blue triangles), -0.10035 mA (navy-blue squares), -0.1008 mA (light-blue triangles), -0.10135mA (yellow diamonds) , -0.1017 mA (light-brown pentagons), 0.10225 mA (dark-brown triangles). (b) Intrinsic phase shift φ_{DC} as a function of d at $I_{DC,2} = -0.10035$ mA. Inset: time trace of the input AC current $I_{AC,1}$ and the magnetoresistance ΔR for $I_{DC,2} = -0.10035$ mA and distance $d = 450$ nm.

Finally, the modeling of the complete magneto-elastic dynamics is studied. When the mechanical resonance is at least 10 times larger than the external acceleration a_{ext}, the latter can be determined from the equilibrium conditions of a forced harmonic oscillator: $a_{ext} = \omega_0^2\, d$. To demonstrate that this formulation can be applied in our MTJ-based MEMS accelerator, we solve the Eq. (1.78) with $m_{tot} = 1$ μg, $k_{el} = 1$ kN/m [79, 83] and damping ratio $\zeta = b/\sqrt{4k_{el}m_{tot}} = 0.75$, for the fixed MTJ in injection-locking regime and free MTJ in self-oscillation with $I_{AC,2} = -0.10035$ mA, the time evolution of distance d for different constant acceleration up to $10g$, where $g = 9.81$ m/s^2 is the acceleration gravity, is shown in Figure 1.39 (a). These results show that the transient elastic dynamics occur in less than 0.5 ms, and the final displacement d corresponds to the forced harmonic case. The transient of the magnetization dynamics occurs in less than 40

ns, that is negligible compared to the elastic one. Figure 1.39 (b) demonstrates the results when a more realistic acceleration is taken into account, revealing the direct mapping between ΔV_{DC}, d and a_{ext} affirming the effectiveness of the proposed approach.

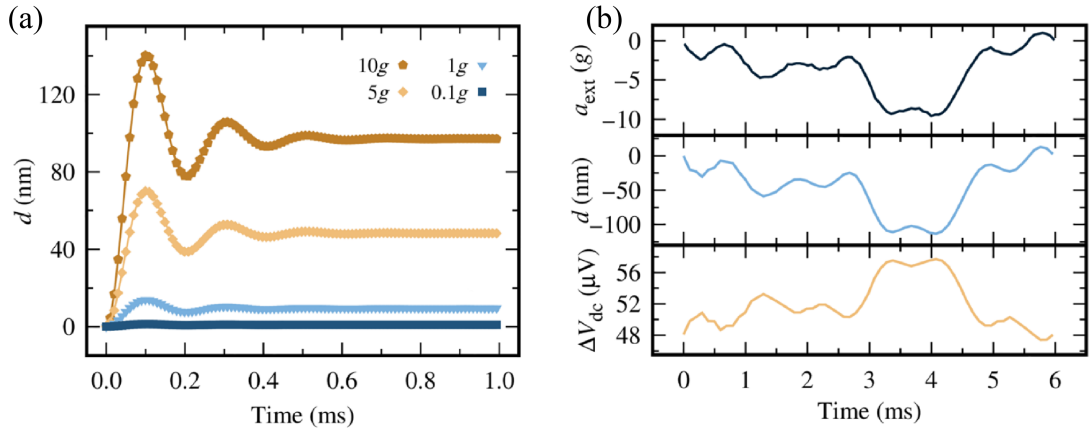

FIGURE 1.39: (a) Time-dependent displacement of the free MTJ relative to its initial position under different constant external accelerations, expressed in units of g. (b) More realistic input time-dependent external acceleration, a_{ext}, in units of g (top panel); relative displacement, d, between the free and fixed MTJs (middle panel); and time-dependent rectification voltage, ΔV_{DC}, measured at the fixed MTJ (bottom panel) in response to a_{ext}.

1.11 Conclusions

Micromagnetism emerges as a robust theoretical framework for investigating magnetization dynamics, and micromagnetic simulations, which numerically integrate the LLG equation, serve as powerful tools for exploring various phenomena of magnetization behavior in spintronic devices. In this chapter, we have introduced a fast and user-friendly micromagnetic solver within the macrospin approximation designed to simulate MTJs in several configurations and operating regimes.

We have presented two impactful applications of MTJs: firstly, an energy harvesting module based on STDs designed to efficiently capture ambient radiofrequency energy. Secondly, an MTJ-based accelerometer was presented, where changes in the rectified voltage of the STD, coupled with an STNO, are correlated with the acceleration of the system. Spintronic devices are particularly appealing due to their low-power consumption and compact size.

Chapter 2

Magnetic skyrmions

Magnetic skyrmions exhibit unique properties and are known to be the smallest textures that can be stabilized in ferromagnetic materials. These textures can have a significant impact in technological developments and, in particular, in storage and unconventional computing architectures. Beyond the mainstream applications, it is interesting to highlight a path toward the use of magnetic skyrmions in biomedical applications, such as their use in transcranial magnetic stimulation. This technique has played a role in treating neurological disorders including depression and chronic pains. Basically, skyrmions stabilized in a track can be shifted with different types of excitations. While moving, these textures modify the spatial distribution of the local magnetic field and, if coupled with a coil, can induce an electrical field that can be used for electrical stimulation [84].

This chapter provides an introduction to magnetic skyrmions and fundamental studies for their static characterizations, exploring several materials' configurations. The final section investigates the dynamics of skyrmions driven by thermal gradients in different magnetic systems.

2.1 Introduction

A skyrmion is a topologically stable field configuration, described as a particle-like object. The name derives from the physicist T. Skyrme [85, 86], who first proposed their existence in 1961. It is characterized by a non-trivial topology, i.e., an integer skyrmion winding number [87]:

$$N_{sk} = \frac{1}{4\pi} \int \boldsymbol{m} \cdot (\partial_x \boldsymbol{m} \times \partial_y \boldsymbol{m}) \, dx \, dy \tag{2.1}$$

N_{sk} represents the number of times the spin direction wraps the 2D surface around a unit sphere. Mathematically, structures with different topological numbers cannot be continuously transformed into one another. This implies that, in a physical system, there is an additional energy barrier for skyrmion annihilation and/or nucleation [88].

Since 1961, skyrmions have been observed in many contexts, including liquid crystal, Bose-Einstein condensates [89], optics [90, 91], and magnetic materials [8, 92, 93]. This thesis focuses on magnetic skyrmions, known for their topological stability, high mobility, and small magnetic configuration, making them valuable solitons for the encoding of information [94–96]. They are promising for diverse technological applications, such as racetrack memories [97], neuromorphic computing [98, 99], and unconventional applications [100, 101].

A magnetic skyrmion is composed of three regions: an inner domain, known as skyrmion core, an outer domain, and a domain wall that determines the rotation of the magnetization from the core toward the outer domain [96]. The skyrmion core is the region where the magnetization goes from out-of-plane magnetization to in plane magnetization $(m_z = 0)$. The radius R of this region defines the skyrmion size [102] (see Figure 2.1).

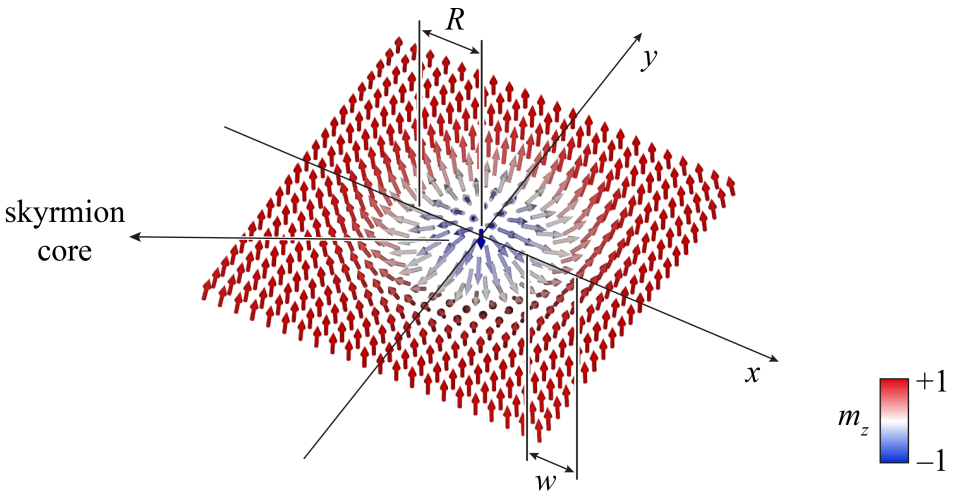

FIGURE 2.1: Schematic diagram of the magnetization of a skyrmion placed in the center of a 2D thin film. The arrows represent the spin directions. The skyrmion core radius R and the domain wall width w are highlighted.

Mathematically, the magnetization variation along the radius, i.e., the skyrmion profile, is expressed as:

$$\boldsymbol{m}(r) = \Big[\sin(\theta(r))\cos(Q_v\varphi + Q_h), \sin(\theta(r))sin(Q_v\varphi + Q_h), \cos(\theta(r))\Big] \tag{2.2}$$

where $\theta\,(r)$ is the radial function which determines the perpendicular component of the magnetization $\boldsymbol{m}\,(r)$; Q_v is the vorticity number, defined by the winding number of the in-plane spin texture; Q_h is the helicity number which indicates the in-plane swirling direction (the phase). These three quantities (N_{sk}, Q_v, Q_h) fully characterize the topological spin texture [103]. An additional index, polarity (p), describes whether the out-of-plane magnetization at the core of the skyrmion points in the positive $(p = 1)$ or negative $(p = -1)$ z-direction [104].

Different types of skyrmions arise from the combination of these numbers. The two most studied are the Bloch and Néel skyrmions. The difference between these two configurations lies in the different orientation of the DW magnetization. Figure 2.2 summarizes the spin configurations of these skyrmions, together with the cross-sections across the skyrmion diameter and the corresponding parameter values (N_{sk}, Q_v, Q_h). In a Néel-type skyrmion, the magnetization rotates along the radial direction, $Q_h = 0$ for outward chirality and π for inward chirality. In a Bloch-type skyrmion, the magnetization rotates perpendicular to the radial direction, $|Q_h| = \pi/2$, with corresponding chiral state ± 1 for clockwise (CW) and

counter-clockwise (CCW) respectively. For both Néel- and Bloch-type skyrmions, $N_{sk} = p = |1|$.

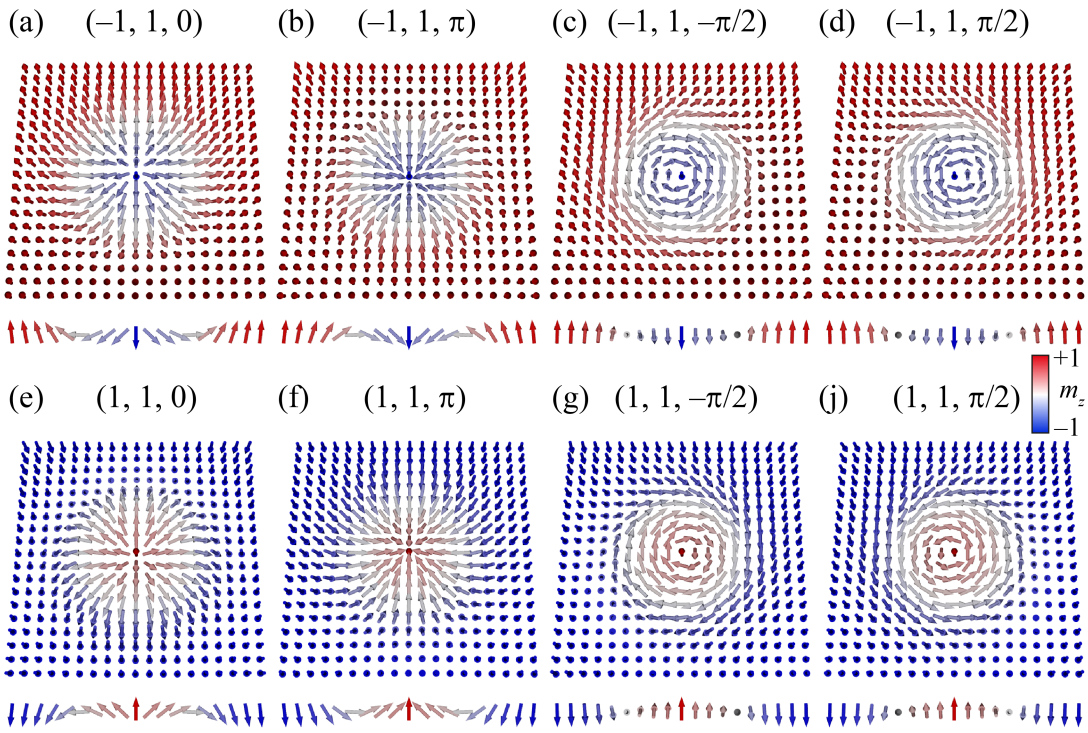

FIGURE 2.2: Spin textures in (a)-(b)-(e)-(f) are Néel-type skyrmions: the spins rotate in the radial planes from the inner domain to the outer domain. Spin textures in (c)-(d)-(g)-(j) are Bloch-type skyrmions: the spins rotate in the tangential plane, that is, orthogonal to the radial directions, when moving from the inner domain to the outer domain. Top: skyrmion number, vorticity number and helicity number, i.e., (N_{sk}, Q_v, Q_h). Bottom: cross-section across the skyrmion diameter.

The spin texture emerges as an equilibrium magnetization configuration influenced by the interplay of different energy interactions and their respective strengths. The balance between interactions like exchange and anisotropy, favoring ferromagnetic alignment of adjacent spins, and others like DMI and dipolar interactions, promoting twisted spin textures, determine the stabilization of skyrmions [96]. Symmetry breaking plays a crucial role in their stability and classification. Skyrmions have been observed in materials with out-of-plane magnetization, which is achievable through an external field or sufficiently large perpendicular anisotropy [105–107]. In the absence of DMI, a trade-off between the dipolar and exchange interactions stabilizes the so-called skyrmion bubbles [108], while,

for large enough DMI, chiral skyrmions are observed. In particular, in bulk materials with *b*DMI, such as B20 materials, Bloch skyrmions are stabilized, while Néel skyrmions are mainly observed in thin magnetic films and heterostructures involving the coupling of FM layers with materials exhibiting strong spin-orbit coupling, like heavy metals (HM), therefore in presence of *i*DMI [8]. The Néel skyrmions are more promising for practical applications because they can be stabilized at room temperature [109]. The chirality of the skyrmion can be controlled by the sign of the DMI parameter [110]. Several studies have been performed to understand the energy stability of skyrmions. A fundamental theoretical model developed for a single skyrmion relies on the definition of the critical DMI value (D_c) below which a single magnetic skyrmion can be stabilized. At zero temperature and infinite film approximation, $D_c = 4\sqrt{4K_u}/\pi$ [96].

Skyrmions can be observed in different phases, either isolated or forming a lattice, identified by the critical material parameter $\kappa = \pi D/4\sqrt{AK_u} = D/D_c$. For $\kappa > 1$, the skyrmions are stable and form a lattice, whereas for $0 < \kappa < 1$, they are metastable and isolated [111, 112].

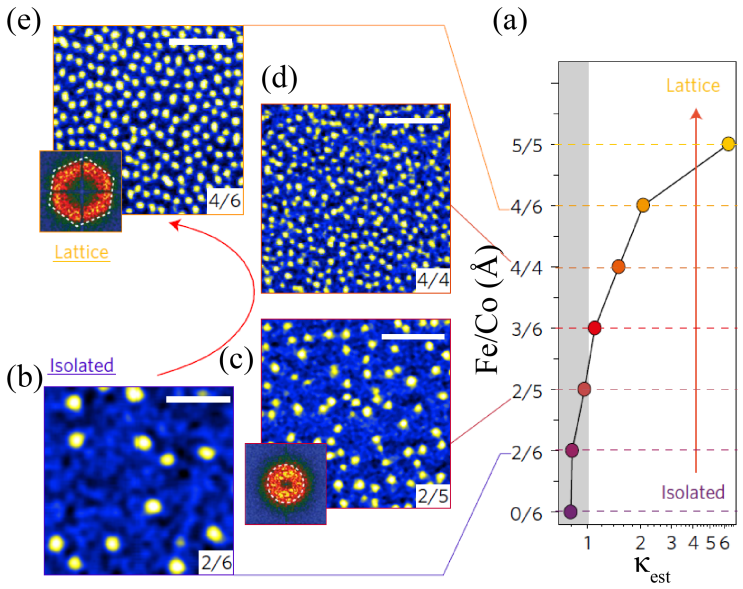

FIGURE 2.3: Tuning skyrmion stability with Fe/Co composition. (a) Estimation of skyrmion stability parameter κ for Fe/Co samples with different composition. (b)-(e) experimental images of skyrmion configuration in sample (b) Fe(2)/Co(6) (c) Fe(2)/Co(5) (d) Fe(4)/Co(4) and (e) Fe(4)/Co(6). With increasing κ, there is the transition from isolated skyrmions to a dense lattice [111].

Figure 2.3 shows the experimental results of Soumyanarayanan *et al.* [111], in multilayer films (discussed in the paragraph 2.1.1) with [Ir(10)/ Fe(x)/ Co(y)/ Pt(10)]$_{20}$ stacks of different composition and thickness (layer thickness in Å in parentheses). As the estimated stability parameter κ increases, the skyrmions' configuration evolves from isolated skyrmions (Figure 2.3 (b)) to a dense lattice (Figure 2.3 (e)), accompanied by a change in skyrmion size. This is also evident while comparing Figure 2.3 (b) and (e).

Woo *et al.* [106] studied the stability of a skyrmion lattice within a confined geometry, examining the influence DMI and M_S. Figure 2.4 presents the theoretical phase diagram, annotated with experimental parameters from their Pt/Co/Ta experiment. The skyrmion phase is observed in regions with higher values of M_S and DMI. For low M_S and low DMI, the uniform magnetization state is the only stable configuration. As M_S exceeds 0.2 MA/m and DMI is below 0.5 mJ/m^2, there are stabilized bubbles, while low M_S and high DMI values result in the observation of labyrinth stripes. The labyrinth stripe phase and skyrmion phase are close in energy, and slight parameters adjustments can lead the transition from one configuration to the other (for example see Figure 2.4 (b) $M_S = 0.068\,\mathrm{MAm}^{-1}$ and $D = 1.25 - 1.50\,\mathrm{mJm}^{-2}$).

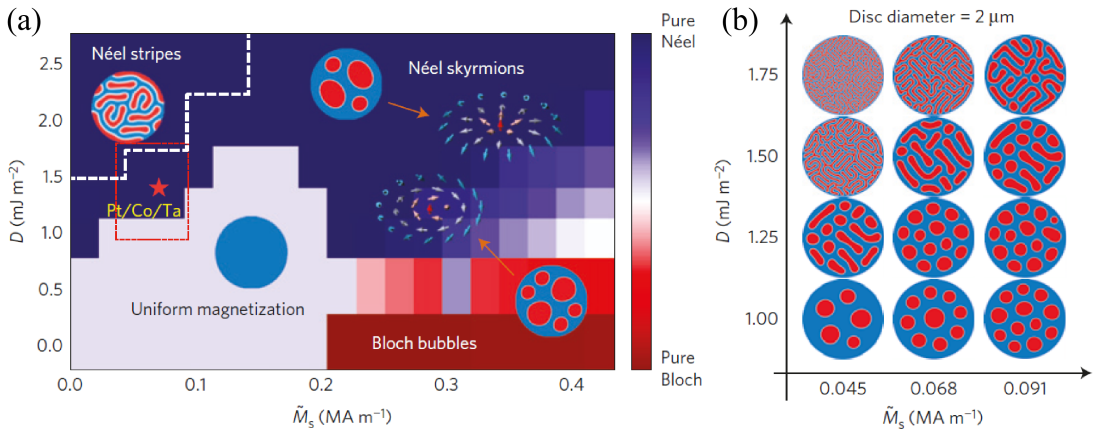

FIGURE 2.4: Phase stability diagram of spin textures as a function of DMI and M_S. (a) Magnetic equilibrium states in Pt/Co/Ta nano discs as a function of the saturation magnetization and DMI. (b) Examples of stable spin textures for different magnetic parameters [106].

2.1.1 Magnetic skyrmions in magnetic multilayers

Skyrmions were first observed experimentally in MnSi in 2009, since then they have attracted a great interest and have been observed in several other materials, such as bulk B20 materials (e.g. MnGe or FeGe) and thin film structures like Fe/Ir [113]. In the former the observation has been achieved below room temperature. For this reason, most of the research directions have been focused on the latter, in particular the first experimental observation was in a heavy metal single ferromagnet bi-layer [114]. However, skyrmions can have a large size, up to the micrometers. To reduce their size to nanoscale, magnetic multilayers with an active tri-layer composition, involving two heavy metals and one ferromagnetic material, are repeated several times along the thickness of the samples [107, 111, 115]. This approach offers tunability of the parameters through variations in constituent components and relative layer thicknesses, leading to an enhanced DMI and thermal stability.

In magnetic multilayers, usually two different types of skyrmions can be stabilized: hybrid and pure Néel skyrmions. Recently, the observation of skyrmionic cocoons has been reported [116].

A skyrmion in multilayer is classified as a pure Néel when a Néel skyrmion is stabilized in each layer, while a hybrid skyrmion is characterized by a thickness-dependent reorientation of its DW chirality [117, 118]. The investigation of these different configurations, initially explored in DW and later extended to skyrmions, has revealed that the value of the DMI plays a key role in the DW chirality [117]. In the absence of DMI, a hybrid DW is observed, characterized by a Néel configuration in proximity of the external layers, with opposite chirality in the topmost and bottommost layers (clockwise and counterclockwise). In the middle layers, a Bloch DW is hosted. By increasing the $|D|$ values the preference for a single chirality shifts the position of the Bloch DW from the middle layer to higher or lower layers, depending on the sign of DMI (see Figure 2.5). Beyond a threshold value of DMI, the Block DW is completely expelled from the structure and a pure Néel DW is observed (see Figure 2.5 (d)).

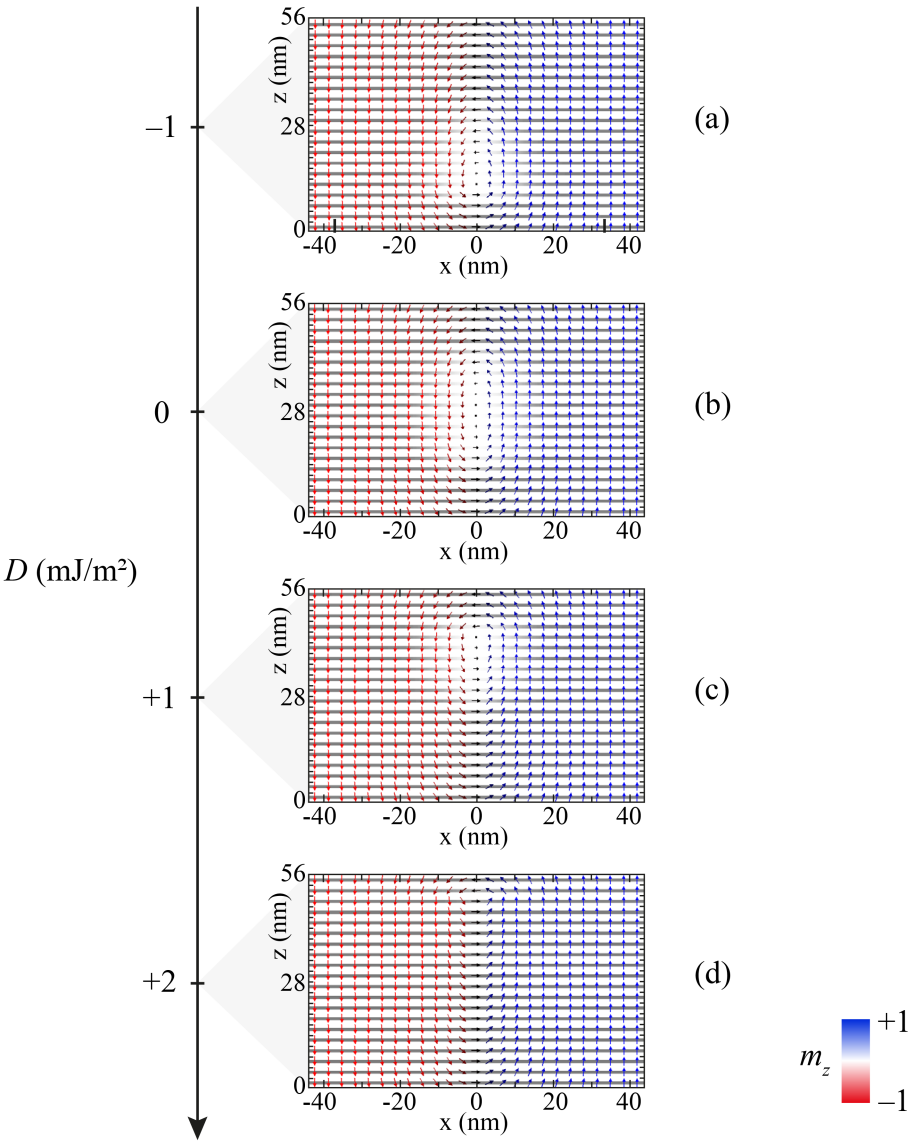

FIGURE 2.5: Cross-section of a magnetic multilayer with DW stabilized with $D = -1, 0, 1$ and 2 mJ/m^2 from (a) to (d) [117].

These complex magnetization profiles are stabilized by a competition between the *i*DMI and the dipolar interactions among all the layers. Figure 2.6 shows an example of hybrid skyrmion stabilized in 16-repeat magnetic multilayers studied by Li *et al*. [118] (see Figure 2.6 (a)). It is possible to identify mainly Néel-type skyrmions in the topmost and bottommost layers, with opposite chirality – inward and outward chirality, respectively (compare Figure 2.6 (c) and (d)) –, and a Bloch-type skyrmion in the 10th magnetic layer (see Figure 2.6 (d)). Figure 2.6 (b) summarizes the helicity angle as a function of the number of magnetic layers

for $D = 0.4\ \mathrm{mJ/m^2}$.

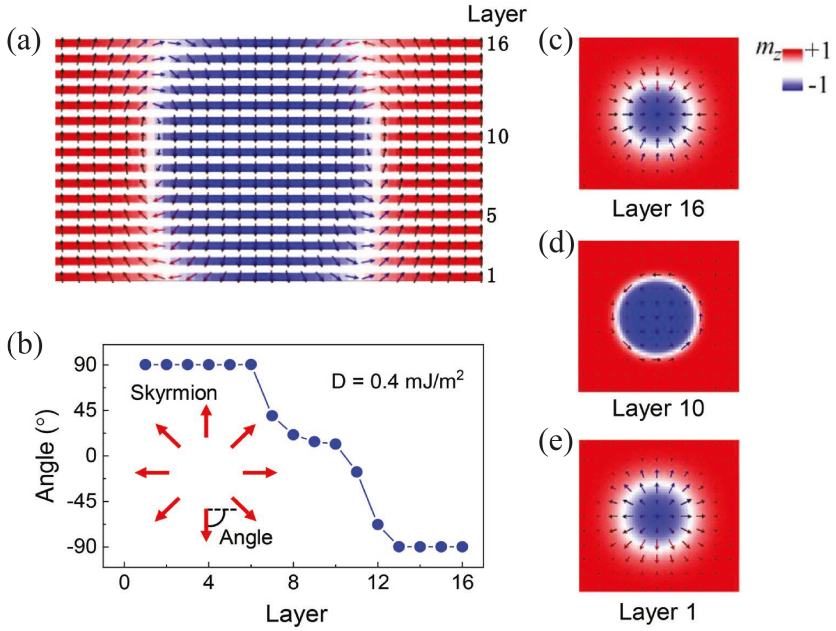

FIGURE 2.6: Micromagnetic simulations of a single skyrmion in a magnetic multilayer. (a) Cross-section of the 16-repeat multilayer sample. (b) Helicity angle as a function of the position of the layers, showing the transition from an outward Néel skyrmion in layer 1 (c), to a Bloch skyrmion in layer 10 (d), and an inward Néel skyrmion in layer 16(e) [118].

Furthermore, the skyrmion size depends on the layer position in the sample. Specifically, skyrmions tend to be larger in the central layers and smaller in the external layers [117, 119].

2.1.1.1 Magnetic skyrmion in synthetic antiferromagnet materials

A particular class of magnetic multilayer structures are SAFs materials, where magnetic skyrmions have been experimentally observed [120, 121]. A SAF typically consists of two thin FMs layers separated by a spacer, which is a thin non-magnetic metallic material such as ruthenium or platinum. The spacer couples the two FM layers through an interlayer exchange interaction, of the Ruderman-Kittel-Kasuya-Yoshida (RKKY) type [94, 122, 123]. The sign of the interlayer exchange constant (A^{ex}) depends on the thickness of the spacer: (i) a positive value results in the alignment the two ferromagnets in the same direction, forming synthetic ferromagnets; (ii) a negative value leads to anti-parallel alignment of the

two ferromagnets, stabilizing an SAF. Figure 2.7 shows an antiferromagnetic Néel skyrmion configuration in an SAF, characterized by a skyrmion with positive core and inward chirality in the lower FM layer, and a skyrmion with negative core and outward chirality in the upper FM layer [124]. The advantages of the SAF structures over previous multilayer will be discussed in paragraph 2.3.

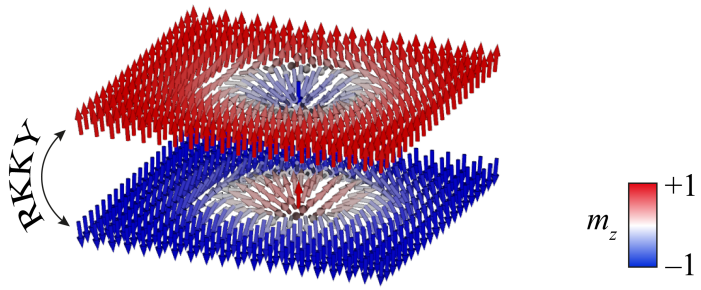

FIGURE 2.7: Skyrmion configuration in an SAF material: a skyrmion with positive core and inward chirality in the lower FM layer is coupled via RKKY-type interaction with a skyrmion with negative core and outward chirality in the upper FM layer.

2.2 Characterization of the spin configuration of magnetic skyrmions

Part of the activities that we have implemented in this Ph.D. program are linked with collaborations with experimental groups. In particular, before exploring potential spintronic applications, it is important to conduct static investigations, with the primary goal of characterizing the spin configurations of the skyrmions. Understanding these configuration is crucial due to their impact on the skyrmion dynamics [117]. Most of these studies use magnetic microscopies to obtain two-dimensional spatial resolution of the spin texture. The results we have analyzed have been imaged at the Lawrence Berkeley National Laboratory and the samples are from the lab of Prof. Wanjun Jiang. As already discussed in paragraph 2.1.1, in multilayers, skyrmions can have a three-dimensional structure.

Sophisticated imaging methods using photons or electrons, can be used to characterize those 3D structures. For example, the X-ray magnetic circular dichroism (XMCD) method projects the direction of the magnetization onto the photon beam, allowing a distinction between out-of-plane and in-plane components,

which is crucial for the 3D characterization of the skyrmions. The full-field magnetic transmission X-ray microscopy (MTXM) [106], which uses Fresnel zone plates as an X-ray optical system, obtains a 3D spin configuration for samples mounted on a rotatory stages. 2D MTXM images are taken with the X-ray ptychography as a function of the rotation angle [119] where the sample is raster scanned while the focused X-ray beam remains fixed and a full diffractive pattern is collected for each of the scanning steps.

While electron- and photon-based magnetic microscopy techniques require sources to produce their respective probes, a wide range of scanning probe methods are also available, notably magnetic force microscopy (MFM). The MFM maps magnetic fields by a measurement of the interaction of the magnetic moment of the tip with the stray field of the sample. It is one of the most used technique [111, 115, 119] although it cannot reveal the spin chirality [125].

Recent studies also introduced indirect methods to identify the type of skyrmions. Duong *et al*. [119] have demonstrated that systems with pure Néel skyrmions and hybrid skyrmions exhibit different characteristics in the first-order reversal-curve (FORC) diagrams.

Another indirect approach we have worked on is based on the different collapsing dynamics observable for pure Néel and hybrid skyrmions driven by changing perpendicular magnetic field as discussed in detail in the subparagraph 2.2.1.

2.2.1 Field-driven collapsing dynamics of skyrmions in magnetic multilayers

In this section, we will show a qualitatively different collapsing dynamics for pure Néel and hybrid skyrmions induced by a perpendicular magnetic field in two representative multilayers systems, $[Pt/Co/Ir]_{15}$ and $[Ta/\ CoFeB/\ MgO]_{15}$. In the first system, skyrmions undergo a first morphological transition at zero field to labyrinth domains and followed by a second morphological transition to skyrmions with opposite polarity and chirality, when the direction of the perpendicular fields is reversed. On the other hand, skyrmions in $[Ta/CoFeB/MgO]_{15}$ multilayers exhibit a continuous field-dependent transition, which is mainly related to a reversible change of the skyrmion size. These conclusions arise from

a combination of experimental results and micromagnetic simulations. A comprehensive micromagnetic phase diagram is provided to identify these two collapsing mechanisms, which depend on the material parameters, since the two different collapsing dynamics rely on the detailed layer-dependent spin textures of skyrmions. We wish to stress the potential use of them as fingerprints of the skyrmion type.

The main results of this study have been published in Ref. [126].

2.2.1.1 Experimental measurements

Two multilayers samples, well known to host nanoscale skyrmions at room temperature [106, 107, 127] are investigated. Sample #1 [Pt(1.5 nm)/ Co(1 nm)/ Ir(1.5 nm)]$_{15}$ and #2 [Ta(3 nm)/ Co_{20} Fe_{60} B_{20}(1 nm)/ MgO(2 nm)]$_{15}$ (values in parentheses represent the thickness) were fabricated onto thermally oxidized silicon substrates using an ultrahigh-vacuum magnetron sputtering system. Figure 2.8 (a) and (c) provide a schematic illustration of the two samples.

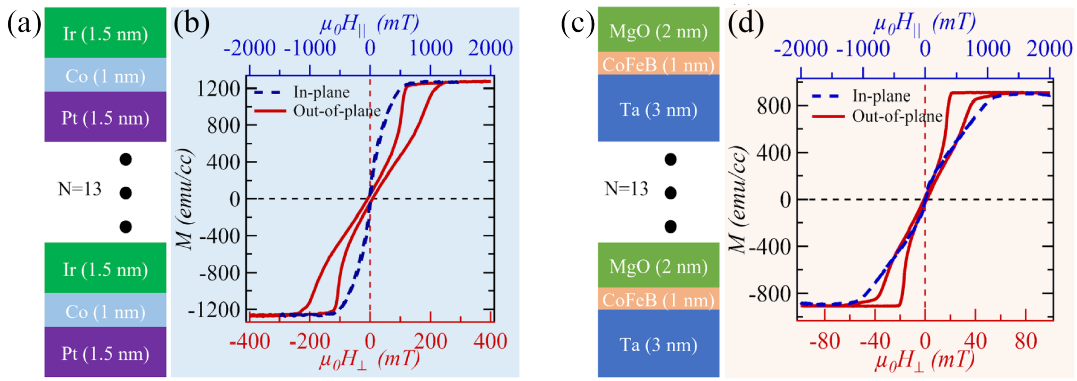

FIGURE 2.8: (a) A schematic representation of the [Pt(1.5 nm)/Co(1 nm)/Ir(1.5 nm)]$_{15}$ multilayer and (b) its in-plane (dashed blue) and out-of-plane (solid red) magnetic hysteresis loops. (c) A schematic representation of the [Ta(3 nm)/$Co_{20}Fe_{60}B_{20}$(1 nm)/MgO(2 nm)]$_{15}$ multilayer and (d) its in-plane (dashed blue) and out-of-plane (red solid) magnetic hysteresis loops. The $H_\perp$ and $H_{||}$ indicated in the x-axes of the figures are the applied magnetic fields oriented parallel or perpendicular to the plane of the film, respectively.

The magnetic properties of these samples were characterized via using a superconductor quantum interference device (SQUID) magnetometer (MPMS, Quantum Design). The resulting in-plane and out-of-plane magnetic hysteresis loops

for the sample #1 are shown in Figure 2.8 (b), and for the sample #2 in Figure 2.8 (d). The estimated M_S and anisotropy field are $M_S = 1200$ emu/cc and $\mu_0 H_k = 500$ mT for the $[Pt/Co/Ir]_{15}$ multilayer, and $M_S = 900$ emu/cc and $\mu_0 H_k = 1000$ mT for the $[Ta/\ Co_{20}\ Fe_{60}\ B_{20}/\ MgO]_{15}$ multilayer.

These multilayers were deposited on 100-nm-thick Si_3N_4 membranes for imaging analysis by using the full-field soft X-ray transmission microscopy with a spatial resolution of approximately 20 nm, which is performed at the beamline 6.1.2, Advanced Light Source, Lawrence Berkeley National Laboratory. We use this imaging approach to capture the collapsing dynamics of Néel- or hybrid-type skyrmions that are driven by perpendicular magnetic fields.

Figure 2.9 (a) shows a series of magnetic images of the $[Pt/Co/Ir]_{15}$ multilayer, captured at the Co L3 edge (778.5 eV) under different perpendicular fields $H_\perp$. At an applied magnetic field of $\mu_0 H_\perp = 141$ mT, isolated quasicircular Néel skyrmions are observed. As magnetic fields decrease toward zero, these Néel skyrmions expand and change shape, resulting in a mixed phase that includes both isolated larger skyrmions and elongated ones. When the magnetic field direction is reversed, this mixed phase transitions into a labyrinthine domain configuration (at $\mu_0 H_\perp = -93$ mT). Further increasing the magnetic field leads to the dissection of labyrinthine domains into isolated skyrmions, with an inverse magnetization of their core compared to the starting one. In contrast, a very different collapsing behavior is observed in the $[Ta/CoFeB/MgO]_{15}$ multilayer, as shown in Figure 2.9 (b), with magnetic images captured at the Fe L3 edge (708.5 eV) for different $H_\perp$. At $H_\perp = 47.8$ mT, the presence of circular domains is indicative of isolated hybrid skyrmions. By decreasing $H_\perp$ the skyrmions continuously increase in size, thanks also to the reversed field direction parallel to the skyrmions' core. Further increasing $H_\perp$ causes the skyrmions to coalesce and form large band domains, with the magnetization in the center aligned along the field direction (at $\mu_0 H_\perp = -67.0$ mT).

These qualitatively different collapsing dynamics of the skyrmions resulting from experimental observations imply different spin profiles across the thickness direction of the multilayers. To study the three-dimensional profile of the skyrmions, micromagnetic simulations will be performed as discussed ahead in the text.

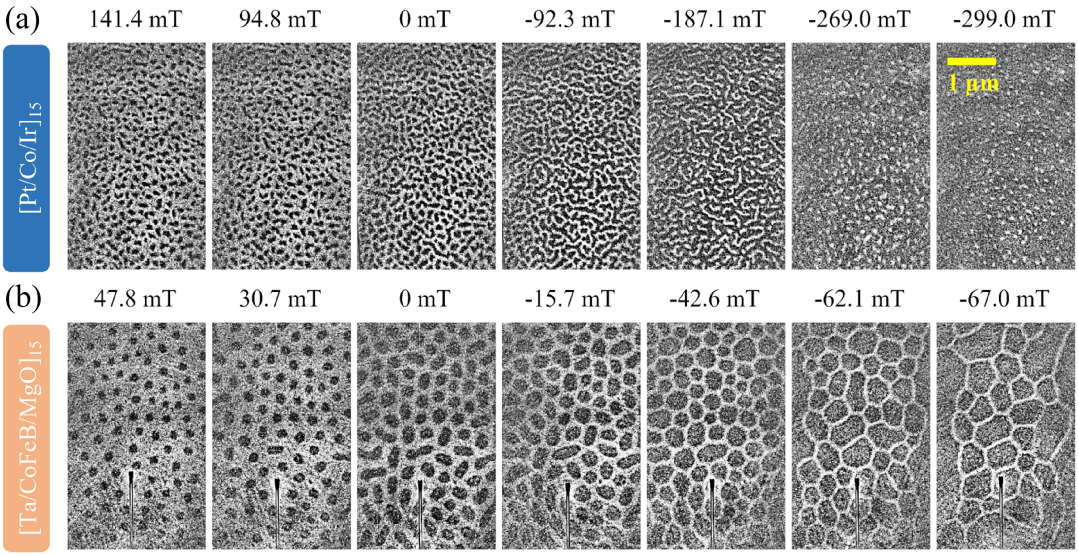

FIGURE 2.9: Experimental results of the collapsing dynamic of skyrmions driven by out-of-plane field in (a) $[Pt/Co/Ir]_{15}$ and $[Ta/CoFeB/MgO]_{15}$ multilayers. The color white (black) corresponds to the local magnetization pointing out of the film plane $m_z > 0$ $(m_z < 0)$

2.2.1.2 Micromagnetic model

We perform micromagnetic simulations based on the typical parameters of the $[Pt/Co/Ir]_{15}$ [107] and $[Ta/CoFeB/MgO]_{15}$ [118] multilayers. Table 2.1 summarizes micromagnetic and computational parameters used for the simulations.

TABLE 2.1: Summary of micromagnetic and computational parameters used to simulate experimental multilayer samples.

Parameter	**$[Pt/Co/Ir]_{15}$**	**$[Ta/CoFe/MgO]_{15}$**
M_S (MA/m)	1.2	0.91
A_{ex} (pJ/m)	10	10
D (mJ/m^2)	0.5	0.5
K_u (MJ/m^3)	1.29	0.52
Discretization cell size (nm^3)	$2.5 \times 2.5 \times 1$	$4 \times 4 \times 1$
Number of cells	$400 \times 400 \times 17$	$250 \times 250 \times 21$

In simulations, both samples are characterized by five repetitions of FM layer of

thickness 1 nm, interposed by a nonmagnetic layer of 3 and 4 nm thickness in sample #1 and #2, respectively. *i*DMI boundary conditions are present in all the simulations: $\frac{d\boldsymbol{m}}{dn} = \frac{D}{2A}(\hat{z} \times \mathbf{n}) \times \boldsymbol{m}$ [9, 10], where $\mathbf{n}$ is the unit vector normal to the edge of the sample (see paragraph 1.3.2 for details).

Figure 2.10 shows the equilibrium configurations of skyrmions in sample #1 with an applied field $H_\perp = 141$ mT, and in sample #2 with $H_\perp = 47.9$ mT. Sample #1 hosts a Néel skyrmion in all the layers, with a partial size reduction in the external layers. As discussed in section 2.1.1, the same chirality in each layer is due to the large contribution of the DMI, while the thickness-dependent size of the skyrmion is due to the magnetostatic field. On the contrary, sample #2, with a smaller DMI, hosts a hybrid skyrmion, where the Bloch-type skyrmion is shifted to layer 4, due to the non-zero DMI.

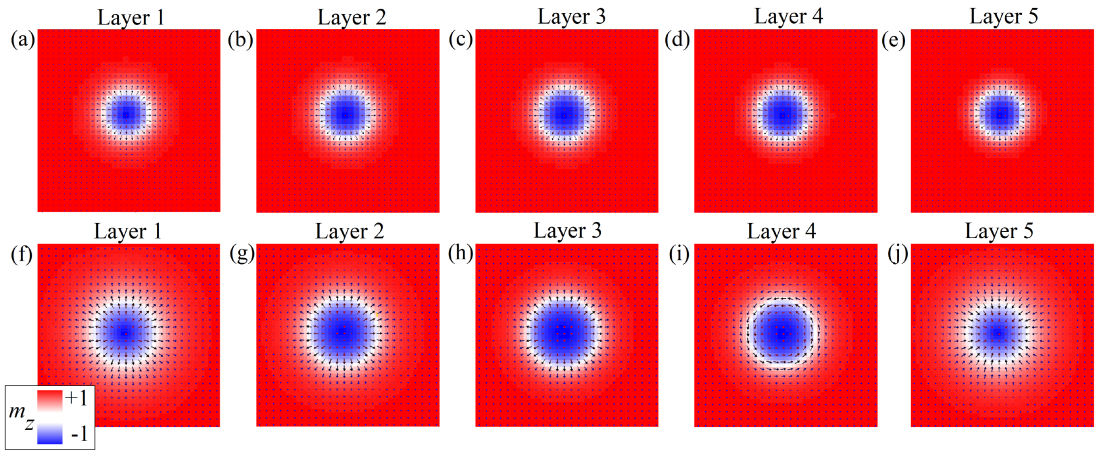

FIGURE 2.10: Spatial spin configuration of skyrmions in multilayer samples. (a)-(e) Néel skyrmions in FM layers of $[Pt/Co/Ir]_{15}$ at $H_\perp = 141$ mT. (f)-(j) Hybrid skyrmions in FM layers of $[Ta/CoFeB/MgO]_{15}$ at $H_\perp = 47.9$ mT.

The outcomes of our micromagnetic simulations support the earlier hypothesis of the presence of two distinct types of skyrmions in these two different samples. Once the static configuration of the skyrmions in the samples is known, we can try to describe the experiments and study the collapsing dynamics of the skyrmions with a gradual reduction of the out-of-plane magnetic field.

Figure 2.11 shows the results for both samples. In sample #1 we start from an initial configuration with six pure Néel skyrmions and $H_\perp = 141$ mT. The skyrmions are small, isolated and have a circular shape, as in the experimental results. With a reduction of the field toward zero, a labyrinth domain configuration is observed ($H_\perp = -92.3$ mT). This configuration is broken into small skyrmions with a reversed core compared to the initial state by a further increase of the negative field.

In sample #2, we start with nine isolated hybrid skyrmions and $H_\perp = 47.9$ mT. Reducing the field toward zero the skyrmions become larger and deformed with respect to the circular shape. An inversion of the field leads to the coalescence of the skyrmions and the formation of large domains with magnetization in the same direction of the applied field ($H_\perp = -29.8$ mT).

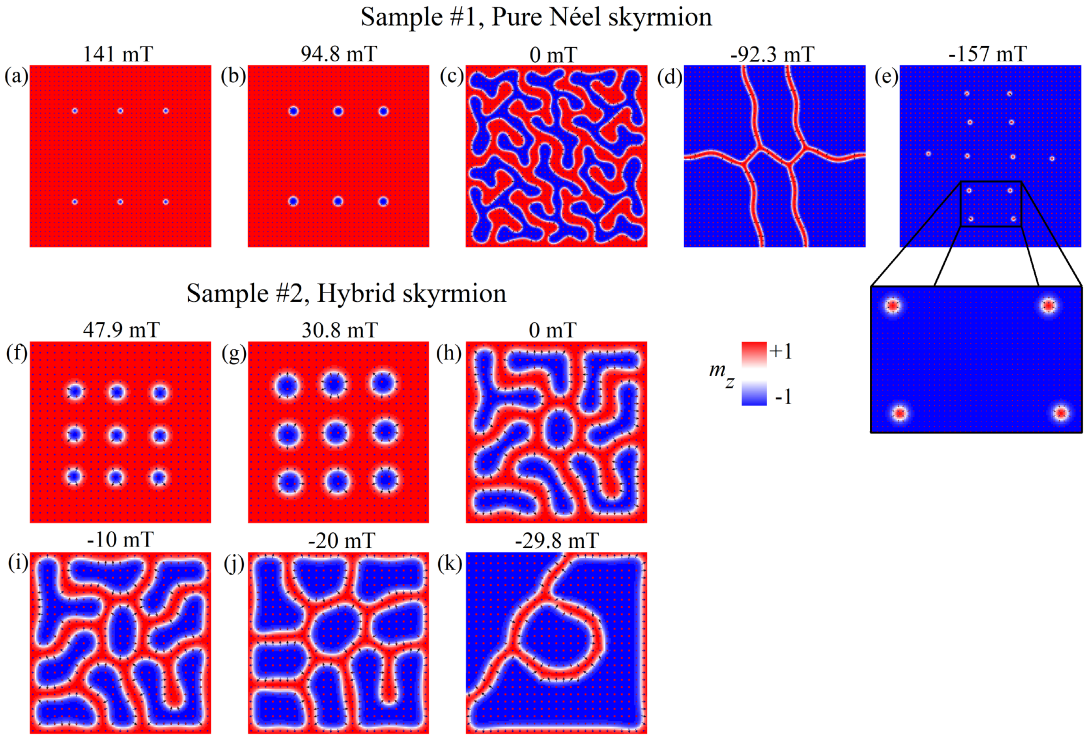

FIGURE 2.11: Spin configurations obtained by micromagnetic simulations showing the collapsing dynamics of the skyrmions (a)-(e) in sample #1 and (f)-(k) in sample #2.

In conclusions, we can state that micromagnetic simulations well reproduce the experimental measurements. The next step is to study the origin of the two different types of collapsing dynamics.

2.2.1.3 Micromagnetic results: explanation

We evaluate the energy as a function of the out-of-plane applied field for a Néel skyrmion and compare it with the energy of the uniform state, as shown in Figure 2.12. This evaluation can be extended to the pure Néel skyrmions stabilized in the sample #1 [128]. The skyrmion is stable in range 0 μT $\leq \mu_0 H_\perp < 4$ μ T (its energy is lower that the energy of the uniform state), while in range 4 μT $\leq \mu_0 H_\perp < 150$ mT the skyrmion is in a metastable state. This can justify the collapsing dynamics in sample #1: the skyrmions are metastable at $\mu_0 H_\perp \leq 141$ mT, and become stable in range -92.3 mT $< \mu_0 H_\perp < 0$ mT, therefore labyrinth domains are observed. Skyrmions become again metastable at higher field.

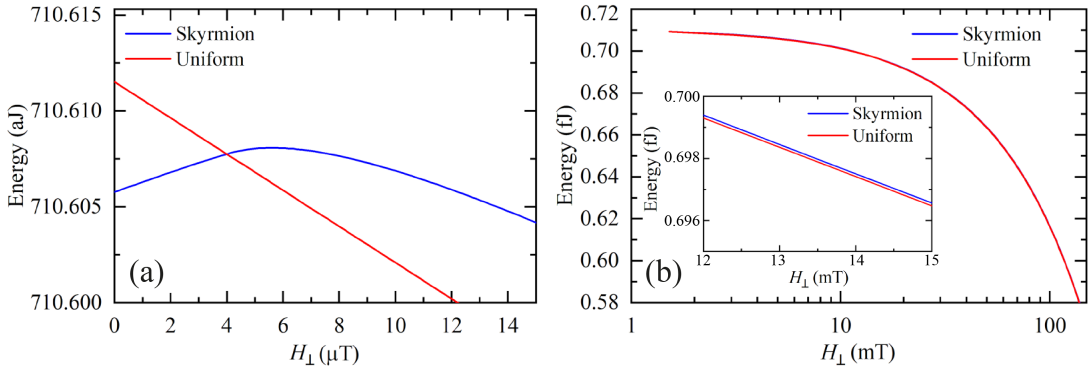

FIGURE 2.12: Energy of a Néel skyrmion compared to the energy of the uniform ground state as a function of the applied out-of-plane field in range (a) 0 μT $< \mu_0 H_\perp <$ 15 μT and (b) 0 mT $< \mu_0 H_\perp <$ 150 mT in logarithmic scale. Inset: magnetic field region (12 mT $< \mu_0 H_\perp <$ 15 mT) where the skyrmion is in a metastable state.

To understand the collapsing dynamic of the hybrid skyrmions in sample #2 we can take advantage of the previous results of magnetic bubbles in bulk materials [129–133]. In fact, their energy landscape is very similar: both are stabilized for a minimization of the magnetostatic energy, and therefore have a similar response to the external field. Based on quality factor $Q = 2K_u/\mu_0 M_S^2$, it is possible to identify three scenarios:

1.) $Q < 1$: the magnetostatic field is stronger than the perpendicular anisotropy field, therefore the easy axis is in-plane. Only in a confined structure magnetic bubbles can be stabilized.

2.) $1 < Q < 2$: the magnetostatic field is comparable or weaker than the perpendicular anisotropy field, therefore the easy axis is out of plane. Magnetic bubbles are energetically favored.

3.) $Q > 2$: the perpendicular anisotropy field is stronger than the magnetostatic field, therefore the easy axis is out-of-plane. In a small sample, magnetic bubbles are observed at zero field, while, in large dots, labyrinth domains are obtained.

The sample #2 has a $Q \cong 1$, therefore it falls in the second case. Figure 2.13 shows the micromagnetic simulation results of magnetic bubbles within a bulk material with perpendicular magnetic anisotropy and zero DMI, and the same micromagnetic and geometrical parameters of sample #2 (see Table 2.1). As expected, the collapse dynamics of magnetic bubbles is qualitatively similar to that of hybrid skyrmions. Magnetic bubbles are stabilized by a positive field $H_\perp = 200$ mT, and when the field decreases the bubbles change shape into elongated bubbles. The reversing of the field direction transforms them into large domains with the core magnetization aligned in the same direction of the applied field ($H_\perp = -150$ mT). It is important to note that, unlike bulk samples, in magnetic multilayers each FM layer is coupled via dipolar interactions, and *i*DMI is present due to the asymmetric interfaces.

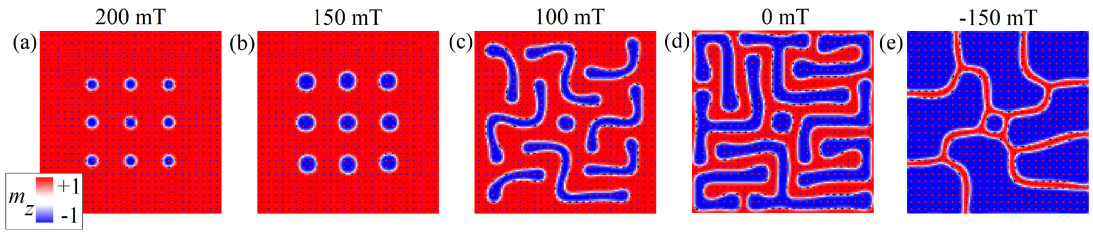

FIGURE 2.13: Spin configurations obtained using micromagnetic simulations, showing the collapsing dynamics of magnetic bubbles in perpendicular bulk materials.

In order to gain a more comprehensive understanding of the collapsing dynamics of skyrmions in magnetic multilayers, we perform systematic micromagnetic

simulations across various material parameters. The results are summarized in Figure 2.14, which presents a phase diagram of the collapsing dynamics of skyrmions in Q-d space ($d = 2A/D$) [128].

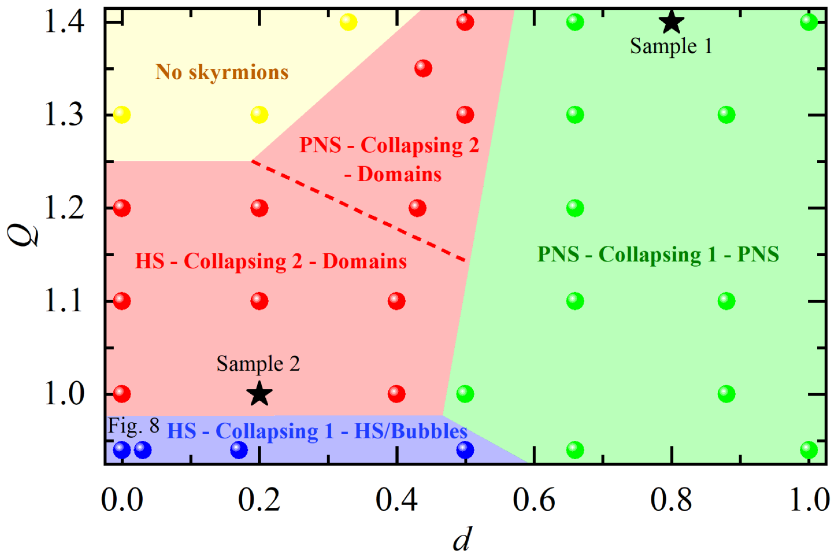

FIGURE 2.14: Phase diagram of the micromagnetically simulated collapsing dynamics of skyrmions in Q-d space. Each color represents a different final state (domains, hybrid skyrmions: HS or pure Néel skyrmions: PNS) and collapsing dynamics (type 1: similar to the sample #1, or type 2: similar to the sample #2). The circular points correspond to the simulations. The experimental samples are indicated with black stars. An example of the collapsing dynamics within the blue region is presented in Figure 2.15.

From the phase diagram five regions can be identified:

1.) $Q < 1$ and $0 < d < 0.55$ (blue region): at the initial state hybrid skyrmions (HS) are stabilized. The collapsing dynamics of the skyrmions is similar to the sample #1 (referred to as collapsing dynamics of type 1) and it is shown in Figure 2.15. Notably, the *i*DMI is not enough strong to stabilize skyrmions in all the layers, therefore it exists a mixed phase which includes hybrid skyrmions and magnetic bubbles.

2.) $1 < Q < 1.25$ and $0 < d < 0.5$ (red region): at the initial state hybrid skyrmions are stabilized. The collapse dynamics of the skyrmions is similar to the sample #2 (referred to as collapsing dynamics of type 2), therefore in the final state large domains are observed. The black star identifies the experimental sample #2.

3.) $1.25 < Q < 1.4$ and $0.2 < d < 0.4$ (red region): at the initial state pure Néel skyrmions (PNS) are stabilized. However, the collapsing dynamics is similar to the sample #2 (collapsing dynamics type 2) leading to the formation of large band domains.

4.) $1.25 < Q < 1.4$ and $0 < d < 0.3$ (yellow region): the equilibrium state is characterized by a uniform out-of-plane configuration, as the high perpendicular magnetic anisotropy precludes the existence of skyrmions.

5.) $1 < Q < 1.4$ and $0.5 < d < 1$ (green region): at the initial state pure Néel skyrmions (PNS) are stabilized. The collapsing dynamics of the skyrmions is similar to the sample #1 (referred to as collapsing dynamics of type 1), therefore in the final state Néel skyrmions with opposite polarity are observed. The black star identifies the experimental sample #1.

By referring to the full phase diagram, we can establish a direct correlation between the type of skyrmions and the associated collapse dynamics, which can be observed experimentally using imaging measurement techniques that do not resolve the three-dimensional structure of the spins.

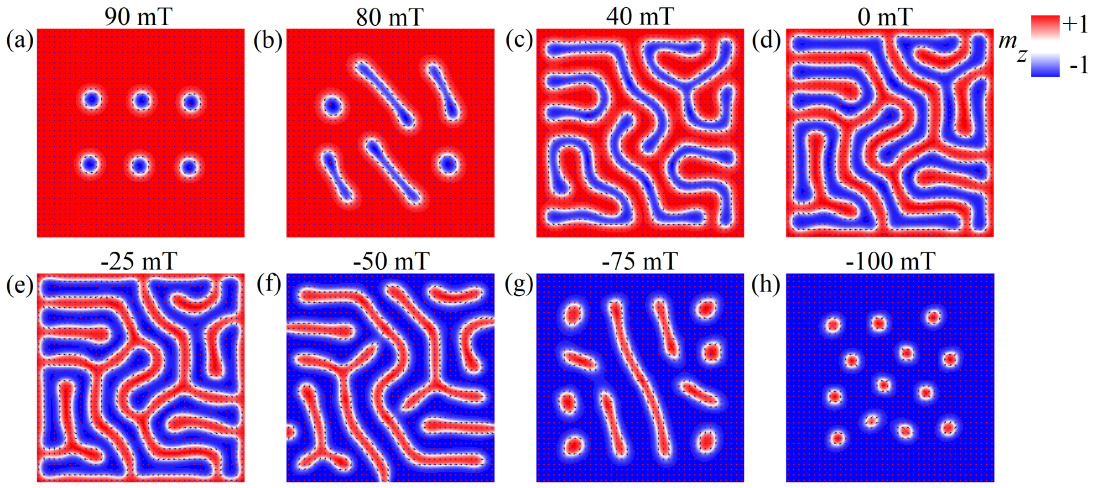

FIGURE 2.15: Spin configurations obtained using micromagnetic simulations showing the collapsing dynamics (of type 1) of hybrid skyrmions leading to the formation of mixed phase of HS and magnetic bubbles. The parameters are $Q = 0.94$ and $d = 0$, corresponding to the blue region of the phase diagram in Figure 2.14.

2.3 Dynamic studies of skyrmions

One of the key features of skyrmions that has made them promising candidates for spintronic applications, such as storage, is that they can be "easily" manipulated. Looking at the skyrmion as a particle-like object, its dynamics can be analytically described by Thiele's equation, which is directly derived from the LLG equation [97, 134, 135]. As a rigid entity, the motion of the skyrmion can be related to the motion of its center of mass **R**, which corresponds to the skyrmion core [136]. The center of mass is defined as the weighted average of out-of-plane magnetic moments m_z in the region enclosed by the domain wall, i.e., $m_z = 0$. The Thiele's equation is given by:

$$\mathbf{G} \times \mathbf{v} - \alpha_G \mathcal{D} \cdot \mathbf{v} + \mathbf{F} = 0 \tag{2.3}$$

where **G** is the gyrocoupling vector, $\mathbf{v} = d\mathbf{R}\,(t)\,/dt$ is the velocity of the skyrmion center, with $\mathbf{v} = (v_x,\ v_y)$ the longitudinal and transversal components, respectively, α_G is the Gilbert damping, $\mathcal{D}$ is a dissipative or viscosity tensor describing the effect of the dissipative forces on the skyrmion motion, and **F** comprises forces acting on the skyrmion, such as repulsion from the edges of the samples and pinning from local defects.

The skyrmion motion due to a constant excitation is characterized by an in-plane deflection with respect to the excitation itself. This effect is similar to the Magnus force which occurs when a spinning object is moving within a flowing fluid. A similar phenomenon, called Hall effect, arises when, in presence of a perpendicular external field, the charged particles flowing in a conductor are deflected toward two sides, creating a voltage across the conductor itself. For skyrmions, this effect is called skyrmion Hall effect and the angle between the skyrmion trajectory and the external excitation is known as skyrmion Hall angle, $\phi_{SkH} = \arctan\left(\frac{v_y}{v_x}\right)$ (see Figure 2.16). An exception is the motion of the skyrmion in SAF materials, where the skyrmion Hall effect vanishes due to the fact that the two coupled skyrmions are subjected to a Magnus force of the same magnitude but in opposite direction, thus the net force perpendicular to the external excitation vanishes [123, 124, 137].

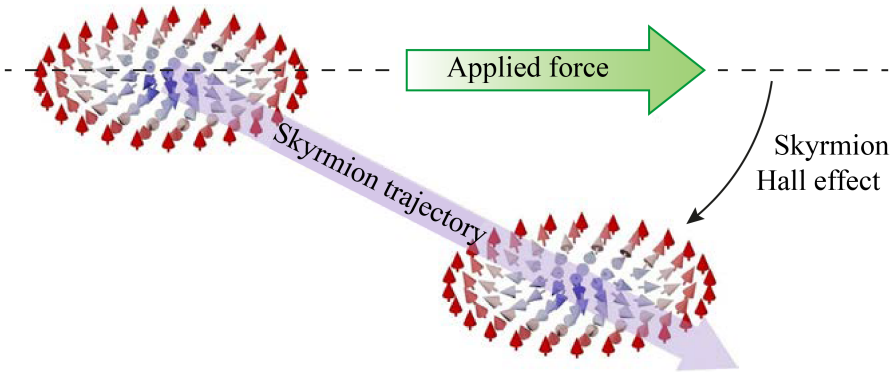

FIGURE 2.16: Sketch of the skyrmion Hall effect. The motion of the skyrmion is tilted with respect to the direction of the external excitation [94].

2.3.1 Review of skyrmion motion driven by different external forces

The most studied approach to manipulate skyrmions is by spin-polarized current through the conventional spin-transfer torque (STT) [138, 139] and spin-orbit-torques (SOTs) [106, 120, 140–142].

When an electrical current flows through a nonuniform magnetization configuration, it undergoes an adiabatic realignment of electron spins with the local magnetization. This process involves the transfer of the spin angular momentum to the local magnetization, consequently inducing dynamics in the magnetization and, therefore, the skyrmion shifting [94]. This effect has also been studied in the context of the DW motion and most of the findings can also be linked with the dynamics of skyrmions [8].

Although electrical current-induced skyrmion motion is a suitable approach from a theoretical and experimental point of view, alternative methods have been proposed, including the use of external field [143, 144], perpendicular anisotropy gradient [145] and thermal gradients [127, 146]. The latter is particularly promising due to its low energy consumption and it is the basis of an emerging research area known as skyrmion caloritronics [127]. In this scenario, we move the topic forward with the analytical and numerical demonstration of the skyrmion motion driven by thermal gradients in different magnetic systems (see subparagraph 2.3.2).

2.3.2 Temperature-gradient-driven magnetic skyrmion motion

In this section, the motion of the skyrmion induced by a thermal gradient will be explained by identifying the role of entropic torques due to the temperature dependence of magnetic parameters. Our studies show that, in single-layer ferromagnets with *i*DMI, the skyrmions move toward higher temperatures, while, in magnetic multilayers, they move to lower temperatures. We provide both analytical and numerical demonstration that the opposite behaviors are attributed to different scaling relations of the material parameters as well as to the presence of a non-negligible magnetostatic field gradient in multilayers. Furthermore, we observe a spatially dependent skyrmion Hall angle in multilayers hosting hybrid skyrmions, which arises from the change of thickness-dependent chirality as the skyrmion moves along the temperature gradient.

The main results of this study are published in Ref. [147].

2.3.2.1 Introduction

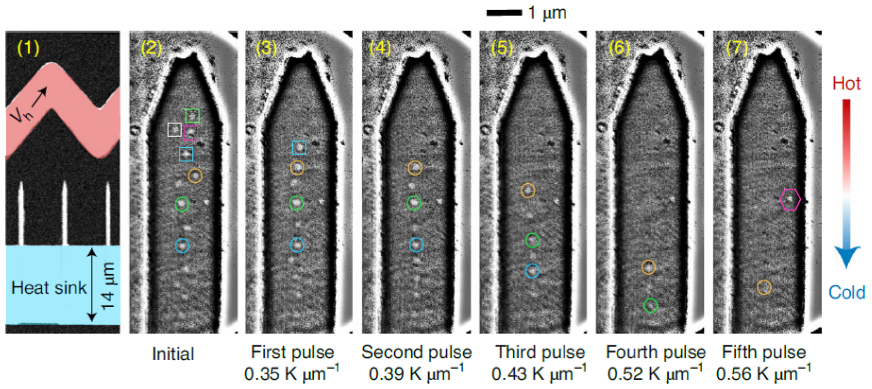

FIGURE 2.17: (1) Scanning electron microscopy image of the multilayer device under investigation. (2)-(7), Snapshots at increased temperature gradients, the time step between snapshots is fixed at 500 ms. The skyrmions follow a unidirectional diffusion from the hot to the cold region.

Wang *et al.* [127] have shown experimentally a unidirectional diffusion of skyrmions induced by thermal gradients, with their movement from hot to cold regions. Figure 2.17 reports the experimental results where the temperature increases from the bottom to the top of the multilayer device. For example, by following the skyrmion circled in orange it is possible to identify its motion toward the cold region. This behavior has been explained by considering a combination

of factors, including the repulsive forces between skyrmions, thermal SOTs [148], magnonic spin torques [149, 150], as well as entropic forces.

Gong *et al*. [151] explains the observed skyrmion motion with the concept of spin currents generated by thermal gradients. From their study, they found that skyrmions can move in both directions along the temperature gradient depending on the material parameters.

Tomasello *et al*. [128] have found, via atomistic calculations, the scaling relations of magnetic parameters (A_{ex}, D, K_u) as a function of the temperature, and they use these relations to study the stationary properties of a skyrmion in a single-layer.

Inspired by the experimental results of Wang [128], we study the effects of thermal gradients on the motion of the skyrmion within different magnetic systems: in single-layer FM with *i*DMI, in multilayer, and in SAF. We use the already known thermal scaling relations to study the thermally-induced skyrmion motion in a single-layer with *i*DMI, while, for the multilayer systems, in collaboration with Prof. Joseph Barker, we computed the scaling relations via atomistic simulations.

We focus on two effects: the entropic torque, that in a deterministic scenario generates the movement of the skyrmion toward the region where its free energy is minimized, and the magnonic torque arising from thermal spin waves [150]. By performing micromagnetic simulations we observe that, driven by the entropic torque, skyrmions in single layers move toward the hotter region characterized by a finite skyrmion Hall angle, while in multilayers they move in the opposite direction (toward the colder region). Furthermore, we have corroborated the micromagnetic results with a generalized Thiele's equation that takes into account variations in the size of the skyrmion along its trajectory.

Moreover, we show that, similar to the current-driven skyrmions, the skyrmion Hall angle vanishes in SAFs.

2.3.2.2 Theoretical model

We perform micromagnetic simulations of a squared $1200 \times 1200\ \mathrm{nm}^2$ sample for the single-layer FM hosting a Néel skyrmion with outward chirality in the center.

The same sample size is used for the SAF with two FM repetitions of 1 nm separated by 1-nm-thick non-magnetic layers. A squared 900×900 nm^2 sample is simulated for the multilayer system, with five FeCo FM repetitions of 1 nm thickness, separated by 2-nm-thick non-magnetic Pt/Ir layers. The multilayer sample hosts a hybrid skyrmion in the center. We consider a thermal gradient from 100 to 300 K applied by a linear function of the position along the x-direction, with the minimum value on the left side of the sample and the maximum on the right. We include this gradient in the temperature dependence of the macroscopic parameters. The change of M_S with the temperature follows the relation $M_S(T) = M_S(0)\left(1 - \left(\frac{T}{T_{lim}}\right)^{\delta}\right)$, where $M_S(0)$ is the value of M_S of the ferromagnet at zero temperature, $\delta = 1.5$ and the Curie temperature $T_{lim} = 1120$ K [152–154]. For the other parameters, we use the 2D scaling relations found in Ref.[128]:

$$\begin{aligned} A_{ex}(T) &= A_{ex}(0)\ m(T)^{\alpha}, \\ D(T) &= D(0)\ m(T)^{\beta}, \\ K_u(T) &= K_u(0)\ m(T)^{\gamma} \end{aligned} \tag{2.4}$$

where $m(T) = M_S(T)/M_S(0)$ and (0) refers to the value of the parameters at zero temperature, that are listed in Table 2.2 for each of the three simulated systems: single-layer FM with *i*DMI, multilayer, and SAF. In the latter, we consider an antiferromagnetic interlayer exchange coupling constant of $A^{ex} = -5e^{-4}$ J/m^2 [124, 155].

TABLE 2.2: Summary of the micromagnetic parameters at zero temperature the three different simulated systems.

Parameter	**Single-layer FM [61]**	**Multilayer**	**SAF**
M_S (kA/m)	1060	1300	770
A_{ex} (pJ/m)	20	15	20
D (mJ/m^2)	2.2	1.0	2.5
K_u (MJ/m^3)	0.90	1.20	0.60
Out-of-plane H_{ext} (mT)	15	60	0

In Ref. [128] the temperature scaling relations refers to the single-layer FM with

$\alpha = \beta = 1.5$ and $\gamma = 3.0$. To obtain these scaling relations for the magnetic multilayer we perform atomistic simulations.

We model the thin film as an fcc (111) lattice with two layers of Fe (adjacent to Ir), one layer of 50:50 mixed Fe and Co, and then two layers of Co (adjacent to Pt). The Hamiltonian is given by:

$$H = \sum_{\langle ij \rangle} J_{ij} \mathbf{S}_i \cdot \mathbf{S}_j + \sum_{\langle ij \rangle} \mathbf{D}_{ij} \cdot (\mathbf{S}_i \times \mathbf{S}_j) - \sum_{\langle ij \rangle} K_{ij} S_{zi} S_{zj} \tag{2.5}$$

where the first term is the isotropic exchange, the second is the DMI, active only at the Ir-Fe and Co-Pt interfaces, and the third is the two-ion anisotropy, which only influences the Co-Pt interface. The angle brackets, $\langle ij \rangle$, indicate that only the nearest neighbors are considered. Exchange, anisotropy and DMI constants are parametrized using values from ab initio calculations in Ref. [111]: $J_{ij}\,(Fe - Fe) = 24.2$ meV, $J_{ij}\,(Co - Co) = 29.0$ meV, $J_{ij}\,(Fe - Co) = 26.6$ meV, $D_{ij}\,(Fe - Ir) = -0.854$ meV, $D_{ij}\,(Fe - Pt) = 1.281$ meV , $K_{ij}\,(Co - Co) = 0.59$ meV and use magnetic moments $\mu\,(Fe) = 1.7\ \mu$B and $\mu\,(Co) = 1.3\ \mu$B [156].

The constrained Monte Carlo method is used to obtain the temperature dependence of magnetic anisotropy [157], while the temperature dependence of exchange stiffness and *i*DMI is obtained from the softening [158] and shifting asymmetry of the spin-wave spectra (see Supplemental Material of Ref. [128] for details).

We find that the scaling parameters for the Ir/FeCo/Pt trilayer are $\alpha = 1.7$, $\beta = 2.0$ and $\gamma = 2.5$. These parameters can be tuned by changing the properties of the material.

Micromagnetic simulations are corroborated by a generalized Thiele's equation developed for this scenario, where an adiabatic evaluation of the changes in the skyrmion size is also included. It is important to note that for the given range of temperatures the radius of the skyrmion is approximatively constant (34.6 nm + 0.2 nm from micromagnetic simulation in single-layer FM). Following the Thiele's formulation, the dynamic evaluation of the motion of the skyrmion at each instant is given by:

$$\frac{d\boldsymbol{m}}{d\tau}\,(\mathbf{x},\ \tau) = -\mathbf{v}\,(\mathbf{x},\ \tau) \cdot \nabla \boldsymbol{m}\,(\mathbf{x},\ \tau) \tag{2.6}$$

where $\mathbf{v} = v_x\hat{\mathbf{x}} + v_y\hat{\mathbf{y}}$ is the velocity of the skyrmion center. By substituting Eq. (2.6) into the LLG equation (1.41) and projecting along $\boldsymbol{m} \times \partial_i \boldsymbol{m}$, with $i = x,\ y$, we obtain a generalized Thiele's equation (see Supplemental Material of Ref. [147] for details). With this formulation we derive the velocity of the skyrmion as:

$$v_x = -\frac{4\pi\alpha_G D_{ex} F_x}{\alpha_G^2 D_{ex}^2 + (4\pi)^2} \quad \text{and} \quad v_y = -\frac{4\pi F_x}{\alpha_G^2 D_{ex}^2 + (4\pi)^2} \tag{2.7}$$

where $D_{ex} = \int d^2x \left(\partial_x \boldsymbol{m} \cdot \partial_x \boldsymbol{m}\right) = \int d^2x \left(\partial_y \boldsymbol{m} \cdot \partial_y \boldsymbol{m}\right)$ is the viscosity tensor components for a radially symmetric skyrmion, and $F_x = \partial_x V$ is the force generated by a gradient of the effective field along the x-axis, where $V(\mathbf{x}') = \int d^2x \left(\boldsymbol{m}(\mathbf{x}',\ \tau) \cdot \boldsymbol{h}_{eff}(\mathbf{x},\ \tau)\right)$. When a thermal gradient, represented as a variation of the magnetic parameters, is applied along the x-direction, the $\boldsymbol{h}_{eff}$ depends on the x-coordinate, resulting in a motion of the skyrmion. For large skyrmions, this means that their radius is bigger than the DW width $\Delta = \sqrt{A/K_{eff}}$. We can assume that $m_z = \arccos\left(2\arctan\left((R/r)\, e^{\xi(R-r)}\right)\right)$, with $\xi = (1/\Delta)\sqrt{2K_{eff}/\mu_0 M_S^2}$ [128], and obtaining:

$$V = 2\pi\sigma_{DW} R + 2\pi M_S H_T R^2 \tag{2.8}$$

where $\sigma_{DW} \approx 4\sqrt{AK_{eff}} - \pi D$ is the domain wall energy density [9], $H_T = H_z - b\mu_0 M_S$ is the external field with an additional contribution to incorporate the variation of M_S along the sample, with b depending on the properties of the film.

2.3.2.3 Results

The results of micromagnetic simulations show that a skyrmion subjected to a thermal gradient moves along qualitatively opposite trajectories in single-layer FM and multilayer. Figure 2.18 (a) shows that a skyrmion hosted in a single-layer FM moves from the cold to the hot region, which means it has a positive velocity in both the x and y directions. Conversely, Figure 2.18 (b) shows that a skyrmion hosted in a multilayer moves from the hot to the cold region, which means it has a negative velocity in both the x and y directions. The latter results are qualitatively in agreement with the experimental observations reported in Figure 2.17.

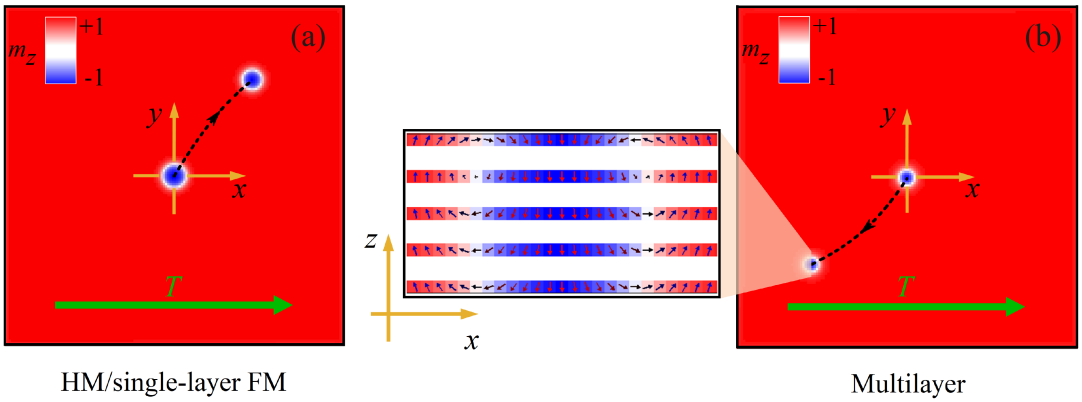

FIGURE 2.18: Micromagnetic simulation results of the trajectory of the skyrmion induced by a linear thermal gradient in a (a) single-layer FM, and (b) multilayer with five FM repetitions. The cross-section along the thickness of the multilayer shows the stabilization of a hybrid skyrmion in (b).

The first step to understand the origin of this different behavior is to analyze the effect of a linear gradient along the x-axis of only a single micromagnetic parameter at a time, regardless of the link with the temperature. We want to point out that: the K_u gradient can be achieved by inserting an additional wedge layer of a HM [159]; the D gradient can be obtained by tuning the HM thickness [160]; the M_S and A_{ex} gradients can be induced by a wedge layer of the FM. Practically, a gradient of M_S always implies a gradient of A_{ex}. The outcomes of these micromagnetic simulations are shown in Figure 2.19. The trajectories of the skyrmions refer to the single-layer FM, but similar results are observed in a multilayer. Each range of the parameter is chosen after a systematic study of the skyrmion stability. Two antagonistic effects are observed, leading to two qualitatively opposite skyrmion Hall angles. The gradient of perpendicular K_u and A_{ex} moves the skyrmion to the region where those parameters are smaller, therefore, in terms of temperature, from the cold to the hot region. On the contrary, the gradients of M_S (magnetostatic field), D, and the combination of M_S and A_{ex}, promote the motion of the skyrmion to the region where those parameters are larger, thus from the hot to the cold region. These behaviors can be explained by energy considerations. Basically, the skyrmion moves toward the region where the local value of the parameters minimizes its energy, favoring the existence of a larger skyrmion. From the Eq.(2.8), it is possible to identify the following trade-off: increase of exchange and anisotropy energies increases the skyrmion size, while increase of saturation magnetization and DMI energy decreases the skyrmion size.

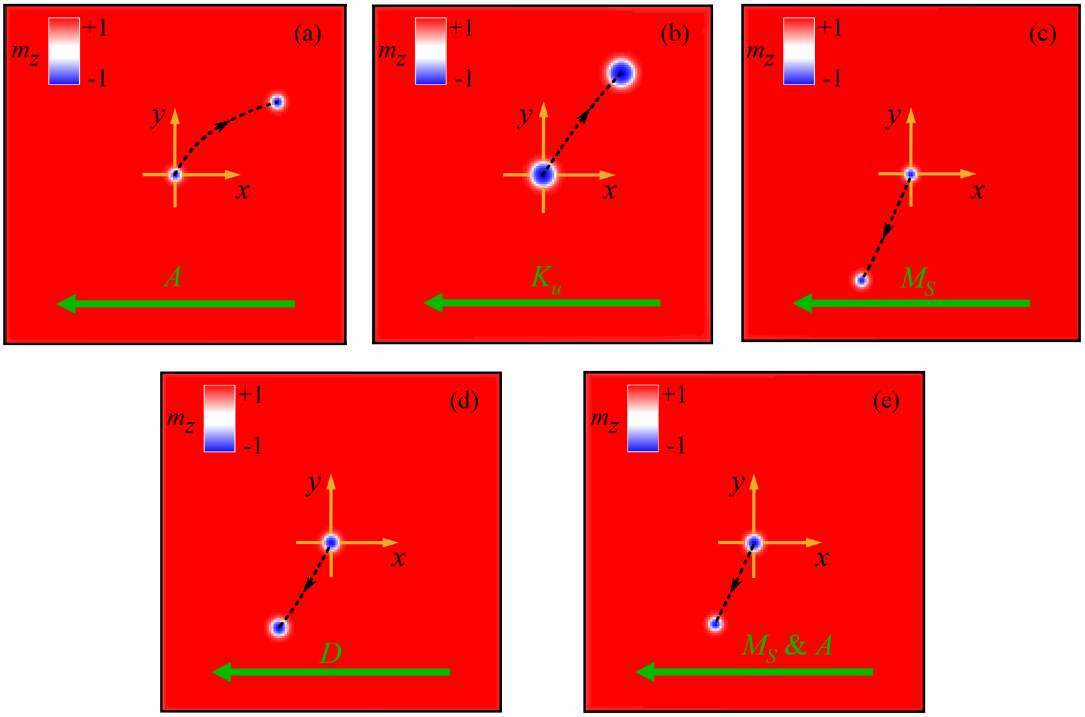

FIGURE 2.19: Micromagnetic simulation results of the trajectory of the skyrmion in a single-layer FM induced by a linear gradient of: (a) A_{ex} (b) K_u (c) M_S (d) D (e) combination of M_S and A_{ex}.

Taking into account the combinations of all parameters' gradients (see Figure 2.18), the final effect on the skyrmion motion relies on the predominance of one or the other effects, A_{ex} and K_u versus D and M_S).

We focus on the single-layer FM. Figure2.18 (a) implies that the scaling relations lead to the dominance of A_{ex} and K_u over D and M_S. To better understand and control this behavior, we consider two degrees of freedom: (i) the scaling exponents, and (ii) values of the magnetic parameters at zero temperature. In particular, we focus on the *i*DMI scaling relation, since D can be easily tuned by simply changing the materials at the interfaces; for example, using a different HM or modifying its thickness [160].

First, we perform a systematic study by changing the scaling exponent β within a range of stability of the skyrmion and fixing all the other parameters. Figure 2.20 (a) shows results for $1.5 \leq \beta \leq 2.7$ where the skyrmion moves from the cold to the hot region, therefore in the same direction of the previous results shown in Figure

2.18 (a). On the other hand, for $2.8 \leq \beta \leq 4.0$ the motion of the skyrmions is in the opposite direction, therefore from hot to cold region. Then, we can conclude that a threshold value of β exists that reverses the motion of the skyrmion.

The second study involves the change of *i*DMI at zero temperature, $D(0)$, for two fixed scaling exponents $\beta = 4.0$ and $\beta = 1.5$, while the other parameters are fixed. Figure 2.20 (b) shows that the trajectories of the skyrmion is barely affected by the $D(0)$ for both values of β.

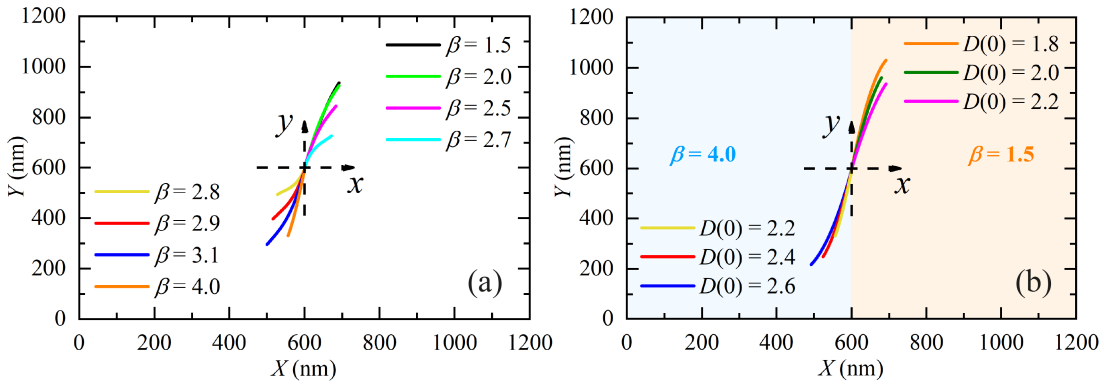

FIGURE 2.20: (a) Trajectories of the skyrmion as a function of different scaling exponents of *i*DMI β. (b) Trajectories of the skyrmion as a function of different *i*DMI at zero temperature $D(0)$, for $\beta = 1.5$ on the left side and $\beta = 4.0$ on the right side of the figure.

We also conduct a systematic investigation of the influence of the thermal gradient's magnitude on the velocity of the skyrmion. Figure 2.21 (a) shows that the velocity increases linearly with the gradient, and the same qualitative results are obtained in magnetic multilayers (see Figure 2.21 (b))

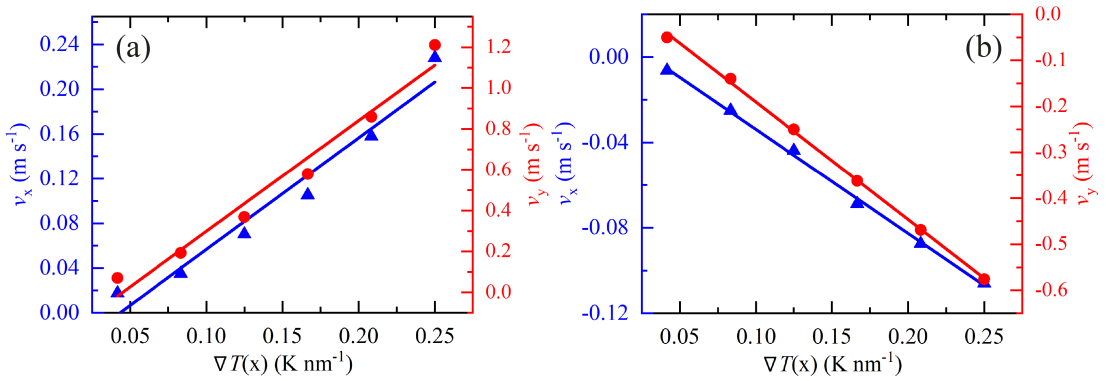

FIGURE 2.21: Skyrmion velocity as a function of the thermal gradient's magnitude in (a) single-layer and (b) multilayers. The blue triangles (red dots) correspond to the x-component (y-component) of the velocity obtained with micromagnetic simulations, while the solid lines are a linear fitting of the data.

Once we have understood the skyrmion motion in the single-layer FM, we will focus on magnetic multilayers. In particular, we study the motion of hybrid skyrmions under a linear *i*DMI gradient. We perform micromagnetic simulations with a *i*DMI from 0 to -2 mJ/m^2. At the starting point of the simulation, the hybrid skyrmion is placed at the center of the sample, which has a $D = -1$ mJ/m^2. Figure 2.22 (a) shows the trajectory of the hybrid skyrmion, which exhibits a change in the trajectory slope when moving toward the edges. To understand why this change occurred, we study the three-dimensional profile of the skyrmion with the calculation of the helicity angle expressed in degrees. In particular, from the cross-section S1 in Figure 2.22, we see that *i*DMI value shifts the Bloch skyrmion from the middle layer (at zero *i*DMI) to the second layer of the 5-repeat multilayer. Therefore, the helicity of the skyrmion in the second layer is computed, and the result is shown Figure 2.22 (b). The angle at the starting point is about 107°, which corresponds to a Bloch skyrmion with a tilt of the chirality toward a Néel inward chirality. With the skyrmion motion toward larger $|D|$ values, the angle tends to approach 180°. This suggests that the Bloch skyrmion has shifted further downward, being replaced by a Néel skyrmion with inward chirality, as shown in the cross-section S2-S5. Comparing the change in slope in Figure 2.22 (a) with the corresponding helicity angle in Figure 2.22 (b), we can conclude that the variation of the trajectory results from the change of the hybrid skyrmion profile along the thickness of the multilayers.

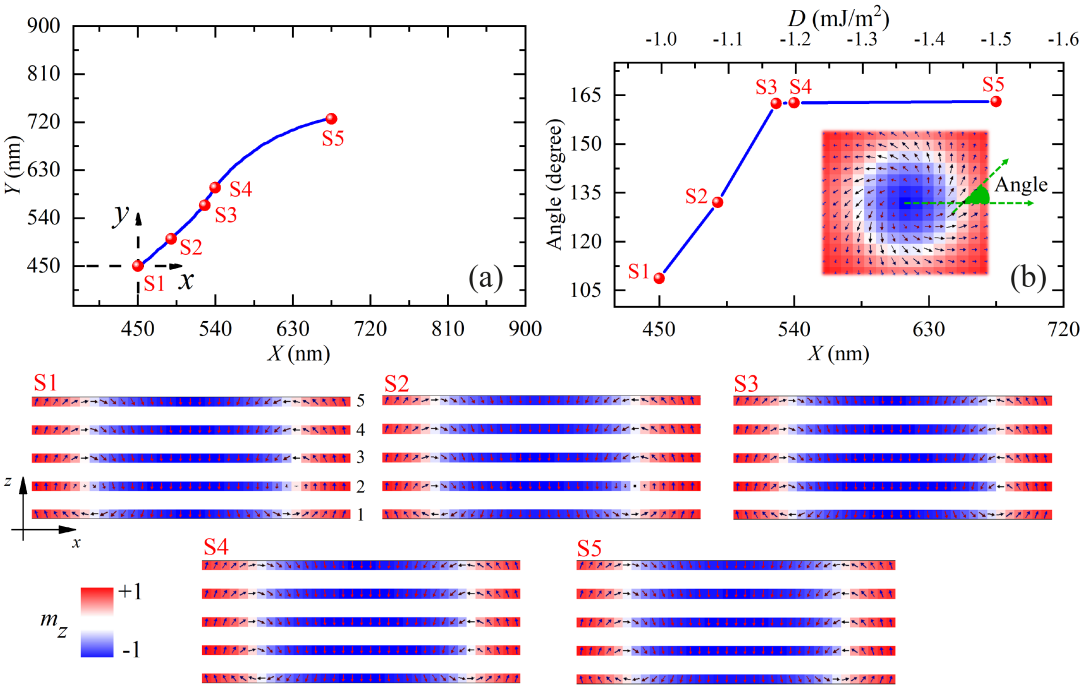

FIGURE 2.22: (a) Trajectory of the hybrid skyrmion in a 5-repeat multilayer induced by a linear gradient of *i*DMI. (b) Helicity angle of the skyrmion in the second layer as a function of the position of the skyrmion along the *x*-axis and the corresponding value of *i*DMI. Inset: illustration of the skyrmion highlighting the helicity angle of the magnetization vector. The snapshots S1 to S5 show the cross-section along the thickness of the multilayer for the points in (a) and (b).

Nonetheless, the previous result does not justify the different trajectories observed between the single-layer FM and the magnetic multilayers.

Once we know the behavior of the skyrmion in both systems, single-layer FM and multilayers, we conduct a "numerical experiment" performing a micromagnetic simulation of a single layer using the scaling relations obtained for the multilayer system. From the result shown in Figure 2.23 we can see that the Néel skyrmion moves toward the colder region, similarly to the hybrid skyrmion in the multilayer. Therefore, the scaling relations play the key role in the predominance of *i*DMI effect over the other parameters.

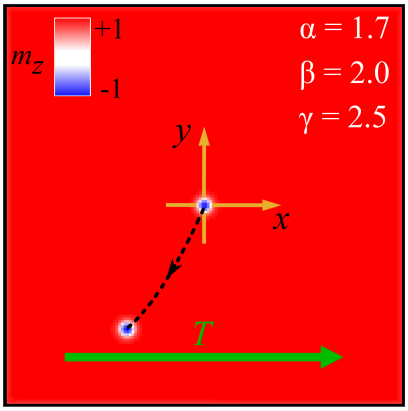

FIGURE 2.23: Trajectory of the skyrmion in single-layer FM with scaling relations of magnetic multilayers as computed via a micromagnetic simulation

The micromagnetic results are corroborated by the Thiele's equation. Figure 2.24 (a) and Figure 2.24 (b) show the skyrmion trajectory obtained with the Thiele methods for the single-layer FM and multilayer systems, respectively, which are in agreements with the micromagnetic simulations.

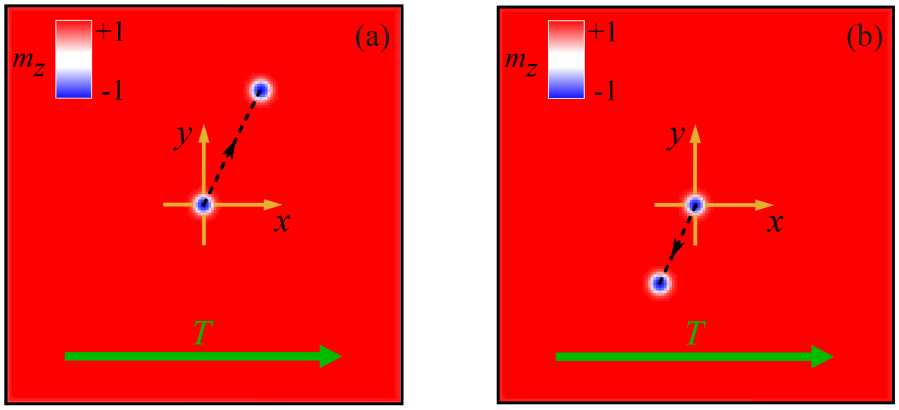

FIGURE 2.24: Trajectory of the skyrmion obtained by Thiele's equation with scaling relations (a) single-layer FM, (b) multilayers.

Once the influence of the entropic torques are clear, we analyze the effect of the magnonic torque in a single-layer FM. We perform stochastic micromagnetic simulations including a linear thermal field [161, 162] gradient from 0 to 100 K by performing different realizations, as shown in Figure 2.25. The skyrmion moves toward the hotter region but with a stochastic dispersion of the skyrmion Hall angle due to thermal fluctuations.

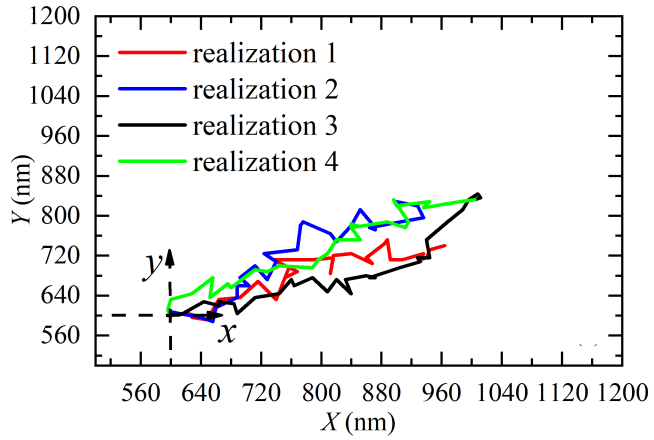

FIGURE 2.25: Trajectories of the skyrmion in a single-layer FM due to a linear stochastic thermal field and for different realizations.

The last part of this study concerns the motion of the skyrmion in SAF, where we decide to use the scaling relations of the magnetic multilayers. The results of the simulations are in agreement with those obtained in ferromagnetic systems, with the difference that, as expected, in SAF the skyrmion Hall angle vanishes, therefore the skyrmion moves along the direction of the applied linear gradient (x-axis). Figure 2.26 (a) and (b) show the skyrmion trajectory driven by a linear gradient of either iDMI, M_S, or thermal field gradient (top (a) and bottom (b) layer of the SAF). The SAF skyrmion moves toward the colder region. We want to point out that, by using the scaling relations of the single-layer FM, the skyrmion under a thermal gradient moves toward the hotter region. On the other hand, Figure 2.26 shows the skyrmion trajectory under a linear gradient of either K_u, or A_{ex}. (top (c) bottom (d) layer of the SAF).

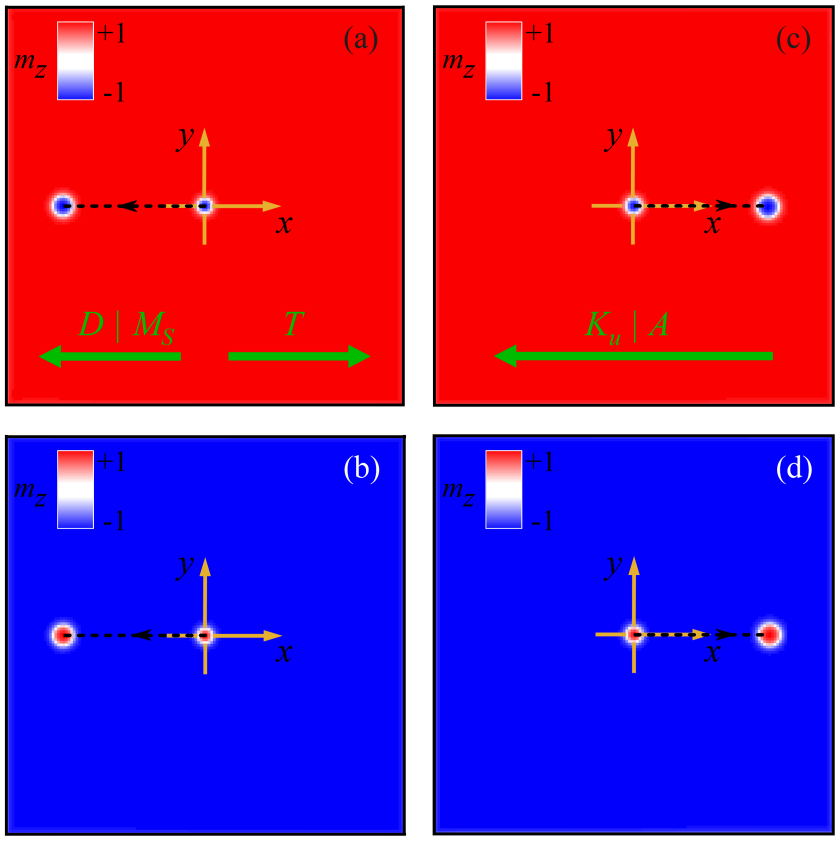

FIGURE 2.26: (a)-(b) Trajectories of the skyrmion under a linear gradient of either *i*DMI, M_S, or thermal gradient in the top and bottom layer of the SAF, respectively. (c)-(d) Trajectories of the skyrmion under a linear gradient of either K_u , or A_{ex} in the top and bottom layer of the SAF, respectively.

2.4 Conclusions

Magnetic skyrmions have been topologically classified, and the stability conditions for different configurations have been outlined. Our method for characterizing skyrmions in magnetic multilayers, based on the different field-driven collapsing dynamics of pure Néel and hybrid skyrmions, has been explained through experimental and micromagnetic simulations. This approach provides an effective means of characterizing skyrmions in magnetic multilayers, requiring only a 2D imaging analysis. Following the static characterization of skyrmions, we have presented a dynamic study of skyrmion behavior. Our results on the thermal-gradient-driven motion of magnetic skyrmions in various systems — single-layer FMs, multilayer FMs, and SAFs — were explained. The qualitatively

opposite motion observed in single and multilayer systems, as shown in the micromagnetic simulations, was further validated using Thiele's equation, and the findings were consistent with experimental results. This study represents an important advancement in the understanding of the dynamics of skyrmions and contributes to the emerging field of skyrmion caloritronics.

Chapter 3

Neuromorphic spintronics

Neuromorphic spintronics is a field of study that focuses on the implementation of the building blocks of neuromorphic computing with spintronic technology. This novel research topic can have a significant impact in biomedical applications. First of all, as already discussed in the previous chapters, spintronics is emerging as an ultralow power technology that is also CMOS compatible. Hence, any hardware implementation of neurons and synapses, fundamental concepts in neuromorphic computing, can be implemented with MTJs, as discussed below. Neuromorphic spintronics offers a technology that can be used in a variety of biomedical applications where the energy cost is the key parameter, and it can indeed impact the development of AI and deep learning in a broader sense.

More in detail, ANNs are the main building blocks of deep learning. These models have driven an impressive improvement in machine learning and artificial intelligence. Conventional machine learning techniques rely on engineered features, necessitating human intervention in the decision-making process. On the other hand, deep learning models can autonomously extract distinctive features directly from data [163] (see Figure 3.1).

This chapter introduces the basic concepts of artificial neural networks – neurons and synapses – and the idea of transfer learning and knowledge distillation based on dark knowledge. These latter approaches aim to leverage existing knowledge of well-trained neural network models to speed-up the training process and deployment of more effective and precise models.

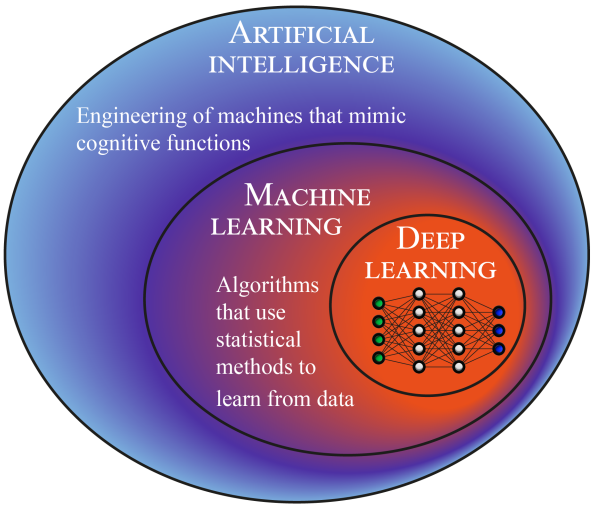

FIGURE 3.1: An illustration of the relationship between artificial intelligence, machine learning and deep learning.

The research activities discussed in this chapter focus on neuromorphic spintronics. We wish to stress that the main promises of this technology are the low energy consumption while maintaining high computational speed (GHz), offering compatibility not only with CMOS, but also with memristors [164], field-programmable gate arrays [165], or serving as a standalone alternative [93, 166–169]. In particular, we explain how spintronic technology can impact the implementation of artificial neural networks, with a focus on the fully connected and convolution layers of neural networks. In detail, we present:

i) a study of the reliability of transfer learning from software to hardware based on spintronics neurons;

ii) the concept of analog multiplication based on STDs and its impact on knowledge distillation;

iii) the idea of dynamical neurons implemented with STNOs.

3.1 Basic concepts of artificial neural networks

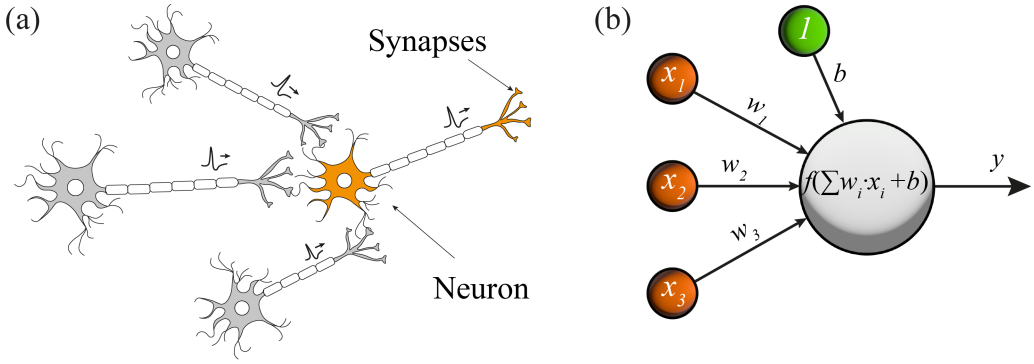

FIGURE 3.2: (a) Illustration of a biological neural network, depicting neurons interconnected with each other through synapses. (b) Schematic representation of an artificial neuron.

ANNs are a computational abstraction of biological neural networks. Biological neural networks rely on the transmission of electrical signals through neurons interconnected by synapses (see Figure 3.2 (a)). By analogy, the building block of ANNs are both synapses, and the artificial neuron or perceptron. The latter has been introduced by Frank Rosenblatt in 1958 [170]. This concept was first investigated in 1943 in a work by the neurophysiologist McCulloch and the mathematician Pitts [171]. The perceptron receives input signals from the other neurons connected with weighted synapses, performing a weighed sum called multiply-accumulate operation (MAC). A nonlinear transformation, known as activation function (AF), is then applied to the output (see Figure 3.2 (b)). The AF can exhibit different nonlinearities, which can be reproduced by spintronic devices, as detailed later in this chapter.

Mathematically, the perceptron can be described by:

$$z_i = \sum_{j=1}^{n} \left(w_{ij} x_j\right) + b_i \tag{3.1}$$

$$y_i = f\left(z_i\right) \tag{3.2}$$

where n is the number of neurons connected to the neuron i, w_{ij} are the synaptic weights, x_i the input signals, z_i is the results of the MAC operations, and b_i

is a bias value. y_i is the output of the neurons after applying a nonlinear transformation f to z_i. During the so-called training phase, the synaptic weights are adjusted/optimized to improve the performance of the ANNs.

Based on the nature of the input data, there are three main learning algorithms: supervised, unsupervised, and reinforcement learning. The first two learn from data (labeled in the first case and unlabeled in the second one) while the latter learns from experience. This thesis focuses on solving classification problems, which are compatible with supervised learning algorithms. For this reason, all the concepts from now on refer to this paradigm. In supervised learning, the network is trained using a labeled dataset, comprising of training and validation datasets, with the model performance being evaluated on a separate test dataset to ensure generalizability.

The training procedure involves two steps: forward propagation and backpropagation of the error. In the forward step, the ANN predicts the response for a given input. The error between the predicted response y_i and the true response t_i is quantified by a task-specific loss function. For multiclass classification, the categorical cross-entropy loss is computed:

$$L = -\sum_{i=1}^{n} t_i \ln(y_i) \tag{3.3}$$

where n is the number of output neurons. The softmax AF, which is typically implemented in the last layer of the ANN, transforms the predicted output into probabilities:

$$y_i = f(z_i) = \frac{e^{z_i}}{\sum_{j=1}^{n} e^{z_j}} \tag{3.4}$$

The cost function averages individual losses computed across the entire dataset during the training. It is worth noting that, when commenting the performance of a neural network, the cost function itself is often referred to as the "loss" of the network. Backpropagation employs the gradient descent algorithm to minimize the error by adjusting synaptic weights. First, the gradient of the cost function with respect to synaptic weights $\partial L/\partial w$ is calculated, and then the chain rule of the derivative is used to propagate the error back through the network [163]. Once the gradients are computed, they are used to adjust the synaptic weights

(3.5) according to the following formula:

$$w \leftarrow w - \eta \frac{\partial L}{\partial w} \tag{3.5}$$

where η is the learning rate, a critical hyperparameter that controls the trade-off between the training speed and convergence. Different learning rate annealing schedules are proposed to optimize the gradient descent algorithms [172]. Three gradient descent algorithms differ in the amount of data used to calculate the gradient: (i) the batch gradient descent updates weights using the entire training dataset; (ii) the stochastic gradient descent updates after each training sample; (iii) the mini-batch gradient descent updates using a subset (mini-batch) of n training samples. This study employs mini-batch gradient descent for a stable convergence, computational efficiency and enhanced model generalization [172]. An epoch marks one complete iteration through the training data.

The number of epochs is a crucial hyperparameter that has to be properly set in order to prevent both underfitting and overfitting of the model. Underfitting occurs when the model is not able to perform well on the task due to an insufficient number of epochs, as illustrated in Figure 3.3 (red region). On the other hand, overfitting occurs when the model memorizes the training data, typically due to an excessive number of epochs, leading to a compromised ability to generalize effectively to new, unseen data, as illustrated in Figure 3.3 (green region). To continually assess the performance of the ANN during the training, a subset of the training dataset (not used during the training), known as validation dataset, is used to test the ANN at the conclusion of each epoch. To mitigate the risk of overfitting, an early stopping technique can be implemented, which periodically evaluates the model's performance on the validation dataset and stops training once the validation error exhibits signs of increasing or plateauing.

In addition to the loss, accuracy is a key metric for evaluating ANN performance in a classification task. The accuracy measures the percentage of correctly predicted samples compared to the total number of samples in a set of data. The training accuracy represents the ability of the ANN to fit the training data, the validation accuracy assess overfitting/underfitting, while the test accuracy measures the effective goodness of the ANN in performing the assigned task.

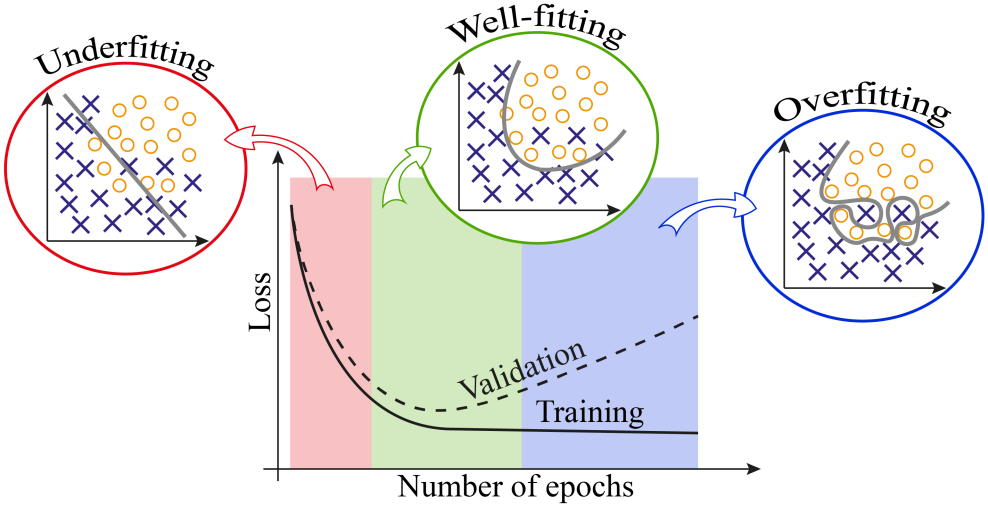

FIGURE 3.3: Example of loss function versus number of epochs for training and validation error, to evaluate the model performance. By comparing the two curves, it is possible to identify underfitting (red region) and overfitting (blue region) of the model. A simple pictorial representation of underfitting, well-fitting and overfitting is shown.

3.2 Layers of an artificial neural network

Different architectures of ANNs arise from a different arrangement of the neurons and synapses.

3.2.1 Fully connected neural network

The perceptron perform a linear transformation of the inputs, so it is not able to solve complex nonlinear tasks [173]. To address this problem, the neurons are organized in layer, and multiple layers of neurons are stacked. When there is at least one middle layer, known as hidden layer, between the input layer and the output layer of neurons, the resulting structure is called deep neural networks. A layer where each neuron is connected to all the neurons of the next layer is referred to as fully connected (FC) or dense. In a fully connected neural network or a multi-layer perceptron (MLP) there are multiple fully connected layers stacked, as illustrated in Figure 3.4.

The depth of the ANN refers to the number of hidden layers, while its width refers to the number of neurons in a given layer. To avoid overfitting, a regularization technique, known as dropout, is commonly implemented. During each epoch, a fraction of random neurons or synapses, typically less than 50% of the

total, are temporarily "dropping out" [174], i.e., they are not used in the computation.

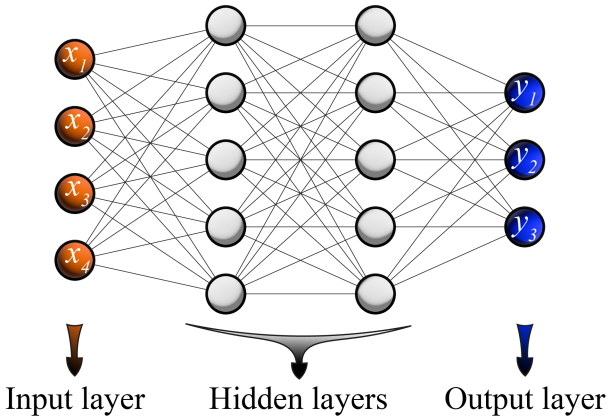

FIGURE 3.4: An example of fully connected neural network with one input layer, two hidden layers and one output layer.

3.2.2 Convolutional neural network

Convolutional neural networks (CNNs) have emerged as the most important tool in applying neural networks to computer vision tasks. The popularity of CNN starts in 2012 when Alex Krizhevsky and his team outperform other participants in the ImageNet ILSVRC challenge [175] with a deep CNN named AlexNet [176].

The key advantages of the CNNs lies in the use of weighted filters rather than fully connected neurons. This introduces parameters sharing, as the same weights are reused across different spatial locations. Consequently, this reduces the number of training parameters and increases the computational efficiency. Furthermore, the local connections create a translation invariant property, as the network can thus recognize features in a different spatial configuration. This property is derived from the convolution operation performed in the convolutional layer, where a filter slides across the image, computing the dot product and storing results in a feature map, as illustrated in Figure 3.5. Therefore, each unit of the feature map is connected to a local area of the previous layer through a set of weights.

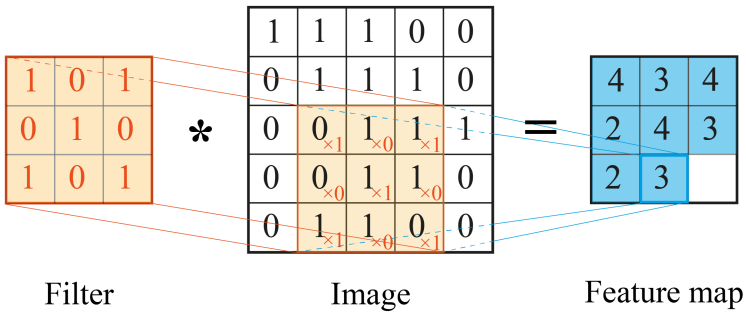

FIGURE 3.5: Example of 2D convolution of an input image of size 5×5 and a filter of size 3×3. Each element of the output feature map is the sum of the element-wise matrix multiplication of a subset of the input image and the weights of the filter.

The discrete convolution can be mathematically expressed as:

$$z_{i,j,f} = \sum_{c=0}^{n_c-1} \sum_{d=0}^{m-1} \sum_{a=0}^{m-1} w_{a,d,c,f}\, x_{(a+i)(d+j),\,c} + b_f \tag{3.6}$$

where w is the weight of a $m \times m$ filter, with a and d being the vertical and horizontal coordinates, c the index of the input channel, and f the index of the feature map. b is the bias, while x is the input data, with i and j being the vertical and horizontal coordinates of the pixel position in the feature maps. Channels are essentially the feature maps from the previous layers, and they are equal to the number of filters. Usually, in a CNN, several convolutional layers are stacked, as shown in Figure 3.6 (a).

As an input propagates through the layers, abstract features are extracted. Figure 3.6 (b) shows an example of features learned by a CNN where it is evident that the first convolutional layer detects simple features, like edges, the second one detects simple shapes, and the third ones detects more complex features [177]. In a CNN, nonlinearities and pooling layers are also applied to these feature maps. The pooling layer uses operations such as maximum or average calculation over a set of values to merge similar features, thereby reducing the spatial dimension of the feature maps. The final feature maps, obtained after all convolutional layers, are typically flattened, i.e., transformed into one-dimensional vector which is then connected to a fully connected part of the neural network. The part of the neural network in which this flattening operation is performed is called flatten layer. In summary, the convolutional layers act as feature detectors, extracting

relevant information, while the FC layers leverage these features for the final classification task, as highlighted in Figure 3.6 (a).

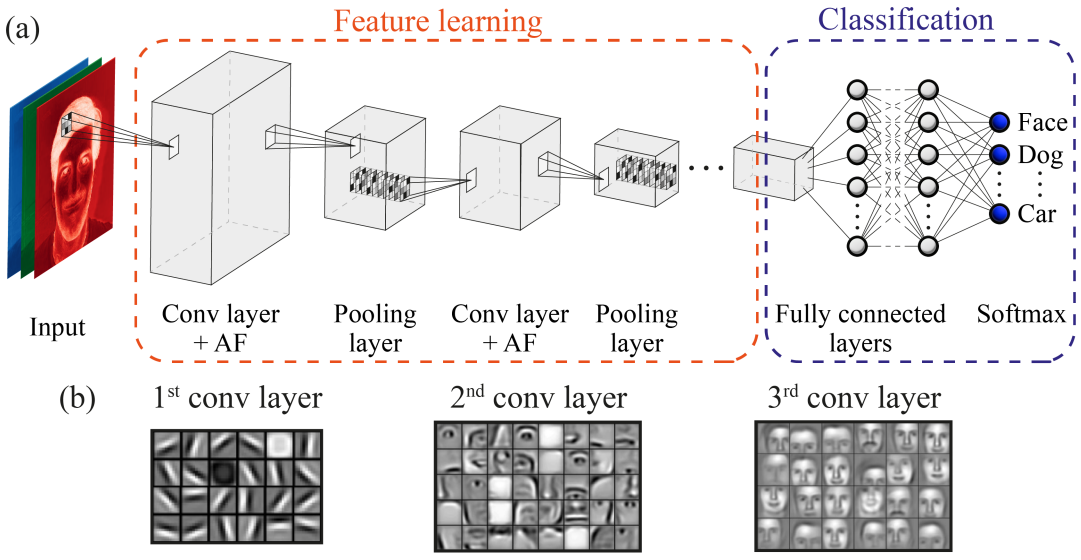

FIGURE 3.6: (a) A schematic of a convolutional neural network architecture. The input image is processed by convolutional layers that extract relevant features ("features maps"), which are highlight by the nonlinear activation function. Then the pooling layers perform dimensional space reduction of the feature maps. A sequence of fully connected layers and a softmax classify the input image. (b) Learned features in convolutional layers: deeper convolutional layers extract progressively more abstract and high-level features from input. Source of pictures [178].

3.3 Knowledge transfer techniques

Knowledge transfer techniques can be crucial for improving the training efficiency and performance of ANN models, making them essential techniques for the deployment. The concept is based on transferring knowledge from one ANN model to another. In this thesis, we focus on two promising techniques: transfer learning and knowledge distillation.

The transfer learning technique involves training a wide and deep ANN on a large amount of data (source dataset). This pre-trained ANN is then leveraged to solve a different, usually smaller, dataset, as illustrated in Figure 3.7 (a). Knowledge distillation, as depicted in Figure 3.7 (b), employs a wide and deep teacher ANN to imparts/transfer its knowledge to a smaller and shallower student ANN.

This technique aims to distill the learned knowledge from the complex teacher model into a more compact student model.

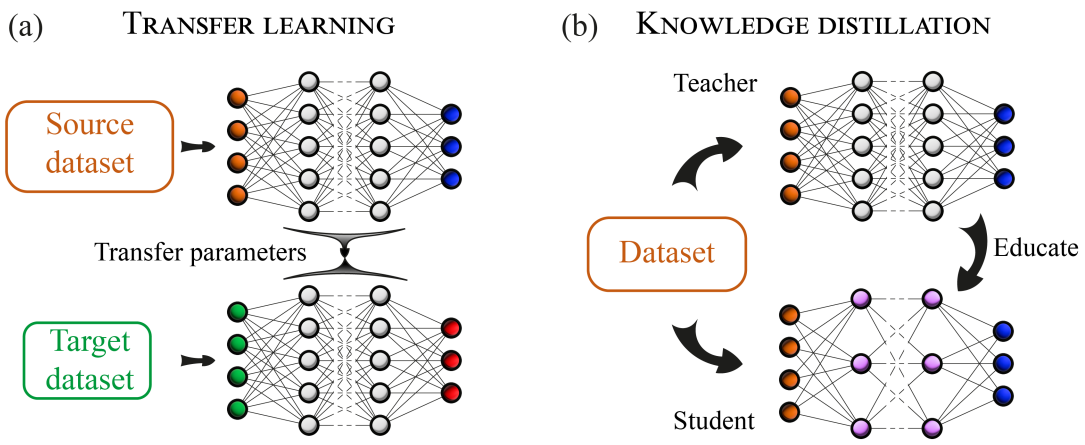

FIGURE 3.7: A schematic representation of (a) Transfer learning: the weights of wide and deep ANN, trained on a source dataset with a large amount of data (top), are used to solve a target dataset with few samples (bottom). (b) Knowledge distillation: a wide and deep teacher ANN (top) is used to educate/transfer knowledge to a small and shallow student ANN (bottom).

3.3.1 Transfer learning

Transfer learning leverages the idea that individuals can efficiently apply an established knowledge to face new problems [179]. This approach involves using a wide and deep ANN initially trained on a huge and general dataset, such as ImageNet [180], as a starting point for addressing a new problem with limited data. The features learned from a large amount of data can be useful to solve a new dataset. As already discussed, the early layers of an ANN extract features that are general, like edges and lines [181], while the latter layers are more task-related. Therefore, in transfer learning, only the final layers are replaced and trained in order to extract features relevant to the new task. Fine-tuning the ANN with the new dataset may be necessary for performance improvement. The main advantages of transfer learning over training a model from scratch include: saving training time; achieving better ANN performance; and mitigating the need for a large amount of data.

3.3.2 Knowledge distillation

Knowledge distillation involves transferring knowledge from a large, complex ANN model, called teacher model, to a smaller and simpler one, known as student model [182, 183]. This process is valuable for compressing the model, making it more suitable for deployment on hardware with limited resources, such as an Internet of things node or a mobile phone. The idea is that the student model mimics the teacher model, that could be a pre-trained ANN.

However, the information learned from hard targets of the teacher model, consisting of output probabilities calculated by the softmax, may not by sufficient. Therefore, the teacher model provides the student with additional information known as dark knowledge. Dark knowledge is revealed by soft targets, which effectively smooth out the probability distribution and reveal inter-class relationships. The soft targets are achieved by increasing the temperature coefficient (T) of the softmax function (typically $T = 1$):

$$y_i = \frac{e^{\frac{z_i}{T}}}{\sum_{j=1}^{n} e^{\frac{z_j}{T}}} \tag{3.7}$$

When $T \to \infty$ all the classes have the same probability. Figure 3.8 shows an intuitive example of soft and hard targets to better understand the concept of dark knowledge [184]. The probabilities indicating the similarity between a "dog" and a "cat" are higher than the probabilities associating it to a "cow" and a "car".

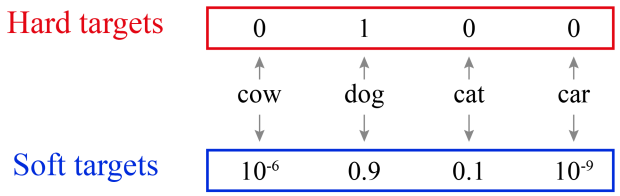

FIGURE 3.8: Intuitive example of hard and soft targets for dark knowledge explanation [184].

3.4 Computing with spintronics technology

3.4.1 Challenges in modern computing

Training an ANN is the more expensive part of deep learning algorithms. It demands a lot of time and energy, especially for state-of-the-art ANNs having a huge number of parameters. Neuromorphic computing tries to address these challenges with the development of energy efficient and fast hardware optimized for neural network models [185].

For example, the energy consumption of the state-of-the-art natural language processing deep neural network BERT [186, 187], developed in 2018 by Google, is 1 MWh, with 10^8 synaptic weights. In contrast, the estimated power consumption of the human brain during an intellectual activity is about 20 W, with 10^{15} synapses and 10^{11} neurons. This comparison highlights that, with the same amount of energy, the brain operates for 6 years, with multiple tasks in parallel (such as vision, natural language processing, social interactions and so on) and the ability to accumulate knowledge over time, even being able to extrapolate patterns from few examples and apply the newly acquired knowledge in several tasks [185].

Over the years, to enhance the performance, ANNs have expanded in both depth and width. However, the computational demand for training larger models continues to grow exponentially [188]. For instance, the training of ChatGPT, a language model with 175 billion trainable parameters developed by OpenAI in 2020 [189], consumes more than 1 GWh of energy, roughly equivalent to the annual amount of energy of 120 typical U.S. households. Figure 3.9 shows that the energy required for computing will exceed the world's energy productions in 2040 [190].

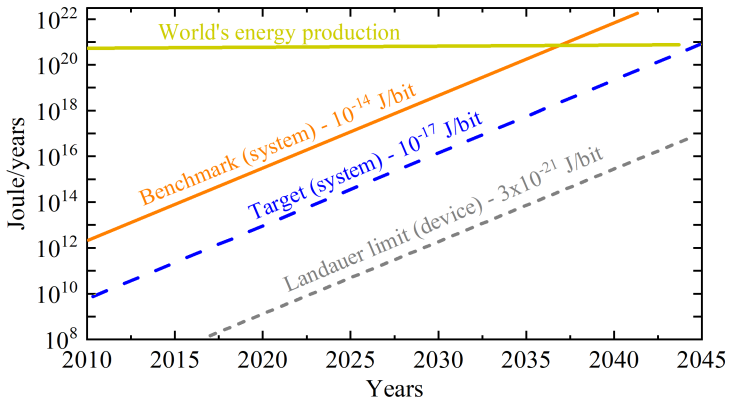

FIGURE 3.9: Energy consumption trend in computing vs. the world energy production, over year. Source: [190].

The energy inefficiency in the hardware implementation of ANNs is closely tied to the von Neumann architecture, where memory and computation hardware are separated into two physically distinct units, as shown in Figure 3.10 (a). For each computational step, a huge amount of data is read, processed, and then transferred back to the memory. This continuous data transfer consumes time and energy, creating a bottleneck in performance [191]. The graphics processing units (GPUs) and tensor processing units (TPUs) only partially solve the von Neumann bottleneck by incorporating multiple cells containing both processing and memory, enabling parallel computations. In contrast, neuromorphic computing, inspired by the topology of the brain, aims to design circuits where neurons (processing part) are interconnected by synapses with in-situ memory (see Figure 3.10 (b)). Unfortunately, this architecture cannot be implemented solely using CMOS technology. The current research focuses on discovering and developing nanoscale devices that emulate neurons and synapses, offering characteristics such as low energy consumption, high endurance, ease to connect in large networks, tunability and reconfigurability [185].

Several solutions have been proposed, such as optical devices [192, 193], memristors [164], field-programmable gate arrays [165] and spintronic devices [93, 166–169, 185, 194]. Spintronics devices such as MTJs, have the characteristics required by neuromorphic computing and, in addition, offer the advantages of having a working speed in the GHz and potentially in the THz (antiferromagnetic spintronics [195]), on top of intrinsic nonlinearity, non-volatility, and compatibility with CMOS systems. The recent popularity of these devices for neuromorphic computing applications has given birth to the field of neuromorphic spintronics

[166].

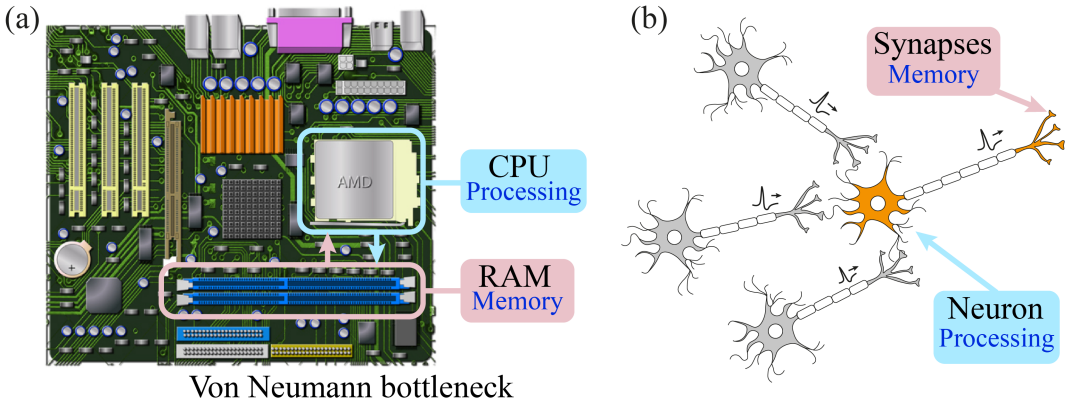

FIGURE 3.10: (a) Illustration depicting the von Neumann architecture, to highlight the separation between processing (CPU) and memory (RAM), known as "von Neumann bottleneck". (b) A schematic representation of a biological neural network, in which neurons (processing part) are interconnected with synapses (memory part).

3.4.2 State-of-the-art of neuromorphic spintronics

In recent years, a significant progress has been made in the development of spintronic devices designed to emulate the functions of neurons and synapses. Within the existing literature, MTJs have played a crucial role, particularly in embodying the nonlinearity essential for neuron functionalities, effectively serving as activation functions.

Cai *et al*. [196] have performed an MTJ-based FC ANN built by voltage-controlled superparamagnetic MTJs (see Figure 3.11 (a)), in which the probability of switching was also controlled by the VCMA effect. This solution was able to reproduce the sigmoidal activation function and its tunability was proposed to implement adaptive neurons.

Pan *et al*. [197] proposed a multilevel cell-based STT-MRAM for in-memory computing. The architecture for a binary convolutional neural network is shown in Figure 3.11 (b). The multilevel cell structure is composed of an MTJ on top of a large MTJ, and two bits are stored in one cell.

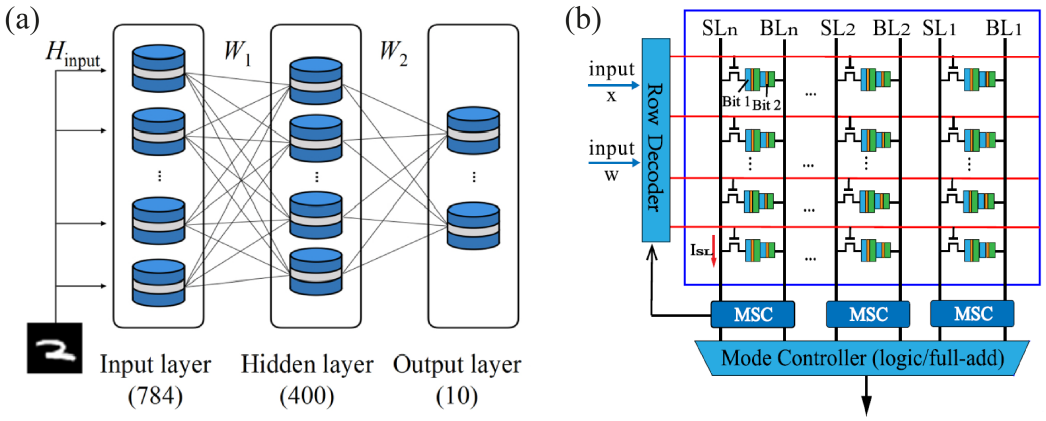

FIGURE 3.11: (a) Structure of ANN implemented with voltage-controlled spintronic stochastic neuron based on MTJs [196] (b) Multilevel cell STT magnetic RAM-based computing with in-memory accelerator for binary CNN [197].

Torrejon *et al.* [194] demonstrated that a single STNO can emulate 400 neurons using time multiplexing (see Figure 3.12 (a)): the oscillator periodically allocates an interval in time for different neurons' states and uses finite relaxation time to emulate coupling between neurons. This approach has been successfully used to implement a reservoir computer to recognize the spoken digits with an accuracy of 99.6%.

Romera *et al.* [198] demonstrated that coupled STNO-based neural networks can classify signals at microwave frequency, and they used it for vowel recognition, with an accuracy of 89%. The first layer of their network consists of two independent neurons (A and B) implemented by two microwave sinusoidal sources of frequency f_A and f_B. The microwave outputs of the first layer are sent, through a strip line, in the second layer, consisting of four all-to-all-connected STNO neurons (see Figure 3.12 (b-left)). The main idea is that the synchronization of two oscillators simulate a strong synaptic coupling. If the ith neuron in the second layer is synchronized with neuron A in the first layer, due the same frequency, a strong synaptic coupling is simulated. On the hand, if neuron A and neuron i have independent dynamics and frequencies, a weak synaptic coupling between them is simulated (see Figure 3.12 (b-right)). The strength of these synapses can be tuned by changing the bias current of each oscillator in the second layer.

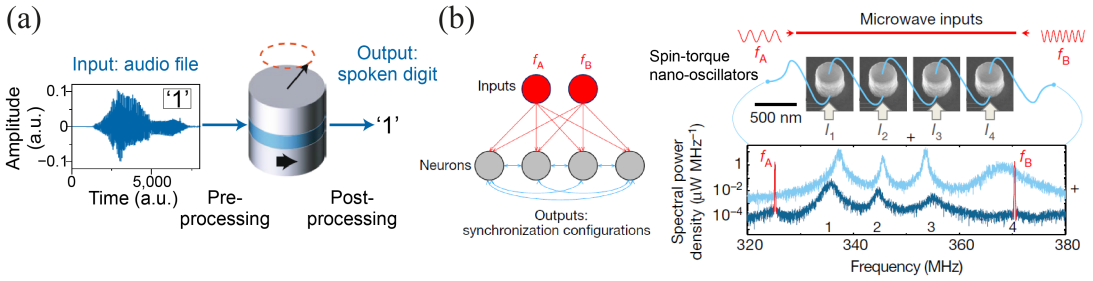

FIGURE 3.12: (a) Reservoir computing with a single STNO. The spoken digit "1" to recognize is pre- and post-processed using time multiplexing and a single STNO [166, 194]. (b) Left: a schematic representation of ANN. Right: a schematic representation of the experimental set-up, consisting of four STNO electrically connected in series and coupled through their emitted microwave currents. Two microwave signals, encoding information in their frequencies f_A and f_B, are applied as inputs to the system via a strip line, generating two microwave fields. The overall microwave output of the oscillator network is recorded using a spectrum analyzer [198].

There are also many other different types of ANNs proposed including solutions using domain walls and skyrmions [98, 99].

One of the main advantages of neuromorphic spintronics is the implementation of the nonlinearity of the neuron with a single spintronic device. On top of those solutions, a study of robustness in terms of device-to-device variation is still missing and this study aims to fill this gap as described in the rest of this chapter.

3.4.3 Reliability of neural networks based on spintronic neurons

Previous works have demonstrated that the intrinsic nonlinearity of spintronic devices can be leveraged for neuromorphic computing [196, 199, 200] and in particular it can be used to implement the activation function with a single device. However, the existing literature highlights a notable gap in achieving a large scale realization of spintronic-based ANNs. The projections from theoretical studies often assume the same activation functions for all the devices. Here, we focused on the fact that geometrical and physical characteristics are device dependent and device-to-device variations are inevitable in the hardware implementation of spintronic neurons. As shown in Figure 3.13, we have studied the effect of transfer learning from software to hardware in presence of device-to-device variations, which can be found in a real stack of devices. These variations are reflected in the spread of the slope of the activation functions, as discussed in paragraph 3.4.3.1.

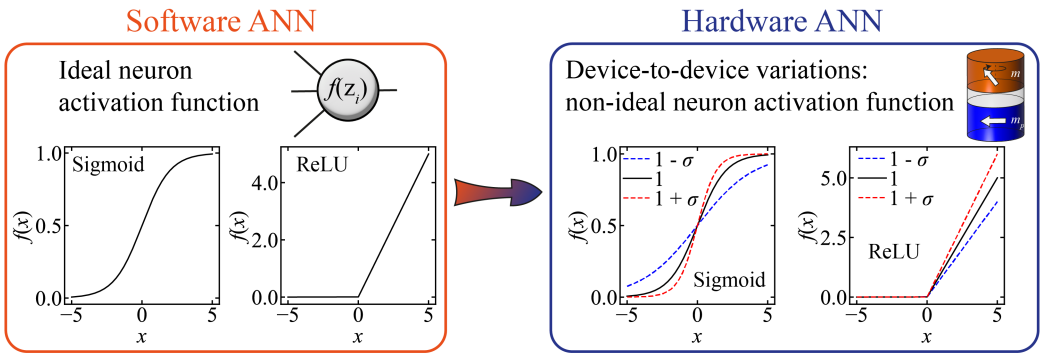

FIGURE 3.13: Workflow. On the left, the ideal neurons of a software ANN with sigmoid and ReLU activation functions are depicted. On the right, the deployment of the ANN on hardware introduces device-to-device variations, simulated by the spread of the slope of the activation functions.

The main results of this study are published in Ref. [70].

3.4.3.1 Spintronic neurons

3.4.3.1.1 Sigmoidal AF

The first study is based on the data by Cai *et al.* [196], where an experimental implementation of a sigmoidal AF was based on a superparamagnetic MTJ. At a fixed magnetic field and voltage, time-domain traces of stochastic switching in the resistance state of the MTJ are observed. The switching probability is given by $P = N_{RAP}/N_{total}$, where $N_{R_{AP}}$ is the number of high-resistance states readout and N_{total} is the total number of samples. The switching probability can be tuned with an external perpendicular magnetic field. A large-enough positive (negative) field leads to a high (low) P. A sigmoidal behavior is shown in Fig. 2 (d) of Ref. [196]. However, this configuration has a drawback: it requires some time, of the order of µs, to average a trustworthy output resistance value which can be used for the calculation of the output of the AF.

To overcome this limitation, we have proposed a way to implement a deterministic sigmoidal AF designed through micromagnetic simulations. It can be obtained by using a hybrid MTJ with out-of-plane FL magnetization $\boldsymbol{m}$ and in-plane PL magnetization $\boldsymbol{m}_p$, as shown in Figure 3.14 (a). The simulated MTJ is an elliptical cylinder of size 20 $\times$ 18 $\times$ 1 nm^3 with discretization cell of 1 $\times$ 1 $\times$ 1 nm^3. The micromagnetic parameters are: M_S = 1100 kA/m, A = 20 pJ/m,

$K_u = 0.6215$ MJ/m^3, $\alpha_G = 0.02$. The MTJ's dimensionless resistance is calculated with Eq. (1.58), with $R_P = 0$ and $R_{AP} = 1$. The PL magnetization is fixed along the positive x-direction, therefore only the x-component m_x gives rise to the magnetoresistive signal, i.e., $\cos(\theta) = m_x$. At zero external field the FL magnetization is perpendicular, therefore $R(\pi/2) = 0.5$. The equilibrium direction of the magnetization can be controlled using an external field H_x applied along the x-axis. For a large-enough positive (negative) H_x the magnetization is aligned with the field and a low (high) resistance state is reached. The field is generated by a DC current, as explained below. Figure 3.14 (b) shows the results of the simulations (red dots) which are well-fitted by a sigmoid function. As shown in the sketch in Figure 3.14 (a), the H_x can be generated by a DC current I_{DC} flowing in a nanowire positioned on top of the MTJ. In particular, in our simulations a positive (negative) I_{DC} generates negative (positive) H_x. The behavior observed confirms that the proposed configuration of the MTJ can be used for a deterministic sigmoid AF of the neurons.

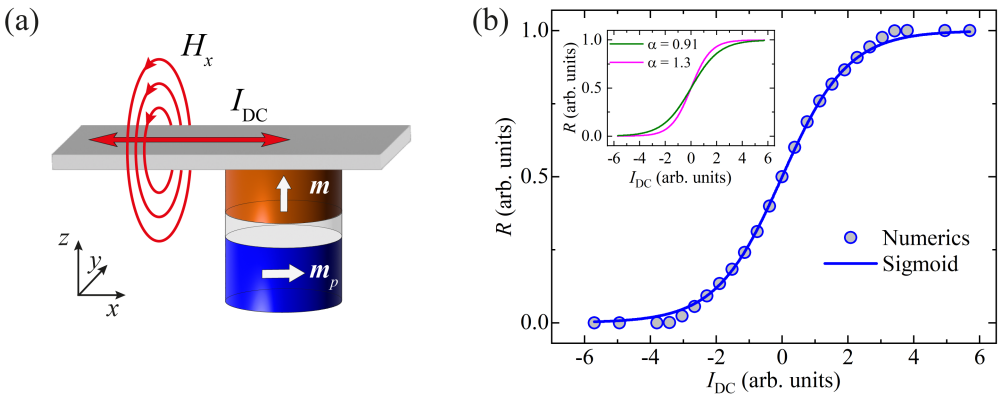

FIGURE 3.14: (a) A sketch of MTJ structure to obtain a deterministic sigmoid AF. The DC current, I_{DC}, generates the in-plane magnetic field, H_x, which brings the FL magnetization $\boldsymbol{m}$ to be parallel or antiparallel to the PL magnetization $\boldsymbol{m}_p$. (b) Magnetoresistance curve of the MTJ device as a function of DC current, I_{DC}, computed from micromagnetic simulations for $K_u = 0.6215$ MJ/m^3 (blue dots) fitted by the ideal sigmoid function (blue line). (Top-left inset) Magnetoresistance curves of the MTJ device vs I_{DC}, for $K_u = 0.6225$ and 0.6200 MJ/m^3, which can be described by a sigmoid with a slope coefficient $\alpha = 0.91$ and 1.3, respectively.

To investigate the impact of device-to-device variations in the accuracy of the network, a change of the anisotropy constant K_u is then considered. In detail, we have performed simulations with K_u ranging from 0.6200 to 0.6225 MJ/m^3. These are the lowest values that guarantee a perpendicular FL magnetization at zero temperature, while also being in agreement with a 5% variation of MTJ parameters deposited with same nominal thickness. Furthermore, we consider small variations because the anisotropy can be also controlled by fine tuning it with a voltage applied across the MTJ [25, 58, 201, 202]. The curves obtained from the simulations with these values of K_u are still sigmoid functions $f(x) = 1/(1 + e^{-\alpha x})$, with a slope coefficient which varies between $\alpha = 0.91$ and $\alpha = 1.30$, respectively, as also depicted in top-left inset of Figure 3.14 (b).

The presence of the thermal fluctuations can affect the stability region (physical parameters and/or geometry) of the sigmoidal AF. For this reason, we have performed a systematic study finding the anisotropy region of K_u to have a stable sigmoidal response. We have performed simulations with temperature $T = 300$ K and, despite the stochasticity, a sigmoidal behavior is shown for $K_u = 0.6225$ MJ/m^3 (see Figure 3.15 (a)). The inset of Figure 3.15 (b) shows an example of the time domain trace of the x-component of the FL magnetization m_x for $I_{DC} = 3.68$ (arb. units). Blue dots in Figure 3.15 (a) are obtained from the time-averaged value $\langle m_x \rangle$ shown in the Figure 3.15 (b).

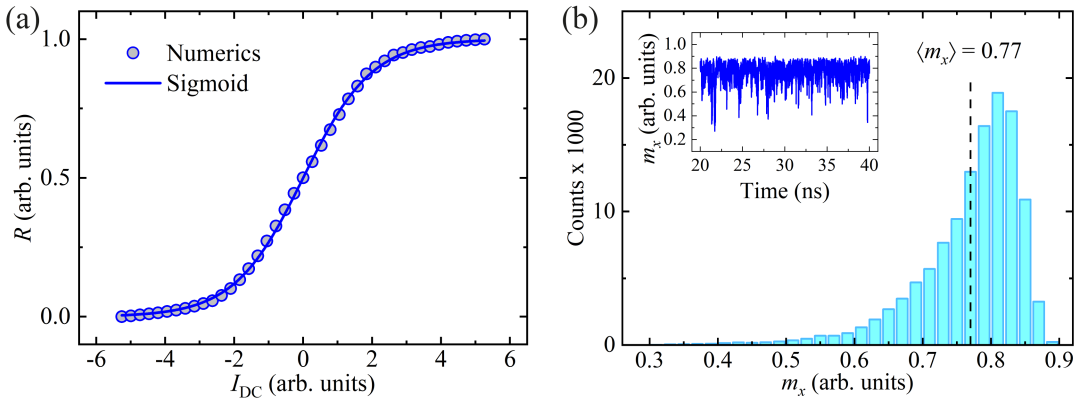

FIGURE 3.15: (a) Sigmoidal AF as obtained in presence of thermal fluctuations at room temperature $T = 300$ K. The blue dots are the results of the micromagnetic simulations, while the black line represents an ideal sigmoidal function. (b) Histogram of the values of the x-component of the FL magnetization for $T = 300$ K, where the time-averaged value is indicated by a black dashed line. Inset: time evolution of the x-component of the FL magnetization.

Figure 3.16 shows the time trace of m_x and its time-averaged value, where it is possible to observe that the average time to achieve a reliable resistive signal is predicted to be of the order of 5 ns. This short time makes spintronic devices robust against thermal fluctuations when properly designed.

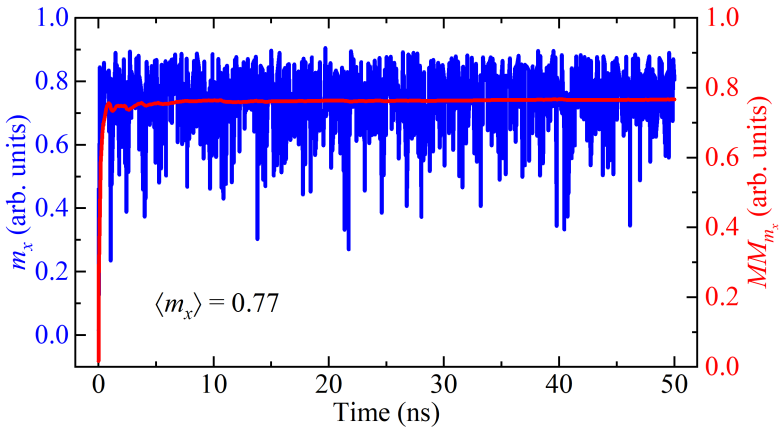

FIGURE 3.16: (Blue line) Time evolution of the x-component of the FL magnetization under the effect of thermal fluctuations at room temperature $T = 300$ K. The x-component gives rise to the magnetoresistive signal (the polarizer is oriented in the x-direction). (Red line) Corresponding moving mean of the FL magnetization x-component.

The deterministic sigmoid AF can be also implemented with the use of the spin-transfer torque generated from a spin-polarized current. The scheme consists of two hybrid MTJs connected in parallel, according to the sign of the bias current applied to the MTJ branch, which is selected thanks to a diode, see Figure 3.17 (a). This dual-device scheme is necessary because a positive current drives the rotation of the FL magnetization, while, for a negative current, self-oscillations are excited [47, 51, 203, 204]. The simulations (blue dots in Figure 3.17 (b)) are performed with the same parameters of Figure 3.15 with a spin polarization parameter $P = 0.66$.

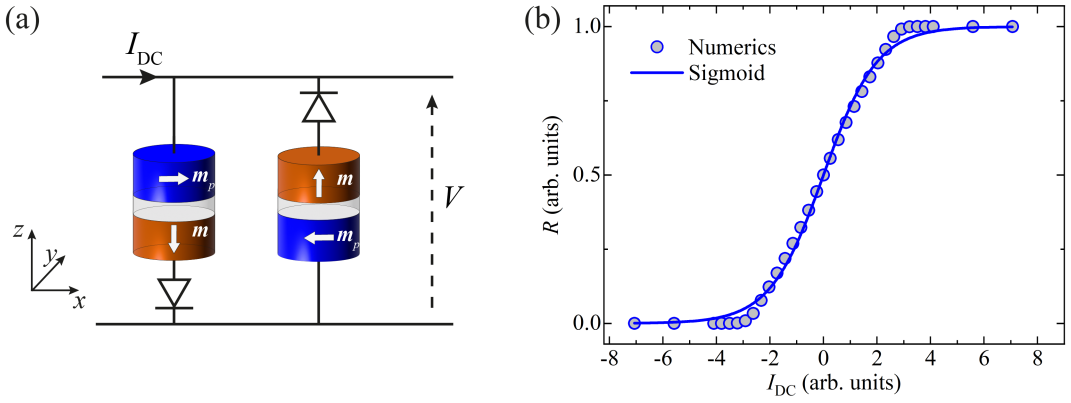

FIGURE 3.17: (a) A sketch of circuit involving two MTJs and two diodes, designed to obtain a deterministic sigmoid AF. (b) Magnetoresistance curve as a function of the I_{DC}. The micromagnetic simulations' results (blue dots) are fitted by an ideal sigmoid function (solid blue line).

3.4.3.1.2 ReLU-like AF

Cai *et al*. [199] proposed the implementation of a ReLU-like AF from the ascending branch of the rectification curve V_{DC} of a spin-torque diode (STD) as a function of the DC bias current I_{DC}, opening the path toward neural networks with microwave neurons. An example of those curves is shown in Fig. 3 (a) of Ref. [199] and reported in Figure 3.18 (a). For this application, the best device should have the rectification curve as asymmetric as possible with the largest possible ascending branch of the rectification curve. For this reason, here we consider a high sensitivity STD (10^5 V/W) working at zero bias field as reported by Zhang *et al*. [57] experimentally. The MTJ's structure has a tilted FL magnetization and an in-plane PL magnetization (see inset Figure 3.18). The selected experimental data of V_{DC} as a function of I_{DC} can be fitted with a third-order polynomial function (see Figure 3.18).

To study the impact of device-to-device variation, we consider AFs which are sampled between the green and blue line shown in the inset of Figure 3.18 (b). Those curves have been identified together with experimentalists according to measured data, and it can be seen as a rotation of the reference curve with a clockwise or counterclockwise rotation of 5 degrees ($\theta = \pm 5°$). Alternatively, the microwave power applied to the STD can be tuned to reduce the device-to-device variation, see for example the rectification curve at different powers as shown Fig.

3 (a) of [199] (0.32 and 0.56 µW) and reported here in Figure 3.18 (a) for clarity.

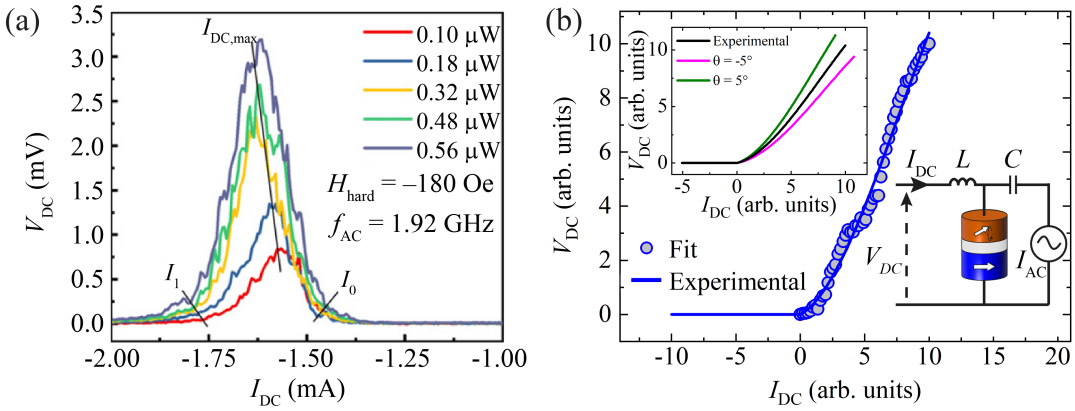

FIGURE 3.18: Experimental rectified voltage V_{DC}, as a function of DC current I_{DC} (a), from Ref. [199], and for different powers (b), from Ref. [57] (blue dots). The data is fitted by a third-order polynomial function (blue line). (Top-left inset) Fitted experimental data with different spreading angles θ, as indicated in the legend. (Bottom-right inset) Sketch of the MTJ spintronic diode implemented in Ref. [57] where the rectification effect is achieved via the injection locking due to a locally injected AC current, I_{AC}.

3.4.3.2 Application in convolutional neural networks

In order to study the reliability of an ANN model with non-ideal AFs, a vanilla CNN is trained to solve classification tasks using the Mixed National Institute of Standards and Technology (MNIST) [205] and Fashion-MNIST [206] database. Both databases consist of 28 × 28 = 784 pixel gray scale images divided into ten categories, for a total of 70000 samples (60000 for training and validation, 10000 for test). The first database contains images of handwritten digits while the second contains Zalando's article images, and it is more difficult to solve than the MNIST. The CNN structure is shown in Figure 3.19. A single convolutional layer with 64 filters of size 3 × 3 performs the feature extraction. The resulting feature maps are passed through the ReLU AF and its spatial dimensions are halved into a max pooling layer. The outputs are flattened and connected to an FC layer with 128 neurons, and sigmoid or ReLU-like AF is adopted as the neurons' AF in the FC layer. The last layer of the FC part has ten neurons that are activated with a softmax AF to obtain the output probability of the classes. Dropout layer and early stopping are used to prevent overfitting during the training process.

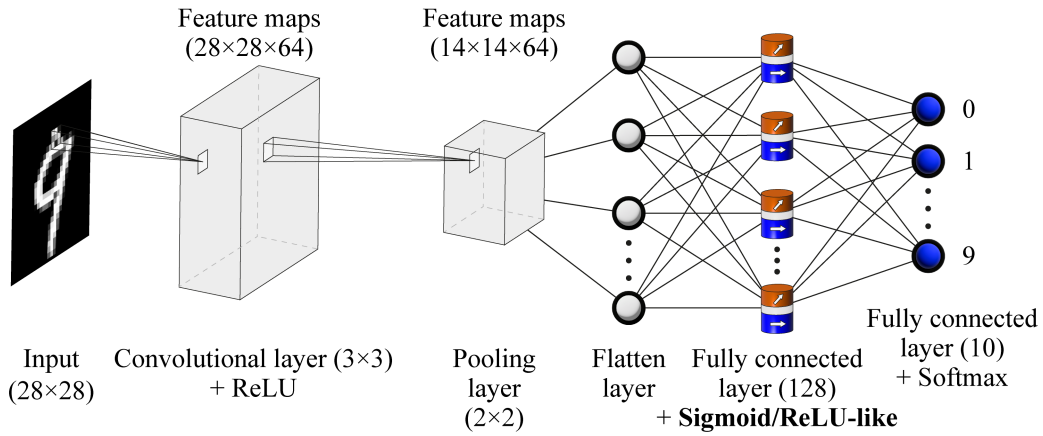

FIGURE 3.19: The CNN architecture consists of one convolutional layer with ReLU AF, pooling layer, one FC layer with 128 neurons (replaced with spintronic neurons) and the last FC layer.

To perform our numerical experiments, we first train the CNN by considering all the neurons having the same AF. Finally, we use this pre-trained model for a transfer learning technique to emulate the hardware implementation of the model. We simulate 10000 different instances of the CNN where each of them has nonideal AFs for neurons of the FC layer. Below, we provide more details of the two studies performed.

3.4.3.2.1 Results for the sigmoid AF

The CNN is trained using neurons of the FC layer having an ideal sigmoid AF, therefore $\alpha = 1$. For the MNIST and Fashion-MNIST dataset the validation accuracy obtained is 98.93% (Figure 3.20 (a)) and 92.26% (see Figure 3.21 (a)), respectively. The test accuracy is 98.89% (ideal accuracy in Figure 3.20 (b)) for MNIST and 91.81% (ideal accuracy in Figure 3.21 (b)) for Fashion-MNIST. We use this pre-trained ideal CNN as a starting point to test its robustness against device-to-device variation, that we simulate with different magnetic anisotropy values. We select different slopes α for the sigmoid function by sampling 128 random values from a normal distribution with a mean of 1 (representing the slope of the ideal sigmoid) and a standard deviation of 0.2 (negative values are discarded and resampled). To obtain a reasonable statistic of the test accuracy, 10000 instances of the CNN are simulated. The results for the MNIST dataset are summarized in Figure 3.20, the ones for the Fashion-MNIST are in Figure 3.21 (b). A Gaussian distribution of the results is observed with a mean of 98.87% and 98.81% for

MNIST and Fashion-MNIST respectively, with a standard deviation of few points percentage from the average.

3.4.3.2.2 Results for the ReLU-like AF

The same CNN is also trained using neurons in the FC layer having a ReLU-like AF as described in section 3.4.3.1.2. For the MNIST and Fashion-MNIST dataset the validation accuracy obtained is 98.95% (see Figure 3.20 (c)) and 91.93% (see Figure 3.21 (c)), respectively. The test accuracy is 98.92% (ideal accuracy in Figure 3.20 (d)) for MNIST and 91.89% (ideal accuracy in Figure 3.21 (d)) for Fashion-MNIST. These results are comparable with the test accuracy of 98.87% obtained considering the ideal ReLU AF. With the same procedure of the sigmoid AF, we study the effect of device-to-device variation. We select different ReLU-like AFs between -5°$< \theta <$ +5°by sampling in a Gaussian distribution with mean of zero and standard deviation of 3. The CNN accuracy is computed over 10000 different instances. The results for the MNIST dataset are summarized in Figure 3.20 (d) while the ones for the Fashion-MNIST are shown in Figure 3.21 (d). A Gaussian distribution of the results is observed with a mean of 98.91% and 98.85% for MNIST and Fashion-MNIST, respectively.

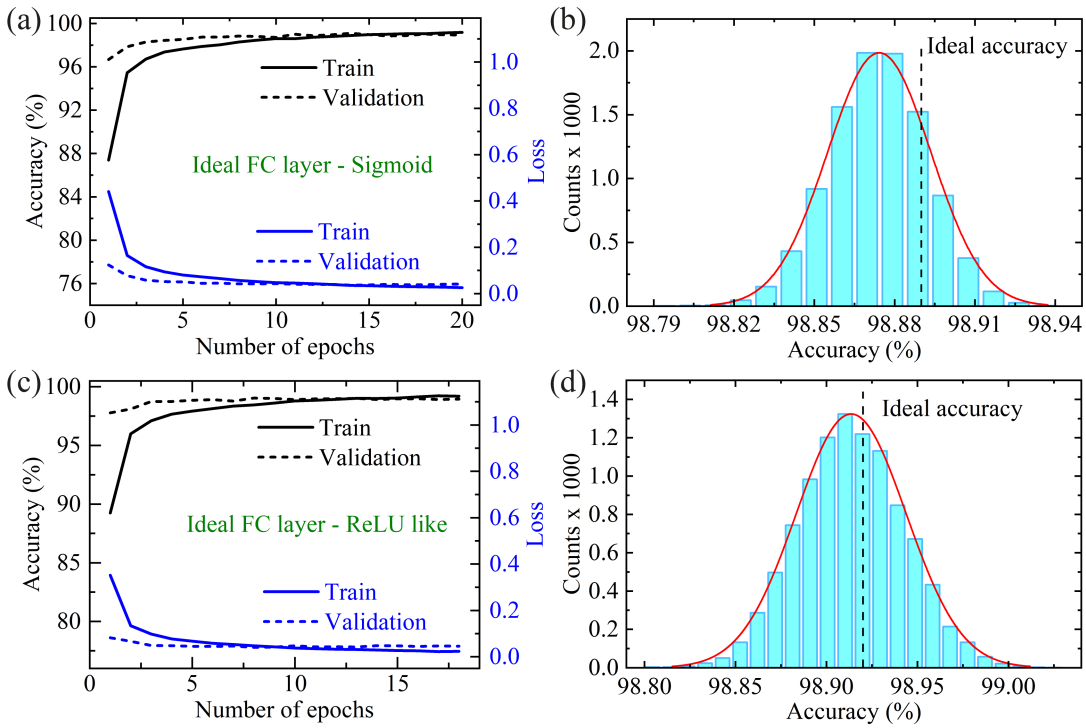

FIGURE 3.20: Classification results of MNIST database. (a) and (c) Accuracy versus number of epochs for training and validation achieved for neurons with ideal sigmoid and ReLU-like AFs, respectively. The solid (dashed) blue line represents the train (validation) loss. (b) and (d) Statistics of the test accuracy obtained with the nonideal FC layer composed of spintronic neurons with different sigmoid and ReLU-like AFs.

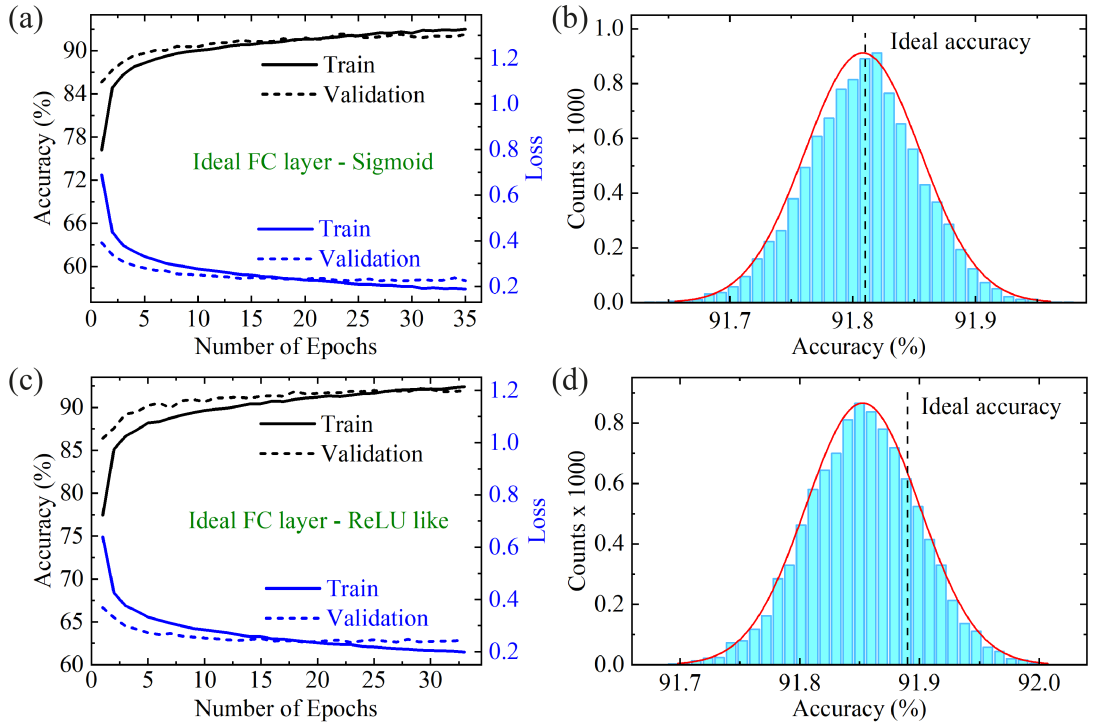

FIGURE 3.21: Classification results of Fashion-MNIST database. (a) and (c) Accuracy versus number of epochs for training and validation achieved for neurons with ideal sigmoid and ReLU-like AFs, respectively. The solid (dashed) blue line represents the train (validation) loss. (b) and (d) Statistics of the test accuracy obtained with the non-ideal FC layer composed of spintronic neurons with different sigmoid and ReLU-like AFs.

In summary, the average test accuracy over 10000 instances is a few percentages less than the ideal test accuracy for both configurations studied.

3.4.4 Computing with injection-locked spintronic diodes

This section explores the use of STDs for implementing analog multiplication, which is one of the key operations in ANNs, including CNNs. The concept of degree of rectification (DOR) in injection-locked STDs is introduced. The working range of STDs for the DOR implementation is studied by performing micromagnetic simulations and considering experimental data from literature. The applicability of DOR-based multiplication is tested for both image processing and CNN models.

The main results of this study are published in Ref. [67].

3.4.4.1 Introduction to the concept of degree of rectification

As we already discussed, the inputs of a CNN are convoluted with filters for feature extraction, this implies a huge amount of multiplication operations. Digital multiplication can be implemented with several solutions, such as multiple adders, and carryover systems. These approaches are scalable, but the drawbacks are the computational time, energy consumption, and area occupancy [207]. An analog solution can overcome these bottlenecks but seems difficult to achieve nowadays mainly due to the susceptibility to noise and offset voltage [208]. Analog solutions based on optical devices [209], photonic devices [210, 211], and memristors [164, 212] have already been proposed. However, the main problems of memristors for a CNN application are the significant device-to-device variation and conductance degradation, which can be smoothed with a continuous in-situ training of the model [212].

Given two values, F and G, the analog multiplication, FG, can be implemented by considering a physical observable P characterized by a parabolic input-output relation $P(X) = aX^2 + bX + c$, where X is the input and the coefficients a, b and c are characteristic of the physical system. The multiplication FG, can be implemented combining three measurements (3.8):

$$FG = \frac{P(F-G) - P(F) - P(-G) + c}{-2a} \tag{3.8}$$

The first idea to implement the multiplication of Eq. (3.8) dates back to the concept of degree of match (DOM). It is based on the interaction between two nonlinear oscillators, and it is a measure that quantifies the synchronization (or similarity) in their oscillations. The DOM is defined as (3.9):

$$z_{DOM}(t) = \frac{1}{2}\left|z_1(t) + z_2(t)\right| \tag{3.9}$$

Each oscillator is characterized by power $p = |z|^2$ and phase $\phi = \arg(z)$, where $z(t)$ is the complex oscillating variable describing the behavior of each oscillator. Considering two spintronic oscillators with approximately constant output power in the locking region, the DOM can be written as (3.10):

$$z_{DOM} \cong |\sqrt{p}| \cos\frac{\Delta\phi}{2} \tag{3.10}$$

where $\Delta\phi = \phi_1 - \phi_2$ is the phase difference between the time-domain traces of two oscillators. The working point of the oscillators can be set and controlled by a bias current [213]. In this point $\Delta\phi$ is close to zero, and the cosine function can be approximated using a second-order polynomial through the Taylor expansion. Hence, the DOM can be considered eligible as observable P in the Eq. (3.8), where X represents the phase difference between the oscillators. The aforementioned observations can be generalized to the scenario of two different oscillators [214]. However, the DOM's read-out is one of the key challenge due to difficulties in on-chip estimation of the oscillator amplitudes and phases.

We have introduced the concept of DOR, which is based on the Eq. (3.8) where the observable P is the rectification voltage V_{DC} of an injection-locked STDs, while the input is its bias current I_{DC}. The applicability of the DOR is studied by performing micromagnetic simulations. The simulation results show a parabolic relationship between V_{DC} and I_{DC} [57], which is also in agreement with the experimental data in Ref. [46]. This approach has the intrinsic advantages of spintronic technology (such as CMOS compatibility, scalability, and low power dissipation), the read-out mechanism is simpler than the DOM and can be implemented with a single device.

We use a vanilla CNN model to solve the MNIST dataset considering, for the multiplication, the one implemented with the DOR. The reliability of this approach is also tested considering device-to-device variations. Furthermore, we also demonstrate the robustness of DOR-based multiplication for dark knowledge extraction, opening a path in the use of nonlinear operators to extract the dark knowledge.

3.4.4.2 Device concept and micromagnetic simulation results

The device structure is a hybrid MTJ with out-of-plane FL magnetization (1.63-nm-thick Co_{20} Fe_{60} B_{20}) and in-plane PL magnetization (synthetic antiferromagnet Co_{70} Fe_{30} (2.3 nm)/Ru (0.85 nm)/Co_{40} Fe_{40} B_{20} (2.4 nm) and exchange biased by a PtMn (15 nm) layer, as illustrated in Figure 3.22 (a). The MTJ has an elliptical cross-section 150 $\times$ 60 nm^2, with resistance state $R_P = 640\,\Omega$ and $R_{AP} = 1200\,\Omega$. It has been experimentally demonstrated that this device operates at zero field. We perform micromagnetic simulations, and the micromagnetic parameters are: $M_S = 950$ kA/m, $A_{ex} = 20$ pJ/m, $K_u = 0.545$ MJ/m^3, $\alpha_G = 0.02$, $P = 0.66$. The field-like torque of the STT has a ratio $q_{STT} = 0.1$; the results are qualitatively the

same for $q_{STT} = 0$ and $q_{STT} = 0.2$ with a variation of the oscillation frequency by less than 3% [215].

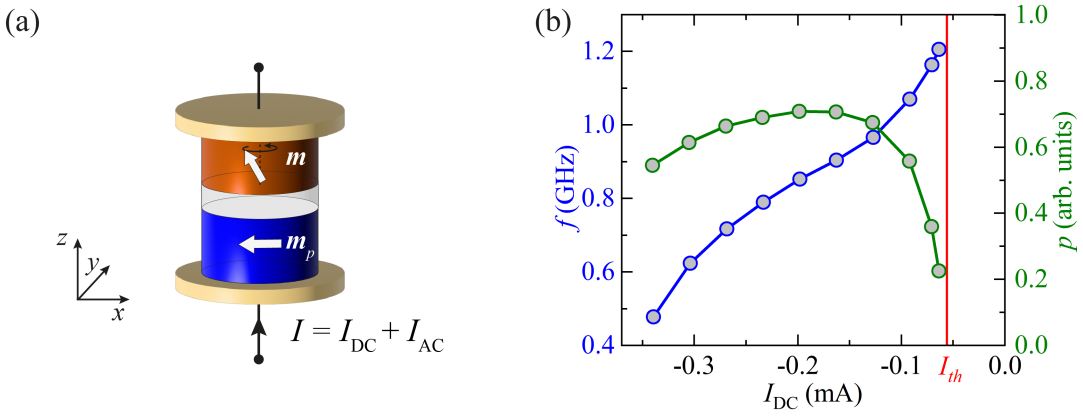

FIGURE 3.22: (a) Sketch of the hybrid STD with perpendicular FL magnetization and in-plane polarizer along -x direction. (b) Frequency (blue squares) and power (green triangles) of FL magnetization oscillation as a function of the applied DC current, obtained using micromagnetic simulations. The vertical line indicates the threshold current $|I_{th}| = 0.056$ mA.

Figure 3.22 (b) summarizes the frequency f_0 (blue dots) and the power p_0 (green dots) of self-oscillation of the MTJ as a function of the DC current I_{DC} . The threshold current is $|I_{th}| = 0.056$ mA. The nonlinear frequency shift, N, which links the oscillation frequency and power of the self-oscillation near the $I_{th} - f_0 = f_0(I_{th}) + Np_0/2\pi$ [47] - is $N/2\pi = df_0/dp_0 \cong -411$ MHz. This parameter plays a crucial role in the magnetization dynamics in the injection-locking regime. As discussed in the paragraph 1.8 , this regime is achieved when the frequency of the applied AC current, f_{AC}, approaches the self-oscillation frequency f_0. In this locking regime, the magnetoresistance oscillates at the same frequency of the AC current, giving rise to a rectification voltage [216, 217]. Within the locking range, a variation of I_{DC} does not change the frequency. However, it can change the amplitude of the oscillating magnetization, $\Delta m_x(I_{DC})$, which is related to the oscillator power p $(\Delta m_x \sqrt{p})$, and the intrinsic phase shift $\varphi(I_{DC})$ between the AC current and the oscillating magnetoresistive signal [218]. The output voltage can be then computed using the following expression [46]:

$$V_{DC} = \frac{(R_{AP} - R_P)\sqrt{p}}{4} I_{AC,max} \cos[\varphi(I_{DC})] \tag{3.11}$$

The rectification voltage obtained at $I_{AC,max} = 70.7$ µA, $f_{AC} = 800$ MHz and $\varphi_{AC} = 0$ is shown in Figure 3.23 (a), with the maximum value at $I_{DC,\,0} = -0.134$ mA, which corresponds to a phase shift close to zero. The corresponding Δm_X (green dots) and φ (blue dots) are shown in Figure 3.23 (b).

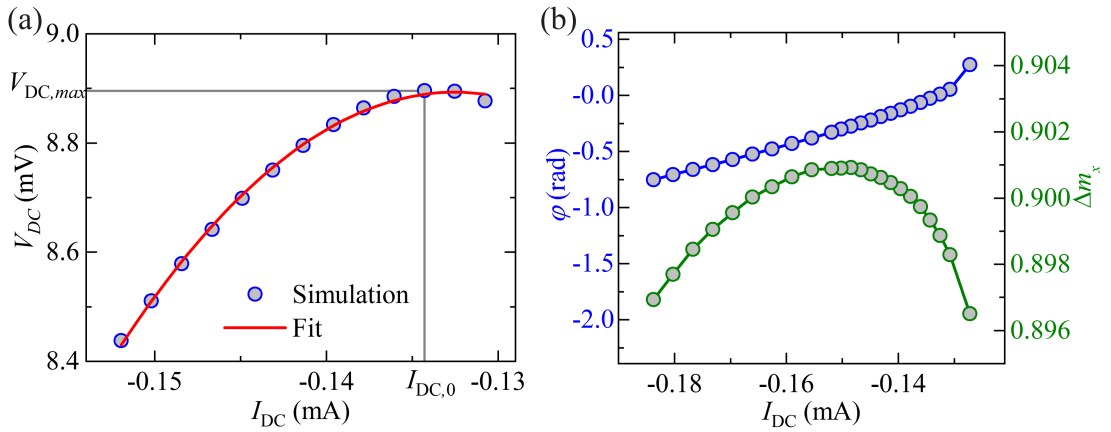

FIGURE 3.23: (a) Micromagnetic data of rectified voltage, V_{DC}, as a function of the DC current, I_{DC}, applied to the STD (blue dots) with $I_{AC,max} = 70.7$ µA and $f_{AC} = 800$ MHz, and parabolic fit (red line). (b) Intrinsic phase shift (blue dots) and amplitude of x-component of the magnetization, Δm_X, (green dots) as a function of DC current for the same $I_{AC,max}$ and f_{AC} as those in (a).

The amplitude of the magnetization displays a weak current-dependence: a change of less than 3% is observed. This outcome is in agreement with the behavior expected for an oscillator characterized by a large nonlinear frequency shift. This is clear if we look at the expression of the power p of the injection-locked oscillator $p/p_0 = 1 + \sigma I_{AC,max}/\sqrt{1 + (N/P\xi)^2}$, where $\xi = I_{DC}/I_{th}$ (eq 1.69) is the supercriticality of the DC bias current, and P is the effective damping rate [47]. In our devices, N/P is larger than 15, leading to a reduced dependence of oscillator power on I_{DC} [47]. The quasi-linear behavior of the intrinsic phase shift as a function of the I_{DC}, with a deviation at the edge of the locking region (see Figure 3.23 (b)), was already observed in Refs. [218, 219]. This behavior can be approximated by $\varphi(I_{DC}) = mI_{DC} + n$, where the fitting parameters can be identified from the rectified voltage in Eq. (3.11) at $I_{DC,0}$ (see Figure 3.23 (a)), therefore $\varphi(I_{DC}) = 0$ and the $n = -mI_{DC,0}$. Furthermore, the coefficient m can be estimated from the

second order derivative of the rectified voltage with respect the DC current evaluated at $I_{DC,0}$, $\left.\frac{d^2V_{DC}}{dI_{DC}^2}\right|_{I_{DC}=I_{DC,0}} = -m^2V_{DC,max}$. This approach can be applied to experimental data as well to extract information about the intrinsic phase shift.

To estimate the DOR, we are looking for a parabolic behavior, and the Eq. (3.11) can be rearranged into a parabolic function (3.12):

$$V_{DC}\left(I_{DC}\right) = aI_{DC}^2 + bI_{DC} + c \tag{3.12}$$

where $a = -(1/2)V_{DC,max}m^2$, $b = V_{DC,max}m^2I_{DC,0}$ and $c = V_{DC,max}\left\{1 - \left[\left(mI_{DC,0}\right)^2/2\right]\right\}$.

Figure 3.24 (a) shows the micromagnetic data (already shown in Figure 3.23 (a)) fitted by a parabolic fit (red line) and analytical evaluation (dashed line); we can clearly observe the excellent agreement.

(a)

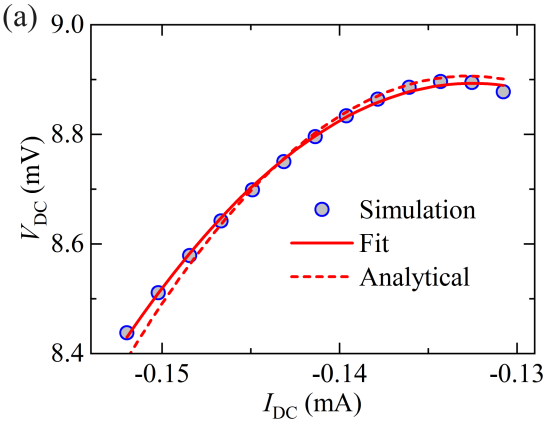

(b)

Parabolic DOR

$V_{DC}(I_{DC}) = aI_{DC}^2 + bI_{DC} + c$		
Parameters	**Fit**	**Analytical**
a (mV/mA^2)	-1.225×10^3	-1.397×10^3
b (mV/mA)	-325.0	-371.0
c (mV)	-12.6	-15.7

FIGURE 3.24: (a) Micromagnetic data of rectified voltage, V_{DC}, as a function of the DC current, I_{DC}, (blue circles) (already shown in Figure 3.23 (a)) with the parabolic fit (red line) and the parabola obtained with the analytical data (dashed line). The table (b) summarizes the coefficients of the two parabolas, obtained from the parabolic fit and the analytical process.

Indeed, for the successful implementation of a multiplier using spintronic diodes, it is crucial that the devices operate with specific currents and microwave input frequencies to achieve an intrinsic phase shift ϕ close to 0 or π.

Figure 3.25 (a) provides an overview of the systematic study of φ as a function of I_{DC} and f_{AC}, while maintaining $I_{AC,max} = 70.7$ µA. The horizontal line represents the working point for the data presented in Figure 3.23 (a) and Figure 3.23 (b). Notably, in this device's geometry, the value $\varphi = 0$ can be achieved close to the edge of the injection-locking range. Figure 3.25 (b) shows the time-evolution of the spatially averaged x-component of the FL magnetization for a $I_{DC} = -0.48$ mA and $f_{AC} = 800$ MHz (circle in Figure 3.25 (a)) and the AC current. A constant time shift can be noted from the comparison of the time traces. However, in Fourier space the dynamics of the magnetization has a predominant first harmonic (with 76% of the total energy) and also high-order harmonics which could potentially impact the measurements. For this reason, it is more appropriate to compute this parameter in the Fourier space.

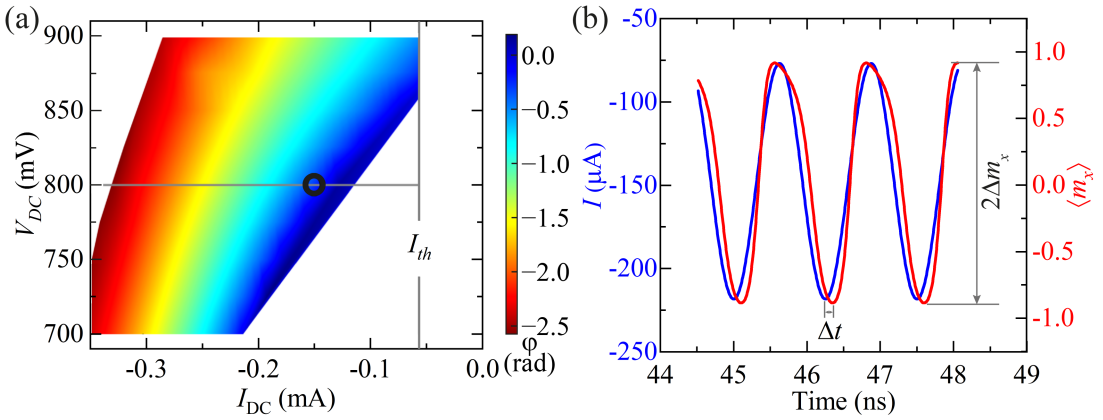

FIGURE 3.25: (a) Phase diagram of the intrinsic phase shift, φ, as a function of microwave frequency, f_{AC}, and DC current, I_{DC}, for $I_{AC,max} = 70.7$ µA. The vertical line is the auto-oscillation current threshold, $|I_{th}| = 0.056$ mA, while the horizontal line is the microwave frequency value used in Figure 3.23 (a)-(b). (b) Time traces of the applied current I (left y-axis) and spatially-averaged x-component of magnetization dm_x (right y-axis) for the working point indicated with a circle in (a). The time shift, Δt, between the two-time traces is indicated.

Figure 3.26 (a) shows the time-evolution of the spatially-averaged x-component of the FL magnetization for $I_{DC} = -0.48$ mA and $f_{AC} = 800$ MHz during the application of a DC current step to achieve the injection-locking regime. The transient time is about 10 ns, and it provides a reliable estimation of the speed of the multiplication operation. A smaller transient time is observed in presence of thermal fluctuations at room temperature as shown in Figure 3.26 (b). The frequency of the self-oscillation is smaller in presence of a thermal field, at least

for the simulation with $f_{AC} = 543$ MHz.

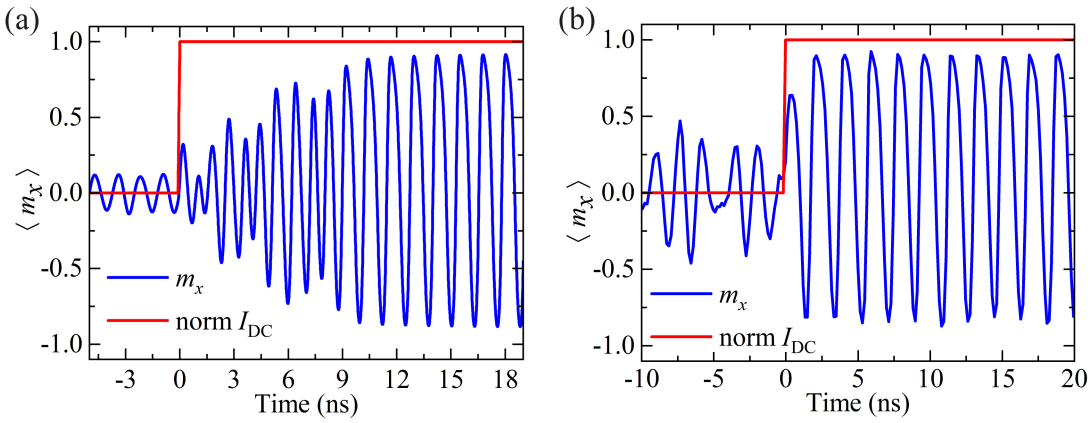

FIGURE 3.26: (a) Time domain trace of the injection locking of the x-component of the magnetization (blue line) achieved after application of a DC current step from 0 to -0.148 mA. The normalized DC current is shown in red line. The amplitude of AC current is $I_{AC} = 70.7$ µA and the frequency $f_{AC} = 800$ MHz. (b) Same as (a) but with $f_{AC} = 543$ MHz and at room temperature.

Figure 3.27 (a) shows the experimental data from Ref. [46], which exhibits a behavior similar to the theoretical curves. Figure 3.27 (b) shows the parabolic fit of the data for a wider range of input. In order to achieve high sensitivity, the variation of the DC resistance induced by the microwave input, R_{DC}, is added in the rectified voltage: $V_{DC}(I_{DC}) = aI_{DC}^2 + (b + R_{DC})\, I_{DC} + c$. This term is proportional to the I_{DC} and it introduces a linear shift of the parabolic equation [46].

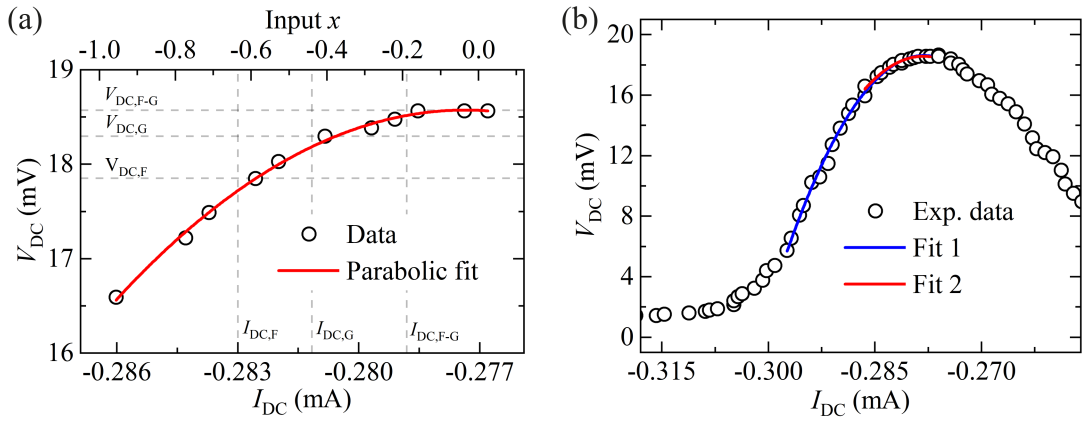

FIGURE 3.27: (a) Experimental data (black dots) of output DC voltage, V_{DC}, as a function of DC current, I_{DC}, in injection locked STD from Ref. [46] (bottom axis), and the corresponding numeric input for the even parabola (top axis). The solid red line represents the parabolic fit of the data. The points corresponding to the input values $F = -0.62$, $G = -0.44$, and $(F - G) = -0.18$ are shown. (b) Experimental data of (a) are fitted by ideal parabolas considering a smaller (red curve) and a wider range (blue curve). Near the peak, the red curve overlaps the blue one.

3.4.4.3 DOR-based multiplication

The computation of the DOR-based multiplication is built on the Eq. (3.12). For simplicity, the range of input currents is scaled to be in the range $[-1, 0]$ with a linear transformation: $I_{DC} = |I_{DC,0} - I_{DC,-1}|\, x + I_{DC,0}$, where $I_{DC,0}$ ($I_{DC,-1}$) is the current value associated with the numeric inputs 0 (-1). By making this transformation, we obtain an even parabolic equation $V_{DC}(x) = V_{DC}(-x)$ given by:

$$V_{DC}(x) = a'x^2 + c' \tag{3.13}$$

where $a' = a\,|I_{DC,0} - I_{DC,-1}|^2$ and $c' = V_{DC,max}$ (see Figure 3.27 (a)). Based on the Eq. (3.8), the steps to compute the multiplication between F and G consists in the evaluation of the voltages for $x = F, G, (F - G)$. To give an example, we consider the experimental data of the rectified V_{DC} as a function of the I_{DC} and input value x (top x-axis), showed in Figure 3.27 (a). For this example, we have$F = -0.62$, $G = -0.44$ and $(F - G) = -0.18$. The respective V_{DC} are: $V_{DC,F} = 17.85$ mV, $V_{DC,G} = 18.30$ mV, and $V_{DC,F-G} = 18.57$ mV. We use Eq. (3.8) to perform the multiplication considering the coefficients $a = -2.0476$ mV and $c = 18.565$ mV. The DOR-based product is $FG = 0.241$, which is very close to the ideal value $FG = 0.273$.

The hardware implementation of the DOR can be realized sequentially with a single STD, to minimize the area occupancy, or in parallel, with three STDs, to maximize the computational performance. On the other hand, with three STDs used for each multiplication, the calculation is three time faster, and the speed of the DOR operation depends on the time required for the injection-looking and the time required for the CMOS circuity to perform the addition.

3.4.4.4 Performance evaluations

As a first step, we have studied a comparison between the ideal multiplication with the micromagnetic and experimental DOR-based multiplication.

Figure 3.28 (a) and Figure 3.28 (b) show the correlation results of 200 multiplications obtained using the DOR-based multiplication on micromagnetic data (blue dots in Figure 3.23 (a)) and experimental data (black dots in Figure 3.27 (a)), compare with ideal multiplication (red line). The Pearson correlation coefficient between the ideal multiplication and the micromagnetic (experimental) DOR-based multiplication is 99.93% (99.83%). The high correlation values indicate that both the micromagnetic and experimental DOR-based multiplications closely match the ideal case, a promising result in term of accuracy and precision of the DOR method for performing multiplication operations.

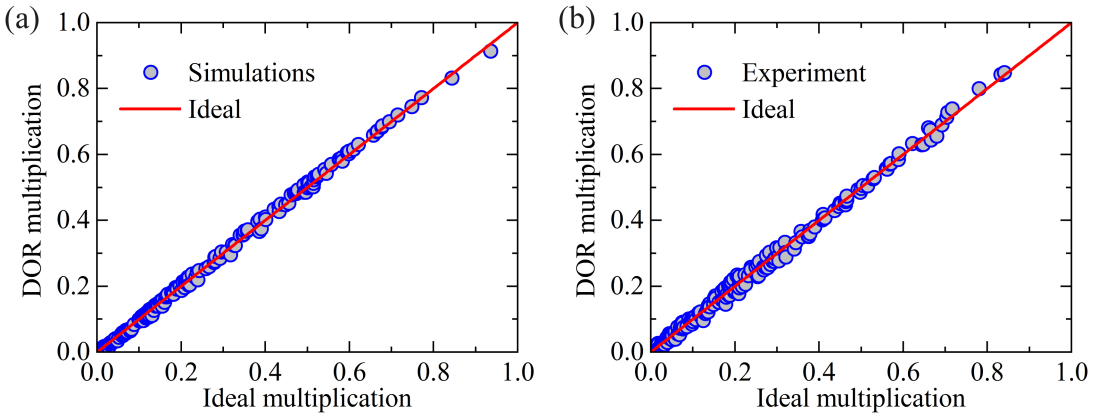

FIGURE 3.28: (a) Comparison between DOR multiplications based on micromagnetic simulations (blue dots) and the ideal multiplication (red line) versus the ideal multiplication. (b) Same comparison as in (a) but using the experimental curve from Ref. [46] for DOR-based multiplication.

In the second test, we have performed the convolution operation with the DOR-based multiplication.

Figure 3.29 (a)-(d) illustrate results of the convolution between an image of a snail (taken from the ImageNet dataset [180]) and the 3 $\times$ 3 blurring filter (see Figure 3.29 (a)), using ideal, simulated, and experimental DOR-based multiplication, respectively. The blurring filter represents a limited case since each its element has the same weight so the multiplication errors add up.

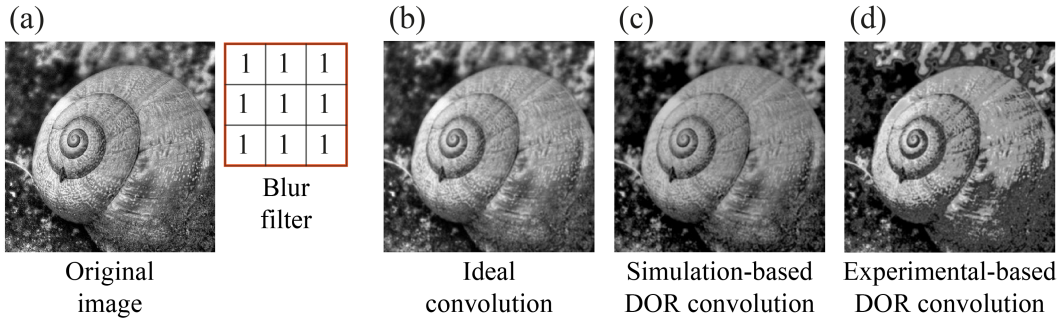

FIGURE 3.29: (a) Image of a snail, from ImageNet dataset; inset, 3 $\times$ 3 blur filter used to perform the convolution with (b) ideal multiplication, (c) DOR-based multiplication obtained via micromagnetic data, (d) DOR-based multiplication obtained via experimental data.

As an example, we compute the convolution operation between an image of a snail and several 3 $\times$ 3 filters, using both ideal multiplication and DOR-based multiplication. The comparison of the results is evaluated through the Pearson correlation (see Figure 3.30 (a)). Figure 3.30 (b) shows the probability density functions (PDFs) of the Pearson correlation coefficients, r, obtained by considering 10000 random instances of filters. The average correlation coefficients are $\bar{r}_{sim} = 99.41$ % for the simulation data and $\bar{r}_{sim} = 97.87$ % for the experimental data. The smaller average correlation and larger dispersion observed in the experimental data are attributed to the less-accurate parabolic behavior.

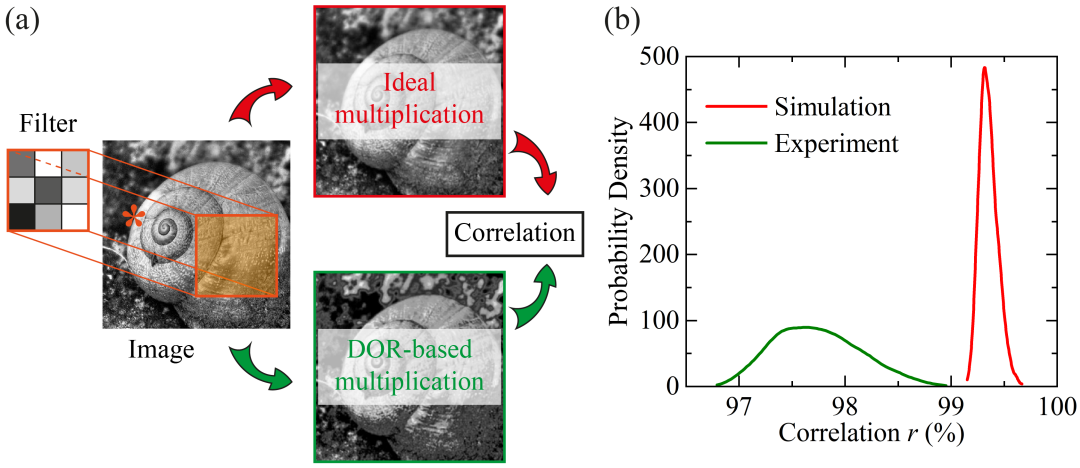

FIGURE 3.30: (a) A schematic representation of the process: correlation between the results of convolution of an image of a snail and a random filter using ideal multiplication and DOR-based multiplication. (b) Correlation probability density functions obtained by the convolution between an image of a snail (in (a)) and 10000 random filters, considering DOR multiplication through simulation (red curve) and experimental data (green line).

The third test of the DOR-based multiplication is performed with a vanilla CNN considering the experimental data. Figure 3.31 (a) shows the CNN architecture used to solve the MNIST dataset [205] ($28 \times 28 = 784$ pixel gray scale images divided into ten categories). A single convolutional layer with 16 filters of size 3×3 performs the features extraction. The resulting feature maps are passed through a ReLU AF and its spatial dimensions are halved using max pooling layer. The outputs are flattened and connected to a FC layer with 10 neurons and a softmax AF is used to obtain the output probability of the classes. Dropout layers and early stopping are used to prevent overfitting. The CNN model is implemented in Python with TensorFlow framework. The training dataset is composed by 48000 images, the validation dataset by 12000 images and the test dataset by 10000 images. The training accuracy reached is 98.64% and the test accuracy 98.57% (see Figure 3.31 (b)).

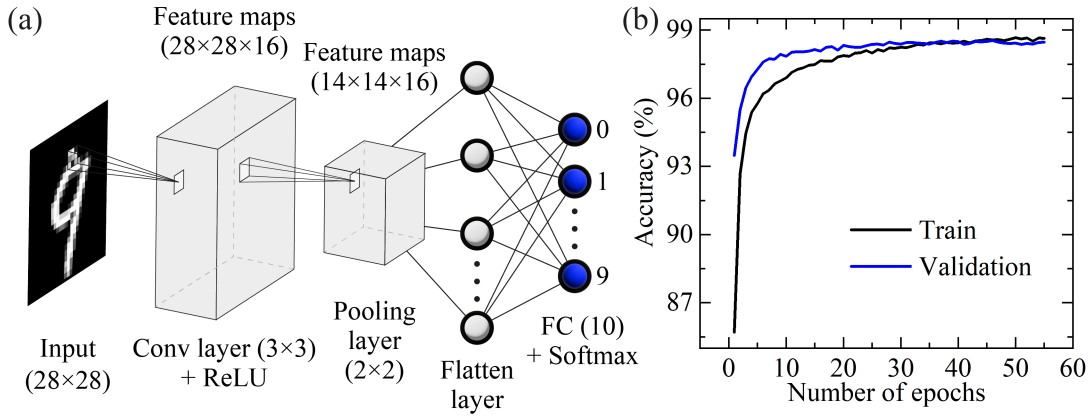

FIGURE 3.31: (a) CNN architecture consists of a convolutional layer, ReLU activation function, pooling layer, FC layer. (b) Percentage of recognition accuracy versus number of epochs for training (black line) and validation (blue line) of the CNN.

In order to mimic the spintronic hardware implementation of the model, we transfer the trained weights into a CNN model with DOR-based multiplications. After replacing the multiplication only in the convolutional layer ($Conv_{DOR}$), the test accuracy achieved is 96.83%; when extending the replacement to both the convolutional layer and the FC layer ($Conv_{DOR}$+ FC_{DOR}), the test accuracy is reduced to 94.72%. However, a fine-tuning of the FC layer, considering DOR-based multiplications only in the convolution layer ($Conv_{DOR}$+ trainFC), increases the test accuracy to 98.40%, see Table 3.1 (row a). Therefore, only an additional training of the last layer of the model is enough to restore the high accuracy obtained in the ideal case.

TABLE 3.1: Summary of test accuracy for the CNN trained, respectively, with ideal multiplication (Ideal), with DOR-based multiplication in the convolutional layer ($Conv_{DOR}$), with DOR-based multiplication in both the convolutional and FC layers ($Conv_{DOR}$+FC_{DOR}), and with DOR-based multiplication in the convolutional layer and an additional training of the FC layer ($Conv_{DOR}$+trainFC). (a) Test accuracy obtained with the main curve (represented in Figure 3.23 and Figure 3.27 (red curve)); (b) test accuracy obtained considering device-to-device variations of the STDs; (c) test accuracy obtained using the curve with a larger input-current range (Figure 3.27, blue curve).

	Test accuracy (%)			
	Ideal	**$Conv_{DOR}$**	**$Conv_{DOR}$+FC_{DOR}**	**$Conv_{DOR}$+trainFC**
a	98.57	96.83	94.72	98.40
b		85.51	51.18	98.33
c		97.07	93.11	98.35

We also perform a study taking into account the device-to-device variation of the STDs by simulating random variations in the coefficient a' and c' of the parabola used in the DOR-based multiplication (Eq. (3.13)). Specifically, we added ±2.5% random variation to the coefficient to account for the nonideal behavior of the device. The results are summarized in Table 3.1 row b, for the cases described above. The test accuracy has drastically decreased; nonetheless, also in this is case, good performances are achieved with an additional fine-tuning the FC layer.

In addition, we perform the same analysis considering a large current region for the input (see Figure 3.27 (b)). The results are shown in Table 3.1 row c. It is important to highlight that an additional training can adapt weights to better match the specific characteristics of the DOR-based multiplication and can effectively correct the errors introduced by using this non-ideal multiplication and improve the accuracy of the computation.

As an example, Figure 3.32 shows some feature maps from a test image generated using ideal multiplication (top) and DOR-based multiplication (bottom).

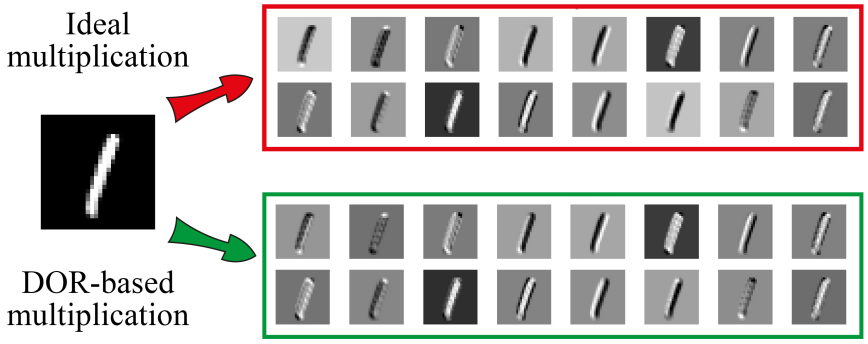

FIGURE 3.32: Feature maps of a test image. The images of the upper section are obtained with the convolutional layer with ideal multiplication, while in the lower section with DOR-based multiplication.

3.4.4.4.1 Dark knowledge analysis

We have also investigated the impact of the DOR-based multiplication on the extraction of the dark knowledge. As discussed in paragraph 3.3.2, to bring out the dark knowledge the temperature of the softmax has to be increased. In Figure 3.33 (a) the output probability of the most probable class for two representative

images is plotted as a function of temperature (similar results are obtained for other images) for ideal multiplication (solid line) and DOR-based multiplication (dashed line). Additionally, the inset shows the probability of the second-most-probable class as a function of temperature. These results suggest that the DOR-based multiplication does not significantly affect the extraction of dark knowledge. Figure 3.33 (b) provides a summary of the probability for all classes at $T = 10$. In addition, we can anticipate that the non-linear response achieved with the non-ideal DOR can introduce some features in the extraction of the dark knowledge which can be beneficial. However, this is a direction which has to be explored properly.

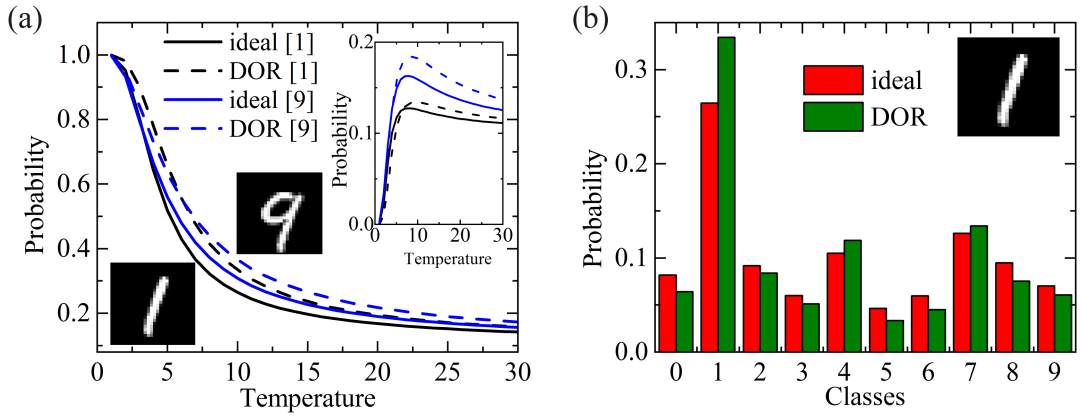

FIGURE 3.33: Dark knowledge extraction from CNN. (a) The probability of the most probable class as a function of the temperature coefficient for the two test images (black line for the image of a handwritten digit one, and blue line for the image of handwritten digit nine) obtained with a CNN based on ideal multiplication (solid lines) and a CNN with DOR-based multiplication for the convolutional layer and additional training of the FC layer (dashed lines). The graph in the inset shows the probability of the second-most-probable class as a function of temperature. (b) Probability of all classes for $T = 10$ for the represented image of a handwritten digit one, obtained from CNN based on ideal multiplication (red) and CNN with DOR-based multiplication applied to the convolutional layer with additional training of the FC layer (green).

3.4.5 Dynamical neural network based on spin transfer nano-oscillators

In ANNs, information propagates through layers with nonlinearity in between. This process can be also expressed as the time evolution of a dynamical system, therefore new paradigms of ANN models are based on dynamical systems and can be modeled as ordinary differential equations rather than nonlinear AFs. A significant difference between these approaches is the reduction of weight parameters. Here, we propose the STNOs as a physical dynamical system. If properly designed, STNOs can naturally emulate memory and intrinsic nonlinearity, making them a suitable building block for ANNs. Nonlinear classification is solved by properly tuning STNOs with few control signals, allowing the devices to project the initial configuration of states into regions of the phase space where states are linearly separable, therefore a single FC layer at the end of the model is enough to perform the classification. The training of the model is performed using optimal control theory. We test the proposed dynamical neuronal network with two types of datasets, and its reliability against the device-to-device variations is demonstrated. Although these systems are computationally expensive, their hardware implementation is straightforward and cost-effective. The main results of this study are published in Ref [220].

3.4.5.1 Introduction to neural networks with dynamical systems

We have already discussed the advantages and necessity of the hardware implementation of neural networks, highlighting the advantages of using spintronic devices. The implementation of physical neural networks based on the evolution of dynamical systems is a topic of great interest for reservoir computing and dynamical neural networks. For this purpose several solutions have already been proposed including optical and mechanical ones [221, 222].

It has been already demonstrated that, for such dynamical neural networks, the information propagation through multilayers can be expressed as a time evolution of dynamical systems [223, 224]. This idea was inspired by the simplified version of the forward propagation in residual neural networks (ResNet) [225]: $\boldsymbol{z}_{j+1} = \boldsymbol{z}_j + f(\boldsymbol{z}_j, \boldsymbol{w}_j)$ for $j = 0, \ldots N-1$, where N is the number of layers, z is the output of the hidden layer and f is the activation function. In other words,

this expression can be seen as an explicit Euler discretization of the nonlinear ordinary differential equation (ODE) $z_{t+1} = z_t + f(z_t, t, w)$, with $z(0) = z_0$, over a time $t = [0, T]$.

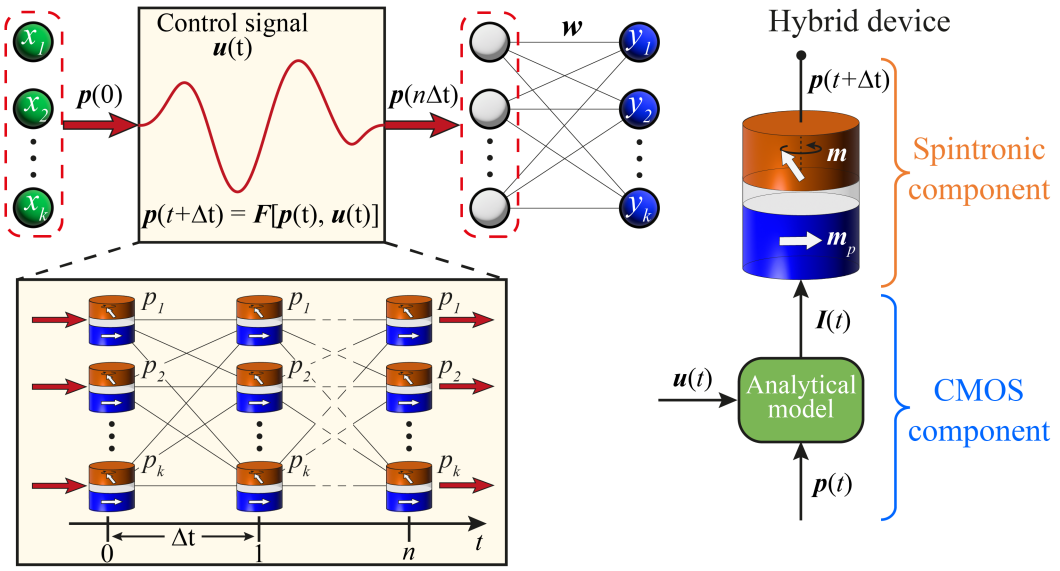

FIGURE 3.34: A schematic representation of the structure of the dynamical neural network. The dataset is encoded as the initial state of the input power $\boldsymbol{p}(0)$ of the dynamic system. The state at the end time $T_e = n\Delta t$, $\boldsymbol{p}(n\Delta t)$ is the input of a FC layer for classification tasks. The trainable parameters are the control signal $\boldsymbol{u}(t)$ and the weights $\mathbf{w}$. (Bottom-left) Schematic of a STNO-based virtual neural network. (Right) Basic hybrid unit of the neural network: a CMOS component reads the power and current, which after calculation is injected back into the STNO. The resistance of the STNO depends on the relative orientation between the FL and PL magnetization.

As physical dynamical neurons, we propose STNOs (see paragraph 1.8). These devices have unique features, such as low-power consumption, nanoscale size and tunability, which make them a reliable and versatile platform for implementing such dynamical neural networks [194, 198]. We consider the time evolution of the power emitted by an STNO, which is a monotonic function of the injected current, as experimentally shown in Ref. [226] and [51]. At each time step, the STNO's output power has a dynamical evolution in response to the input current, which can be considered as a linear combination of the power output from the previous step. Therefore, the information propagation through multiple layers is emulated by the stationary power of the STNOs at each time step. The

STNOs are supposed to be combined with CMOS technology for electrical operations such as reading the output power, calculating and injecting the current at each step. Figure 3.34 shows the proposed dynamical neural networks.

Training the network involves optimizing the control signals and weights of the FC layer, the one placed at the end of the model, to minimize the cost function. This can be done using backpropagation algorithms coupled with the optimal control theory developed in Ref. [222].

The learning algorithm is implemented as follows:

i) The input data $\boldsymbol{x}_k$ are encoded in the initial states of the power $\boldsymbol{p}(0)$; $k = 0, \ldots, K$, where K is the number of input data.

ii) Forward propagation. Integration of the dynamical system (we used Heun's method):

$$\frac{d\boldsymbol{p}(t)}{dt} = \boldsymbol{F}\left[\boldsymbol{p}(t),\ \boldsymbol{u}(t)\right] \tag{3.14}$$

starting from the initial state $\boldsymbol{p}(0) = \boldsymbol{x}_k$ to the final state $t = n\Delta t = Te$, $\boldsymbol{p}_k(T_e)$. $\boldsymbol{u}(t) = \left\{\boldsymbol{A}_{ij}, \boldsymbol{B}_i\right\}$ represents the control signals. $\boldsymbol{p}_k(T_e)$ represents the input of the FC layer that perform the linear separation: $z_{l,k} = \boldsymbol{w}_l \boldsymbol{p}_k(T_e) + \boldsymbol{w}_l^{bias}$ from $l = 0, \ldots, L-1$, where L is the number of output neurons, i.e., the number of categories of the dataset; $\boldsymbol{w}_l$ and $\boldsymbol{w}_l^{bias}$ are the trainable synaptic weights. For the final output, $\boldsymbol{y}_k$, the softmax function is applied.

iii) Compute the cost function, J, using the categorical cross-entropy loss, L.

iv) Backpropagation. The adjoint method developed for optimal control problems is applied to compute the gradient of the loss through the dynamical system. We define the adjoint time-dependent parameter $\boldsymbol{a}_k$, such that it satisfies the following equation: $\boldsymbol{a}_k(T_e) = \left.\dfrac{\partial \boldsymbol{L}_k}{\partial \boldsymbol{p}_k}\right|_{t=T_e}$ for $t = T_e$, $\dfrac{\partial \boldsymbol{a}_k}{dt} = -\boldsymbol{a}_k \dfrac{\partial \boldsymbol{F}_k}{\partial \boldsymbol{a}_k}$ for $0 < t < T_e$. The adjoint is integrated in backward direction from $t = T_e$ to $t = 0$, where $\left.\dfrac{\partial \boldsymbol{L}_k}{\partial \boldsymbol{p}_k}\right|_{t=T_e} = \dfrac{\partial \boldsymbol{L}_k}{\partial \boldsymbol{z}_k}\dfrac{\partial \boldsymbol{z}_k}{\partial \boldsymbol{p}_k} = \dfrac{\partial \boldsymbol{L}_k}{\partial \boldsymbol{z}_k}\boldsymbol{w}$.

v) Compute the variations:

- $\delta \boldsymbol{w} = -\alpha_w \dfrac{\partial \boldsymbol{J}}{\partial \boldsymbol{w}} = -\alpha_w \sum_k \dfrac{\partial \boldsymbol{L}_k}{\partial \boldsymbol{z}_k}\dfrac{\partial \boldsymbol{z}_k}{\partial \boldsymbol{w}} = -\alpha_w \sum_k \dfrac{\partial \boldsymbol{L}_k}{\partial \boldsymbol{z}_k}\boldsymbol{p}_k(T_e)$

- $\delta \boldsymbol{w}^b = -\alpha_w \dfrac{\partial J}{\partial \boldsymbol{w}^b} = -\alpha_w \sum_k \dfrac{\partial \boldsymbol{L}_k}{\partial \boldsymbol{z}_k} \dfrac{\partial \boldsymbol{z}_k}{\partial \boldsymbol{w}^b} = -\alpha_w \sum_k \dfrac{\partial \boldsymbol{L}_k}{\partial \boldsymbol{z}_k}$
- $\delta \boldsymbol{u}(t) = -\alpha_u \sum_k \left(\boldsymbol{p}_k(t) \dfrac{\partial \boldsymbol{F}_k}{\partial \boldsymbol{u}} \right)$

where α_w and α_u are the learning rates.

vi) Update control signals $\boldsymbol{u}(t) \leftarrow \boldsymbol{u}(t) + \delta \boldsymbol{u}(t)$ and weights $\boldsymbol{w} \leftarrow \boldsymbol{w} + \delta \boldsymbol{w}$.

We use this network to solve simple classification tasks and to demonstrate the effectiveness and feasibility of such approach. We aim to test experimental implementations in the future.

3.4.5.2 Dynamical neural networks based on STNOs

3.4.5.2.1 Functional response of STNOs

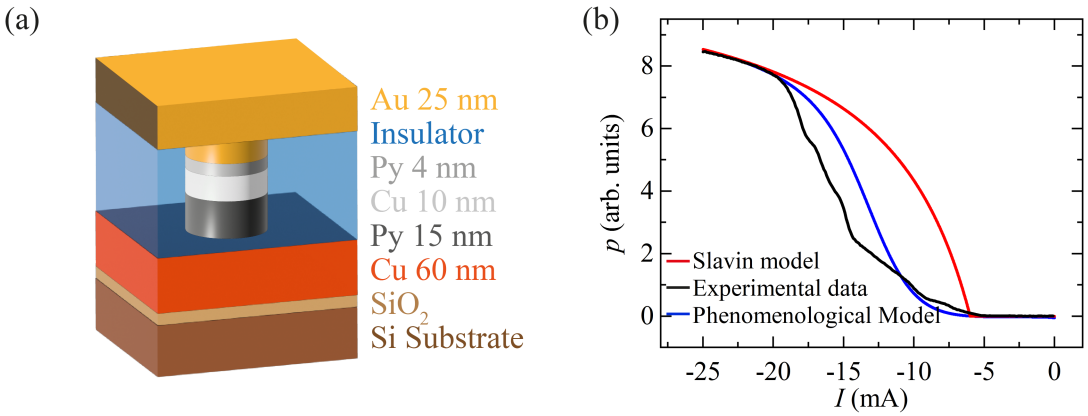

FIGURE 3.35: Structure of the STNO used in the experiment performed in Ref. [226]. (b) A comparison of the power vs current relationship: experimental data from the Ref. [226] measured for an applied perpendicular field of 10 kOe (black line); model described in Eq. (3.15) developed in Ref. [47] (red line) and phenomenological model described in Eq. (3.16) (blue line). Both with $I_{th} = -6$ mA and $Q = 0.1$.

The first set of experimental data of STNOs used for the calculation in this work are from Ref. [226]. Figure 3.35 (a) shows the device structure: two ferromagnetic layers of permalloy (Py = $Ni_{80}Fe_{20}$) separated by a nonmagnetic layer of Copper (Cu). The lower, thicker Py layer has a fixed magnetization direction, while the upper Py layer has a free magnetization that moves in the presence of external

torques. As already explained in paragraph 1.6.1, the electrical current is spin-polarized by the fixed layer magnetization and exerts a spin-transfer torque on the FL magnetization of the adjacent layer. The unitary magnetization of the FL in presence of the STT follows the dynamic described by the LLGS equation (Eq. 1.38).

If the electrical current I is above a certain threshold I_{th}, it triggers an auto-oscillation of the FL magnetization [47, 53]. In the auto-oscillation regime, the magnetization rotates maintaining a fixed component along a direction defined by the effective magnetic field, $\boldsymbol{h}_{eff}$, and the polarizer vector, $\boldsymbol{m}_p$. The power emitted is proportional to this fixed component, making it the key component to obtain the STNO's output power. The power can be measured electrically [227–229]. This power has also been already observed experimentally [226]. In addition, a well-established analytical theory has been developed by Slavin *et al*. [47] (paragraph 1.8.1.1), where the stationary power of an STNO with injected current I is given by (3.15):

$$p\left(I\right) = \frac{I - I_{th}}{I + QI_{th}} \tag{3.15}$$

where Q quantifies the nonlinearity of the system. However, this analytical model does not fit well the exponential tail near the critical current shown by the real data [226] (see Figure 3.35(b)). Therefore, based on the Slavin model [47], we propose a phenomenological model given by (3.16):

$$p\left(I\right) = \frac{1 + \tanh\left(aI - b\right)}{2} \frac{I - I_{th}}{I + QI_{th}} \tag{3.16}$$

where the added pre-factor function is depending on the fitting parameters a and b, that are directly identified from the experimental data to correctly match the behavior close to the critical current. Different expressions can be used as pre-factor functions, according to the power vs current characteristic of the STNO. The analytical model of Eq. (3.15) fits well with many experimental data of STNO published in literature [46, 50, 230, 231]. The pre-factor introduced here is strictly a way to improve the fitting of experimental data and can be implemented in hardware as a simple circuit coupled with the STNO. State-of-art STNOs further improve the scalability of the dynamical neural network as they require lower currents and no applied external magnetic field [51, 231].

Figure 3.36 shows the experimental power as a function of the injected current emitted by the STNO in Ref. [51] (blue dots), which are the second set of data used. The data are well-fitted by the phenomenological model, Eq. (3.16), (black dots). The device is an MTJ with magnetic stacks of CoFeB, (in-plane polarizer and out-ot-plane FL magnetization), separated by a tunnel barrier of MgO, as shown in Figure 3.36.

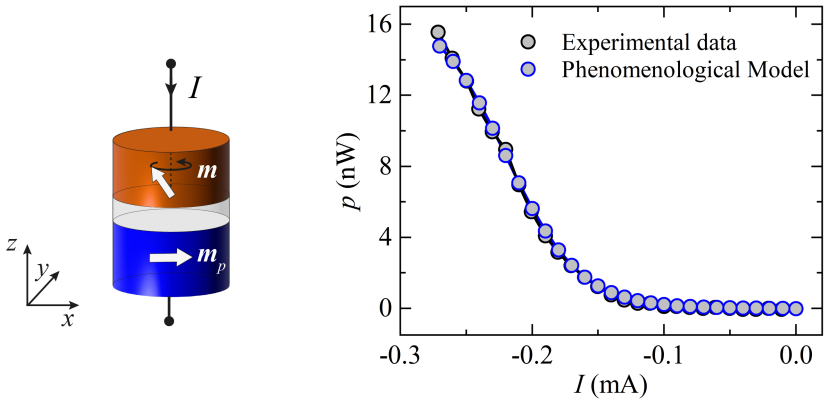

FIGURE 3.36: A comparison between the experimental power vs current data from Ref. [51] (black dots) and the fitted phenomenological model from Eq. (3.16) (blue dots), with $I_{th} = -10$ µA, and $Q = 0.3$. The inset shows the configuration of the STNO used to obtain experimental data.

Experiments show microwave emissions with large output power, peak on the order of 10 nW, excited at ultra-low currents, $I_{th} \approx -10$ µA, and no external magnetic fields. Thinner free layers have also been shown to produce even higher power outputs at lower currents. Moreover, the full experimental results reveal a greater nonlinearity of the emitted power curve, which can increase the performance of the dynamical neural network while decreasing the computation costs in terms of energy for larger problems.

3.4.5.2.2 Dynamical neuron

In the dynamical neural network, the information is encoded in the stationary power output of the k STNOs at each time step, $\boldsymbol{p}(t) = \{p_1(t), \ldots, p_k(t)\}$. The time evolution of the power is governed by the following iterative equation (3.17):

$$p_i(t + \Delta t) = p(I_i(\boldsymbol{p}(t))) \tag{3.17}$$

where the input current of the i-th STNO, I_i, is a linear function of the power output of all the STNOs in the previous time step (3.18):

$$I_i\left(\boldsymbol{p}\left(t\right)\right) = \left(\sum_{j=1}^{k} A_{ij}\left(t\right) p_j\left(t\right) + B_i\left(t\right)\right)^2 \tag{3.18}$$

where the matrix $\boldsymbol{A}\left(t\right)$ and vector $\boldsymbol{B}\left(t\right)$ correspond to controllable external signals (current or field). The input data is mapped to the initial condition of the output power from a different STNOs. For instance, given an image consisting of continuous pixel values, each pixel is linked to an STNO. The pixel value corresponds to a normalized value of the power output of the chosen STNO. The system evolves over time controlled by the external parameters $\boldsymbol{A}\left(t\right)$ and $\boldsymbol{B}\left(t\right)$. At the final time T_e, the initial states are disentangled in different regions of the phase space and become linearly separable, hence easy to classify with a single FC layer. To achieve these results, the physical external parameters and weights of the model are optimized through the minimization of the loss function, as described in the learning algorithm.

3.4.5.2.3 Results

We evaluate the performance of the STNO-based dynamical neural networks on two simple classifications tasks. In both tests, we consider identical STNOs with output power, Eq. (3.16), given by $a = 4$, $b = 5$, $I_{th} = 1$, and $Q = 2$.

First, we solve the binary classification problem given by data spread in a spiral pattern, where each point is labeled with one of two categories, as already presented for an optical-based solution [222]. This dataset has 1000 points: 80% of the data is used for training the ANNs and 20% for testing it (in this study we treat validation as a test). We mapped the two coordinates of the points to the power output of two STNOs. The classification accuracy is 93.88% for the training, and 92.00% in test. Figure 3.37 (a) shows the results of the binary classification. Figure 3.37 (b)-(d) show the distribution of the data at the final state, $\boldsymbol{p}\left(T_e\right)$, for three different epochs during the training of the network. As we can see in Figure 3.37 (d), at the end of the training the spiral dataset is disentangled and becomes linearly separable.

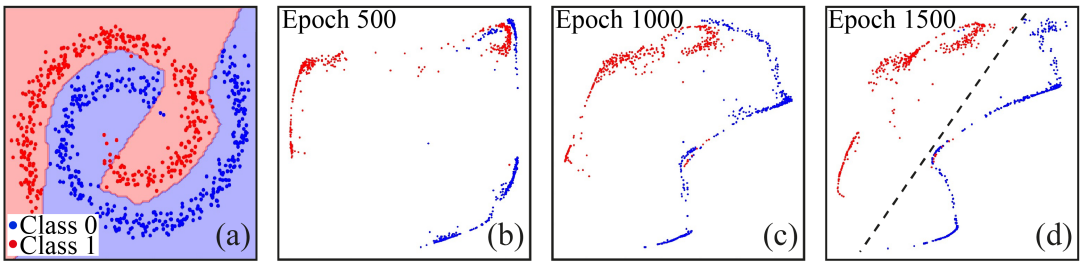

FIGURE 3.37: (a) Spiral dataset and results of binary classification into two regions indicated by red and blue colors. (b)-(d) Configuration of the states at the end time, $\boldsymbol{p}(T_e)$, for three different epochs during the training. (d) Configuration of the states at the last training epoch, where the data becomes linearly separable; the dashed line represents the decision boundary to separate the two regions.

Additionally, we evaluate the reliability of the proposed network against device-to-device variations. To do this, we have used the trained network employed for Figure 3.37 and, to take into account the aforementioned variations, we consider a different value of the parameter a from Eq. (3.16) for each device. This value is sampled from a normal distribution with mean $\mu = 4$ (ideal parameter). Figure 3.38 shows the average accuracy of the test over 10000 runs, plotted against the standard deviation used to sample the a parameters for each device. The network maintains high accuracy for deviations up to $\sigma = 0.25$. Consequently, the proposed network is robust against device-to-device variations.

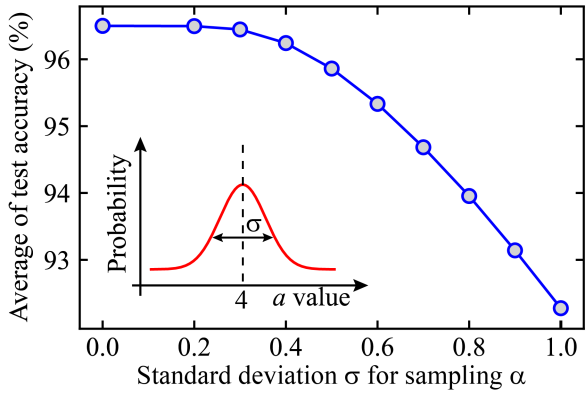

FIGURE 3.38: Average of test accuracy over 10000 runs, as a function of the standard deviation (σ) of the normal distribution from which the parameter a in Eq. (3.16) were sampled. The inset shows the normal distribution of the possible a values and indicated the σ.

In the second case, we evaluate the performance of the network in the multiclass classification of the "DIGIT" dataset. The dataset consists of $8 \times 8 = 64$ pixel gray scale images of handwritten digits from 0 to 9, for a total of 1797 images. The values for each of the 64 pixels were mapped to the power output of 64 STNOs. As in the previous case, we divided the dataset into two: 80% of the data is used for the training of the network and 20% for testing. The accuracy obtained during training is 99.16% while the accuracy of the test set is 97.5%. Figure 3.39 shows the accuracy and loss for the training and the test set, as a function of the number of epochs.

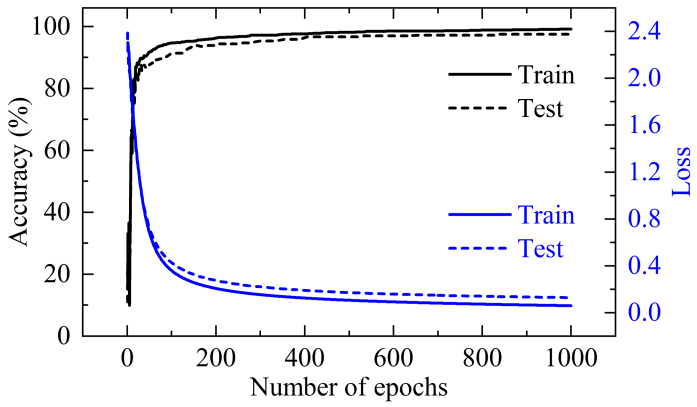

FIGURE 3.39: Accuracy and loss as a function of number of epochs for training and testing of the neural networks, on the "DIGIT" dataset. The solid (dashed) blue line corresponds to the train (validation) loss.

Our results show that a phenomenological model of STNO can be used to design spintronic dynamical neurons and dynamical ANNs. Those promising results achieved for simple datasets are the proof-of-concept of the idea and we believe they may inspire future hardware implementations of this network.

3.5 Conclusions

We have introduced the fundamental concepts of artificial neural networks, highlighting two prominent challenges: the escalating energy demands for ANN training and the von Neumann bottleneck. Neuromorphic spintronics emerges as a potential solution, leveraging spintronic devices for neuromorphic computing. We have discussed the state-of-the-art and explored the applications of MTJs

in neuromorphic spintronic systems. Specifically, we have demonstrated the use of MTJs as neurons, addressing the reliability of ANNs by accounting for device-to-device variations.

Furthermore, we have demonstrated the use of STDs for analog multiplication, in both image processing and CNNs.

In the last part of this section, we propose using STNOs to implement a dynamical neural network. This marks a step forward in exploring new and dynamic approaches to neural network architectures.

Chapter 4

Probabilistic computing

Effective optimization tools are very important for many problems in biomedical engineering. In particular, combinatorial optimization, which aims to find optimal solutions in problems with a finite, discrete set of configurations, can impact the design of clinical trials for the organization of the patients' groups and for searching the optimal dose of drugs. In addition, combinatorial optimization provides a path to systematically address the complexity and scale of many other problems in biomedical engineering, which range from advancements in the research (e.g. drug discovery, genomics), diagnosis (medical imaging analysis), treatment (optimization of the resources), etc.. The integration of combinatorial optimization tools with cutting-edge artificial intelligence presents a very powerful solution to face biomedical problems that were intractable up to recent years. Among all the potential combinatorial optimization tools, this thesis focuses on Ising machines, which are becoming increasingly popular as efficient and hardware-friendly solvers for combinatorial optimization problems. These machines are designed to search for absolute or approximate ground states of the Hamiltonians of Ising models by using proper annealing processes. One approach to solving Ising models is probabilistic computing with p-bits (PC), where the traditional bits are replaced by bistable tunable stochastic bits, which can be naturally implemented in hardware and, in particular, with MTJs. The first part of this chapter provides an introduction to the Ising model formalism and combinatorial optimization problems. The second part presents the PC paradigm and describes its implementation in a homemade C/CUDA solver (PetaIsing). The chapter concludes with results related to MTJ-based PC.

4.1 Ising model

The Ising model is a mathematical model that was originally designed to study phase transitions in ferromagnetic materials [232]. Its origins date back to 1920, when Wilhelm Lenz came up with the idea. Later, his student Ernest Ising solved the one-dimensional model. The model became the subject of interest from physicists after Lars Onsager analytically solved a two-dimensional version in 1944, revealing the phase transition phenomenon within ferromagnetic materials [233].

The ferromagnetic material can be modelled as a lattice with N sites, each site hosting an atom of the magnetic material. Each atom has an intrinsic magnetic moment, called spin, which can have either "up" or "down" direction, as illustrated in Figure 4.1 (a). An independent variable σ_i is assigned to each lattice site $i = 1, \dots N$. This is a binary variable representing the discretized state of the spin, $\sigma_i \in \{-1, +1\}$. An assignment of spins $(\sigma_1, \sigma_2, \dots, \sigma_N)$ to each lattice site is referred to as spin configuration σ of the system [234].

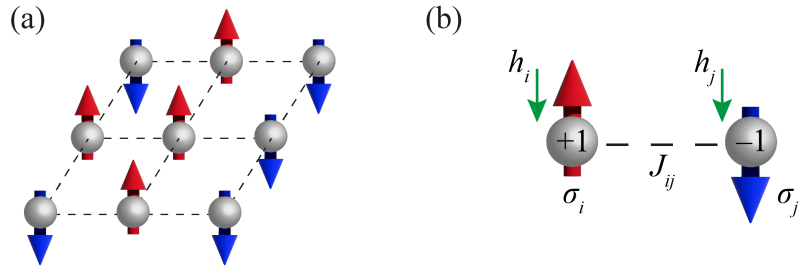

FIGURE 4.1: (a) A schematic representation of a two-dimensional lattice with four sites, using spins up or down to model a ferromagnetic material in the Ising model. (b) A schematic representation of neighboring spins (σ_i, σ_j) with their coupling J_{ij} and external field (h_i, h_j).

In mathematical physics, the Hamiltonian represents the total energy of a system. For the Ising model, the formulation of the Hamiltonian relies on the theoretical assumption that only short-range, "nearest-neighbor" interactions and interactions with an external field contribute to the energy of the system [234]. For each spin configuration, the Hamiltonian is:

$$H(\sigma) = -\sum_{\langle i,j \rangle} J_{ij}\sigma_i\sigma_j - \sum_i h_i\sigma_i \tag{4.1}$$

where the first sum is over all pairs of spins that are nearest neighbors in the lattice, and the second sum is over all the spins. The parameter J_{ij} corresponds to the coupling between nearest-neighbor sites $i, j \in [1, N]$, and the parameter h_i is the external field applied to each site $i \in [1, N]$, as illustrated in Figure 4.1 (b). For a ferromagnet, the coupling J_{ij} is positive, so that a magnetized configuration, where nearest-neighbor pairs have parallel spins $\sigma_i = \sigma_j$, has a lower energy compared to a non-magnetized configuration. The h_i acts as an external magnetic field which tends to align the spins in its direction, favoring lower energy levels.

In a generalized version of the Ising model, these interaction parameters can assume positive, negative, or zero values, representing ferromagnetic, antiferromagnetic, and non-interactions, respectively. The interactions extend beyond neighboring spins; instead, they are all-to-all. This implies that each spin within the system is interconnected with every other spin (provided that these interactions also include zero coupling ones). The Hamiltonian, which reflects the total energy of the system, is consequently redefined to capture this comprehensive interaction scheme:

$$H(\boldsymbol{\sigma}) = -\sum_{i<j} J_{ij}\sigma_i\sigma_j - \sum_i h_i\sigma_i \tag{4.2}$$

The interactions between spins can be collectively represented by a symmetric square matrix $\mathbf{J}$, and the external field by a bias vector $\mathbf{h}$.

The possible spin configurations of a system with N spins are 2^N. For a given temperature T of the system, the probability of being in a particular spin configuration σ can be described by the statistic physics and follows the Boltzmann distribution, which is given by the formula:

$$P_\beta(\boldsymbol{\sigma}) = \frac{e^{-\beta H(\sigma)}}{\sum_\sigma e^{-\beta H(\sigma)}} \tag{4.3}$$

where β is the inverse temperature $\beta = (k_B T)^{-1}$, where k_B is the Boltzmann's constant. The negative sign biases the probability toward states with lower energy. A low value of β, indicative to a high temperature, tends to equalize the distribution of all configurations. Conversely, a high value of β, indicative of low temperature, amplifies the probability of the lowest energy states, also called ground states (GS) [234].

The evolution of the system toward the ground state is governed by an "update equation" of the spin states. As the time approaches infinity, the probability distribution of the systems follows the Boltzmann distribution. Each computational paradigm is characterized by its update equation.

Any approach design to find the absolute or approximate ground states of an Ising model is called Ising machine.

4.2 Complexity classes

Since the 1980s, the Ising model has emerged as an efficient method for solving combinatorial optimization problems (COPs) [235–237]. COPs are problems that become harder and harder to solve as the instances become larger for deterministic methods. The term "deterministic" commonly implies the absence of choice. In a deterministic event, the outcome can be precisely predicted based on prior circumstances. Conversely, the term "non-deterministic" is used to describe an event where the outcome is relies on the choices made by its participants, therefore it cannot be accurately predicted [238]. Figure 4.2 shows the difference between deterministic and non-deterministic algorithms. In a deterministic algorithm, for a given input, the output remains always the same (Figure 4.2 (a)). On the contrary, in a non-deterministic algorithm, for the same input there are several possible outputs, so there is a choice point at which one output is selected (see Figure 4.2 (b)-left). Consequently, if the same input is provided in different algorithm execution, the output may differ. This process can be represented as a "tree of choices", where each node is a choice point, leading to a different path from the root to the leaf of the tree (see Figure 4.2 (b)-right), while in a deterministic algorithm the path from the root to the leaf of the tree is always the same (see Figure 4.2 (a)-right).

The aforementioned classification, applied to Turing machines, serves as a fundamental framework for categorizing algorithmic complexity.

A Turing machine is a mathematical model of computation introduced by Alan Turing in 1936 [239]. This abstract machine manipulates symbols on a strip of tape according to a set of rules, and it is able to implement any computer algorithm.

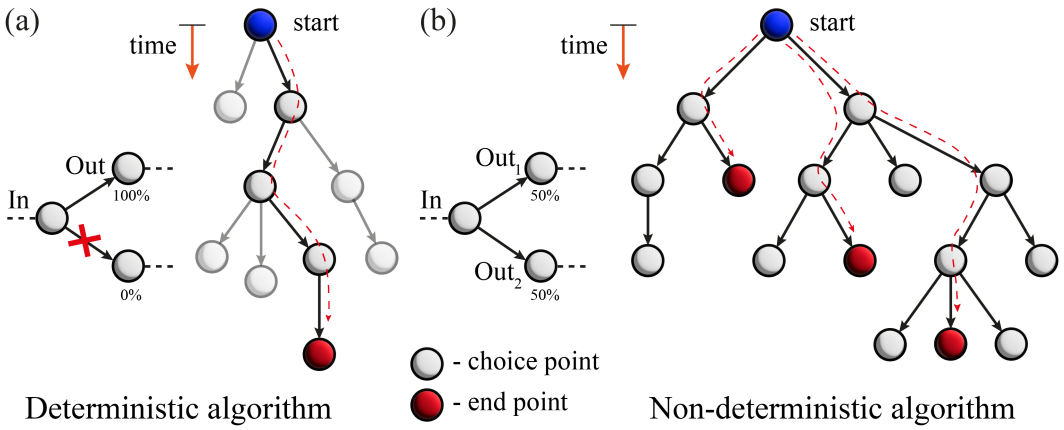

FIGURE 4.2: Comparison of deterministic and non-deterministic algorithms. (a) Deterministic algorithm: the output remains the same for a given input. (b) Non-deterministic algorithm: multiple outputs are possible for a given input, and the choice point selects one. A set of choice points forms a "tree of choices", and each execution of the algorithm may follow a different path from the root to the leaf of the tree.

The complexity of an algorithm, that is, a set of instructions used to solve a problem, usually refers to the computation time as a function of the size of the instances of the problem. Sets of problems that share common characteristics are grouped into what is called complexity class. There are several types of complexity classes, some of which are:

- **P** (polynomial time): it is the class of problems that can be solved by a deterministic Turing machine in polynomial time.
- **NP** (nondeterministic polynomial time): it is the class of problems that can be solved by a non-deterministic Turing machine in polynomial time and the solutions of the problems are verifiable by a deterministic Turing machine in polynomial time.
- **NP-complete**: it is the classes of problems that are in NP and such that every problem in NP can be mapped (reduced) to any NP-complete problem in polynomial time. In other words, solving an NP-complete problem in polynomial time would imply the ability to solve any NP problem in polynomial time.
- **NP-hard**: it is the class of problems such that every problem in NP can be mapped (reduced) to any NP-complete problem in polynomial time. An

NP-hard problem that is in NP is, thus, also NP-complete. NP-hard problems that are not in NP are not verifiable by a deterministic Turing machine in polynomial time.

Figure 4.3 shows the Euler diagram detailing the relationship between P, NP, NP-complete and NP-hard. In particular, NP contains P and intersects with NP-hard, and this intersection is the NP-complete class.

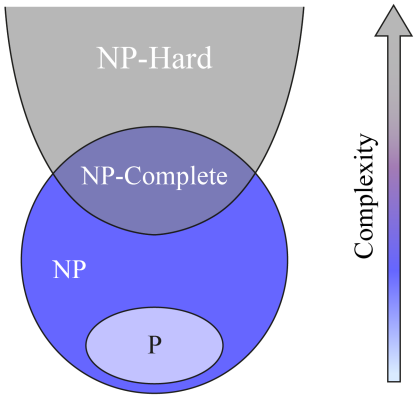

FIGURE 4.3: Euler diagram of complexity classes for P, NP, NP-complete and NP-hard set of problem.

4.3 Invertible logic and NP-hard problems

Most COPs are NP-hard problems. Some examples are the maximum cut problem (Max-Cut), the maximum satisfiability problem (Max-SAT), and planted Ising. When these problems can be described by a logic circuit, it is possible to have a way to map them in the Ising model involving the use of invertible logic [240–242]. Invertible logic is the concept of designing an Ising model to emulate a Boolean logic circuit with the flexibility to operate bidirectionally. The building blocks of this encoding paradigm are the invertible logic gates [242]. The truth table of a Boolean logic operation corresponds to the ground states of these Ising models. The Ising elements ($\mathbf{J}$ and $\mathbf{h}$) are chosen in such a way that the configurations of the spins lead to the truth tables states. As an example, let us focus on the AND logic gate. Figure 4.4 shows the truth table (a) and the Ising elements (b) of the AND gate, with two spins for the input and one for the output. The possible

spin configurations are 2^3, but 4 states are the spin configurations that minimize the energy describing the AND truth table, as shown from the probability distribution of the states shown in the Figure 4.4 (c) with orange bars, where each of these states is equally probable. The main point of invertible gates is that they can be used in reverse mode. A way to program this behaviour is by increasing or decreasing the bias of a specific output spin, in a process called clamping. The clamping of the output leads to a change of the energy landscape toward the input spin configurations compatible with the fixed output. Figure 4.4 (c) shows this process for the AND gate: for a low value of the clamping, which corresponds to $\sigma_C = -1$, there are 3 equally probable spin configurations (000, 010, 100) (green bars), while for a high value, meaning $\sigma_C = +1$, the most explored spin configurations is only $\sigma_A = \sigma_B = 1$ (purple bars) [241].

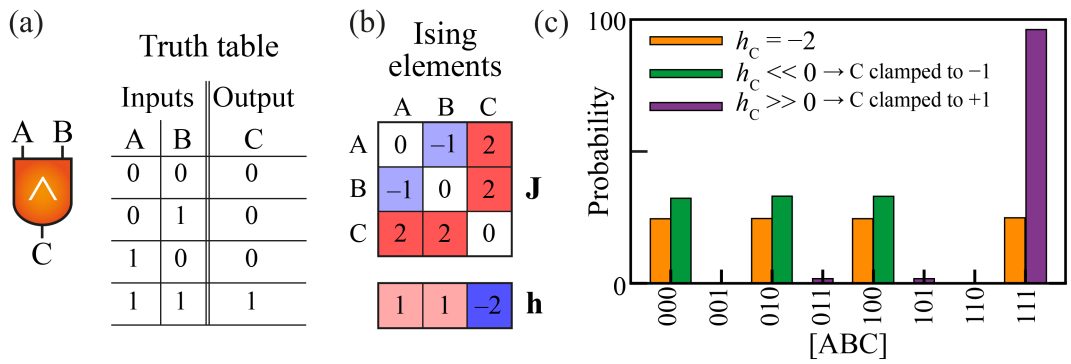

FIGURE 4.4: Logic gate AND. (a) Circuit symbol and truth table (b) Ising elements **J** and **h**. (c) Probability distribution of the Ising model of AND. The orange bars represent the probability of the unclamped AND, the green bars correspond to spin configurations under a positive clamp of the output, and the purple bars for a negative clamp of the output.

The same considerations apply to all logic gates and logic circuits in this encoding paradigm in general.

We wish to stress that by appropriately combining the Ising elements of several logic gates it is possible to map COP described by logic circuits in the Ising model [242, 243]. This thesis delves into the study of several problems, which are introduced in the next sections.

4.3.1 Maximum cut problem (Max-Cut)

Given an undirected graph, the Max-Cut problem aims to group the vertices of the graph into two partitions such that the number of the edges between them is as large as possible [244]. This problem has an important impact in logistic problems. Figure 4.5 (a) shows a simple example of a graph, where some of the four vertices are connected with edges. In this case, each edge is characterized by a weight, which describes the coupling strength between the two connected vertices. In fact, a more generalized version of the problem is the weighted Max-Cut which aims to maximize the total weight of the edges between the two partitions, rather the number of edges.

The Max-Cut problem is NP-hard and can be mapped in polynomial time into an Ising model where each vertex of the graph is an Ising spin σ_i, and the connections between vertices define the coupling J_{ij}. The spin value encodes the group to which a vertex belongs. Directly connected vertices in different groups $(\sigma_i \neq \sigma_j)$ have to lead to a reduction of energy, and this is achieved by assigning a negative coupling between them $(H(\boldsymbol{\sigma}) = -J_{ij}\sigma_i\sigma_j)$. Figure 4.5 (b) shows the solution of the graph in (a) mapped into the Ising model, where the vertices are separated into two partitions that maximize the cut value. Figure 4.5 (c) shows the corresponding Ising elements.

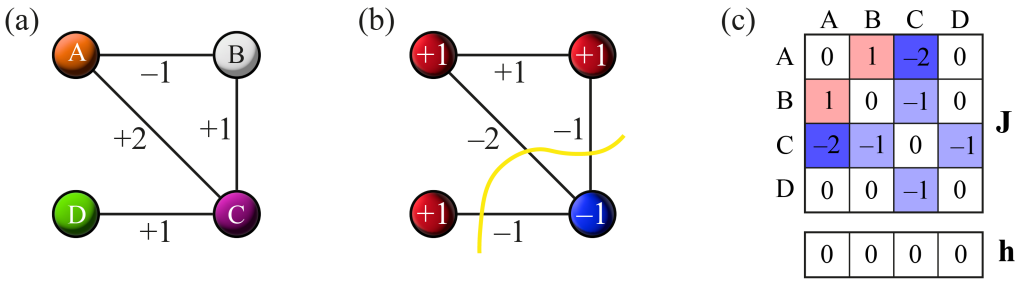

FIGURE 4.5: Max-Cut problem illustration. (a) A schematic illustration of a weighted graph with four vertices. (b) The graph in (a) is encoded in an Ising model in which the spins (vertices) are separated into two groups. This leads to maximizing the sum of the weights of the edges connecting the partitions. The optimal value of the cut is 4, highlighted with a solid yellow line. (c) Ising elements **J** and **h** of the graph in (b).

4.3.2 Planted Ising

Planed Ising problems are constructed based on predetermined ground-state configurations, known as planted solutions, making them particularly suitable for benchmarking purposes [245]. The basic idea involves generating several small Hamiltonians with known ground states and then summing them together to create a nontrivial problem with a known solution [243]. This process allows the generations of several instances of the problems with different size and difficulty. Figure 4.6 illustrates a graph with Pegasus topology [246], a lattice employed to generate instances of problems solved in this thesis. Planted Ising can be also created on cubic graphs and Zephyr topologies.

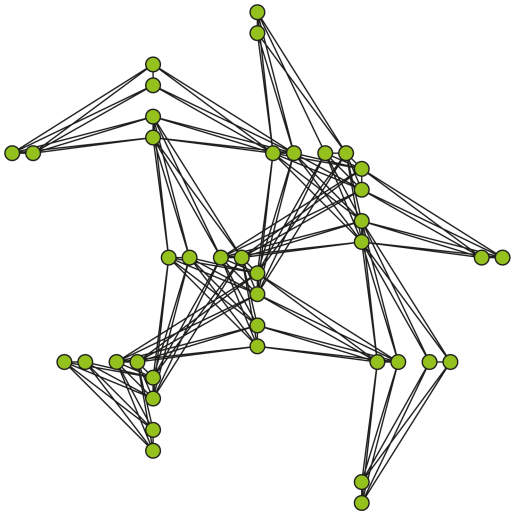

FIGURE 4.6: An example of graph with Pegasus topology.

4.3.3 Maximum satisfiability problem (Max-SAT)

Max-SAT is an optimization problem for propositional formulas in conjunctive normal form (CNF). In CNF, a propositional formula is a conjunction of clauses, where each clause is a disjunction of literals. For a Boolean variable x, a literal is defined as x or its negation -x. The goal of Max-SAT is to find an assignment of the variables that maximizes the number of satisfied clauses [247]. In this thesis, we measure the "solution cost", which represents the number of unsatisfied clauses.

A more general version of Max-SAT is the weighted Max-SAT, where each clause is assigned a non-negative weight (in standard Max-SAT this weight is one), and the goal is to find an assignment that maximizes the combined weight of the satisfied clauses.

A Max-SAT instance can be represented as a logic circuit, where literals in a clause are connected by OR gates, and all clauses are connected by AND gates, as illustrated in Figure 4.7. The regular gates are replaced with their equivalent invertible gates, and the instance is then mapped into the Ising model elements [242].

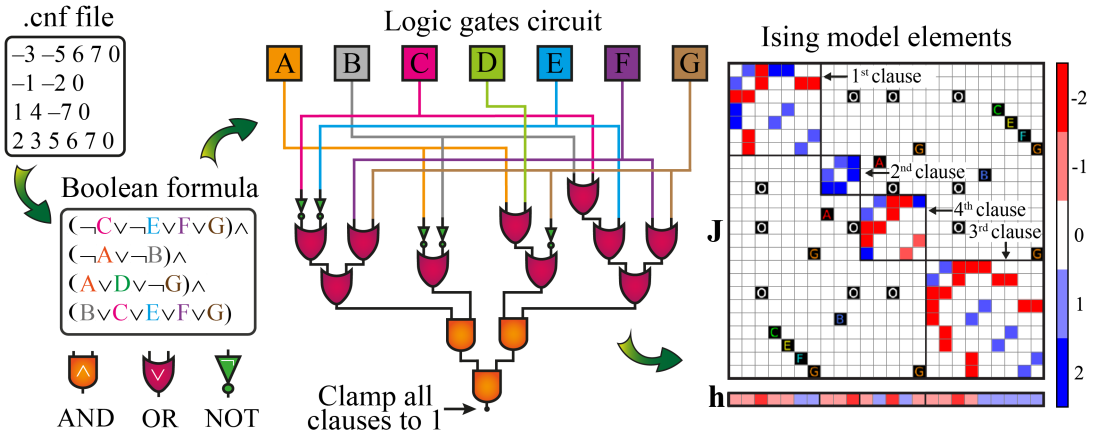

FIGURE 4.7: A schematic representation of the Max-SAT encoding into an Ising model. A toy Max-SAT instance in its ".cnf" file format is converter into a logical representation, with corresponding logic gate circuit that can be mapped onto the Ising model elements [242].

4.3.4 Integer factorization

The integer factorization problem is the decomposition of a positive integer C into a product of integers, known as factors, C=A·B. For a non-trivial solution, the factors must be greater than 1. Of particular interest is the prime factorization, where A and B are prime numbers, forming the foundation of cryptography [248]. Despite various deterministic algorithms designed to address this problem, achieving scaling for large numbers of bits remains elusive.

This problem can be managed by IMs by using invertible logic gates to encode the problem [249]. Figure 4.8 shows an example of a circuit operating in reverse

mode, clamping the number to be factorized as the input of the IM, which attempts to identify the prime integer factors.

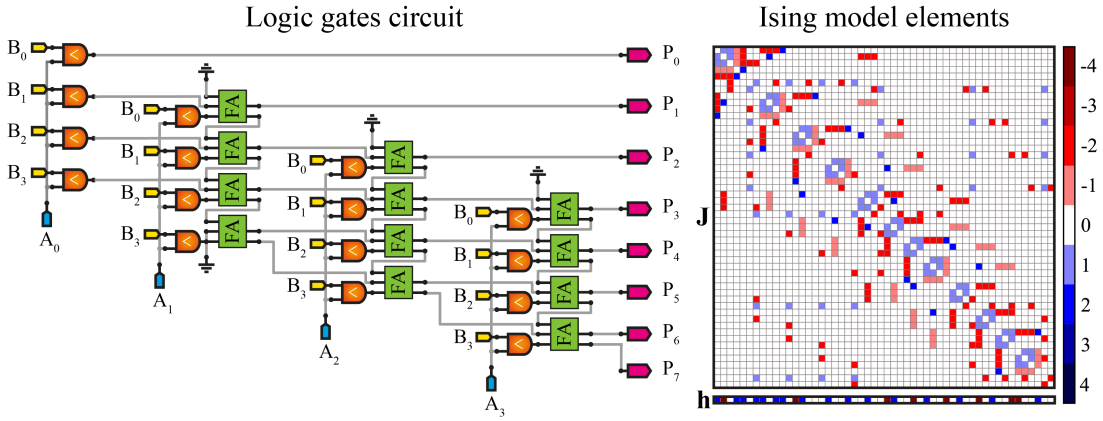

FIGURE 4.8: (a) A schematic representation of logic gates circuit to solve 8 bits integer factorization with an IM operating in reverse mode. (b) Ising model elements **J** and **h**.

4.4 Hardware implementation of Ising machines

Ising machines are hardware solvers designed to find the absolute or approximate ground state of the Ising model. Over the years, several hardware implementations of the Ising model have been investigated, involving both digital hardware accelerators and analog computing approaches. Mohseni *et al*. in Ref. [244], provides a comprehensive review of IMs as hardware solvers for COPs.

Figure 4.9 summarizes some physical implementation of IMs (from [244]), including magnetic devices [240, 242, 243], memristors [250], electrical oscillators [251], single atoms [252] and optics [253]. For instance, in oscillator-based IMs, each Ising spin σ_i is encoded in the phase of an oscillator's dynamics. In optical systems, this corresponds to the phase of light. Memristor crossbars are used to perform an analog matrix multiplication of the Ising matrix. A stochastic MTJ can be used to replace a conventional bit with a probabilistic bit, which is the building block for a type of probabilistic computing approach for solving COPs discussed in the paragraph 4.6.

Digital-electronic approaches of IMs include hardware accelerators using CMOS applications [254, 255], FPGAs [256] and GPUs [257–259].

Classical IM paradigms are commonly benchmarked against quantum computing, i.e. quantum annealers. It is important to notice that quantum hardware development requires a lot of resources, facing challenges such as decoherence, error control, limited connectivity, and need for cryogenic temperatures. Nowadays, D-Wave System has emerged as a pioneering company able to implement systems with a large number of quantum bits (qubits) for quantum annealers [244, 260]. Given the key role of quantum effects in D-Wave machine [261], algorithms inspired by quantum system have been developed for IMs.

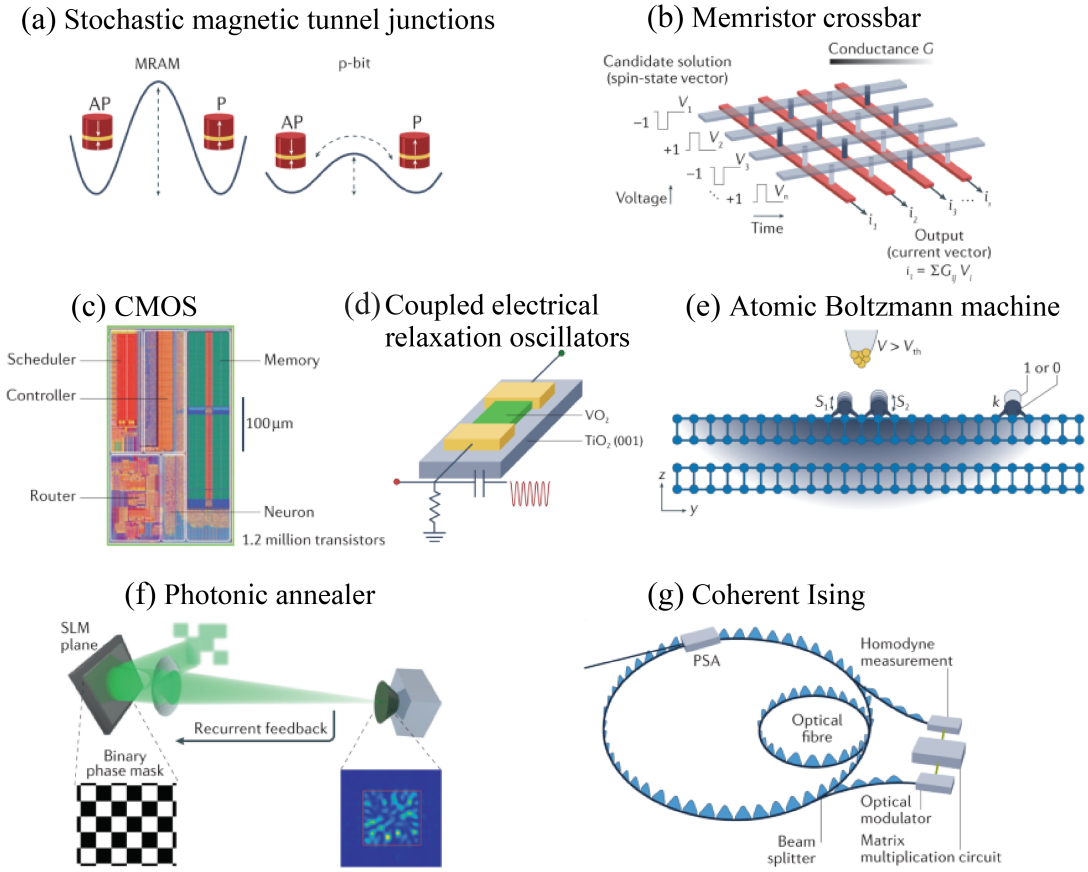

FIGURE 4.9: Summary of technologies used to implement IMs [244]. (a) Stochastic MTJ illustrating the difference between conventional MRAM and the probabilistic bit [240]. (b) Memristor crossbar array for matrix-vector multiplication [250]. (c) CMOS chip implementing a 1 million spin Boltzmann machine [262]. (d) Metal-insulator VO_2 system realizing coupled electrical oscillators [251]. (e) Co atoms on the surface of black phosphorus interacting with a scanning tunneling microscope to implement a Boltzmann machine [252]. (f) Spatial light modulator-based photonic annealer [253]. (g) Coherent Ising machine measurement-feedback loop [263].

4.5 Energy minimization algorithms

One of the crucial aspects for an effective approach for solving an Ising model is the choice of the energy minimization algorithm. As discussed in paragraph 4.1, the inverse temperature β plays a key role in determining the probability distribution of the states. Consequently, many algorithms tune this parameter to find the spin configuration with lowest energy. Another important hyper-parameter is the number of copies of the system (known as replicas) that are randomly initialized. The most basic algorithm is the sampling, but more sophisticated algorithms have been developed, such as simulated annealing, parallel tempering and simulated quantum annealing, all of which are discussed in the following sections.

4.5.1 Sampling

The system evolves at a fixed temperature, as illustrated in Figure 4.10. The choice of β is crucial; a low value fails to encourage the system to reside in energy minima; a high value does not allow the system to escape from shallow local minima.

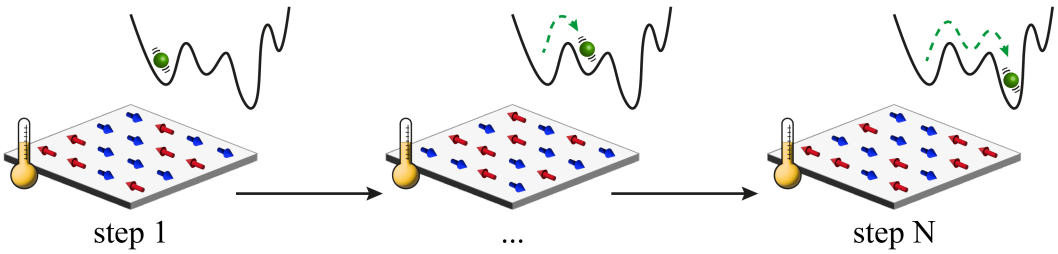

FIGURE 4.10: A schematic representation of the sampling algorithm. At each time step the temperature of the system remains constant.

4.5.2 Simulated annealing

The SA is one of the most popular energy-minimization algorithms [236]. It draws inspiration from the annealing process in metallurgy, where a material is heated to a high temperature and then gradually cooled, promoting the removal of defects and leading to a more ordered and stable structure. Similarly, SA starts

with a random spin configuration at high temperature (low β), which promotes the exploration of the spin configuration space. The temperature gradually decreases during the evolution of the system leading toward the lowest energy state. Once the system reaches this state, it is "frozen" with not much energy to escape from the minimum. Figure 4.11 illustrates a schematic representation of the algorithm. The choice of the annealing schedule is crucial, as it determines the rate at which the algorithm explores and converges. A standard approach is to have β increase linearly from a low to a high value, although alternative behaviors can be employed [264].

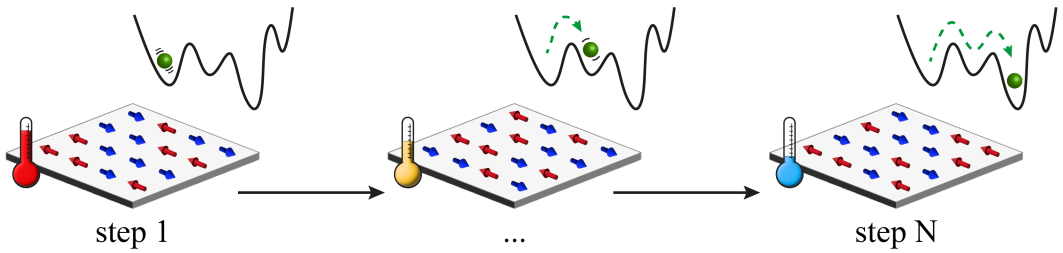

FIGURE 4.11: A schematic representation of the SA algorithm. At each time step the temperature gradually decreases.

4.5.3 Parallel tempering

PT algorithm provides an important improvement over SA, albeit at a higher computational cost [265, 266]. In PT, multiple replicas of the system are used, each at a different temperature [244]. In order to find the solution, the PT algorithm compares the energy of the replicas and apply different operators to perform swaps of the states between replicas. For example, a deterministic operator we implemented here works as follow. The energies of the replicas are compared, if the energy of the hotter replica is lower that the energy of the colder replica, a swap occurs, as illustrated in Figure 4.12.

For non-deterministic approaches, the probability of swap can be governed by certain rules linked to a probability function, allowing in some cases also swaps that can be energetically disadvantageous. The higher temperature replicas facilitate diversification by exploring a larger spin configuration space, while the lower temperature replicas act as an intensification element by improving the

state through the exploration of a local solution until a minimum is found [242].

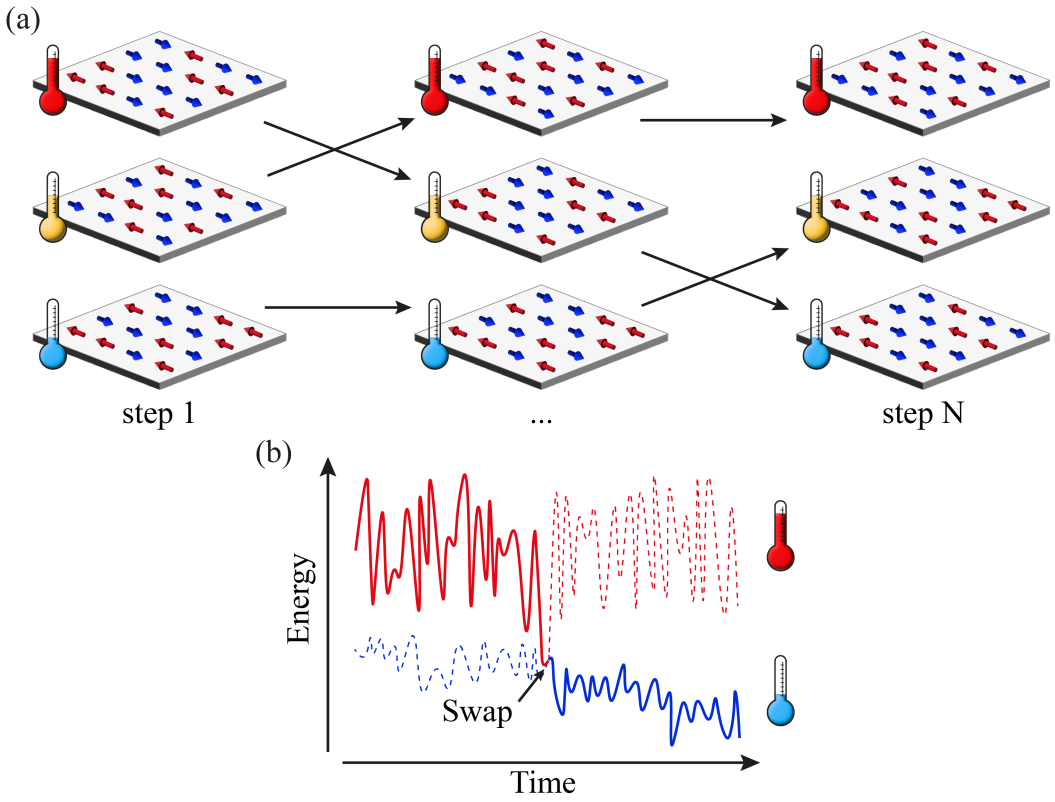

FIGURE 4.12: A schematic representation of the PT algorithm. (a) Multiple replicas of the system evolve in parallel at different temperatures and can swap their states during the algorithm's progression. (b) Illustration highlighting the swapping rule between two replicas - one at high temperature and one at low temperature.

Energy is the most general metric governing the swapping rules, although other problem-related metrics can be employed, as it will be discussed in the next sections.

The choice of hyper-parameters such as the values of β and the number of replicas is crucial for solving problems.

4.5.4 Simulated quantum annealing

SQA is a quantum-inspired algorithm that simulates the quantum tunneling phenomena in an Ising model with a transverse field [256, 267]. Multiple replicas at the same temperature interact with each other via a transverse field, simulating

the superposition of all possible spin configurations. Figure 4.13 illustrates the working principle of the algorithm.

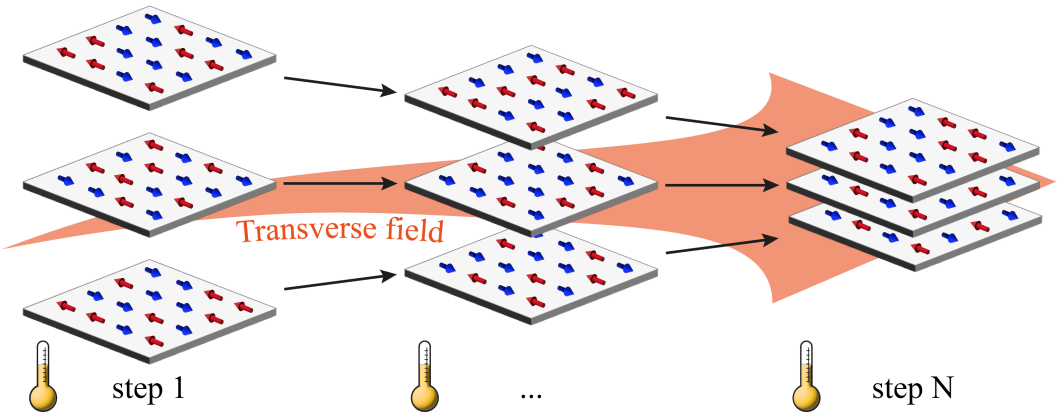

FIGURE 4.13: A schematic representation of the SQA algorithm. Multiple replicas at the same temperature interact with each other via a transverse field. The transverse field starts from zero and increases over time, gradually forcing the replicas to converge to the same state.

The transverse field is close to zero at the beginning of the simulation, allowing the replicas to evolve relatively independently. This field smoothly increases over time until it diverges near the end of the simulation, causing the replicas to become strongly coupled and ideally "collapse" into one spin configuration. The formulation of the strength of transverse coupling between replicas used in this thesis is given by:

$$J_T(n) = -J_{T0} \log\left(\tanh\left(\beta \frac{N-n}{N-1} G_x\right)\right) \tag{4.4}$$

where J_{T0} is the scaling parameters, G_x is the transverse field, N is the number of steps in the simulation, and n is the generic step of the simulation.

4.6 Probabilistic computing with p-bits

Conventional/digital computing uses bits to encode information as either 0 and 1, while quantum computing uses qubits which can be used to model superposition of states (0 and 1 in case of a single q-bit). Positioned between these two paradigms of computing we can place the idea of probabilistic computing, which uses p-bits – probabilistic bits (see Figure 4.14(a)). The p-bit fluctuates in time between the states -1 and 1, but at any given time it is in one of the two states [241, 268].

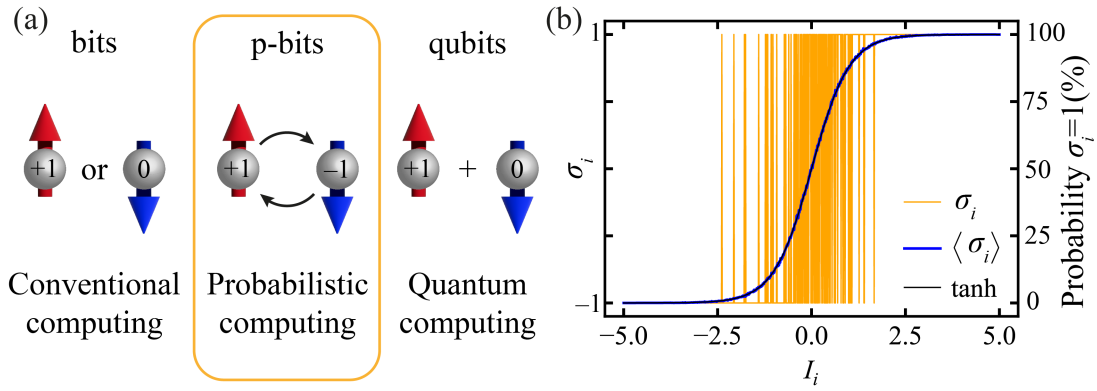

FIGURE 4.14: (a) A schematic representation of bit, p-bit, and qubit. (b) Behavior of the p-bit in response of the input signal. The orange line represents the binary stochastic state response of a single p-bit with input signal values from -5 to $+5$. The blue line is the average over 10^4 runs with the same I_i, which approximates the hyperbolic tangent function (black line).

A simple example of equation governing the time domain dynamic of a p-bits σ_i is:

$$\sigma_i\left(n+1\right) = \text{sgn}\left(\text{rand}\left(-1,\ 1\right) + \tanh\left(I_i\left(n\right)\right)\right) \tag{4.5}$$

where rand$(-1, 1)$ is a random number between -1 and $+1$, and $I_i\left(n\right)$ is the input control signal that tunes the dynamical response of the i^{th} p-bit. It is possible to identify two terms: the stochastic component given by the random number and the deterministic component given by the hyperbolic function. The higher is the value of the I_i, the more deterministically the p-bit is going to act. This behavior can be described in terms of probability of the p-bit being in a given state, i.e., for $I_i = 0$ there is 50% of probability that $\sigma_i = -1$ or $+1$, while for high (low) value of I_i the probability of a p-bit to stay in the state -1 and $+1$ changes. Figure 4.14

(b) shows the behavior of the p-bit σ_i as the input is ramped from -5 to +5. The orange line is the binary stochastic response of the p-bit, the blue line is obtained by averaging over 10^4 runs with the same I_i, which approximates $\tanh(I_i)$ (black line).

The input signal of each p-bit is a function of all the p-bits connected to it:

$$I_i(n) = \beta\left(\sum_j J_{ij}\sigma_j + h_i\right) \tag{4.6}$$

It resembles the input basic neuron of fully connected layers of neural networks. β is the inverse pseudo-temperature, J_{ij} represents the coupling between the i^{th} p-bit, the one being updated, and the j^{th} p-bit at the moment of the update. By updating a system of p-bits in sequence, the state samples the energy landscape of the Ising Hamiltonian. Figure 4.15 illustrates the sequential update of the 3 p-bit AND gate.

The update of each p-bit in a system once is referred to as an "iteration". The update sequence is randomly chosen at each iteration.

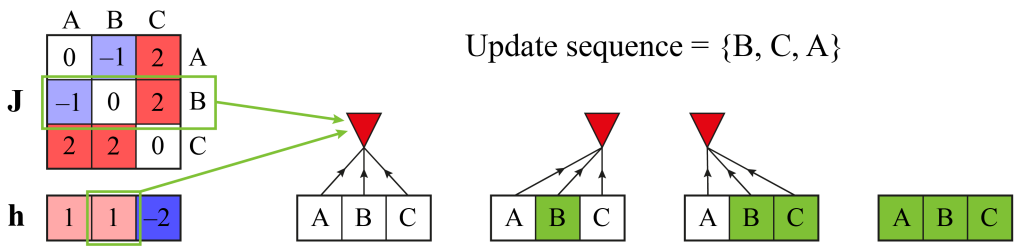

FIGURE 4.15: A schematic representation of sequential p-bit update for the 3 p-bits of the AND gate. The green square represents the updated p-bit.

4.6.1 Probabilistic computing solver

In a work led by Nobel laureate Giorgio Parisi, Bernaschi *et al.* [269], it was demonstrated that an efficient implementation of IMs on GPUs can have performances that are at least 2 orders of magnitude better than the other state-of-the-art devices, such as D-Wave quantum processors [270] and memcomputing machines [271]. Their work led them to leadership in the 3-XORSAT challenge in 2019.

Keeping this in mind, we have developed a PC solver in C/C++ programming language, with a GPU acceleration written in CUDA language that is poised for further improvements.

The code is designed to solve potentially every problem that can be mapped into an Ising model. Given the coupling matrix **J** and the bias vector **h**, it is always possible to calculate the energy of the system. However, many problems have a problem-related metric to check the solution, such as the value of maximum cut in Max-Cut or the solution cost in Max-SAT. For this reason, some of these metrics have been implemented in the solver, as discussed in paragraph 4.6.1.2.

The code is created for straightforward benchmarking through the setting of all the simulation parameters via text files. In particular, the configuration files required to setup the simulations and run the solver are the following (shorthand notation in parenthesis):

- *ProblemType_parameters.txt* (fileProblem).
- *Simulation_parameters.txt* (fileSimu).
- *Computing_parameters.txt* (fileComp).
- *Annealing_parameters.txt* (fileAnn).
- *Output_parameters.txt* (fileOut).

The file name suggests the nature of the parameters it holds. For example, fileProblem holds parameters such as the type of problem to solve, and some problem-related parameters, i.e., the number of clauses and variables in Max-SAT. fileComp holds parameters like the number of iterations, the number of p-bits and the file name of the **J** and **h** text files. In fileSimu it is possible to decide between CPU and GPU version of the solver.

Scalability is one of the key advantages of the code.

The pseudocode reported in the table Algorithm 4.1 describes the main structure of the program PetaIsing. All simulation parameters are stored in variables or pointers, organized in several structures, commonly referred as structs. To improve memory usage, performance, and flexibility we decide to employ only 1D pointers. At the beginning of the program, the variables in the structs are populated with configuration parameters loaded from files. The subsequent step

involves setting of the pointers with values loaded from text files, including **J**, and **h**, along with added clamp values.

The program allows for multiple runs of the PC solver, each with a different seed, thus starting from distinct initial state of the p-bits. In particular, the initialization of p-bits can be done either by the code with initial values randomly set to -1 or $+1$, or by loading them from a text file. Despite being a probabilistic solver, the code is designed to ensure reproducibility for a given seed of the random number generators.

To find the solution of a problem a huge number of iterations can be required. To deal with this, we divided the total number of iterations into B blocks. In other words, we perform B blocks, each consisting of N iterations, resulting in a total number of $B \times N$ iterations for the entire simulation. The results of each block are stored using double pointers, that point at each block. At the end of each block, the results, like the energies, the losses, and the spin configurations, are saved in text files.

Algorithm 4.1: Main structure of PetaIsing

structs ← DEFINESTRUCT()

structs ← LOADINPUTS(structs)

J, **h**, ... ← SETINPUTS(structs)

for *run* ← 0 to *nRun* **do**
  σ ← INITPBITS(structs)
  for *block* ← 0 to *B* **do** ▷ *B* number of blocks
    σ ← UPDATEPBITS(σ, *block*, structs)
  end
end

UPDATEPBITS is the main function of the PC solver, where the update of each p-bit is performed, as detailed in the table Algorithm 4.2. For a system of M p-bits and R replicas, the indices of each p-bit are stored in the pointer **x**, which is shuffled every iteration (N) to randomize the update order. At the beginning of each iteration, the random component of the update equation (Eq. (4.5)) for each p-bit of the replicas is stored, enhancing the efficiency in the PC-CUDA. In

PC-CUDA, the MAC operation between the p-bits and their coupling, with the addition of the bias, is parallelized.

The function COMPUTEβ returns the value of β for each replica at every iteration, enabling the implementation of several annealing algorithms. For random sampling and SQA algorithm, β remains constant throughout each iteration. In PT, each replica is assigned a different value of β, while in SA, β changes over the iteration number, from a low value β_L to a high value β_T. Typically, in SA, β follows a linear behaviour, implemented as: $\beta \leftarrow \beta_L + \frac{n}{BN-1}(\beta_T - \beta_L)$. Furthermore, the solver accommodates custom annealing schedules via an appropriately configured text file.

At the conclusion of each iteration, the energy and the objective function associated with the problem, referred to as loss, are computed. The function COMPUTELOSS will be further discussed in paragraph 4.6.1.2.

Algorithm 4.2: p-bits update function

$\mathbf{x} \leftarrow [0,\ 1,\ 2,\ \ldots, M-1]_R$ ▷ **x** `containing all the indices of the` M `p-bits`

for $n \leftarrow blockN$ to $(block+1)\,N$ **do** ▷ `Loop over` N `iterations`

  $\mathbf{x} \leftarrow$ shuffle(**x**)

  rd $\leftarrow$ [rand(-1,1)]$_R$

  for $i \leftarrow 0$ to $M-1$ **do** ▷ `Loop over` M `p-bits`

    for $r \leftarrow 0$ to $R-1$ **do** ▷ `Loop over` R `replicas`

      $S_r \leftarrow \sum J_{ij}\sigma_j + h_i$ ▷ `MAC + bias`

    end

    $\boldsymbol{\beta} \leftarrow$COMPUTE$\beta(n,i)$

    for $r \leftarrow 0$ to $R-1$ **do** ▷ *

      $ii \leftarrow x_{r,i}$

      $I \leftarrow \beta_r S_r$

      $\sigma_{r,ii} \leftarrow \mathrm{sgn}(\mathrm{rd}_{r,ii} + \tanh(I))$ ▷ `Update` i^{th} `p-bit of` r^{th} `replica`

    end

  end

  for $r \leftarrow 0$ to $R-1$ **do**

    $E_r \leftarrow -\left(\sum\sum \frac{1}{2} J_{ij}\sigma_{r,i}\sigma_{r,j} + \sum h_i\sigma_{r,i}\right)$ ▷ `Energy of` r^{th} `replica`

    $L_r \leftarrow$COMPUTELOSS(σ)

  end

end

4.6.1.1 Implementation of energy minimization algorithms

Random sampling and SA can be easily implemented by properly setting the value of β and its time domain evolution, as discussed in the previous paragraph.

As explained in the paragraph 4.5.3, PT involves the comparison between replicas based on either energy or loss computation according to the COPs to solve. The table Algorithm 4.3 details the process for the energy, but the same considerations apply to the loss. Replicas can be set to swap either every iteration or after a

chosen number of iterations N_{PT} (if it is not specified $N_{PT} = 1$). The replicas are arranged from the coldest at replica 0 to the hottest at replica $R - 1$. Starting from the hottest replicas, if its energy is lower than the energy of the colder neighbor, the swap occurs.

Algorithm 4.3: PT algorithm

if $n \bmod N_{PT} = 0$ **then**
  for $r \leftarrow R$ to 1 **do**
    $E_r \leftarrow -\left(\sum\sum \frac{1}{2} J_{ij}\sigma_{r,i}\sigma_{r,j} + \sum h_i \sigma_{r,i}\right)$
    $E_{r-1} \leftarrow -\left(\sum\sum \frac{1}{2} J_{ij}\sigma_{r-1,i}\sigma_{r-1,j} + \sum h_i \sigma_{r-1,i}\right)$
    if $E_r < E_{r-1}$ **then**
      tmp$\leftarrow \sigma_r$
      $\sigma_r \leftarrow \sigma_{r-1}$
      $\sigma_{r-1} \leftarrow$ tmp
    end
  end
end

Expanding upon the PT concept, the code integrates various methods of exchanges between replicas. These include reordering the replicas based on their energy or loss, initiating swaps or changes in the state of a set of replicas if a given metric of the coldest replicas remains stuck for a certain number of iterations.

The SQA involves the interaction between replicas via a transverse field I_{trans} added to the input signal. The table Algorithm 4.4 summarizes the loop marked with * in the table Algorithm 4.2, including the additional I_{trans} term. The strength of transverse coupling between replicas (J_T) as given by Eq. (4.5) is computed at the beginning of the simulation in the functions SETINPUTS or can be configurated via a text file.

Algorithm 4.4: SQA algorithm

$$\mathbf{J_T} = -J_{T0} \log\left(\tanh\left(\beta \frac{N-n}{N-1} G_x\right)\right)$$

for $r \leftarrow 0$ to $R-1$ **do**

$ii \leftarrow x_{r,i}$

$I_{local} \leftarrow \beta_r S_r$

$I_{trans} = J_{Tn}\left(\sigma_{r-1,ii} + \sigma_{r+1,ii}\right)$

$I \leftarrow I_{local} + I_{trans}$

$\sigma_{r,ii} \leftarrow \mathrm{sgn}\left(\mathrm{rd}_{r,ii} + \tanh\left(I\right)\right)$

end

4.6.1.2 Result

As previously mentioned in section 4.6.1, the PC solver is designed to address every problem that can be mapped into an Ising model. While it is feasible to compute the energy of any given problem, it is often more insightful to also observe the trends of a problem-related objective function (loss). This is particularly true as encoding a problem in the Ising model necessitates a significant number of auxiliary p-bits that increase the computational cost of the energy. In the following sections, we will delve into a detailed explanation of the objective function and present results from the comparative analysis of SA, PT and SQA for Max-Cut, Max-SAT and integer factorization.

4.6.1.2.1 Max-Cut

The table Algorithm 4.5 details the pseudocode implementation for computing the maximum cut, which is the objective function for Max-Cut problems, on a weighted graph (refer to paragraph 4.3.1 for details).

Algorithm 4.5: Maximum cut in Max-Cut problems

for $r \leftarrow 0$ to $R-1$ **do**
  for $i \leftarrow 0$ to $M-1$ **do**
    for $j \leftarrow i+1$ to $M-1$ **do**
      if $\sigma_{r,i} \neq \sigma_{r,j}$ **then**
        $L_r \leftarrow -J_{i,j}$
      end
    end
  end
end

The performance of PC with different energy minimization algorithms were compared attempting to solve several hard Max-Cut instances from G-set graphs, problems generated by the machine-independent graph generator "rudy" of G. Rinaldi. Each instance is attempted 100 times for each algorithm with 1000 iterations, and the cut value as a function of the iteration was recorded. Table 4.1 summarizes the results of the comparison. For each instance, we report both the average cut score and the best one achieved among the 100 runs. In addition, we also show the number of times the best result was reached. The list of parameters for each algorithm are the following:

- SA: 1 replica with linear annealing from $\beta_L = 0$ and $\beta_T = 1.5$.
- PT: 10 replicas. The values of β for each replicas: $\beta_0 = 1.5$, $\beta_1 = 0.70$, $\beta_2 = 0.60$, $\beta_3 = 0.50$, $\beta_4 = 0.45$, $\beta_5 = 0.40$, $\beta_6 = 0.35$, $\beta_7 = 0.30$, $\beta_8 = 0.28$, $\beta_9 = 0.23$.$N_{PT} = 1$.
- SQA: 10 replicas, $\beta = 0.4$, $J_{T0} = 0.5$, $G_x = 3.0$.

TABLE 4.1: Results of solving attempts of instances of the G-set performed using SA, PT and SQA. The average cut and the best cut found among the 100 trials for each instance are presented, along with the number of times the best result was achieved. The best cut among each algorithm is highlighted.

		SA			**PT**			**SQA**		
Instance name	**N° of p-bits**	**Mean ±std**	**Best**	**N° of best**	**Mean ±std**	**Best**	**N° of best**	**Mean ±std**	**Best**	**N° of best**
g1	800	11595.61 ± 16.23	11624	9	11616.24 ± 6.51	11624	19	11599.19 ± 16.16	11624	6
g2	800	11590.95 ± 11.30	11616	1	11610.54 ± 4.06	**11619**	1	11593.29 ± 9.23	11616	2
g3	800	11598.74 ± 14.14	**11622**	4	11617.57 ± 3.42	**11622**	11	11604.47 ± 11.20	11621	5
g4	800	11627.5 ± 12.14	11646	8	11642.72 ± 3.13	11646	30	11627.88 ± 11.27	11646	2
g5	800	11610.32 ± 14.45	11631	4	11625.92 ± 3.64	11631	8	11611.01 ± 12.50	11631	2
g6	800	2154.33 ± 16.95	**2178**	3	2173.71 ± 4.02	**2178**	6	2156.73 ± 13.18	2177	1
g7	800	1982.42 ± 13.62	2006	6	1996.87 ± 3.72	2006	1	1983.06 ± 9.20	2006	1
g8	800	1984.64 ± 10.96	**2005**	2	1999.68 ± 3.35	**2005**	5	1986.82 ± 7.51	2003	3
g9	800	2027.47 ± 15.84	**2054**	2	2045.50 ± 4.56	**2054**	2	2032.82 ± 11.06	2053	1
g10	800	1975.62 ± 14.96	**2000**	2	1993.45 ± 3.91	**2000**	2	1979.68 ± 10.99	1999	2
g11	800	553.56 ± 3.44	560	6	554.40 ± 2.06	**562**	1	553.94 ± 2.58	560	1
g12	800	547.22 ± 3.42	**554**	1	546.40 ± 2.40	552	1	548.70 ± 2.88	**554**	5
g13	800	571.92 ± 3.38	**580**	1	570.80 ± 2.26	576	2	572.94 ± 2.99	**580**	2
g14	800	3043.53 ± 4.5	3055	1	3035.88 ± 4.13	3050	1	3052.65 ± 5.03	**3061**	4

g15	800	3028.43 ± 6.09	3042	1	3018.61 ± 5.23	3032	1	3037.25 ± 4.10	3046	2
g16	800	3030.05 ± 5.38	3045	1	3021.52 ± 4.73	3034	1	3039.26 ± 4.20	**3047**	5
g17	800	3025.92 ± 4.81	3035	3	3017.69 ± 5.06	3030	2	3035.28 ± 3.60	**3047**	1
g18	800	976.45 ± 7.16	987	3	975.58 ± 5.28	986	1	979.88 ± 6.58	**990**	1
g19	800	891.77 ± 9.37	**906**	1	892.35 ± 4.76	902	1	896.06 ± 6.70	904	3
g20	800	928.39 ± 8.60	941	1	930.97 ± 5.16	941	2	930.51 ± 9.19	941	6
g21	800	914.66 ± 7.81	**929**	1	916.04 ± 4.94	926	2	917.00 ± 5.60	927	1
g22	2000	13314.27 ± 17.38	13357	1	13331.39 ± 12.41	13355	1	13319.02 ± 20.04	**13358**	1
g23	2000	13313.08 ± 11.80	13336	1	13312.64 ± 8.73	13329	1	13311.46 ± 15.11	**13337**	1
g24	2000	13300.82 ± 13.07	13329	1	13306.36 ± 9.14	13331	1	13302.04 ± 15.04	**13333**	1
g25	2000	13305.08 ± 12.16	**13330**	1	13308.31 ± 9.17	13329	1	13309.18 ± 9.96	13328	3
g26	2000	13294.97 ± 10.55	**13321**	1	13295.29 ± 9.25	13316	1	13295.07 ± 12.29	13320	1
g27	2000	3302.43 ± 13.88	3334	1	3307.16 ± 7.57	3324	1	3304.34 ± 15.74	**3339**	2
g28	2000	3268.06 ± 13.66	3293	1	3269.98 ± 7.83	3285	1	3269.27 ± 14.04	**3295**	1
g29	2000	3361.10 ± 13.5	3398	1	3367.17 ± 10.22	3393	1	3366.48 ± 13.39	**3402**	1
g30	2000	3381.80 ± 13.93	3407	1	3383.24 ± 9.15	3402	3	3380.67 ± 17.19	**3410**	2
g31	2000	3277.44 ± 12.92	3304	1	3280.72 ± 8.21	3299	1	3277.52 ± 14.25	**3306**	1

g32	2000	1379.78 ± 6.15	1392	1	1377.28 ± 4.63	1388	1	1384.88 ± 5.20	**1398**	2
g33	2000	1352.36 ± 5.47	1366	1	1351.98 ± 3.74	1364	1	1360.32 ± 4.37	**1370**	1
g34	2000	1357.50 ± 4.66	1368	2	1354.60 ± 3.33	1364	1	1362.34 ± 4.17	**1372**	1
g35	2000	7623.56 ± 9.10	7654	1	7602.17 ± 7.59	7625	1	7652.86 ± 7.42	**7671**	1
g36	2000	7618.78 ± 10.00	7646	1	7593.75 ± 7.50	7610	1	7644.61 ± 7.61	**7663**	1
g37	2000	7628.12 ± 9.37	7647	1	7603.71 ± 7.66	7628	1	7655.21 ± 7.45	**7672**	1
g38	2000	7627.93 ± 8.76	7651	1	7603.72 ± 7.03	7621	1	7652.1 ± 6.21	**7664**	5
g39	2000	2361.76 ± 12.66	2385	1	2338.06 ± 17.36	2375	1	2374.82 ± 11.56	**2400**	1
g40	2000	2349.57 ± 13.43	2390	1	2329.32 ± 17.81	2374	1	2363.98 ± 12.55	**2392**	1
g41	2000	2353.02 ± 13.17	2391	1	2335.29 ± 16.04	2375	1	2367.36 ± 13.75	**2401**	1
g42	2000	2432.50 ± 12.39	2455	3	2406.09 ± 17.71	2449	1	2443.41 ± 12.25	**2465**	4
g43	1000	6641.98 ± 11.60	6660	6	6654.09 ± 2.94	6660	2	6645 ± 10.24	6660	2
g44	1000	6635.52 ± 9.82	6650	5	6643.36 ± 3.51	6650	1	6636.89 ± 8.12	6650	3
g45	1000	6635.25 ± 8.48	**6654**	1	6644.51 ± 4.89	**6654**	1	6637.29 ± 7.95	6653	3
g46	1000	6630.80 ± 8.00	6649	1	6639.93 ± 3.61	6649	1	6635.78 ± 7.20	6649	1
g47	1000	6640.71 ± 9.00	6656	6	6648.45 ± 4.27	6656	4	6642.10 ± 8.61	6656	8
g48	3000	5962.04 ± 55.03	6000	66	6000.00 ± 0.00	6000	100	5962.22 ± 52.96	6000	66

g49	3000	5940.04 ± 36.92	6000	19	5967.76 ± 28.11	6000	40	5943.92 ± 39.21	6000	25
g50	3000	5841.88 ± 18.86	**5876**	1	5839.02 ± 13.37	5870	2	5843.98 ± 15.38	5874	1
g51	1000	3821.10 ± 5.51	3832	1	3810.68 ± 4.76	3825	1	3833.54 ± 5.37	**3845**	1
g52	1000	3823.92 ± 5.71	3837	1	3814.57 ± 5.04	3829	1	3834.43 ± 4.24	**3844**	1
g53	1000	3823.70 ± 5.72	3837	2	3813.00 ± 4.92	3824	2	3834.53 ± 4.25	**3845**	1
g54	1000	3823.49 ± 5.61	3838	1	3811.00 ± 4.69	3824	1	3834.00 ± 4.58	**3846**	1

The main result of these tests is that SQA outperforms SA and PT in instances mapped with a high number of p-bits. This result can open the path to high parallel approaches to solve combinatorial optimizations inspired by quantum physics. On the other hand, for small problems, SA and PT exhibit better cut attempts compared to SQA.

In general, both PT and SQA achieve better results than SA as the number of replicas increases.

4.6.1.2.2 Max-SAT

The table Algorithm 4.6 details the code implementation to compute the solution cost of Max-SAT problems (refer to paragraph 4.3.3 for details).

To assess the performance of the PC solver for Max-SAT, we selected a Max-SAT instance of average difficulty from the international Max-SAT competition 2016, namely “s3v70c700-1.cnf”. This instance is characterized by 70 variables and 700 clauses (with 3 literals for each clause), encoded with 771 p-bits. The optimal solution for this instance is 21.

Algorithm 4.6: Max-SAT solution cost

$\mathbf{X} \leftarrow [x_0,\ x_1, x_2, \ldots, x_{Z-1}]$ ▷ **X** containing indices of Z variables

$\mathbf{Y} \leftarrow [y_0,\ y_1,\ y_2,\ \ldots, y_{D-1}]$ ▷ **Y** containing value of L literals of each clause. $D = C \times L$, whit C number of clauses.

$\mathbf{S} \leftarrow [s_0,\ s_1,\ s_2, \ldots, s_{D-1}] \in [-1, 1]$ ▷ **S** containing sing of L variables of each clause.

$\mathbf{W} \leftarrow [w_0,\ w_1,\ w_2,\ \ldots, w_{C-1}]$ ▷ **W** containing weight each clause.

for $r \leftarrow 0$ to $R - 1$ **do**
  for $z \leftarrow 0$ to $Z - 1$ **do**
    $i \leftarrow X_z$
    $v_{r,z} \leftarrow \sigma_{r,i}$
  end
end
for $r \leftarrow 0$ *to* $R - 1$ **do**
  for $c \leftarrow 0$ to $C - 1$ **do**
    truthValue$\leftarrow 0$
    for $l \leftarrow 0$ to $L - 1$ **do**
      $g \leftarrow y_{c,l}$
      if $v_{r,g}\ s_{c,l} > 0$ **then**
        truthValue$\leftarrow 1$
      end
    end
    if truthValue $= 1$ **then**
      $L_r \leftarrow L_r + w_c$
    end
  end
end

Figure 4.16 illustrates a comparison of the solution cost evolution for a successful run of the problem using PT (a) and SQA (b) with 10 replicas. These results

shed light on the distinctions between these two energy minimization algorithms, as discussed in paragraph 4.5. In the case of PT, each replica explores different regions of the spin configuration space, while in SQA, as the strength of the transverse field increases (black solid line) the replicas become more coupled until, at the end of the simulation, they "collapse" in single spin configuration state. Further investigation has revealed that, for a considerable number of replicas, there is not a single emerging state, but rather different clusters.

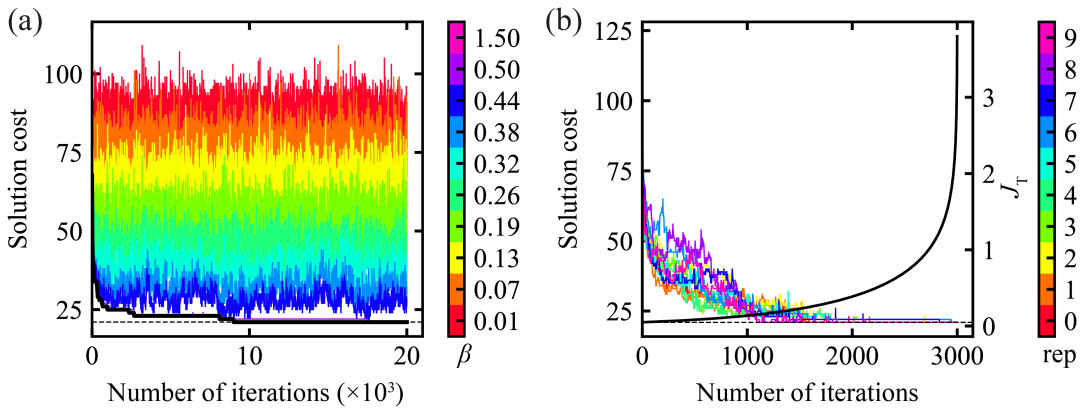

FIGURE 4.16: Solution cost of the instance "s3v70c700-1.cnf", characterized by 70 variables and 700 clauses, using (a) PT and (b) SQA with 10 replicas. (a) Each colored line represents the evolution of the solution cost of a replica at constant value of β, linearly distributed from 0.50 and 0.01 with one replica at 1.50, indicated in the color bar. The solid black line is a "replica" that saves the best results among all the replicas. The dashed black line highlighted is the optimal solution cost of 21. (b) Each replica has $\beta = 0.5$. The black solid line represents the value of the transverse coupling between replicas, which increases as a function of the iterations.

Figure 4.17 shows a comparison of SA, PT and SQA with 5 replicas (a) and 1000 replicas, across 100 runs of 1000 iterations. The solid line represents the average at that iteration, while the shaded area the standard deviation. For the SA, β linearly increases from 0.0 and 1.5, and the different replicas represent different runs of the problem. For PT, the value of β of each replica is linearly distributed from 0.01 and 0.5, with a replica at $\beta = 1.5$. For SQA, $\beta = 0.5$, $J_{T0} = 1.0$ and $G_x = 3.0$. The results shows that, for few replicas, SQA performs worse compared to SA and PT, as discussed in Ref.[272] where the selected parameters highligthed this behaviour. However, for a large number of replicas SQA outperforms SA and PT.

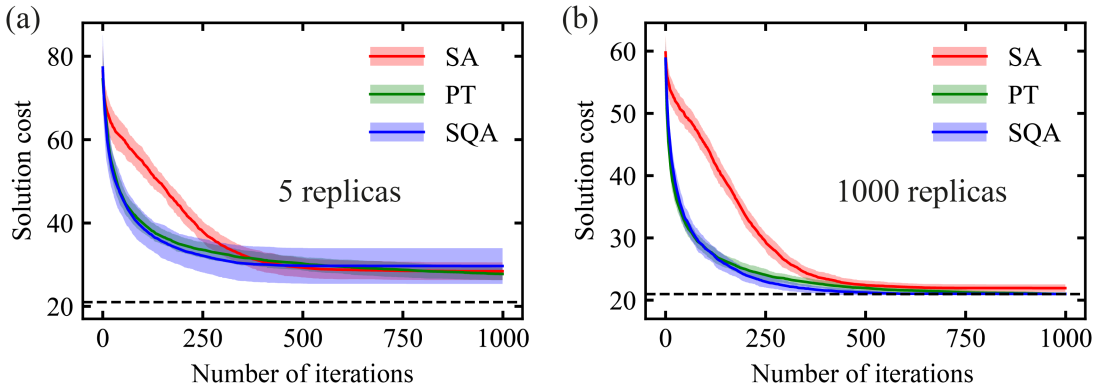

FIGURE 4.17: Results of the comparison of SA, PT and SQA in terms of Max-SAT solution cost of the instance "s3v70c700-1.cnf". (a)-(b) Envelope curves of 5 (1000) replicas of the solution cost computed for 1000 iterations with SA (red), PT (green) and SQA (blue). For both numbers of replicas, a total of 100 runs for each algorithm have been performed. The solid line is the trend of the average best solution cost at that iteration; the area around the solid line is the standard deviation. The dashed black line is the optimal value 21.

Intrigued by these results, we performed a systematic study using the same parameters of Figure 4.17, varying the number of replicas, as shown in Figure 4.18. The results reveal that, for more than 500 replicas, SQA reaches the optimal solution with a probability close to 100%, whereas PT requires more replicas to achieve similar results. It is important to note that these outcomes are strongly influenced by the chosen parameters, which are selected heuristically. When the number of replicas is fixed, only four parameters need to be chosen for SQA, while PT requires setting a value of β for each replica. Hence, finding parameters that lead to optimal solution in SQA appears to be a more straightforward process compared to PT.

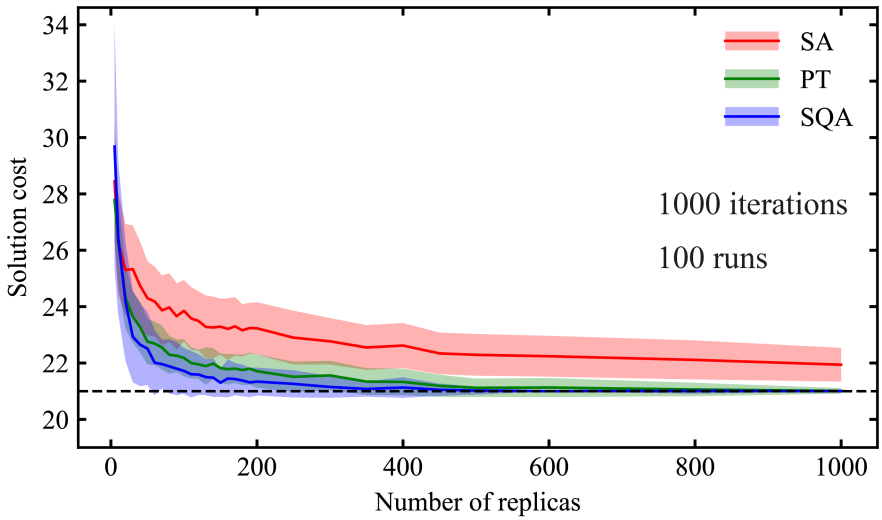

FIGURE 4.18: Results of the comparison of SA (red), PT (green) and SQA (blue) for increasing number of replicas in terms of Max-SAT solution cost of the instance "s3v70c700-1.cnf". The solid line is the trend of the average best solution cost at iteration 1000 over 100 runs; the area around the solid line is the standard deviation. The dashed black line is the optimal value 21.

4.6.1.2.3 Integer factorization

The table Algorithm 4.7 details the code implementation for computing the loss of integer factorization, that is, the difference between the number to factor C and the product of the factors obtained by the PC solver (refer to paragraph 4.3.4 for details).

To assess the performance of the PC solver with the integer factorization problem, we have chosen to show a 34-bit semiprime number $(16883648723 = 128813 \times 131071)$, and we performed 100 runs of 1000 iterations using SA, PT and SQA. For the SA, β linerly increases from 0.0 and 1.2. For PT, the value of β of each replica is linearly distributed from 0.01 and 0.5, with a replica at $\beta = 1.5$. For SQA, $\beta = 0.5$, $J_{T0} = 1.0$ and $G_x = 3.0$. Figure 4.19 shows the probability of obtaining the correct factors as a function of the number of replicas. PT outperforms over SA and SQA. In particular, when employing 1000 replicas, PT achieves a probability of factorizing the semiprime number higher than 50%. Furthermore, the linear scaling behaviour observed implies that the probability is expected to increase with a higher number of replicas.

Algorithm 4.7: Integer factorization loss

C$\leftarrow$ *Integer* ▷ `C is the number to be factorized`

$\mathbf{A} \leftarrow [a_0,\ a_1, a_2, \ldots, a_{F-1}]$ ▷ **A** `containing indices of factor A. F number of bits`

$\mathbf{B} \leftarrow [b_0,\ b_1, b_2, \ldots, b_{F-1}\ ]$ ▷ **B** `containing indices of factor B`

for $r \leftarrow 0$ to $R-1$ **do**

  for $i \leftarrow 0$ to $F-1$ **do**

    a,b$\leftarrow A_i, B_i$

    $\sigma_{A_{r,i}},\ \sigma_{A_{r,i}} \leftarrow \dfrac{\sigma_{r,a}+1}{2},\ \dfrac{\sigma_{r,b}+1}{2}$ ▷ $[0,1] \leftarrow [-1,1]$

    $f_{A_r}, f_{B_r} \leftarrow \text{BINTODEC}(\sigma_{A_{r,i}}), \text{BINTODEC}(\sigma_{B_{r,i}})$

  end

  $p_r \leftarrow\ f_{A_r}\ f_{B_r}$

  $L_r \leftarrow \text{abs}\,(\text{C} - \text{p}_r)$

end

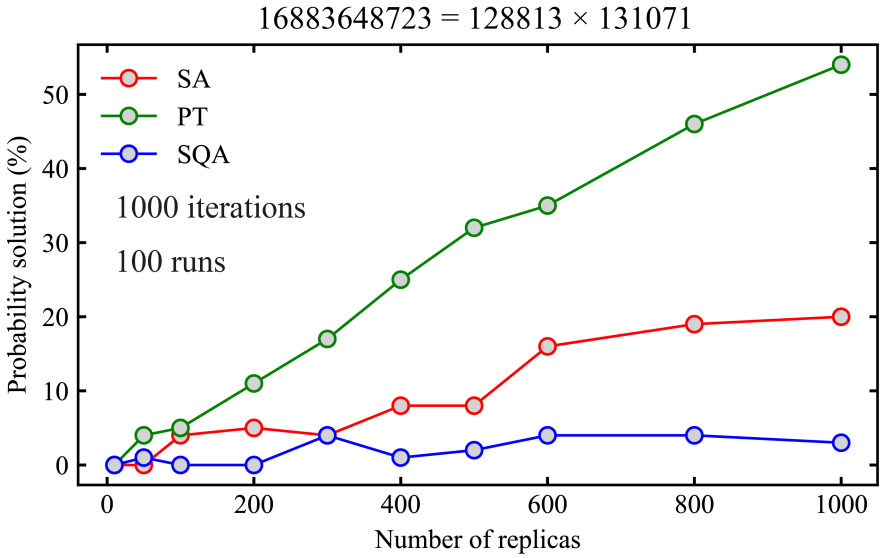

FIGURE 4.19: Results of the comparison of SA (red), PT (green) and SQA (blue) in terms of probability of obtaining the correct factors as a function of the number of replicas. Each point averages 100 runs with 1000 iterations for a 34 bits number.

4.7 Probabilistic computing with spintronic devices

The hardware implementation of p-bits requires a natural element that is substantially unstable, yet controllable. The spintronic technology is one of the best candidates, taking advantage of the probabilistic nature of the switching between two states in MTJs [240–242, 256, 268, 273–275]. Figure 4.20 shows the experimental demonstration of the p-bit using a stochastic MTJs, from Ref. [240]. Borders *et al*. [240] adeptly exploited spintronic-based PC to experimentally realize invertible logic gates circuit, successfully solving integer factorizations problems of numbers described by 8 p-bits. This innovative approach marks a significant stride in the practical implementation of p-bits for complex problem-solving.

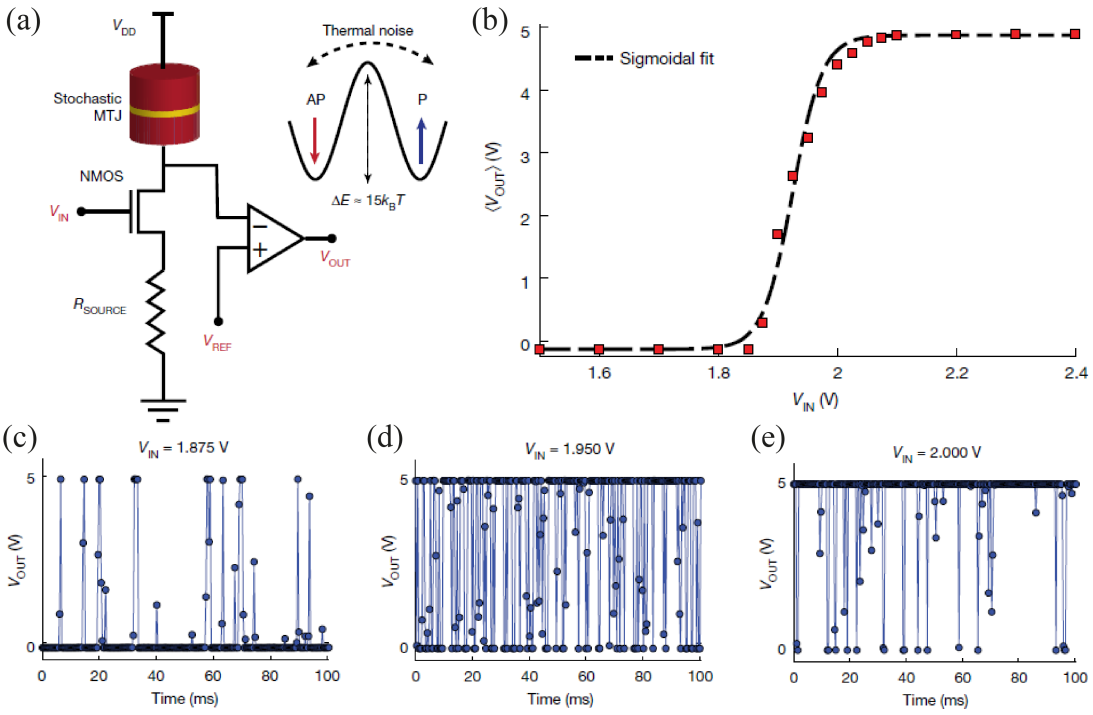

FIGURE 4.20: Experimental demonstration of a p-bit. (a) A schematic representation of a p-bit with a stochastic MTJ and NMOS transistor. A representation of the MTJ's FL fluctuates between two stable configurations, activated by thermal noise. (b) Sigmoidal behavior exhibited by the time-averaged output voltage, VOUT, as a function of the applied input. (c)-(e) Time snapshots of VOUT for three different input VIN [240]. In (c) a low input voltage; in (d) a voltage causing the MTJ to behave purely stochastically; in (e) a high input voltage.

As discussed in Chapter 3 on neuromorphic computing, it is important to take

into account the device-to-device variation in hardware implementations. This holds true for PC as well, where the device-to-device variation of each p-bit can potentially undermine the overall performance in solving complex problem. Before delving into the intricacies of this challenge, we advocate for a preliminary exploration of a hybrid p-bit implementation, which integrates spintronic devices with well-established CMOS technology.

4.7.1 Random number generation in a digital implementation of a p-bit

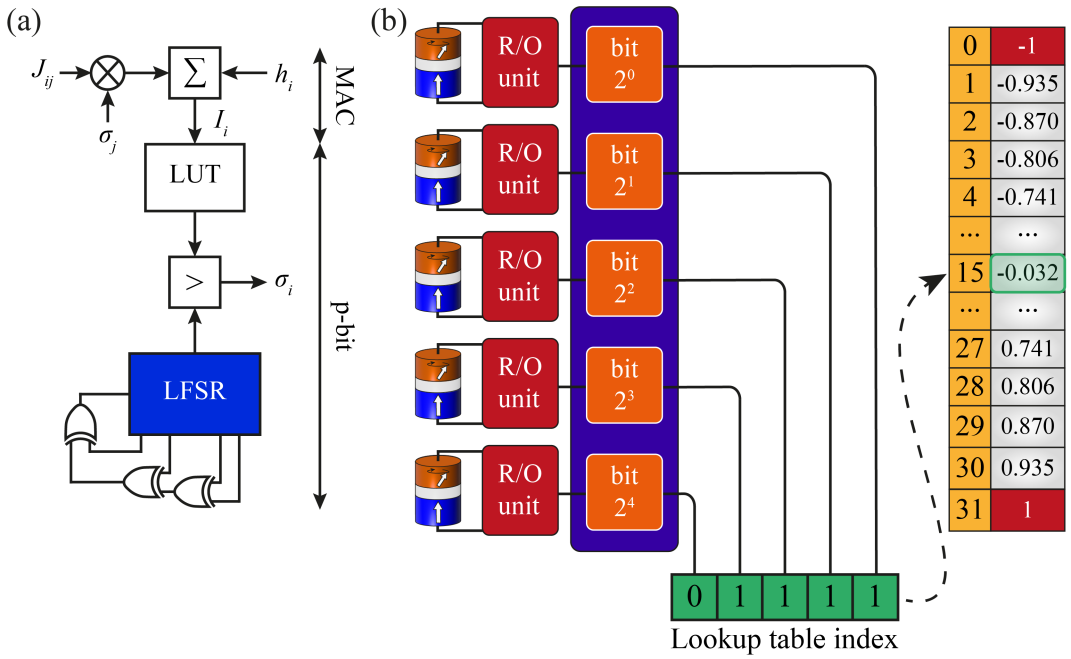

FIGURE 4.21: Example of CMOS architecture implementing the MAC (Eq. (4.6) and p-bit (Eq. (4.5)) equations. The hyperbolic tangent function is realized through a lookup table and the random number generation employs a LFSR [249]. (b) A schematic representation of mapping binary output from MTJs (measured via readout R/O units) to true random decimal number within the range $(-1, 1)$, used in Eq. (4.5) [72].

Figure 4.21 shows the CMOS architecture employed to realize a p-bit [240, 249]. One of main issues is the generation of the random numbers, since LFSR is a PRNG. After a certain number of iterations, the pseudorandom sequence starts to repeat, posing challenges for PC, as sometimes a large number of iterations is required to converge to the ground state. The quality of the RNG emerges as a

critical factor during the benchmark of the PC solver, significantly impacting PC results [276].

One way to address these issues is to replace the LFSR with MTJs, known for being a TRNG. In Ref. [72], we propose a stable voltage-controlled perpendicular MTJs, leveraging the VCMA effect for the dynamic generation of true random numbers [277, 278]. This approach boasts several advantages, including high update speed of the p-bits, and scalability to a large number of MTJs.

Moreover, we design a new way of implementing p-bits using only unbiased MTJs, i.e., MTJs generating random bitstreams with 50% probability of being in -1 or $+1$ state. Indeed the sequence of random numbers passes all the NIST tests. Therefore, there is no need for a fine-tuning of MTJ inputs, eliminating the necessity for analog feedback loops and enhancing circuit scalability. Figure 4.21 (b) shows our design to obtain a random number within the range $(-1, 1)$, as used in Eq. (4.5) for p-bit updates. A series of n MTJs, subjected to voltage pulses, generates an n-bit binary number, b, which can be mapped to a decimal number within $(-1, 1)$ using $-1 + 2b/\left(2^n - 1\right)$. For instance, in the example illustrated in Figure 4.21 (b), 5 MTJs provide a binary number 01111, equivalent to 15 in decimal. This can be mapped to $-1 + \dfrac{2 \cdot 15}{(2^5 - 1)} = -0.032$ using a lookup table.

We preliminarily tested this approach on the invertible AND gate and then we applied it to solve integer factorization of semiprime numbers [72].

The performance of PC is intricately tied to the precision of the number, determined by the number of MTJs utilized to segment the range $(-1, 1)$. In a systematic study, we examined the probability of obtaining optimal solutions for the Max-SAT instance "s3v70c700-1.cnf" as a function of the precision. Figure 4.22 shows the results from 1000 runs with 1000 iterations, using PT with 1000 replicas. As expected, the probability of attaining the optimal solution increases with the number of MTJs. In particular, the probability is 0% for less than 8 MTJs, progressively approaching the performance achieved with a software implementation of a double precision RNG when 16 MTJs are considered.

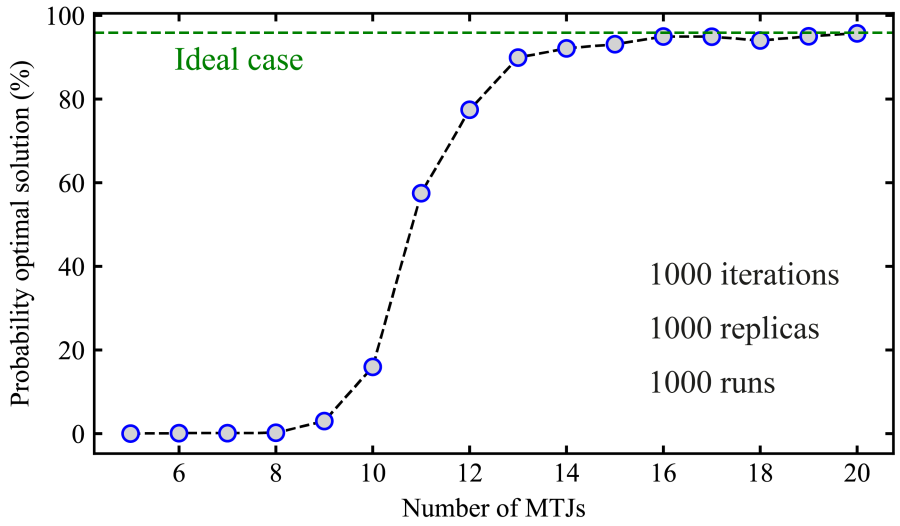

FIGURE 4.22: Probability of obtaining the optimal solution for the Max-SAT instance "s3v70c700-1.cnf" with 771 p-bits as a function of the number of MTJs employed to span the range $(-1, 1)$, as detailed in Figure 4.21 (b). The probability is derived from 1000 runs with 1000 iterations, using PT with 1000 replicas.

4.7.2 MTJ-based p-bit

Conventional MTJ-based p-bit designs rely on MTJs with a low energy barrier, where the randomness arises from the thermal fluctuation of the FL magnetization [240, 242, 268, 274]. However, this approach has several drawbacks. Generating random bits at high rates requires a very low energy barrier, a parameter that is challenging to control effectively. Moreover, maintaining the same energy barriers across devices fabricated on a chip proves to be a complex task, as this value is very sensitive (exponential dependence) on the thickness of the ferromagnet, leading to significant device-to-device variation of the energy barrier.

To address these issues, we propose a p-bit implementation with three-terminal MTJs [71]. Through micromagnetic simulations within the macrospin approximations, we simulated a perpendicular MTJ with a circular cross section of 50 nm $\times$ 50 nm, and FL thickness of 1.4 nm, as illustrated in Figure 4.23 (a). The micromagnetic parameters of the simulation are: $M_s = 0.80$ MA/m, $K_u = 0.06$ MJ/m^3, $J_{SOT} = 100.00$ MA/cm^2, $J_{STT} = [-0.40, 0.40]$ MA/cm^2, $q_{FLT} = 0.10$, and room temperature. The MTJ is designed so that the energy landscape of the FL magnetization has two stable minima along the z-axis. The application of an SOT current aligns the FL magnetization with the direction of the spin-current (y-axis),

creating a metastable state. When the SOT is switched off, the FL magnetization relaxes with equal probability toward one direction along the z-axis, as depicted in Figure 4.23 (b). The switching probability is tuned with an STT current applied to the third terminal, resulting in a sigmoidal curve when averaging the FL magnetization after the SOT pulse across 10^4 runs, as shown in Figure 4.23 (c).

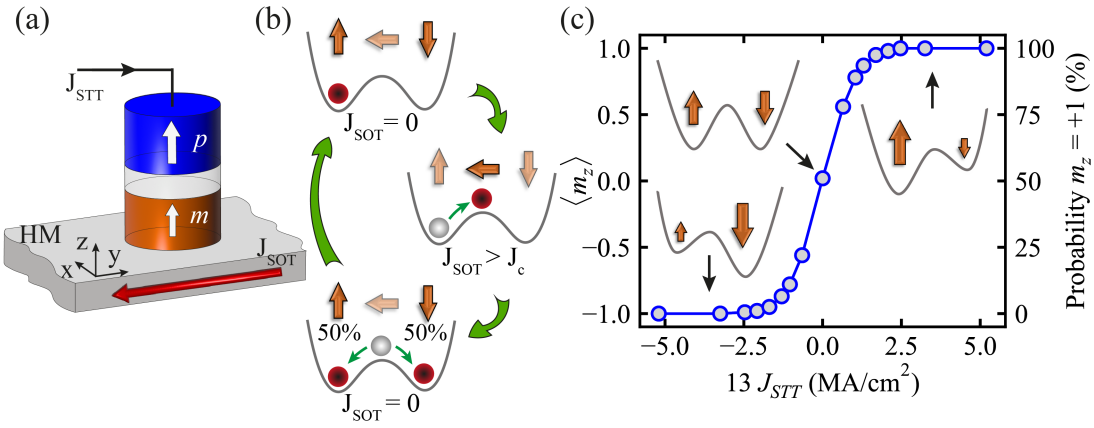

FIGURE 4.23: (a) A sketch of the three-terminal perpendicular MTJ designed for a hardware p-bit implementation. (b) A schematic representation outlining the three-step process of tunable RNG, as described in the text. (c) Average magnetization response as a function of the input STT current, resulting in a sigmoidal behavior. In the insets, the energy landscape of the three main states involved in this process.

In collaboration with the group of Prof. Pedram Khalili Amiri at Northwestern University, we experimentally investigated another hardware p-bit implementation based on a two-terminal superparamagnetic perpendicular MTJ illustrated in Figure 4.24 (a). At room temperature the MTJ resistance, which depends on the z-component of the magnetization, switches between the parallel and antiparallel states stochastically. A fine-tuning of the switching probability becomes possible through the application of an STT current generated by the applied bias voltage V. Figure 4.24 (b) shows experimental results of three different devices. The experimental data fitted with a hyperbolic tangent function show that the key difference between the curves is in their slope.

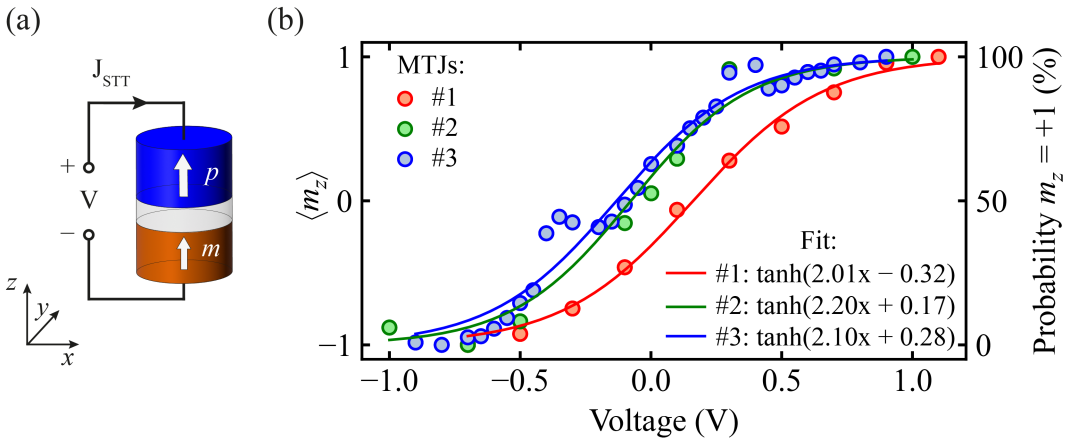

FIGURE 4.24: (a) A sketch of the two-terminal perpendicular MTJ designed for hardware p-bit implementation. (b) Experimental data of three devices (red, green and blue dots) fitted with a hyperbolic tangent function (red, green and solid lines, respectively).

4.7.3 Investigating PC reliability due to the device-to-device variations

Drawing insights from experimental observations, our analysis delves into the reliability of PC, acknowledging the inherent device-to-device variation reflected in distinct slopes (α) for each p-bit. The update equation of the i^{th} p-bit becomes: $\sigma_i(n+1) = \text{sgn}(rand(-1, 1) + \tanh(\alpha I_i(n)))$, where α acts as an additional temperature scaling parameter, which is now p-bit dependent. Our systematic study involved sampling the α values from a Gaussian distribution with unitary mean (representing the ideal p-bit) and increasing the values of the standard deviation σ. For realistic assumptions, the α values are confined within the range $[1-\sigma, 1+\sigma]$. Figure 4.25 (a) schematizes this process. Reliability assessments of PC are conducted using PT and SQA, across 3 different problems:

- Max-SAT instance "s3v70c700-1.cnf", with 771 p-bits, 1000 iterations, 1000 replicas. For PT, the value of β of each replica is linearly distributed from 0.01 and 0.5, with a replica at $\beta = 1.5$. For SQA, $\beta = 0.5$, $J_{T0} = 1.0$ and $G_x = 3.0$ (Figure 4.25 (b)).
- wMax-SAT instance "s3v70c700-1.wcnf", with 771 p-bits, 1000 iterations, 1000 replicas. For PT, the value of β of each replica is linearly distributed from 0.01 and 0.5, with a replica at $\beta = 1.5$. For SQA, $\beta = 0.05$, $J_{T0} = 1.0$ and $G_x = 30.0$ (Figure 4.25 (c)).

- Planted Ising with Pegasus topology graph instance, with 1288 p-bits, 2000 iterations, 1000 replicas. For PT, the value of β of each replica is linearly distributed from 0.01 and 5.0, with a replica at $\beta = 10.0$. For SQA, $\beta = 1.0$, $J_{T0} = 1.0$ and $G_x = 0.5$ (Figure 4.25 (d)).

Examining the robustness in terms of the probability of obtaining the optimal solution over 100 runs for a given problem, as shown in Figure 4.25, reveals that SQA outperforms PT. SQA exhibits remarkable insensitivity to the device-to-device variations, positioning it as a robust solution for practical applications. While PT shows a greater susceptibility to these variations, it is noteworthy that for small values of σ, the impact is only marginal.

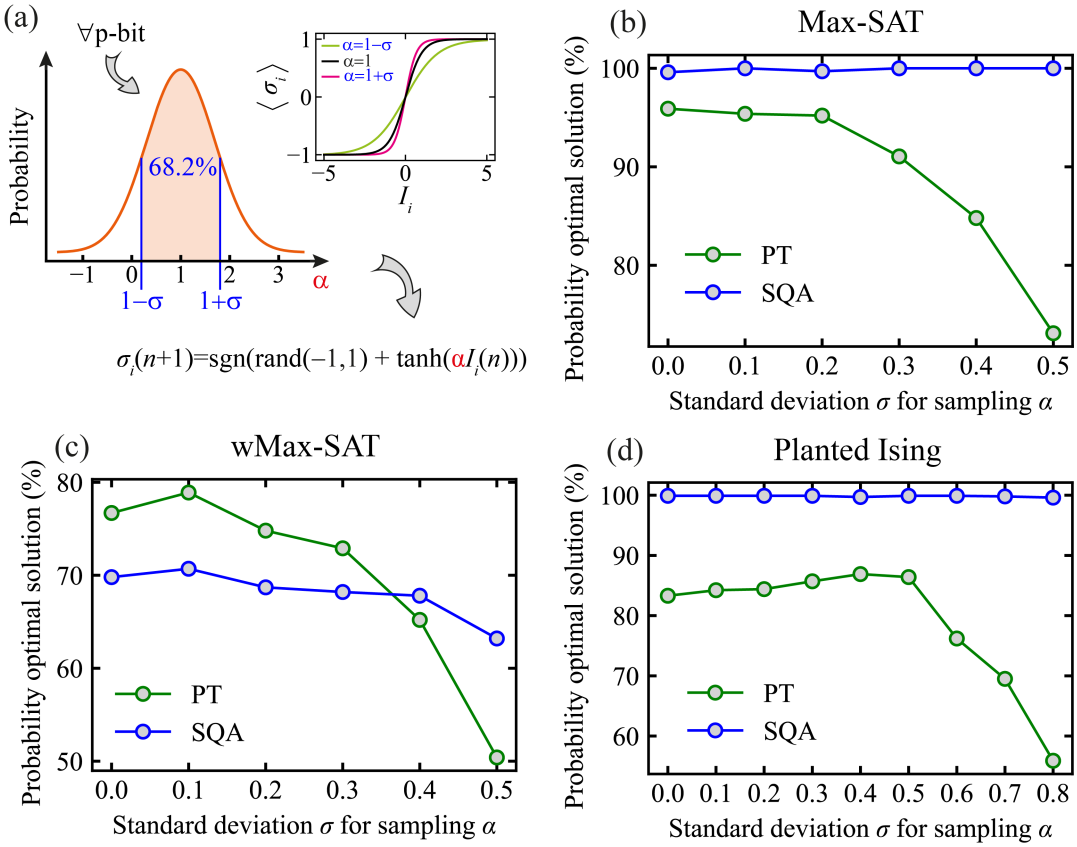

FIGURE 4.25: (a) A schematic representation illustrates the computation of variability of each p-bit in PC simulations. For each p-bit, a different slope α is sampled in a Gaussian distribution with unitary mean and different standard deviation σ. Inset: ideal curve of the p-bit (black line), and two representative curves, one for $\alpha = 1 - \sigma$ (green line) and the other for $\alpha = 1 + \sigma$ (magenta line). (b)-(d) Probability of obtaining the optimal solution over 100 runs, as a function of increasing variability in (b) Max-SAT (c) wMax-SAT and (d) planted Ising with Pegasus topology graph.

4.8 Conclusions

Ising models have proven to be effective tools for addressing NP-hard problems, particularly COPs. Among the many IM paradigms, our focus lies on PC. In this chapter, we have provided a detailed description of the PC solver, designed to address any problem that can be mapped into an Ising model. The implementation includes different energy minimization algorithms, and their performance across different problems is compared. The hardware realization of PC leverages MTJs as p-bits. Our studies reveal that the SQA algorithm emerges as the most robust choice in terms of handling of device-to-device variations.

Bibliography

[1] G. Bertotti, *Hysteresis in Magnetism*. Elsevier, 1998, ISBN: 9780120932702. DOI: 10.1016/B978-0-12-093270-2.X5048-X.

[2] L. Landau and E. Lifshitz, "On the theory of the dispersion of magnetic permeability in ferromagnetic bodies," in Elsevier, 1992, vol. 169, pp. 51–65. DOI: 10.1016/B978-0-08-036364-6.50008-9. [Online]. Available: https://linkinghub.elsevier.com/retrieve/pii/B9780080363646500089.

[3] W. F. Brown, *Micromagnetics*. lnterscience Tracts on Physics and Astronomy, 1963.

[4] W. F. Brown, "Micromagnetics, Domains, and Resonance," *Journal of Applied Physics*, vol. 30, S62–S69, 4 Apr. 1959, ISSN: 0021-8979. DOI: 10.1063/1.2185970.

[5] L Lopez-Diaz *et al.*, "Micromagnetic simulations using Graphics Processing Units," *Journal of Physics D: Applied Physics*, vol. 45, p. 323 001, 32 2012, ISSN: 0022-3727. DOI: 10.1088/0022-3727/45/32/323001.

[6] I. Dzyaloshinsky, "A thermodynamic theory of "weak" ferromagnetism of antiferromagnetics," *Journal of Physics and Chemistry of Solids*, vol. 4, pp. 241–255, 4 Jan. 1958, ISSN: 00223697. DOI: 10.1016/0022-3697(58)90076-3.

[7] T. Moriya, "New Mechanism of Anisotropic Superexchange Interaction," *Physical Review Letters*, vol. 4, pp. 228–230, 5 Mar. 1960, ISSN: 0031-9007. DOI: 10.1103/PhysRevLett.4.228.

[8] G. Finocchio *et al.*, "Magnetic skyrmions: From fundamental to applications," *Journal of Physics D: Applied Physics*, vol. 49, 42 2016, ISSN: 13616463. DOI: 10.1088/0022-3727/49/42/423001.

[9] S. Rohart and A. Thiaville, "Skyrmion confinement in ultrathin film nanostructures in the presence of Dzyaloshinskii-Moriya interaction," *Physical Review B*, vol. 88, p. 184 422, 18 Nov. 2013, ISSN: 1098-0121. DOI: 10.1103/PhysRevB.88.184422.

[10] R. Tomasello, M. Carpentieri, and G. Finocchio, "Influence of the Dzyaloshinskii-Moriya interaction on the spin-torque diode effect," *Journal of Applied Physics*, vol. 115, pp. 2012–2015, 17 2014, ISSN: 10897550. DOI: 10.1063/1.4867750.

[11] A. J. Newell, W. Williams, and D. J. Dunlop, "A generalization of the demagnetizing tensor for nonuniform magnetization," *Journal of Geophysical Research: Solid Earth*, vol. 98, pp. 9551–9555, B6 Jun. 1993, ISSN: 0148-0227. DOI: 10.1029/93JB00694.

[12] D. F. C. de Almeida, "Spintronic micromagnetic simulations using parallel computations," June Jul. 2013. DOI: 10.14201/gredos.122956.

[13] J. C. Slonczewski, "Current-driven excitation of magnetic multilayers," *Journal of Magnetism and Magnetic Materials*, vol. 159, pp. L1–L7, 1-2 Jun. 1996, ISSN: 03048853. DOI: 10.1016/0304-8853(96)00062-5.

[14] L Berger, "Emission of spin waves by a magnetic multilayer traversed by a current," *Physical Review B*, vol. 54, pp. 9353–9358, 13 Oct. 1996, ISSN: 0163-1829. DOI: 10.1103/PhysRevB.54.9353.

[15] X. Fong *et al.*, "Spin-Transfer Torque Devices for Logic and Memory: Prospects and Perspectives," *IEEE Transactions on Computer-Aided Design of Integrated Circuits and Systems*, vol. 35, pp. 1–22, 1 Jan. 2016, ISSN: 0278-0070. DOI: 10.1109/TCAD.2015.2481793.

[16] A. Meo *et al.*, "Spin-transfer and spin-orbit torques in the Landau–Lifshitz–Gilbert equation," *Journal of Physics: Condensed Matter*, vol. 35, p. 025 801, 2 Jan. 2023, ISSN: 0953-8984. DOI: 10.1088/1361-648X/ac9c80.

[17] S. Zhang, P. M. Levy, and A. Fert, "Mechanisms of Spin-Polarized Current-Driven Magnetization Switching," *Physical Review Letters*, vol. 88, p. 236 601, 23 May 2002, ISSN: 0031-9007. DOI: 10.1103/PhysRevLett.88.236601.

[18] J. C. Sankey *et al.*, "Measurement of the spin-transfer-torque vector in magnetic tunnel junctions," *Nature Physics*, vol. 4, pp. 67–71, 1 Jan. 2008, ISSN: 1745-2473. DOI: 10.1038/nphys783.

[19] H. Kubota *et al.*, "Quantitative measurement of voltage dependence of spin-transfer torque in MgO-based magnetic tunnel junctions," *Nature Physics*, vol. 4, pp. 37–41, 1 Jan. 2008, ISSN: 1745-2473. DOI: 10.1038/nphys784.

[20] A. Chanthbouala *et al.*, "Vertical-current-induced domain-wall motion in MgO-based magnetic tunnel junctions with low current densities," *Nature Physics*, vol. 7, pp. 626–630, 8 Aug. 2011, ISSN: 1745-2473. DOI: 10.1038/nphys1968.

[21] A. A. Timopheev *et al.*, "Respective influence of in-plane and out-of-plane spin-transfer torques in magnetization switching of perpendicular magnetic tunnel junctions," *Physical Review B*, vol. 92, p. 104 430, 10 Sep. 2015, ISSN: 1098-0121. DOI: 10.1103/PhysRevB.92.104430.

[22] J. E. Hirsch, "Spin Hall Effect," *Physical Review Letters*, vol. 83, pp. 1834–1837, 9 Aug. 1999, ISSN: 0031-9007. DOI: 10.1103/PhysRevLett.83.1834.

[23] P. K. Amiri *et al.*, "Electric-Field-Controlled Magnetoelectric RAM: Progress, Challenges, and Scaling," *IEEE Transactions on Magnetics*, vol. 51, pp. 1–7, 11 Nov. 2015, ISSN: 0018-9464. DOI: 10.1109/TMAG.2015.2443124.

[24] P. K. Amiri and K. L. Wang, "VOLTAGE-CONTROLLED MAGNETIC ANISOTROPY IN SPINTRONIC DEVICES," *SPIN*, vol. 02, p. 1 240 002, 03 Sep. 2012, ISSN: 2010-3247. DOI: 10.1142/S2010324712400024.

[25] W.-G. Wang, M. Li, S. Hageman, and C. L. Chien, "Electric-field-assisted switching in magnetic tunnel junctions," *Nature Materials*, vol. 11, pp. 64–68, 1 Jan. 2012, ISSN: 1476-1122. DOI: 10.1038/nmat3171.

[26] T. Nozaki *et al.*, "Recent Progress in the Voltage-Controlled Magnetic Anisotropy Effect and the Challenges Faced in Developing Voltage-Torque MRAM," *Micromachines*, vol. 10, p. 327, 5 May 2019, ISSN: 2072-666X. DOI: 10.3390/mi10050327.

[27] F. Ibrahim *et al.*, "Anatomy of electric field control of perpendicular magnetic anisotropy at Fe/MgO interfaces," *Physical Review B*, vol. 93, p. 014 429, 1 Jan. 2016, ISSN: 2469-9950. DOI: 10.1103/PhysRevB.93.014429.

[28] F. Bonell *et al.*, "Reversible change in the oxidation state and magnetic circular dichroism of Fe driven by an electric field at the FeCo/MgO interface," *Applied Physics Letters*, vol. 102, 15 Apr. 2013, ISSN: 0003-6951. DOI: 10.1063/1.4802030.

[29] S. E. Barnes, J. Ieda, and S. Maekawa, "Rashba Spin-Orbit Anisotropy and the Electric Field Control of Magnetism," *Scientific Reports*, vol. 4, p. 4105, 1 Feb. 2014, ISSN: 2045-2322. DOI: 10.1038/srep04105.

[30] L. Xu and S. Zhang, "Electric field control of interface magnetic anisotropy," *Journal of Applied Physics*, vol. 111, pp. 2012–2015, 7 Apr. 2012, ISSN: 0021-8979. DOI: 10.1063/1.3670002.

[31] V. B. Naik *et al.*, "Effect of electric-field on the perpendicular magnetic anisotropy and strain properties in CoFeB/MgO magnetic tunnel junctions," *Applied Physics Letters*, vol. 105, 5 Aug. 2014, ISSN: 0003-6951. DOI: 10.1063/1.4892410.

[32] W. Kang *et al.*, "Modeling and Exploration of the Voltage-Controlled Magnetic Anisotropy Effect for the Next-Generation Low-Power and High-Speed MRAM Applications," *IEEE Transactions on Nanotechnology*, vol. 16, pp. 387–395, 3 May 2017, ISSN: 1536-125X. DOI: 10.1109/TNANO.2017.2660530.

[33] H. Lee *et al.*, "Analysis and Compact Modeling of Magnetic Tunnel Junctions Utilizing Voltage-Controlled Magnetic Anisotropy," *IEEE Transactions on Magnetics*, vol. 54, pp. 1–9, 4 Apr. 2018, ISSN: 0018-9464. DOI: 10.1109/TMAG.2017.2788010.

[34] T. Nozaki *et al.*, "Large Voltage-Induced Changes in the Perpendicular Magnetic Anisotropy of an MgO-Based Tunnel Junction with an Ultrathin Fe Layer," *Physical Review Applied*, vol. 5, pp. 1–10, 4 2016, ISSN: 23317019. DOI: 10.1103/PhysRevApplied.5.044006.

[35] F. García-Redondo, P. Prabhat, M. Bhargava, and C. Dray, "A compact model for scalable MTJ simulation," *SMACD / PRIME 2021 - International Conference on Synthesis, Modeling, Analysis and Simulation Methods and Applications to Circuit Design and 16th Conference on PhD Research in Microelectronics and Electronics*, pp. 92–95, July 2021.

[36] W. Brown, "Thermal fluctuation of fine ferromagnetic particles," *IEEE Transactions on Magnetics*, vol. 15, pp. 1196–1208, 5 Sep. 1979, ISSN: 0018-9464. DOI: 10.1109/TMAG.1979.1060329.

[37] V. K. Joshi, P. Barla, S. Bhat, and B. K. Kaushik, "From MTJ Device to Hybrid CMOS/MTJ Circuits: A Review," *IEEE Access*, vol. 8, pp. 194 105–194 146, October 2020, ISSN: 2169-3536. DOI: 10.1109/ACCESS.2020.3033023.

[38] A. S. Jenkins *et al.*, "Electrical characterisation of higher order spin wave modes in vortex-based magnetic tunnel junctions," *Communications Physics*, vol. 4, pp. 1–7, 1 2021, ISSN: 23993650. DOI: 10.1038/s42005-021-00614-3.

[39] S. Li *et al.*, "Experimental demonstration of skyrmionic magnetic tunnel junction at room temperature," *Science Bulletin*, vol. 67, pp. 691–699, 7 2022, ISSN: 20959281. DOI: 10.1016/j.scib.2022.01.016.

[40] Y. Guang *et al.*, "Electrical Detection of Magnetic Skyrmions in a Magnetic Tunnel Junction," *Advanced Electronic Materials*, vol. 9, pp. 1–8, 1 2023, ISSN: 2199160X. DOI: 10.1002/aelm.202200570.

[41] T. Scheike, Z. Wen, H. Sukegawa, and S. Mitani, "631% room temperature tunnel magnetoresistance with large oscillation effect in CoFe/MgO/CoFe(001) junctions," *Applied Physics Letters*, vol. 122, 11 Mar. 2023, ISSN: 0003-6951. DOI: 10.1063/5.0145873.

[42] J. C. Slonczewski, "Conductance and exchange coupling of two ferromagnets separated by a tunneling barrier," *Physical Review B*, vol. 39, pp. 6995–7002, 10 Apr. 1989, ISSN: 0163-1829. DOI: 10.1103/PhysRevB.39.6995.

[43] E. Kowalska *et al.*, "Spin-transfer dynamics in MgO-based magnetic tunnel junctions with an out-of-plane magnetized free layer and an in-plane polarizer," *Physical Review B*, vol. 101, p. 024 430, 2 Jan. 2020, ISSN: 2469-9950. DOI: 10.1103/PhysRevB.101.024430.

[44] E. Deng *et al.*, "High-Frequency Low-Power Magnetic Full-Adder Based on Magnetic Tunnel Junction with Spin-Hall Assistance," *IEEE Transactions on Magnetics*, vol. 51, pp. 1–4, 11 2015, ISSN: 00189464. DOI: 10.1109/TMAG.2015.2449554.

[45] D. Marković *et al.*, "Detection of the Microwave Emission from a Spin-Torque Oscillator by a Spin Diode," *Physical Review Applied*, vol. 13, p. 044 050, 4 Apr. 2020, ISSN: 2331-7019. DOI: 10.1103/PhysRevApplied.13.044050.

[46] B. Fang *et al.*, "Giant spin-torque diode sensitivity in the absence of bias magnetic field," *Nature Communications*, vol. 7, pp. 1–7, 2016, ISSN: 20411723. DOI: 10.1038/ncomms11259.

[47] A. Slavin and V. Tiberkevich, "Nonlinear Auto-Oscillator Theory of Microwave Generation by Spin-Polarized Current," *IEEE Transactions on Magnetics*, vol. 45, pp. 1875–1918, 4 Apr. 2009, ISSN: 0018-9464. DOI: 10.1109/TMAG.2008.2009935.

[48] Z. Zeng, G. Finocchio, and H. Jiang, "Spin transfer nano-oscillators," *Nanoscale*, vol. 5, p. 2219, 6 2013, ISSN: 2040-3364. DOI: 10.1039/c2nr33407k.

[49] K. D. Sattler, Ed., *Handbook of Nanophysics*. CRC Press, Sep. 2010, ISBN: 9781420075533. DOI: 10.1201/9781420075533.

[50] Z. Zeng *et al.*, "High-Power Coherent Microwave Emission from Magnetic Tunnel Junction Nano-oscillators with Perpendicular Anisotropy," *ACS Nano*, vol. 6, pp. 6115–6121, 7 Jul. 2012, ISSN: 1936-0851. DOI: 10.1021/nn301222v.

[51] Z. Zeng *et al.*, "Ultralow-current-density and bias-field-free spin-transfer nano-oscillator," *Scientific Reports*, vol. 3, p. 1426, 2013, ISSN: 20452322. DOI: 10.1038/srep01426.

[52] V. Tiberkevich, A. Slavin, and J.-V. Kim, "Microwave power generated by a spin-torque oscillator in the presence of noise," *Applied Physics Letters*, vol. 91, 19 Nov. 2007, ISSN: 0003-6951. DOI: 10.1063/1.2812546.

[53] J. V. Kim, V. Tiberkevich, and A. N. Slavin, "Generation linewidth of an auto-oscillator with a nonlinear frequency shift: Spin-torque nano-oscillator," *Physical Review Letters*, vol. 100, pp. 1–4, 1 2008, ISSN: 00319007. DOI: 10.1103/PhysRevLett.100.017207.

[54] P. N. Skirdkov and K. A. Zvezdin, "Spin-Torque Diodes: From Fundamental Research to Applications," *Annalen der Physik*, vol. 532, pp. 1–11, 6 2020, ISSN: 15213889. DOI: 10.1002/andp.201900460.

[55] A. A. Tulapurkar *et al.*, "Spin-torque diode effect in magnetic tunnel junctions," *Nature*, vol. 438, pp. 339–342, 7066 2005, ISSN: 14764687. DOI: 10.1038/nature04207.

[56] G. Finocchio *et al.*, "Perspectives on spintronic diodes," *Applied Physics Letters*, vol. 118, 16 Apr. 2021, ISSN: 0003-6951. DOI: 10.1063/5.0048947.

[57] L. Zhang *et al.*, "Ultrahigh detection sensitivity exceeding 10 5 V/W in spin-torque diode," *Applied Physics Letters*, vol. 113, p. 102 401, 10 Sep. 2018, ISSN: 0003-6951. DOI: 10.1063/1.5047547.

[58] J. Zhu *et al.*, "Voltage-Induced Ferromagnetic Resonance in Magnetic Tunnel Junctions," *Physical Review Letters*, vol. 108, p. 197 203, 19 May 2012, ISSN: 0031-9007. DOI: 10.1103/PhysRevLett.108.197203.

[59] J. C. Sankey *et al.*, "Spin-Transfer-Driven Ferromagnetic Resonance of Individual Nanomagnets," *Physical Review Letters*, vol. 96, p. 227 601, 22 Jun. 2006, ISSN: 0031-9007. DOI: 10.1103/PhysRevLett.96.227601.

[60] B. Fang *et al.*, "Experimental Demonstration of Spintronic Broadband Microwave Detectors and Their Capability for Powering Nanodevices,"

Physical Review Applied, vol. 11, p. 014 022, 1 Jan. 2019, ISSN: 2331-7019. DOI: 10.1103/PhysRevApplied.11.014022.

[61] L. Zhang *et al.*, "Enhanced Broad-band Radio Frequency Detection in Nanoscale Magnetic Tunnel Junction by Interface Engineering," *ACS Applied Materials and Interfaces*, vol. 11, pp. 29 382–29 387, 32 2019, ISSN: 19448252. DOI: 10.1021/acsami.9b06706.

[62] J. M. Algarín *et al.*, "High rectification sensitivity of radiofrequency signal through adiabatic stochastic resonance in nanoscale magnetic tunnel junctions," *Applied Physics Letters*, vol. 115, 19 Nov. 2019, ISSN: 0003-6951. DOI: 10.1063/1.5123466.

[63] R. Tomasello *et al.*, "Low-Frequency Nonresonant Rectification in Spin Diodes," *Physical Review Applied*, vol. 14, p. 024 043, 2 Aug. 2020, ISSN: 2331-7019. DOI: 10.1103/PhysRevApplied.14.024043.

[64] S. Miwa *et al.*, "Highly sensitive nanoscale spin-torque diode," *Nature Materials*, vol. 13, pp. 50–56, 1 Jan. 2014, ISSN: 1476-1122. DOI: 10.1038/nmat3778.

[65] A. S. Jenkins *et al.*, "Spin-torque resonant expulsion of the vortex core for an efficient radiofrequency detection scheme," *Nature Nanotechnology*, vol. 11, pp. 360–364, 4 2016, ISSN: 17483395. DOI: 10.1038/nnano.2015.295.

[66] X. Cheng, J. A. Katine, G. E. Rowlands, and I. N. Krivorotov, "Nonlinear ferromagnetic resonance induced by spin torque in nanoscale magnetic tunnel junctions," *Applied Physics Letters*, vol. 103, 8 Aug. 2013, ISSN: 0003-6951. DOI: 10.1063/1.4819179.

[67] L. Mazza *et al.*, "Computing with Injection-Locked Spintronic Diodes," *Physical Review Applied*, vol. 17, p. 014 045, 1 Jan. 2022, ISSN: 2331-7019. DOI: 10.1103/PhysRevApplied.17.014045.

[68] A. Meo *et al.*, "Magnetomechanical Accelerometer Based on Magnetic Tunnel Junctions," *Physical Review Applied*, vol. 20, p. 034 003, 3 Sep. 2023, ISSN: 2331-7019. DOI: 10.1103/PhysRevApplied.20.034003.

[69] A Giordano *et al.*, "Semi-implicit integration scheme for Landau-Lifshitz-Gilbert-Slonczewski equation," *Journal of Applied Physics*, vol. 111, p. 07D112, 7 Apr. 2012, ISSN: 00218979. DOI: 10.1063/1.3673428.

[70] E. Raimondo *et al.*, "Reliability of Neural Networks Based on Spintronic Neurons," *IEEE Magnetics Letters*, vol. 12, pp. 1–5, 2021, ISSN: 19493088. DOI: 10.1109/LMAG.2021.3100317.

[71] A. Grimaldi *et al.*, "Evaluating Spintronics-Compatible Implementations of Ising Machines," *Physical Review Applied*, vol. 20, p. 024 005, 2 Aug. 2023, ISSN: 23317019. DOI: 10.1103/PhysRevApplied.20.024005.

[72] Y. Shao *et al.*, "Probabilistic computing with voltage-controlled dynamics in magnetic tunnel junctions," *Nanotechnology*, vol. 34, p. 495 203, 49 Dec. 2023, ISSN: 0957-4484. DOI: 10.1088/1361-6528/acf6c7.

[73] H. H. Ibrahim *et al.*, "Radio Frequency Energy Harvesting Technologies: A Comprehensive Review on Designing, Methodologies, and Potential Applications," *Sensors*, vol. 22, p. 4144, 11 May 2022, ISSN: 1424-8220. DOI: 10.3390/s22114144.

[74] U. Olgun, C.-C. Chen, and J. L. Volakis, "Wireless power harvesting with planar rectennas for 2.45 GHz RFIDs," IEEE, Aug. 2010, pp. 329–331, ISBN: 978-1-4244-5155-5. DOI: 10.1109/URSI-EMTS.2010.5637008.

[75] R. Sharma *et al.*, "Electrically connected spin-torque oscillators array for 2.4 GHz WiFi band transmission and energy harvesting," *Nature Communications*, vol. 12, p. 2924, 1 May 2021, ISSN: 2041-1723. DOI: 10.1038/s41467-021-23181-1.

[76] D. Eddy and D. Sparks, "Application of MEMS technology in automotive sensors and actuators," *Proceedings of the IEEE*, vol. 86, pp. 1747–1755, 8 1998, ISSN: 00189219. DOI: 10.1109/5.704280.

[77] A. D'Alessandro, S. Scudero, and G. Vitale, "A Review of the Capacitive MEMS for Seismology," *Sensors*, vol. 19, p. 3093, 14 Jul. 2019, ISSN: 1424-8220. DOI: 10.3390/s19143093.

[78] R. Xu, S. Zhou, and W. J. Li, "MEMS Accelerometer Based Nonspecific-User Hand Gesture Recognition," *IEEE Sensors Journal*, vol. 12, pp. 1166–1173, 5 May 2012, ISSN: 1530-437X. DOI: 10.1109/JSEN.2011.2166953.

[79] M. Benmessaoud and M. M. Nasreddine, "Optimization of MEMS capacitive accelerometer," *Microsystem Technologies*, vol. 19, pp. 713–720, 5 May 2013, ISSN: 0946-7076. DOI: 10.1007/s00542-013-1741-z.

[80] R. R. Katti, *ACCELEROMETER USING MAGNETIC TUNNEL JUNCTION*, 2021.

[81] R. R. Katti, *MAGNETIC SPIN HALL EFFECT SPINTRONIC ACCELEROMETER*, 2021. [Online]. Available: https://patents.google.com/patent/US11054438B2/en?oq=US11054438B2.

[82] R. R. Katti, *SPINTRONIC ACCELEROMETER*, 2020.

[83] M. Keshavarzi and J. Y. Hasani, "Design and optimization of fully differential capacitive MEMS accelerometer based on surface micromachining," *Microsystem Technologies*, vol. 25, pp. 1369–1377, 4 Apr. 2019, ISSN: 0946-7076. DOI: 10.1007/s00542-018-4187-5.

[84] R. Saha, K. Wu, D. Su, and J.-P. Wang, "Tunable magnetic skyrmions in spintronic nanostructures for cellular-level magnetic neurostimulation," *Journal of Physics D: Applied Physics*, vol. 52, no. 46, p. 465 002, Nov. 2019, ISSN: 0022-3727. DOI: 10.1088/1361-6463/ab39a7.

[85] T. H. R. Skyrme and P. R. S. L. A, "A non-linear field theory," *Proceedings of the Royal Society of London. Series A. Mathematical and Physical Sciences*, vol. 260, no. 1300, pp. 127–138, Feb. 1961, ISSN: 0080-4630. DOI: 10.1098/rspa.1961.0018.

[86] T. H. Skyrme, "A unified field theory of mesons and baryons," *Nuclear Physics*, vol. 31, no. C, pp. 556–569, 1962, ISSN: 00295582. DOI: 10.1016/0029-5582(62)90775-7.

[87] H. B. Braun, "Topological effects in nanomagnetism: From superparamagnetism to chiral quantum solitons," *Advances in Physics*, vol. 61, pp. 1–116, 1 2012, ISSN: 00018732. DOI: 10.1080/00018732.2012.663070.

[88] F. Büttner, I. Lemesh, and G. S. Beach, "Theory of isolated magnetic skyrmions: From fundamentals to room temperature applications," *Scientific Reports*, vol. 8, pp. 1–12, 1 2018, ISSN: 20452322. DOI: 10.1038/s41598-018-22242-8.

[89] U. Al Khawaja and H. Stoof, "Skyrmions in a ferromagnetic Bose–Einstein condensate," *Nature*, vol. 411, no. 6840, pp. 918–920, Jun. 2001, ISSN: 0028-0836. DOI: 10.1038/35082010.

[90] L. Du, A. Yang, A. V. Zayats, and X. Yuan, "Deep-subwavelength features of photonic skyrmions in a confined electromagnetic field with orbital angular momentum," *Nature Physics*, vol. 15, no. 7, pp. 650–654, Jul. 2019, ISSN: 1745-2473. DOI: 10.1038/s41567-019-0487-7.

[91] S. Tsesses *et al.*, "Optical skyrmion lattice in evanescent electromagnetic fields," *Science*, vol. 361, no. 6406, pp. 993–996, Sep. 2018, ISSN: 0036-8075. DOI: 10.1126/science.aau0227.

[92] A. Fert, N. Reyren, and V. Cros, "Magnetic skyrmions: advances in physics and potential applications," *Nature Reviews Materials*, vol. 2, no. 7, p. 17 031, Jun. 2017, ISSN: 2058-8437. DOI: 10.1038/natrevmats.2017.31.

[93] G. Finocchio *et al.*, "The promise of spintronics for unconventional computing," *Journal of Magnetism and Magnetic Materials*, vol. 521, p. 167 506, P1 2021, ISSN: 03048853. DOI: 10.1016/j.jmmm.2020.167506.

[94] G. Finocchio and C. Panagopoulos, Eds., *Magnetic Skyrmions and Their Applications*. Elsevier, 2021, ISBN: 9780128208151. DOI: 10.1016/C2019-0-02206-6.

[95] W. Kang *et al.*, "Skyrmion-Electronics: An Overview and Outlook," *Proceedings of the IEEE*, vol. 104, pp. 2040–2061, 10 2016, ISSN: 15582256. DOI: 10.1109/JPROC.2016.2591578.

[96] K. Everschor-Sitte, J. Masell, R. M. Reeve, and M. Kläui, "Perspective: Magnetic skyrmions - Overview of recent progress in an active research field," *Journal of Applied Physics*, vol. 124, 24 2018, ISSN: 10897550. DOI: 10.1063/1.5048972.

[97] R. Tomasello *et al.*, "A strategy for the design of skyrmion racetrack memories," *Scientific Reports*, vol. 4, pp. 1–7, 1 Oct. 2014, ISSN: 20452322. DOI: 10.1038/srep06784.

[98] T. Yokouchi *et al.*, "Pattern recognition with neuromorphic computing using magnetic field–induced dynamics of skyrmions," *Science Advances*, vol. 8, pp. 1–8, 39 2022, ISSN: 23752548. DOI: 10.1126/sciadv.abq5652.

[99] K. M. Song *et al.*, "Skyrmion-based artificial synapses for neuromorphic computing," *Nature Electronics*, vol. 3, pp. 148–155, 3 Mar. 2020, ISSN: 2520-1131. DOI: 10.1038/s41928-020-0385-0.

[100] H. Zhang *et al.*, "Stochastic Computing Implemented by Skyrmionic Logic Devices," *Physical Review Applied*, vol. 13, p. 1, 5 2020, ISSN: 23317019. DOI: 10.1103/PhysRevApplied.13.054049.

[101] J. Zázvorka *et al.*, "Thermal skyrmion diffusion used in a reshuffler device," *Nature Nanotechnology*, vol. 14, pp. 658–661, 7 Jul. 2019, ISSN: 1748-3387. DOI: 10.1038/s41565-019-0436-8.

[102] X. S. Wang, H. Y. Yuan, and X. R. Wang, "A theory on skyrmion size," *Communications Physics*, vol. 1, pp. 1–7, 1 2018, ISSN: 23993650. DOI: 10.1038/s42005-018-0029-0.

[103] X. Zhang *et al.*, "Skyrmion-electronics: Writing, deleting, reading and processing magnetic skyrmions toward spintronic applications," *Journal of Physics Condensed Matter*, vol. 32, 14 2020, ISSN: 1361648X. DOI: 10.1088/1361-648X/ab5488.

[104] F. Zheng *et al.*, "Direct Imaging of a Zero-Field Target Skyrmion and Its Polarity Switch in a Chiral Magnetic Nanodisk," *Physical Review Letters*, vol. 119, pp. 1–6, 19 2017, ISSN: 10797114. DOI: 10.1103/PhysRevLett.119.197205.

[105] X. Z. Yu *et al.*, "Real-space observation of a two-dimensional skyrmion crystal," *Nature*, vol. 465, pp. 901–904, 7300 Jun. 2010, ISSN: 0028-0836. DOI: 10.1038/nature09124.

[106] S. Woo *et al.*, "Observation of room-temperature magnetic skyrmions and their current-driven dynamics in ultrathin metallic ferromagnets," *Nature Materials*, vol. 15, pp. 501–506, 5 2016, ISSN: 14764660. DOI: 10.1038/nmat4593.

[107] C. Moreau-Luchaire *et al.*, "Additive interfacial chiral interaction in multilayers for stabilization of small individual skyrmions at room temperature," *Nature Nanotechnology*, vol. 11, pp. 444–448, 5 2016, ISSN: 17483395. DOI: 10.1038/nnano.2015.313.

[108] L. Kong *et al.*, "Observation of hybrid magnetic skyrmion bubbles in Fe3Sn2 nanodisks," *Physical Review B*, vol. 107, pp. 1–7, 17 2023, ISSN: 24699969. DOI: 10.1103/PhysRevB.107.174425.

[109] O. Boulle *et al.*, "Room temperature chiral magnetic skyrmion in ultrathin magnetic nanostructures," *Nature Nanotechnology*, vol. 11, pp. 449–454, January 2016, ISSN: 1748-3387. DOI: 10.1038/NNANO.2015.315.

[110] S. Zhang *et al.*, "Determination of chirality and density control of Néel-type skyrmions with in-plane magnetic field," *Communications Physics*, vol. 1, pp. 1–7, 1 2018, ISSN: 23993650. DOI: 10.1038/s42005-018-0040-5.

[111] A. Soumyanarayanan *et al.*, "Tunable room-temperature magnetic skyrmions in Ir/Fe/Co/Pt multilayers," *Nature Materials*, vol. 16, pp. 898–904, 9 2017, ISSN: 14764660. DOI: 10.1038/NMAT4934.

[112] O. Ylldlrlm *et al.*, "Tuning the Coexistence Regime of Incomplete and Tubular Skyrmions in Ferromagnetic/Ferrimagnetic/Ferromagnetic Trilayers," *ACS Applied Materials and Interfaces*, 2022, ISSN: 19448252. DOI: 10.1021/acsami.2c06608.

[113] H. Zhang *et al.*, "Magnetic skyrmions: materials, manipulation, detection, and applications in spintronic devices," *Materials Futures*, vol. 2, 3 2023, ISSN: 27525724. DOI: 10.1088/2752-5724/ace1df.

[114] W. Jiang *et al.*, "Blowing magnetic skyrmion bubbles," *Science*, vol. 349, no. 6245, pp. 283–286, Jul. 2015, ISSN: 0036-8075. DOI: 10.1126/science.aaa1442.

[115] D. Maccariello *et al.*, "Electrical detection of single magnetic skyrmions in metallic multilayers at room temperature," *Nature Nanotechnology*, vol. 13, pp. 233–237, 3 2018, ISSN: 17483395. DOI: 10.1038/s41565-017-0044-4.

[116] M. Grelier *et al.*, "Three-dimensional skyrmionic cocoons in magnetic multilayers," *Nature Communications*, vol. 13, p. 6843, 1 Nov. 2022, ISSN: 2041-1723. DOI: 10.1038/s41467-022-34370-x.

[117] W. Legrand *et al.*, "Hybrid chiral domain walls and skyrmions in magnetic multilayers," *Science Advances*, vol. 4, 7 2018, ISSN: 23752548. DOI: 10.1126/sciadv.aat0415.

[118] W. Li *et al.*, "Anatomy of Skyrmionic Textures in Magnetic Multilayers," *Advanced Materials*, vol. 31, pp. 1–7, 14 2019, ISSN: 15214095. DOI: 10.1002/adma.201807683.

[119] N. K. Duong *et al.*, "Magnetization reversal signatures of hybrid and pure Néel skyrmions in thin film multilayers," *APL Materials*, vol. 8, p. 111 112, 11 Nov. 2020, ISSN: 2166-532X. DOI: 10.1063/5.0022033.

[120] W. Legrand *et al.*, "Room-temperature stabilization of antiferromagnetic skyrmions in synthetic antiferromagnets," *Nature Materials*, vol. 19, pp. 34–42, 1 Jan. 2020, ISSN: 1476-1122. DOI: 10.1038/s41563-019-0468-3.

[121] R. Juge *et al.*, "Skyrmions in synthetic antiferromagnets and their nucleation via electrical current and ultra-fast laser illumination," *Nature Communications*, vol. 13, pp. 1–9, 1 2022, ISSN: 20411723. DOI: 10.1038/s41467-022-32525-4.

[122] S. S. Parkin and D. Mauri, "Spin engineering: Direct determination of the Ruderman-Kittel-Kasuya-Yosida far-field range function in ruthenium," *Physical Review B*, vol. 44, pp. 7131–7134, 13 1991, ISSN: 01631829. DOI: 10.1103/PhysRevB.44.7131.

[123] R. A. Duine, K.-J. Lee, S. S. P. Parkin, and M. D. Stiles, "Synthetic antiferromagnetic spintronics," *Nature Physics*, vol. 14, pp. 217–219, 3 Mar. 2018, ISSN: 1745-2473. DOI: 10.1038/s41567-018-0050-y.

[124] R Tomasello *et al.*, "Performance of synthetic antiferromagnetic racetrack memory: domain wall versus skyrmion," *Journal of Physics D: Applied Physics*, vol. 50, p. 325 302, 32 Aug. 2017, ISSN: 0022-3727. DOI: 10.1088/1361-6463/aa7a98.

[125] W. Jiang *et al.*, "Skyrmions in magnetic multilayers," *Physics Reports*, vol. 704, pp. 1–49, 2017, ISSN: 03701573. DOI: 10.1016/j.physrep.2017.08.001.

[126] R. Tomasello *et al.*, "Field-driven collapsing dynamics of skyrmions in magnetic multilayers," *Physical Review B*, vol. 107, pp. 1–9, 18 2023, ISSN: 24699969. DOI: 10.1103/PhysRevB.107.184416.

[127] Z. Wang *et al.*, "Thermal generation, manipulation and thermoelectric detection of skyrmions," *Nature Electronics*, vol. 3, pp. 672–679, 11 Nov. 2020, ISSN: 25201131. DOI: 10.1038/s41928-020-00489-2.

[128] R. Tomasello *et al.*, "Origin of temperature and field dependence of magnetic skyrmion size in ultrathin nanodots," *Physical Review B*, vol. 97, p. 060 402, 6 Feb. 2018, ISSN: 24699969. DOI: 10.1103/PhysRevB.97.060402.

[129] G. D. Skidmore, A. Kunz, C. E. Campbell, and E. D. Dahlberg, "Micromagnetic domain structures in cylindrical nickel dots," *Physical Review B - Condensed Matter and Materials Physics*, vol. 70, pp. 28–31, 1 2004, ISSN: 01631829. DOI: 10.1103/PhysRevB.70.012410.

[130] T. Liu *et al.*, "Reproducible formation of single magnetic bubbles in an array of patterned dots," *Journal of Physics D: Applied Physics*, vol. 49, 24 2016, ISSN: 13616463. DOI: 10.1088/0022-3727/49/24/245002.

[131] J. Choi *et al.*, "Magnetic bubble domain phase at the spin reorientation transition of ultrathin Fe/Ni/Cu(001) film," *Physical Review Letters*, vol. 98, pp. 18–21, 20 2007, ISSN: 00319007. DOI: 10.1103/PhysRevLett.98.207205.

[132] S. Komineas, C. A. Vaz, J. A. Bland, and N. Papanicolaou, "Bubble domains in disc-shaped ferromagnetic particles," *Physical Review B - Condensed Matter and Materials Physics*, vol. 71, pp. 11–14, 6 2005, ISSN: 10980121. DOI: 10.1103/PhysRevB.71.060405.

[133] C. Moutafis *et al.*, "Magnetic bubbles in FePt nanodots with perpendicular anisotropy," *Physical Review B - Condensed Matter and Materials Physics*, vol. 76, pp. 1–5, 10 2007, ISSN: 10980121. DOI: 10.1103/PhysRevB.76.104426.

[134] K. Everschor, M. Garst, R. A. Duine, and A. Rosch, "Current-induced rotational torques in the skyrmion lattice phase of chiral magnets," *Physical Review B - Condensed Matter and Materials Physics*, vol. 84, pp. 1–10, 6 2011, ISSN: 10980121. DOI: 10.1103/PhysRevB.84.064401.

[135] A. A. Thiele, "Steady-State Motion of Magnetic Domains," *Physical Review Letters*, vol. 30, pp. 230–233, 6 Feb. 1973, ISSN: 0031-9007. DOI: 10.1103/PhysRevLett.30.230.

[136] F. Büttner *et al.*, "Dynamics and inertia of skyrmionic spin structures," *Nature Physics*, vol. 11, pp. 225–228, 3 2015, ISSN: 17452481. DOI: 10.1038/nphys3234.

[137] X. Zhang, Y. Zhou, and M. Ezawa, "Magnetic bilayer-skyrmions without skyrmion Hall effect," *Nature Communications*, vol. 7, p. 10 293, 2016, ISSN: 2041-1723. DOI: 10.1038/ncomms10293.

[138] J. Iwasaki, M. Mochizuki, and N. Nagaosa, "Universal current-velocity relation of skyrmion motion in chiral magnets," *Nature Communications*, vol. 4, 2013, ISSN: 20411723. DOI: 10.1038/ncomms2442.

[139] G. Tatara, H. Kohno, and J. Shibata, "Microscopic approach to current-driven domain wall dynamics," *Physics Reports*, vol. 468, pp. 213–301, 6 2008, ISSN: 03701573. DOI: 10.1016/j.physrep.2008.07.003.

[140] W. Jiang *et al.*, "Direct observation of the skyrmion Hall effect," *Nature Physics*, vol. 13, pp. 162–169, 2 2017, ISSN: 17452481. DOI: 10.1038/nphys3883.

[141] K. Zeissler *et al.*, "Diameter-independent skyrmion Hall angle observed in chiral magnetic multilayers," *Nature Communications*, vol. 11, pp. 1–11, 1 2020, ISSN: 20411723. DOI: 10.1038/s41467-019-14232-9.

[142] K. Litzius *et al.*, "Skyrmion Hall effect revealed by direct time-resolved X-ray microscopy," *Nature Physics*, vol. 13, pp. 170–175, 2 2017, ISSN: 17452481. DOI: 10.1038/nphys4000.

[143] A. Casiraghi *et al.*, "Individual skyrmion manipulation by local magnetic field gradients," *Communications Physics*, vol. 2, p. 145, 1 Dec. 2019, ISSN: 2399-3650. DOI: 10.1038/s42005-019-0242-5.

[144] S. L. Zhang *et al.*, "Manipulation of skyrmion motion by magnetic field gradients," *Nature Communications*, vol. 9, 1 2018, ISSN: 20411723. DOI: 10.1038/s41467-018-04563-4.

[145] R. Tomasello *et al.*, "Chiral skyrmions in an anisotropy gradient," *Physical Review B*, vol. 98, pp. 1–8, 2 2018, ISSN: 24699969. DOI: 10.1103/PhysRevB.98.024421.

[146] K. Litzius *et al.*, "The role of temperature and drive current in skyrmion dynamics," *Nature Electronics*, vol. 3, pp. 30–36, 1 Jan. 2020, ISSN: 2520-1131. DOI: 10.1038/s41928-019-0359-2.

[147] E. Raimondo *et al.*, "Temperature-Gradient-Driven Magnetic Skyrmion Motion," *Physical Review Applied*, vol. 18, 2 May 2022, ISSN: 23317019. DOI: 10.1103/PhysRevApplied.18.024062.

[148] D. J. Kim *et al.*, "Observation of transverse spin Nernst magnetoresistance induced by thermal spin current in ferromagnet/non-magnet bilayers," *Nature Communications*, vol. 8, pp. 1–6, 1 2017, ISSN: 20411723. DOI: 10.1038/s41467-017-01493-5.

[149] A. A. Kovalev and Y. Tserkovnyak, "Thermoelectric spin transfer in textured magnets," *Physical Review B - Condensed Matter and Materials Physics*, vol. 80, pp. 1–4, 10 2009, ISSN: 10980121. DOI: 10.1103/PhysRevB.80.100408.

[150] L. Kong and J. Zang, "Dynamics of an insulating skyrmion under a temperature gradient," *Physical Review Letters*, vol. 111, pp. 1–5, 6 2013, ISSN: 00319007. DOI: 10.1103/PhysRevLett.111.067203.

[151] C. Gong, Y. Zhou, and G. Zhao, "Dynamics of magnetic skyrmions under temperature gradients," *Applied Physics Letters*, vol. 120, p. 52 402, 5 Jan. 2022, ISSN: 0003-6951. DOI: 10.1063/5.0080778.

[152] W. Zhao and G. Prenat, *Spintronics-based computing*, W. Zhao and G. Prenat, Eds. Springer International Publishing, 2015, pp. 1–253, ISBN: 9783319151809. DOI: 10.1007/978-3-319-15180-9.

[153] K.-M. Lee, J. W. Choi, J. Sok, and B.-C. Min, "Temperature dependence of the interfacial magnetic anisotropy in W/CoFeB/MgO," *AIP Advances*, vol. 7, p. 065 107, 6 Jun. 2017, ISSN: 2158-3226. DOI: 10.1063/1.4985720.

[154] E. Grimaldi *et al.*, "Single-shot dynamics of spin–orbit torque and spin transfer torque switching in three-terminal magnetic tunnel junctions," *Nature Nanotechnology*, vol. 15, pp. 111–117, 2 Feb. 2020, ISSN: 1748-3387. DOI: 10.1038/s41565-019-0607-7.

[155] S. H. Yang, K. S. Ryu, and S. Parkin, "Domain-wall velocities of up to 750 m s-1 driven by exchange-coupling torque in synthetic antiferromagnets," *Nature Nanotechnology*, vol. 10, pp. 221–226, 3 2015, ISSN: 17483395. DOI: 10.1038/nnano.2014.324.

[156] M. Björck, M. Hedlund, and G. Andersson, "Magnetic moments in Fe-Co/Pt superlattices," *Journal of Magnetism and Magnetic Materials*, vol. 320, pp. 2660–2664, 21 Nov. 2008, ISSN: 03048853. DOI: 10.1016/j.jmmm.2008.05.029.

[157] P. Asselin *et al.*, "Constrained Monte Carlo method and calculation of the temperature dependence of magnetic anisotropy," *Physical Review B - Condensed Matter and Materials Physics*, vol. 82, 5 Aug. 2010, ISSN: 10980121. DOI: 10.1103/PhysRevB.82.054415.

[158] U. Atxitia *et al.*, "Multiscale modeling of magnetic materials: Temperature dependence of the exchange stiffness," *Physical Review B - Condensed Matter and Materials Physics*, vol. 82, pp. 1–10, 13 2010, ISSN: 10980121. DOI: 10.1103/PhysRevB.82.134440.

[159] G. Yu *et al.*, "Room-Temperature Creation and Spin-Orbit Torque Manipulation of Skyrmions in Thin Films with Engineered Asymmetry," *Nano Letters*, vol. 16, pp. 1981–1988, 3 2016, ISSN: 15306992. DOI: 10.1021/acs.nanolett.5b05257.

[160] S. Tacchi *et al.*, "Interfacial Dzyaloshinskii-Moriya Interaction in Pt/CoFeB Films: Effect of the Heavy-Metal Thickness," *Physical Review Letters*, vol. 118, pp. 1–6, 14 2017, ISSN: 10797114. DOI: 10.1103/PhysRevLett.118.147201.

[161] G. Finocchio *et al.*, "Micromagnetic understanding of stochastic resonance driven by spin-transfer-torque," *Physical Review B - Condensed Matter and Materials Physics*, vol. 83, pp. 1–9, 13 2011, ISSN: 10980121. DOI: 10.1103/PhysRevB.83.134402.

[162] L. Borjas *et al.*, "Polimorfismos intragénicos de los genes de los factores VIII y IX y su utilidad en el diagnóstico indirecto de portadoras de Hemofilias A y B," *Investigacion Clinica*, vol. 51, pp. 391–401, 3 2010, ISSN: 05355133.

[163] Y. LeCun, Y. Bengio, and G. Hinton, "Deep learning," *Nature*, vol. 521, pp. 436–444, 7553 May 2015, ISSN: 0028-0836. DOI: 10.1038/nature14539.

[164] C. Li *et al.*, "Efficient and self-adaptive in-situ learning in multilayer memristor neural networks," *Nature Communications*, vol. 9, p. 2385, 1 Jun. 2018, ISSN: 2041-1723. DOI: 10.1038/s41467-018-04484-2.

[165] C. Zhang *et al.*, "Optimizing FPGA-based Accelerator Design for Deep Convolutional Neural Networks," ACM, Feb. 2015, pp. 161–170, ISBN: 9781450333153. DOI: 10.1145/2684746.2689060.

[166] J. Grollier *et al.*, "Neuromorphic spintronics," *Nature Electronics*, vol. 3, pp. 360–370, 7 Jul. 2020, ISSN: 2520-1131. DOI: 10.1038/s41928-019-0360-9.

[167] S. Liu *et al.*, "Controllable Reset Behavior in Domain Wall–Magnetic Tunnel Junction Artificial Neurons for Task-Adaptable Computation," *IEEE Magnetics Letters*, vol. 12, pp. 1–5, 2021, ISSN: 1949-307X. DOI: 10.1109/LMAG.2021.3069666.

[168] Y. Shao *et al.*, "Implementation of Artificial Neural Networks using Magnetoresistive Random-Access Memory-based Stochastic Computing Units," *IEEE Magnetics Letters*, vol. 11, pp. 1–1, 2020 2021, ISSN: 1949-307X. DOI: 10.1109/LMAG.2021.3071084.

[169] R. Tomasello *et al.*, "Role of magnetic skyrmions for the solution of the shortest path problem," *Journal of Magnetism and Magnetic Materials*, vol. 532, p. 167 977, March Aug. 2021, ISSN: 03048853. DOI: 10.1016/j.jmmm.2021.167977.

[170] F. Rosenblatt, "The perceptron: A probabilistic model for information storage and organization in the brain," *Psychological Review*, vol. 65, pp. 386–408, 6 1958, ISSN: 0033295X. DOI: 10.1037/h0042519.

[171] W. S. McCulloch and W. Pitts, "A logical calculus of the ideas immanent in nervous activity," *The Bulletin of Mathematical Biophysics*, vol. 5, pp. 115–133, 4 Dec. 1943, ISSN: 00074985. DOI: 10.1007/BF02478259/METRICS.

[172] S. Ruder, "An overview of gradient descent optimization algorithms," pp. 1–14, Sep. 2016.

[173] Y. Zhao, B. Deng, and Z. Wang, "Analysis and study of perceptron to solve XOR problem," *Proceedings - 2nd International Workshop on Autonomous Decentralized System, IWADS 2002*, pp. 168–173, 2002. DOI: 10.1109/IWADS.2002.1194667.

[174] N. Srivastava *et al.*, "Dropout: A simple way to prevent neural networks from overfitting," *Journal of Machine Learning Research*, vol. 15, pp. 1929–1958, 2014, ISSN: 15337928.

[175] O. Russakovsky *et al.*, "ImageNet Large Scale Visual Recognition Challenge," *International Journal of Computer Vision*, vol. 115, pp. 211–252, 3 2015, ISSN: 15731405. DOI: 10.1007/s11263-015-0816-y.

[176] A. Krizhevsky, I. Sutskever, and G. E. Hinton, "ImageNet Classification with Deep Convolutional Neural Networks," *Advances in Neural Information Processing Systems*, vol. 25, 2012.

[177] S. Albawi, T. A. Mohammed, and S. Al-Zawi, "Understanding of a convolutional neural network," vol. 2018-Janua, IEEE, Aug. 2017, pp. 1–6, ISBN: 978-1-5386-1949-0. DOI: 10.1109/ICEngTechnol.2017.8308186.

[178] H. Lee, R. Grosse, R. Ranganath, and A. Y. Ng, "Unsupervised learning of hierarchical representations with convolutional deep belief networks," *Communications of the ACM*, vol. 54, pp. 95–103, 10 Oct. 2011, ISSN: 0001-0782. DOI: 10.1145/2001269.2001295.

[179] S. J. Pan and Q. Yang, "A survey on transfer learning," *IEEE Transactions on Knowledge and Data Engineering*, vol. 22, pp. 1345–1359, 10 2010, ISSN: 10414347. DOI: 10.1109/TKDE.2009.191.

[180] J. Deng *et al.*, "ImageNet: A large-scale hierarchical image database," *2009 IEEE Conference on Computer Vision and Pattern Recognition*, pp. 248–255, 2010. DOI: 10.1109/cvpr.2009.5206848.

[181] J. Yosinski, J. Clune, Y. Bengio, and H. Lipson, "How transferable are features in deep neural networks?" *Advances in Neural Information Processing Systems*, vol. 4, pp. 3320–3328, January 2014, ISSN: 10495258.

[182] G. Hinton, O. Vinyals, and J. Dean, "Distilling the Knowledge in a Neural Network," Mar. 2015.

[183] J. Gou, B. Yu, S. J. Maybank, and D. Tao, "Knowledge Distillation: A Survey," *International Journal of Computer Vision*, vol. 129, pp. 1789–1819, 6 Jun. 2021, ISSN: 0920-5691. DOI: 10.1007/s11263-021-01453-z.

[184] X. Liu, X. Wang, and S. Matwin, "Improving the interpretability of deep neural networks with knowledge distillation," *IEEE International Conference on Data Mining Workshops, ICDMW*, vol. 2018-Novem, pp. 905–912, 2019, ISSN: 23759259. DOI: 10.1109/ICDMW.2018.00132.

[185] D. Marković, A. Mizrahi, D. Querlioz, and J. Grollier, "Physics for neuromorphic computing," *Nature Reviews Physics*, vol. 2, pp. 499–510, 9 2020, ISSN: 25225820. DOI: 10.1038/s42254-020-0208-2.

[186] J. Devlin, M.-W. Chang, K. Lee, and K. Toutanova, "BERT: Pre-training of Deep Bidirectional Transformers for Language Understanding," *NAACL HLT 2019 - 2019 Conference of the North American Chapter of the Association for Computational Linguistics: Human Language Technologies - Proceedings of the Conference*, vol. 1, pp. 4171–4186, Mlm Oct. 2018.

[187] E. Strubell, A. Ganesh, and A. McCallum, "Energy and policy considerations for modern deep learning research," *AAAI 2020 - 34th AAAI Conference on Artificial Intelligence*, pp. 1393–13 696, 2020, ISSN: 2159-5399. DOI: 10.1609/aaai.v34i09.7123.

[188] D. Amodei and D. Hernandez, "AI and Compute," *Blog Open AI*, pp. 1–11, 2018.

[189] *OpenAI*. [Online]. Available: https://openai.com/.

[190] Semiconductor Industry Association and others, *Rebooting the IT Revolution: A Call to Action*, 2015. [Online]. Available: https://eps.ieee.org/images/files/Roadmap/Rebooting-the-Revolution-SIA-SRC-09-2015.pdf.

[191] "Big data needs a hardware revolution," *Nature*, vol. 554, pp. 145–146, 7691 Feb. 2018, ISSN: 0028-0836. DOI: 10.1038/d41586-018-01683-1.

[192] C. Zhu *et al.*, "Optical synaptic devices with ultra-low power consumption for neuromorphic computing," *Light: Science and Applications*, vol. 11, 1 2022, ISSN: 20477538. DOI: 10.1038/s41377-022-01031-z.

[193] X. Lin *et al.*, "All-optical machine learning using diffractive deep neural networks," *Science*, vol. 361, pp. 1004–1008, 6406 2018, ISSN: 10959203. DOI: 10.1126/science.aat8084.

[194] J. Torrejon *et al.*, "Neuromorphic computing with nanoscale spintronic oscillators," *Nature*, vol. 547, pp. 428–431, 7664 2017, ISSN: 14764687. DOI: 10.1038/nature23011.

[195] A. Kurenkov, S. Fukami, and H. Ohno, "Neuromorphic computing with antiferromagnetic spintronics," *Journal of Applied Physics*, vol. 128, 1 Jul. 2020, ISSN: 0021-8979. DOI: 10.1063/5.0009482.

[196] J. Cai *et al.*, "Voltage-Controlled Spintronic Stochastic Neuron Based on a Magnetic Tunnel Junction," *Physical Review Applied*, vol. 11, p. 1, 3 2019, ISSN: 23317019. DOI: 10.1103/PhysRevApplied.11.034015.

[197] Y. Pan *et al.*, "A Multilevel Cell STT-MRAM-Based Computing In-Memory Accelerator for Binary Convolutional Neural Network," *IEEE Transactions on Magnetics*, vol. 54, 11 2018, ISSN: 00189464. DOI: 10.1109/TMAG.2018.2848625.

[198] M. Romera *et al.*, "Vowel recognition with four coupled spin-torque nano-oscillators," *Nature*, vol. 563, pp. 230–234, 7730 Nov. 2018, ISSN: 0028-0836. DOI: 10.1038/s41586-018-0632-y.

[199] J. Cai *et al.*, "Sparse neuromorphic computing based on spin-torque diodes," *Applied Physics Letters*, vol. 114, 19 2019, ISSN: 00036951. DOI: 10.1063/1.5090566.

[200] Y. B. Chen *et al.*, "Voltage-Driven Adaptive Spintronic Neuron for Energy-Efficient Neuromorphic Computing," *Chinese Physics Letters*, 2020, ISSN: 17413540. DOI: 10.1088/0256-307X/37/7/078501.

[201] M. Carpentieri *et al.*, "Micromagnetic study of electrical-field-assisted magnetization switching in MTJ Devices," *IEEE Transactions on Magnetics*, vol. 50, pp. 4–7, 11 2014, ISSN: 00189464. DOI: 10.1109/TMAG.2014.2327192.

[202] A. Fassatoui *et al.*, "Reversible and Irreversible Voltage Manipulation of Interfacial Magnetic Anisotropy in Pt/Co/Oxide Multilayers," *Physical Review Applied*, vol. 14, p. 064 041, 6 Dec. 2020, ISSN: 2331-7019. DOI: 10.1103/PhysRevApplied.14.064041.

[203] C. Fowley *et al.*, "Zero-field spin-transfer oscillators combining in-plane and out-of-plane magnetized layers," *Applied Physics Express*, vol. 7, p. 043 001, 4 Apr. 2014, ISSN: 1882-0778. DOI: 10.7567/APEX.7.043001.

[204] M. Kazemi, E. Ipek, and E. G. Friedman, "Adaptive Compact Magnetic Tunnel Junction Model," *IEEE Transactions on Electron Devices*, vol. 61, pp. 3883–3891, 11 Nov. 2014, ISSN: 0018-9383. DOI: 10.1109/TED.2014.2359627.

[205] Y. LeCun, C. Cortes, and C. J. Burges, *MNIST handwritten digit database, Yann LeCun, Corinna Cortes and Chris Burges*, 1998. [Online]. Available: http://yann.lecun.com/exdb/mnist/.

[206] H. Xiao, K. Rasul, and R. Vollgraf, "Fashion-MNIST: a Novel Image Dataset for Benchmarking Machine Learning Algorithms," pp. 1–6, 2017.

[207] V. Camus, L. Mei, C. Enz, and M. Verhelst, "Review and Benchmarking of Precision-Scalable Multiply-Accumulate Unit Architectures for Embedded Neural-Network Processing," *IEEE Journal on Emerging and Selected Topics in Circuits and Systems*, vol. 9, pp. 697–711, 4 Dec. 2019, ISSN: 2156-3357. DOI: 10.1109/JETCAS.2019.2950386.

[208] C. Chen and Z. Li, "A Low-Power CMOS Analog Multiplier," *IEEE Transactions on Circuits and Systems II: Express Briefs*, vol. 53, pp. 100–104, 2 2006, ISSN: 15583791. DOI: 10.1109/TCSII.2005.857089.

[209] R. Hamerly *et al.*, "Large-Scale Optical Neural Networks Based on Photoelectric Multiplication," *Physical Review X*, vol. 9, pp. 1–12, 2 2019, ISSN: 21603308. DOI: 10.1103/PhysRevX.9.021032.

[210] C. Ríos *et al.*, "In-memory computing on a photonic platform," *Science Advances*, vol. 5, pp. 1–10, 2 2019, ISSN: 23752548. DOI: 10.1126/sciadv.aau5759.

[211] J. Feldmann *et al.*, "Parallel convolutional processing using an integrated photonic tensor core," *Nature*, vol. 589, pp. 52–58, 7840 2021, ISSN: 14764687. DOI: 10.1038/s41586-020-03070-1.

[212] P. Yao *et al.*, "Fully hardware-implemented memristor convolutional neural network," *Nature*, 2020, ISSN: 14764687. DOI: 10.1038/s41586-020-1942-4.

[213] K. Yogendra *et al.*, "Computing with coupled Spin Torque Nano Oscillators," vol. 25-28-Janu, IEEE, Jan. 2016, pp. 312–317, ISBN: 978-1-4673-9569-4. DOI: 10.1109/ASPDAC.2016.7428030.

[214] L. Mazza, V. Puliafito, M. Carpentieri, and G. Finocchio, "Robustness of using degree of match in performing analog multiplication with spin-torque oscillators," *Solid-State Electronics*, vol. 183, p. 108 045, Sep. 2021, ISSN: 00381101. DOI: 10.1016/j.sse.2021.108045.

[215] M. Carpentieri, E. Martinez, and G. Finocchio, "High frequency spin-torque-oscillators with reduced perpendicular torque effect based on asymmetric vortex polarizer," *Journal of Applied Physics*, vol. 110, p. 093 911, 9 Nov. 2011, ISSN: 0021-8979. DOI: 10.1063/1.3657844.

[216] S. Louis *et al.*, "Low power microwave signal detection with a Spin-Torque Nano-Oscillator in the active self-oscillating regime," *2017 IEEE International Magnetics Conference, INTERMAG 2017*, vol. 53, pp. 6–9, 11 2017. DOI: 10.1109/INTMAG.2017.8007619.

[217] W. H. Rippard *et al.*, "Injection locking and phase control of spin transfer nano-oscillators," *Physical Review Letters*, vol. 95, pp. 10–13, 6 2005, ISSN: 00319007. DOI: 10.1103/PhysRevLett.95.067203.

[218] Y. Zhou, J. Persson, and J. Åkerman, "Intrinsic phase shift between a spin torque oscillator and an alternating current," *Journal of Applied Physics*, vol. 101, pp. 5–8, 9 2007, ISSN: 00218979. DOI: 10.1063/1.2710740.

[219] Y. Zhou *et al.*, "Oscillatory transient regime in the forced dynamics of a nonlinear auto oscillator," *Physical Review B - Condensed Matter and Materials Physics*, vol. 82, pp. 1–4, 1 2010, ISSN: 10980121. DOI: 10.1103/PhysRevB.82.012408.

[220] D. R. Rodrigues *et al.*, "Dynamical Neural Network Based on Spin Transfer Nano-Oscillators," *IEEE Transactions on Nanotechnology*, vol. 22, pp. 800–805, 2023, ISSN: 1536-125X. DOI: 10.1109/TNANO.2023.3330535.

[221] L. G. Wright *et al.*, "Deep physical neural networks trained with backpropagation," *Nature*, vol. 601, pp. 549–555, 7894 2022, ISSN: 14764687. DOI: 10.1038/s41586-021-04223-6.

[222] G. Furuhata, T. Niiyama, and S. Sunada, "Physical Deep Learning Based on Optimal Control of Dynamical Systems," *Physical Review Applied*, vol. 15, p. 034 092, 3 Mar. 2021. DOI: 10.1103/PhysRevApplied.15.034092.

[223] E. Haber and L. Ruthotto, "Stable architectures for deep neural networks," *Inverse Problems*, vol. 34, aa9a90, 1 2018, ISSN: 13616420. DOI: 10.1088/1361-6420/aa9a90.

[224] R. T. Chen, Y. Rubanova, J. Bettencourt, and D. Duvenaud, "Neural ordinary differential equations," *Advances in Neural Information Processing Systems*, vol. 2018-Decem, pp. 6571–6583, NeurIPS 2018, ISSN: 10495258.

[225] K. He, X. Zhang, S. Ren, and J. Sun, "Deep residual learning for image recognition," *Proceedings of the IEEE Computer Society Conference on Computer Vision and Pattern Recognition*, vol. 2016-Decem, pp. 770–778, 2016, ISSN: 10636919. DOI: 10.1109/CVPR.2016.90.

[226] A. Hamadeh *et al.*, "Autonomous and forced dynamics in a spin-transfer nano-oscillator: Quantitative magnetic-resonance force microscopy," *Physical Review B - Condensed Matter and Materials Physics*, vol. 85, pp. 2–5, 14 2012, ISSN: 10980121. DOI: 10.1103/PhysRevB.85.140408.

[227] M. N. Baibich *et al.*, "Giant magnetoresistance of (001)Fe/(001)Cr magnetic superlattices," *Physical Review Letters*, vol. 61, pp. 2472–2475, 21 1988, ISSN: 00319007. DOI: 10.1103/PhysRevLett.61.2472.

[228] S. Kaka *et al.*, "Mutual phase-locking of microwave spin torque nano-oscillators," *Nature*, vol. 437, pp. 389–392, 7057 2005, ISSN: 14764687. DOI: 10.1038/nature04035.

[229] P. M. Braganca *et al.*, "Nanoscale magnetic field detection using a spin torque oscillator," *Nanotechnology*, vol. 21, 23 2010, ISSN: 09574484. DOI: 10.1088/0957-4484/21/23/235202.

[230] L. Martins *et al.*, "Non-volatile artificial synapse based on a vortex nano-oscillator," *Scientific Reports*, vol. 11, pp. 1–7, 1 2021, ISSN: 20452322. DOI: 10.1038/s41598-021-95569-4.

[231] H. Fulara *et al.*, "Giant voltage-controlled modulation of spin Hall nano-oscillator damping," *Nature Communications*, vol. 11, pp. 1–7, 1 2020, ISSN: 20411723. DOI: 10.1038/s41467-020-17833-x.

[232] E. Ising, "Beitrag zur Theorie des Ferromagnetismus," *Zeitschrift für Physik*, vol. 31, pp. 253–258, 1 Feb. 1925, ISSN: 0044-3328. DOI: 10.1007/BF02980577.

[233] L. Onsager, "Crystal Statistics. I. A Two-Dimensional Model with an Order-Disorder Transition," *Physical Review*, vol. 65, pp. 117–149, 3-4 Feb. 1944, ISSN: 0031-899X. DOI: 10.1103/PhysRev.65.117.

[234] B. A. Cipra, "An Introduction to the Ising Model," *The American Mathematical Monthly*, vol. 94, p. 937, 10 Dec. 1987, ISSN: 00029890. DOI: 10.2307/2322600.

[235] A. Lucas, "Ising formulations of many NP problems," *Frontiers in Physics*, vol. 2, pp. 1–14, February 2014, ISSN: 2296-424X. DOI: 10.3389/fphy.2014.00005.

[236] S. Kirkpatrick, C. D. Gelatt, and M. P. Vecchi, "Optimization by Simulated Annealing," *Science*, vol. 220, pp. 671–680, 4598 May 1983, ISSN: 0036-8075. DOI: 10.1126/science.220.4598.671.

[237] Y. Fu and P. W. Anderson, "Application of statistical mechanics to NP-complete problems in combinatorial optimisation," *Journal of Physics A: Mathematical and General*, vol. 19, pp. 1605–1620, 9 1986, ISSN: 03054470. DOI: 10.1088/0305-4470/19/9/033.

[238] J. Cohen, "Non-Deterministic Algorithms," *ACM Computing Surveys (CSUR)*, vol. 11, pp. 79–94, 2 1979, ISSN: 15577341. DOI: 10.1145/356770.356773.

[239] A. M. Turing, "On Computable Numbers, with an Application to the Entscheidungsproblem," *Proceedings of the London Mathematical Society*, vol. s2-42, pp. 230–265, 1 1937, ISSN: 00246115. DOI: 10.1112/plms/s2-42.1.230.

[240] W. A. Borders *et al.*, "Integer factorization using stochastic magnetic tunnel junctions," *Nature*, vol. 573, pp. 390–393, 7774 Sep. 2019, ISSN: 0028-0836. DOI: 10.1038/s41586-019-1557-9.

[241] K. Y. Camsari, R. Faria, B. M. Sutton, and S. Datta, "Stochastic p-bits for invertible logic," *Physical Review X*, vol. 7, p. 031 014, 3 Jul. 2017, ISSN: 21603308. DOI: 10.1103/PhysRevX.7.031014.

[242] A. Grimaldi *et al.*, "Spintronics-compatible Approach to Solving Maximum-Satisfiability Problems with Probabilistic Computing, Invertible Logic, and Parallel Tempering," *Physical Review Applied*, vol. 17,

p. 024 052, 2 Feb. 2022, ISSN: 2331-7019. DOI: 10.1103/PhysRevApplied.17.024052.

[243] N. A. Aadit, A. Grimaldi, G. Finocchio, and K. Y. Camsari, "Physics-inspired Ising Computing with Ring Oscillator Activated p-bits," *Proceedings of the IEEE Conference on Nanotechnology*, vol. 2022-July, pp. 393–396, 2022, ISSN: 19449380. DOI: 10.1109/NANO54668.2022.9928681.

[244] N. Mohseni, P. L. McMahon, and T. Byrnes, "Ising machines as hardware solvers of combinatorial optimization problems," *Nature Reviews Physics*, vol. 4, no. 6, pp. 363–379, 2022, ISSN: 2522-5820. DOI: 10.1038/s42254-022-00440-8.

[245] I. Hen *et al.*, "Probing for quantum speedup in spin-glass problems with planted solutions," *Physical Review A - Atomic, Molecular, and Optical Physics*, vol. 92, pp. 1–24, 4 2015, ISSN: 10941622. DOI: 10.1103/PhysRevA.92.042325.

[246] N. Dattani, S. Szalay, and N. Chancellor, "Pegasus: The second connectivity graph for large-scale quantum annealing hardware," Jan. 2019.

[247] A. Biere, M. Heule, H. V. Maaren, and T. Walsh, *Handbook of Satisfiability*, A. Biere, M. Heule, H. V. Maaren, and T. Walsh, Eds. IOS Press, 2009, vol. 185 Frontiers in Artificial Intelligence and Applications, ISBN: 1586039296.

[248] S. Y. Yan, *Primality Testing and Integer Factorization in Public-Key Cryptography*. Springer US, 2009, vol. 11, ISBN: 978-0-387-77267-7. DOI: 10.1007/978-0-387-77268-4.

[249] N. A. Aadit *et al.*, "Massively parallel probabilistic computing with sparse Ising machines," *Nature Electronics*, vol. 5, pp. 460–468, 7 Jun. 2022, ISSN: 25201131. DOI: 10.1038/s41928-022-00774-2.

[250] F. Cai *et al.*, "Power-efficient combinatorial optimization using intrinsic noise in memristor Hopfield neural networks," *Nature Electronics*, vol. 3, pp. 409–418, 7 2020, ISSN: 25201131. DOI: 10.1038/s41928-020-0436-6.

[251] N. Shukla *et al.*, "Synchronized charge oscillations in correlated electron systems," *Scientific Reports*, vol. 4, pp. 1–6, 2014, ISSN: 20452322. DOI: 10.1038/srep04964.

[252] B. Kiraly *et al.*, "An atomic Boltzmann machine capable of self-adaption," *Nature Nanotechnology*, vol. 16, pp. 414–420, 4 2021, ISSN: 17483395. DOI: 10.1038/s41565-020-00838-4.

[253] D. Pierangeli, G. Marcucci, and C. Conti, "Large-Scale Photonic Ising Machine by Spatial Light Modulation," *Physical Review Letters*, vol. 122,

p. 213 902, 21 2019, ISSN: 10797114. DOI: 10.1103/PhysRevLett.122.213902.

[254] M. Yamaoka *et al.*, "A 20k-Spin Ising Chip to Solve Combinatorial Optimization Problems With CMOS Annealing," *IEEE Journal of Solid-State Circuits*, vol. 51, pp. 303–309, 1 Jan. 2016, ISSN: 0018-9200. DOI: 10.1109/JSSC.2015.2498601.

[255] R. Iimura, S. Kitamura, and T. Kawahara, "Annealing Processing Architecture of 28-nm CMOS Chip for Ising Model with 512 Fully Connected Spins," *IEEE Transactions on Circuits and Systems I: Regular Papers*, vol. 68, pp. 5061–5071, 12 2021, ISSN: 15580806. DOI: 10.1109/TCSI.2021.3114422.

[256] A. Grimaldi *et al.*, "Experimental evaluation of simulated quantum annealing with MTJ-augmented p-bits," *Technical Digest - International Electron Devices Meeting, IEDM*, vol. 2022-Decem, pp. 2241–2244, 2022, ISSN: 01631918. DOI: 10.1109/IEDM45625.2022.10019530.

[257] T. Preis, P. Virnau, W. Paul, and J. J. Schneider, "GPU accelerated Monte Carlo simulation of the 2D and 3D Ising model," *Journal of Computational Physics*, vol. 228, pp. 4468–4477, 12 2009, ISSN: 10902716. DOI: 10.1016/j.jcp.2009.03.018.

[258] B. Block, P. Virnau, and T. Preis, "Multi-GPU accelerated multi-spin Monte Carlo simulations of the 2D Ising model," *Computer Physics Communications*, vol. 181, pp. 1549–1556, 9 2010, ISSN: 00104655. DOI: 10.1016/j.cpc.2010.05.005.

[259] C. Cook *et al.*, "GPU-based Ising computing for solving max-cut combinatorial optimization problems," *Integration*, vol. 69, pp. 335–344, March Nov. 2019, ISSN: 01679260. DOI: 10.1016/j.vlsi.2019.07.003.

[260] *D-Wave Systems | The Practical Quantum Computing Company*. [Online]. Available: https://www.dwavesys.com/.

[261] T. Albash and D. A. Lidar, "Demonstration of a Scaling Advantage for a Quantum Annealer over Simulated Annealing," *Physical Review X*, vol. 8, p. 031 016, 3 Jul. 2018, ISSN: 2160-3308. DOI: 10.1103/PhysRevX.8.031016.

[262] P. A. Merolla *et al.*, "A million spiking-neuron integrated circuit with a scalable communication network and interface," *Science*, vol. 345, pp. 668–673, 6197 Aug. 2014, ISSN: 0036-8075. DOI: 10.1126/science.1254642.

[263] P. L. McMahon *et al.*, "A fully programmable 100-spin coherent Ising machine with all-to-all connections," *Science*, vol. 354, pp. 614–617, 6312 Nov. 2016, ISSN: 0036-8075. DOI: 10.1126/science.aah5178.

[264] Y. Nourani and B. Andresen, "A comparison of simulated annealing cooling strategies," *Journal of Physics A: Mathematical and General*, vol. 31, no. 41, pp. 8373–8385, Oct. 1998, ISSN: 0305-4470. DOI: 10.1088/0305-4470/31/41/011.

[265] D. J. Earl and M. W. Deem, "Parallel tempering: Theory, applications, and new perspectives," *Physical Chemistry Chemical Physics*, vol. 7, p. 3910, 23 Aug. 2005, ISSN: 1463-9076. DOI: 10.1039/b509983h.

[266] R. H. Swendsen and J.-S. Wang, "Replica Monte Carlo Simulation of Spin-Glasses," *Physical Review Letters*, vol. 57, pp. 2607–2609, 21 Nov. 1986, ISSN: 0031-9007. DOI: 10.1103/PhysRevLett.57.2607.

[267] T. Okuyama, M. Hayashi, and M. Yamaoka, "An Ising Computer Based on Simulated Quantum Annealing by Path Integral Monte Carlo Method," vol. 2017-Janua, IEEE, Nov. 2017, pp. 1–6, ISBN: 978-1-5386-1553-9. DOI: 10.1109/ICRC.2017.8123652.

[268] A. Z. Pervaiz, S. Datta, and K. Y. Camsari, "Probabilistic Computing with Binary Stochastic Neurons," IEEE, Nov. 2019, pp. 1–6, ISBN: 978-1-7281-0586-4. DOI: 10.1109/BCICTS45179.2019.8972719.

[269] M. Bernaschi *et al.*, "How we are leading a 3-XORSAT challenge: From the energy landscape to the algorithm and its efficient implementation on GPUs (a)," *Europhysics Letters*, vol. 133, p. 60 005, 6 Mar. 2021, ISSN: 0295-5075. DOI: 10.1209/0295-5075/133/60005.

[270] P. I. Bunyk *et al.*, "Architectural Considerations in the Design of a Superconducting Quantum Annealing Processor," *IEEE Transactions on Applied Superconductivity*, vol. 24, pp. 1–10, 4 Aug. 2014, ISSN: 1051-8223. DOI: 10.1109/TASC.2014.2318294.

[271] F. L. Traversa, P. Cicotti, F. Sheldon, and M. D. Ventra, "Evidence of Exponential Speed-Up in the Solution of Hard Optimization Problems," *Complexity*, vol. 2018, pp. 1–13, Jul. 2018, ISSN: 1076-2787. DOI: 10.1155/2018/7982851.

[272] A. Grimaldi *et al.*, "A Comparison of Energy Minimization Algorithms for Solving Max-Sat Problem with Probabilistic Ising Machines," vol. 2023-July, IEEE, Jul. 2023, pp. 698–702, ISBN: 979-8-3503-3346-6. DOI: 10.1109/NANO58406.2023.10231311.

[273] K. Y. Camsari *et al.*, "Double-Free-Layer Magnetic Tunnel Junctions for Probabilistic Bits," *Physical Review Applied*, vol. 15, p. 1, 4 2021, ISSN: 23317019. DOI: 10.1103/PhysRevApplied.15.044049.

[274] K. Y. Camsari, S. Salahuddin, and S. Datta, "Implementing p-bits with Embedded MTJ," *IEEE Electron Device Letters*, vol. 38, pp. 1767–1770, 12 2017, ISSN: 07413106. DOI: 10.1109/LED.2017.2768321.

[275] S. Chowdhury *et al.*, "A Full-Stack View of Probabilistic Computing With p-Bits: Devices, Architectures, and Algorithms," *IEEE Journal on Exploratory Solid-State Computational Devices and Circuits*, vol. 9, pp. 1–11, 1 2023, ISSN: 23299231. DOI: 10.1109/JXCDC.2023.3256981.

[276] K. Kobayashi *et al.*, "CMOS + stochastic nanomagnets: heterogeneous computers for probabilistic inference and learning," pp. 1–19, 2023. DOI: https://doi.org/10.48550/arXiv.2304.05949.

[277] H. Lee, F. Ebrahimi, P. K. Amiri, and K. L. Wang, "Design of high-throughput and low-power true random number generator utilizing perpendicularly magnetized voltage-controlled magnetic tunnel junction," *AIP Advances*, vol. 7, 5 May 2017, ISSN: 2158-3226. DOI: 10.1063/1.4978320.

[278] A. Fukushima *et al.*, "Recent progress in random number generator using voltage pulse-induced switching of nano-magnet: A perspective," *APL Materials*, vol. 9, 3 Mar. 2021, ISSN: 2166-532X. DOI: 10.1063/5.0038974.